Novel Methods in Polymer Drug Delivery

By

Cameron Baptista

Sc.M., Brown University 2018

Submitted in partial fulfillment of the requirements for the Degree of Doctor of Philosophy in Biomedical Engineering, a joint program in the Division of Biology and Medicine and the School of Engineering at Brown University

Center for Biomedical Engineering
&
Department of Pathology and Laboratory Medicine

PROVIDENCE, RHODE ISLAND
MAY 2022

AUTHORIZATION TO LEND AND REPRODUCE THIS THESIS

As the sole author of this thesis, I authorize Brown University to lend it to other institutions or individuals for the purpose of scholarly research.

Date: _____ Signature: _____
Cameron Baptista, Author

I further authorize Brown University to reproduce this thesis by photocopying or other means, in total or in part, at the request of other institutions or individuals for the purpose of scholarly research.

Date: _____ Signature: _____
Cameron Baptista, Author

This dissertation by Cameron Baptista is accepted in its present form by the School of Engineering and Division of Biology and Medicine, as satisfying the thesis requirements for the degree of Doctor of Philosophy.

Date: _____ Signature: _____

Dr. Edith Mathiowitz, Advisor

Recommended to the Graduate Council

Date: _____ Signature: _____

Edith Mathiowitz Ph.D.

Date: _____ Signature: _____

Anubav Tripathi Ph.D.

Date: _____ Signature: _____

Eric Darling Ph.D.

Date: _____ Signature: _____

Vikas Srivastava Ph.D.

Approved by the Graduate Council

Date: _____ Signature: _____

Andrew G. Campbell, Ph.D., Dean of the Graduate School

CURRICULUM VITAE

Cameron M. Baptista

Providence, Rhode Island
Cameron_Baptista@brown.edu | (908)-763-5516

EDUCATION

Brown University
Providence, Rhode Island
September 2016- Current
Sc.M.: Biomedical Engineering
Ph.D. Candidate: Biomedical Engineering

Rutgers University
New Brunswick, New Jersey
September 2013- May 2016
BS: Chemical and Biochemical Engineering
Overall GPA: 3.5/4.0

Raritan Valley Community College
Branchburg, New Jersey
June 2012- May 2013
Major: Science & Math- Biology
Overall GPA: 3.74/4.0

RESEARCH

Brown University | Dr. Edith Mathiowitz's Lab
Providence, Rhode Island
September 2016- Current

Sanofi GLP-1RA Polymer Nanoparticle R&D:

- Lead research and development towards the formulation of a novel GLP-1 RA peptide nanoparticle delivery system, for long acting treatment of diabetes.
- Characterized encapsulation efficiency, release, size and stability using HPLC, SEM, DLS, and FTIR.

Takeda Entyvio® Polymer Nanoparticle R&D:

- Developed and characterized long acting Entyvio oral nanoparticle formulations.
- Conducted in-vivo isolated-loop PK studies in Wistar rats.
- Assisted in benchtop to pilot manufacturing scale up.

TherapyX Interleukin-10, Interleukin-12, and Other Protein Therapeutic Nanoparticle R&D:

- Managed pilot scale manufacturing of various protein therapeutic formulations for preclinical nonhuman primate studies.
- Directed physiochemical analysis of products.

Graduate Thesis Research:

- Developed manufacturing techniques for processing induced mesophase formation in non-mesogenic biodegradable polymers.
- Characterized mesophase molecular structure and thermal behavior using XRD, DSC, and PLM.
- Lead research and development towards long-acting drug delivery depots containing small molecule hydrophobic drugs.

Rutgers University | Dr. Ashutosh Goel's Lab
New Brunswick, New Jersey
May 2015- July 2015

- Studied the structure of borate glasses, in attempts to better understand their anomalous thermal expansion, melting temperature, and structure.
- Developed hands-on experience utilizing differential scanning calorimetry, dilatometry, and fourier transform infrared spectroscopy.

Rider University | Dr. Bruce Burnham's Lab
Princeton, New Jersey
January 2013- May 2013

- Studied the synthesis and biological activity of pyrrole nucleosides, which may have anticancer and antiviral properties.
- Utilized nuclear magnetic resonance spectroscopy, rotary evaporation, thin layer chromatography, and recrystallization methods.

WORK EXPERIENCE

Molecular MS Diagnostics | Analytical Chemist
Providence, Rhode Island
March 2017- March 2018

- Conducting assay and impurity HPLC tests for drug substances and products.
- Running dissolution and stability tests for drug delivery devices.
- Assisting in method development, verification, and validation to ensure highly accurate and precise results are obtained.
- Following strict protocols to meet both ISO 9000 and GMP standards.

Brown University | Research Assistant
Providence, Rhode Island
September 2017- Current

- Worked on the formulation of a new nanoparticle delivery system for a therapeutic agent.
- Conducted particle synthesis, dynamic light scattering size analysis, SEM imaging, and developed release profiles from HPLC quantified analysis.

Brown University | Teaching Assistant
Providence, Rhode Island
September 2017- January 2018

- Polymer Science for Biomaterials | 3 Semesters
- Drug & Gene Delivery | 2 Semesters
- Biomaterials | 1 Semester
- The Foundation of Living Systems | 1 Semester

Colgate-Palmolive | R&D Co-Op
Piscataway, New Jersey
July 2015- August 2016

- Worked on the formulation of a new oral care product.
- Conducted laboratory tests on products, such as various rheology, uptake, pH, and aging studies, to assess the product's performance and stability.
- Communicated ideas, results and issues to a project team and manager to support key decisions.
- Kept a detailed written record of experimental work, observations and summarized results.

PUBLICATIONS
& PATENTS

- **Cameron Baptista**, Aharon Azagury, Christopher M. Baker, Edith Mathiowitz. The characterization and quantification of the induced mesophases of poly-l-lactic acid. POLYMER, Volume 226, 4 June 2021, 123822. https://doi.org/10.1016/j.polymer.2021.123822

- **Cameron Baptista**, Aharon Azagury, Hyeseon Shin, Christopher M. Baker, Eileen Ly, Rachel Lee, Edith Mathiowitz. The effect of temperature and pressure on polycaprolactone morphology. POLYMER, Volume 191, 16 June 2020, 122227. https://doi.org/10.1016/j.polymer.2020.122227

- US Patent 20210186880A1 entitled "Oral Formulations with Increased Uptake" by Edith Mathiowitz, Aharon Azagury, and **Cameron Baptista**

ACKNOWLEDGMENTS

I would first and foremost like to thank Professor Edith Mathiowitz for the privilege and opportunity to pursue a doctorate degree in her lab. Her continuous guidance, encouragement, and enthusiasm towards this research have made my time as a Ph.D. candidate a rewarding experience. As a mentor she has taught me how to overcome many of the difficulties faced while conducting research, provided constant feedback and guidance to help develop and back my ideas, and curated a working environment that constantly emphasized and inspired the big picture significance of the research at hand. As a member of the Mathiowitz lab, I have worked with a team that I fully admire, aspire to represent, and am endlessly thankful for.

I am grateful to all Mathiowitz lab members, who helped create a collaborative environment and made my time here a rewarding experience: Stacia Furtado, Kosta Milovanovic, Aharon Azagury, Christopher Baker, Deanna Stueber, Alex Perl, Shiffoni Sukhlal, Travis Nguyen, Rosa Kim, Raj Sharan, Arona Mbaye, Anyaa Shah, Arianna Markel, Hyeseon Shin, James Peres-Rogers, Victoria Goldenshtein, Dominick Calvao, Austin Lessin, Tobias Clevinger, Sheila Velagapudi, Derek Rott, and Apoorva Rao.

I would also like to thank the members of my committee as well, Anubav Tripathi Ph.D., Eric Darling Ph.D., and Vikas Srivastava Ph.D.. The opportunity to pursue a doctorate degree at Brown University has been a privilege in every sense, and I am grateful to have a committee of esteemed faculty to challenge and guide me through this pursuit. In addition, thank you to everyone in the Brown community who has contributed towards making the graduate program a rewarding experience: Kareen Coulombe Ph.D., Jessica Bello, Melodie Vincenty, Maxwell Wojnowski, Crystal Miller, just to name a few.

Finally, I would like to thank my parents Dennis and Ann Baptista, my sister Aeriel Baptista, my brother in-law Jeff Hager, and partner Leah Widdicombe for their never-ending support and encouragement throughout my academic career. Without them, none of this would have been possible.

TABLE OF CONTENTS

LIST OF FIGURES

Background

Chapter 1

The Effect of Temperature and Pressure on Polycaprolactone Morphology

Chapter 2

The Characterization and Quantification of the Induced Mesophases of Poly-L-Lactic Acid

Chapter 3

The Impact of Processing-Induced Polycaprolactone Mesophases on the Controlled Release of Dexamethasone

Chapter 4

PLGA Nanoparticles for Long Acting Delivery of a Novel GLP-1 Receptor Agonist Peptide

LIST OF TABLES

ABSTRACT

The ability to encapsulate drugs in a polymer delivery vehicle can have significant practical benefits. Polymers may allow for greater apparent solubility, as well as increased stability of encapsulated drugs. The encapsulation of therapeutic agents in polymer delivery vehicles may also allow for more efficient and effective treatments by providing controlled release of drugs. In the work presented here, we aim to understand select biodegradable polymer behavior and morphology as a function of processing and manufacturing conditions with the ultimate goal of improving their performance as drug delivery vehicles.

The focal points of this thesis work reside in two independent projects, which both fall under the broad umbrella of polymeric drug delivery:

In Project 1, long acting polymeric delivery depots containing small molecule drugs are explored. The overarching goal of this work was to induce mesomorphic phases into non-mesogenic biodegradable polymers, Poly-l-lactic acid (PLA) and Polycaprolactone (PCL), for the application of long-acting implants to deliver small molecule hydrophobic drugs. Herein, we demonstrate a novel hydraulic compression processing approach to induce mesophase formation in both PLA and PCL. Release experiments conducted on PCL tablets loaded with a model small molecules drugs, dexamethasone, suggest that these processing induced mesophases may serve as a novel method for controlling the rate of drug diffusion. This change in diffusion behavior may be explained by the free volume associated with the induced mesophase morphology

In Project 2, polymeric nanoparticle containing biologic drugs are explored. The overarching goal of this project was to understand the impact of solvent and non-solvent choice in the process of Phase Inversion Nanoencapsulation (PIN) to help optimize and develop a poly (lactic-co-glycolic acid) (PLGA) nanoparticle formulation containing a novel glucagon-like peptide-1 receptor agonist (GLP-1 RA) for its long acting oral delivery in the treatment of type 2 diabetes (T2D). Herein, we demonstrate a correlation between the Gibbs energy of mixing between solvent and non-solvent and the resulting particle size, release profile, and encapsulation efficiency. This correlation may be explained though the mechanism of particle formation by supersaturation, nucleation, and growth upon adding a solubilized polymer or drug solution to a miscible non-solvent. Ultimately this correlation between Gibbs energy and particle formation provides a novel approach for the optimization of GLP-1 RA loaded PLGA nanoparticle formulations.

INTRODUCTION

Human civilization is bestowed by our ability to manipulate material properties. In the early days of civilization stone, wood, and ceramics were the defining materials that made up our world. As our intelligence and sophistication advanced, so did our materials. This sentiment that materials and the evolution of civilization are interdependent is expressed by the fact that entire eras are named after materials. First came the stone age, then followed were the iron and bronze ages, with each material ushering new functionality in day to day life. In this way, materials can be considered symbolic of human civilization and intelligence. Today, modern chemistry, physics, and engineering are greatly enhancing the development of materials. Scientists and engineers are now characterizing material structures more accurately, developing relationships between material structures and properties, and devising more material functionality by developing new processing techniques.

Our current era of civilization may very well be defined as the age of polymeric materials, with their prevalence arising only about 100 years ago. For the last century, the use of polymers in engineered products has increased dramatically. Since the Second World War, polymeric materials have been the fasted growing segment of the U.S.' chemical industry, with more than a third of the total chemical research dollars being spent on polymer research.[1] From automobiles and high tech electronic devices, to disposable food packaging and clothing fabric, polymers are undoubtedly one of the most significant materials in our modern society. Particularly, the utilization of polymers as biomaterials has greatly impacted the advancement of modern medicine. Polymers are one of the most commonly used materials for biomedical applications. They have been developed as drug delivery vehicles, prosthetic implants, tissue engineering scaffolds, bone

cement, dental materials, sutures, and a vast number of other products in the biomedical field.[2] This is owed to the fact that polymers have flexible chemistry that allows for a diverse range of mechanical and physical properties to be displayed.

Herein, the work outlined in this dissertation explores novel methods towards improving the use of polymeric biomaterials in drug delivery applications.

SCOPE OF THIS WORK

The ability to encapsulate drugs in polymer delivery vehicles can have significant practical benefits. Polymers may allow for greater apparent solubility, as well as increased stability of encapsulated drugs. The encapsulation of therapeutic agents in polymer delivery vehicles may also allow for more efficient and effective treatments by providing controlled release of drugs, in both constant and cyclic dosages. [3,4] These delivery systems have been successfully developed for all types of therapeutics, both hydrophilic and hydrophobic, ranging from both small molecule to larger biological drugs, such as proteins. [4] Thus, the rational design of polymer systems for tailored drug delivery has dominated the field of pharmaceuticals in recent years.

In utilizing polymer biomaterials for drug delivery applications, many important properties must be considered. These materials must (1) not evoke a sustained immune response; (2) possess a degradation time and drug release coinciding with their therapeutic function; (3) have appropriate mechanical and physical properties for their intended use; (4) produce non-toxic degradation products that can be readily resorbed or excreted; and (5) include appropriate process-ability for their designed application.[2] These properties may be determined by several features of the material. Specifically, material chemistry, structural morphology, and processing history can have a

significant impact on the performance of a polymeric drug delivery device. Thus, in this work, we aim to understand select biodegradable polymer behavior and morphology as a function of processing and manufacturing conditions with the ultimate goal of improving their performance as drug delivery vehicles.

The focal points of this thesis work reside in two independent projects, which both fall under the broad umbrella of polymeric drug delivery:

PROJECT 1:

LONG-ACTING POLYMERIC DELIVERY DEPOTS CONTAINING SMALL MOLECULE DRUGS

The overarching goal of this project is to induce mesomorphic phases into non-mesogenic biodegradable polymers, Poly-l-lactic acid (PLA) and Polycaprolactone (PCL), for the application of long-acting implants to deliver small molecule hydrophobic drugs.

There is currently a limited understanding in regards to how mesophase morphology is manifested in polymers such as PLA and PCL, which are not typically regarded as mesomorphic. In addition, the bulk of literature in this area is limited to this structure formation due to stretch or flow based processes. [5–7,8–11] As a result, the applicational benefits of this phenomenon have been greatly limited to fibers and films. In the work outlined here, the induction of mesophase morphology is assessed using a temperature controlled hydraulic compression processing method.

The novelty of this approach is that by inducing mesophase morphology into non-mesogenic polymers with hydraulic compression, the properties of mesophases could potentially be exploited in products that would not be possible through other conventional engineering

techniques, such as stretch or flow processing. Particularly, many polymeric drug delivery systems are often produced via hydraulic compression. In the application of mesophase polymers as drug delivery vehicles, it is hypothesized that the formation of mesophase morphology could alter the rate of polymer degradation and drug release kinetics when compared to that of an identical amorphous or semi-crystalline material.

The rate at which polymers degrade by hydrolysis is known to be morphology dependent. It has been shown that the amorphous phase degrades more rapidly than the crystalline form during hydrolysis.[12] This can be understood from a thermodynamic perspective as the amorphous phase occupies the highest Gibbs free energy and the crystalline phase occupies the lowest free energy. To this end, polymer mesophases occupy a free energy that is considered intermediate between the crystalline and amorphous phases. Thus, the formation of mesophase morphology may create opportunities to tailor the degradation rate of these materials.

Further, a major challenge in the field of polymeric drug delivery is the ability to control the rate at which a drug is released from the device. The main driving forces of drug release in PCL and PLA systems are diffusion of the drug through the polymer matrix and material degradation in which the drug is released upon hydrolysis of the polymer matrix.[13] The rate of diffusion of drug through a polymer matrix is generally regarded as being dependent on the free volume of the matrix (more free volume, faster diffusion).[14] Thus a decrease or increase in free volume associated with the induced mesophase morphology may serve as a means for controlling the rate of drug diffusion.

To this end, the questions motivating this research are: To what degree can we induce mesophase morphology into non-mesogenic biodegradable polymers via hydraulic compression? What is the structural nature of these induced mesophases? What effect does the resulting

morphology have on the thermal and physical properties of the material? Can we use our findings to engineer a polymer morphology that will help optimize their performance as drug delivery vehicles?

POJECT 2:

POLYMERIC NANOPARTICLES CONTAINING BIOLOGIC DRUGS

The overarching goal of this project is to understand the impact of solvent and non-solvent choice in the process of Phase Inversion Nanoencapsulation (PIN) to help optimize and develop a poly (lactic-co-glycolic acid) (PLGA) nanoparticle formulation containing a novel glucagon-like peptide-1 receptor agonist (GLP-1 RA) for its long acting oral delivery in the treatment of type 2 diabetes (T2D).

There have been a number of studies which report the encapsulation of GLP-1 RAs in PLGA or polylactic acid (PLA) particles. [15–27] However, to our knowledge, AstraZeneca's Bydureon® is the only PLGA particle formulation to reach the market for the delivery of a GLP-1 RA.[28] To this end, Bydureon® is a relatively large particle formulation (particle size ~50 μm) and is currently limited to a once weekly subcutaneous injection.[28,29] Thus, from the perspective of both the pharmaceutical industry and patients alike, the ability to convert an approved injectable peptide or protein into a non-injected formulation would represent a major advance in treatment. However, achieving this has proven to be a challenge.

There are many unique challenges in the formulation of peptide and protein nanoparticle delivery systems that must be addressed to achieve consistent clinical performance. To start, a key

barrier to clinical success is often the ability to achieve a tailored sustained release profile of the drug cargo from the nanoparticle delivery system.[30–33] Compounding this challenge, the size, surface charge, and shape of the nanoparticles must also be tailored as these factors have a key role in the biodistribution and fate of the drug *in vivo*.[34–39] To add, even in instances where successful therapeutic performance is achieved, formulations often face technical challenges associated with drug stability, drug loading efficiency, scale up feasibility, batch to batch consistency, and economic viability. [31,33,40,41]

Currently, the most common methods for producing GLP-1 RA loaded PLGA particles require an initial step of emulsifying a polymer solvent in an aqueous non-solvent. [15–27] This emulsification step poses many challenges for the success of formulations containing peptide and protein drugs. Both the high sheer rate and oil-water interfaces formed during emulsification are prone to destroying the secondary and tertiary structures of biologic APIs.[42–44] These emulsion processes may also be riddled with low encapsulation efficiencies, due to the use of an aqueous phase in which the drug is soluble. In addition, the emulsion droplet size is often a limiting factor on the ultimate size of the nanoparticles produced.[33] In the work presented here, we demonstrate the production of GLP-1 RA loaded PLGA nanoparticle through a method termed phase inversion nanoencapsulation (PIN), which is designed to combat these issues.[45]

The novelty of this approach is that the mechanism of precipitation by phase inversion utilizes solvent and non-solvent pairs which are completely miscible, avoiding the key issues associated with emulsification. In the PIN process, nanoparticles spontaneously precipitate after the immersion of a solubilized polymer solution in a non-solvent. Upon addition, the mechanism of polymer phase inversion is thought to occur in three key steps: supersaturation, nucleation, and growth. [46]

To this end, it is thought that the properties and mixing behavior of the solvent and non-solvent pairs used in the phase inversion process may impact the degree of supersaturation, nucleation and growth that occurs. Ultimately, it is hypothesized that these variations in mixing behavior may impact the size, drug loading efficiency, and drug release profile of the resulting nanoparticles. However, currently there is little to no in-depth or quantitative knowledge regarding this association, nor does a process exist which is designed to specifically exploit the use of different solvent and non-solvent pairs for optimized drug encapsulation and release from polymeric nanoparticles. Thus, herein we seek to fill this gap in knowledge and further the understanding of how solvent choice impacts the PIN process upon encapsulating a GLP-1 RA peptide in PLGA nanoparticles.

The questions motivating this research are: How do varying solvent and non-solvent pairs impact the thermodynamics of drug and particle formation in the PIN process? What properties of the solvent and non-solvent can be used to explain and model this phenomenon of particle formation? Can solvent and non-solvent choice serve as a variable to optimize GLP-1 RA encapsulation efficiency, burst release, and release rate from Poly (lactic-co-glycolic acid) (PLGA) nanoparticles?

SPECIFIC AIMS

PROJECT 1

Long-Acting Polymeric Delivery Depots Containing Small Molecule Drugs

AIM 1: Induce mesophase morphology in biocompatible polymers, PLA and PCL, and characterize their molecular arrangement using: XRD, DSC, and PLM

AIM 2: Develop long acting drug delivery depots containing hydrophobic small molecule drugs utilizing mesophase morphology.

PROJECT 2

Polymeric Nanoparticles Containing Biologic Drugs

AIM 1: Engineer drug and polymer particles using phase inversion nanoencapsulation and assess the impact of solvent and non-solvents pairs on the thermodynamics of particle formation.

AIM 2: Using a GLP-1 receptor agonist, for the treatment of diabetes, develop a polymer nanoparticle formulation (PO, IP, or SC) and investigate the effect of solvent and non-solvents pairs on the drug encapsulation efficiency and release profiles.

BACKGROUND

Project 1:

LONG-ACTING POLYMERIC DELIVERY DEPOTS CONTAINING SMALL MOLECULE DRUGS

LONG-ACTING POLYMERIC DRUG DELIVERY DEPOTS

A major challenge in creating long-acting polymeric drug delivery depots is the ability to control the rate at which a drug is released from the device. The main driving forces of drug release is typically diffusion of the drug through the polymer matrix and material degradation in which the drug is released upon hydrolysis of the polymer matrix.[13] Both rate of diffusion and polymer degradation is known to be dependent on polymer morphology.[14] Thus, here we seek to explore polymer morphology and further our understanding of the impact on drug diffusion.

POLYMER MORPHOLOGY

Polymer morphology is a term used to refer to the structural arrangement of the polymer chains. Polymers are generally classified by their structural arrangement into two categories: amorphous polymers (unstructured) or semi-crystalline polymers. Amorphous polymers have a randomly oriented isotropic structure and are characterized as having a glass transition temperature but no melting temperature. Semi-crystalline polymers consist of both amorphous regions and crystalline regions and are characterized as having both a glass transition temperature and a melting temperature. The crystalline regions of polymers are most commonly a spherulite morphology.

Spherulites are radially-oriented lamellar crystals which are connected by an interlamellar amorphous phase.[1]

Due to the long chain nature of polymers, the amorphous phase can be oriented to obtain anisotropic properties. In orienting, the structural units of the material preferentially align along an orientation axis. This orientation of the polymer structure can be considered a mesophase (derived from the greek word "meso" meaning "in the middle").[47,48] The term mesophase was first coined in 1922 by Friedel, and is used to describe morphology that is an intermediate degree of organization between the conventional amorphous and semi-crystalline phases. The types of mesophases can be classified as liquid crystals, plastic crystals, and conformationally disordered (condis) crystals; these phases have been extensively reviewed by Wunderlich et. al..[48]

This phenomenon of mesophase orientation is most notably seen in liquid crystal polymers. Due to their oriented fluid phase, liquid crystalline polymers are often used as precursors to high-performance solids, such as fibers, films, and injection molded products. A notable example of liquid crystal orientation is Kevlar, which is a material made from polymeric fibers spun from a polyamide liquid crystal. Due to the high degree of orientation in the molten liquid phase, upon cooling Kevlar maintains this orientation and forms highly durable fibers. The large number of Van Der Waals forces that result from Kevlar's oriented structure can provide strength in tension up to 200 Mpa, which is ten times that of steel. This oriented structure also endows Kevlar with a high impact toughness, allowing for its application in bulletproof vests. Kevlar is also a superior insulator, with a thermal conductivity of 0.0482 W/mK, similar to that of fiber glass insulation.[49,50]

It is well established that the oriented nature of liquid crystalline polymers allows for applicational benefits such as increased tensile strength and impact toughness, decreased rate of degradation, increased shelf life, decreased permeability to gases, and increased thermal

conductivity with low electrical conductivity compared to that of conventional amorphous and semi-crystalline polymers.[3,49,51] However, despite these attractive properties, very few liquid crystal or mesomorphic polymers have been commercialized for biomedical applications.

This may be attributed in part to the fact that for a polymer to naturally display mesomorphic properties, it must contain mesogenic moieties within the polymer chain. Mesogens are rigid and linear regions of a polymer that cause it to align in the molten phase. The placement of these mesogens typically controls the type of liquid crystalline polymer formed. Polymer liquid crystals generally can be divided into two types: main-chain liquid crystal polymers and side-chain liquid crystal polymers. Main-chain liquid crystal polymers are formed when the mesogens are themselves part of the main chain of a polymer. Conversely, side chain liquid crystal polymers are formed when the mesogens are connected as side chains to the polymer by a flexible bridge, or spacer. Detailed reviews on the necessary molecular requirements for the formation of a mesogenic moiety and display of mesogenic properties in a polymer has been extensively reviewed elsewhere. [7,52,53] Generally speaking, commonly used biodegradable polymers, such as PLA and PCL, do not contain mesogenic properties and do not spontaneously form these morphologies under typical conditions.

PROCESSING-INDUCED MESOPHASE MORPHOLOGY

Various techniques have been used to induce mesophases into polymers that don't naturally display this morphology under typical conditions. There are essentially two types of methods currently used to induce orientation into non-mesogenic polymers: mechanical stretching techniques and flow techniques.

Mechanical stretching techniques, such as uniaxial drawing and biaxial stretching, are an approach which utilize tensile stretching to elongate the polymer while in the solid state. In order for the polymer to stretch, the secondary bonds between the polymer chains must break. Therefore, heat it often used to reduce the amount of force required to stretch. The result of stretching is an anisotropic mesophase morphology. [5–7]

Flow techniques such as extrusion, rolling, and fiber spinning are an approach which utilize shear flow induced orientation in the molten state. Polymers can be oriented while flowing in the molten state, and this orientation can be maintained in the solid state if the fiber is cooled below the melting point while the alignment is taking place. Although these methods involve very different physical processes from that of mechanical stretching, they all result in similar mesophase morphologies with similar thermal and mechanical properties. [8–11]

Recent work published by the Mathiowitz Lab suggests that polymer mesophase structures may also be induced in non-mesogenic polymers via hydraulic compression, rather than stretching or flow-based methods. The compression method includes the steps of (1) heating the polymer to a desired temperature (2) exposing the polymer to a set pressure for time periods varying between 5 and 15 minutes, while maintaining the temperature; and (3) cooling the polymer while maintaining the elevated pressure. [54]

Prior Work on Pressure-Temperature Induced Mesophases

A systematic characterization of PLA morphology as a function of pressure, temperature, and time processing conditions was previously published by the Mathiowitz lab.[54] This work utilized differential scanning calorimetry, x-ray diffraction, and polarized light microscopy to analyze the morphological changes occurring in PLA under various temperature-pressure-time

profiles. In summary, these results include: (a) characterization of thermal properties, T_g , ΔH_{ER}, and ΔC_p through the application of DSC; (b) quantification of crystallinity through the calculated heat of fusion (ΔH) divided by the theoretical ΔH value of 100% crystalline material; (c) quantification of crystallinity based on XRD profiles; (d) structure analysis through the assessment of birefringent properties under polarized optical light microscopy.[54] This work is briefly described below.

PLA was processed with the method described above. Samples were individually subjected to pressures ranging from 2,000 lb_f to 20,000 lb_f, and temperatures from 52°C to 85°C for time periods between 5 min and 15 min. A representative polarized light microscopy image of the induced orientation can be seen in Figure 1 Crossed polarized images of PLA both before and after treatment taken from Baker et. al.[54]

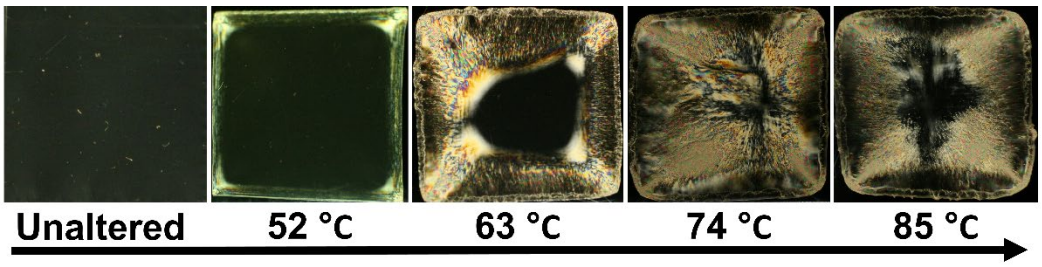

FIGURE 1 CROSSED POLARIZED IMAGES OF PLA BOTH BEFORE AND AFTER TREATMENT TAKEN FROM BAKER ET. AL.54

The T_g, $\Delta H_{ER,}$ and ΔC_p of processed PLA samples were then calculated from the data acquired by the DSC analysis depicted in Figure 2, which depicts 4 pairs of DSC heating profiles representing the first heat (solid line) and the second heat (dotted line) of PLA samples processed at varying temperatures (52°C, 63°C, 74°C, and 85°C). Note that each sample in this graph was processed at 20,000 lb_f for 15 min. It was found that multiple endotherms were present through the glass transition of pressure-temperature treated samples, suggesting the formation of multiple

morphologies during processing. These results analyzed in tandem with the birefringent properties of the sample suggested that the post-T_g endotherm could correspond to a liquid crystal type morphology present in the PLA.[54]

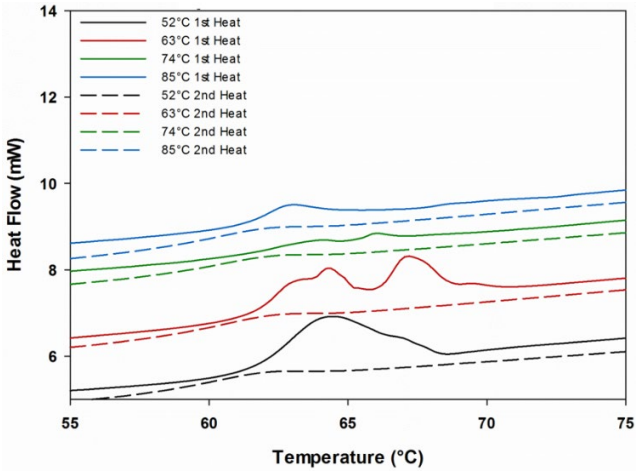

FIGURE 2 DSC HEATING TRACES OF PLA PROCESSED UNDER 20,000 LBF , FOR A DURATION OF 15 MIN, AT VARYING TEMPERATURES (52°C, 63°C, 74°C, AND 85°C) TAKEN FROM BAKER ET. AL.[54]

Typically, birefringence that results from residual processing stresses is anisotropic along a single axis, thus rotating the material under polarized light results in the extinction of the birefringent effect. However, the birefringent analysis of the samples processed in this study showed that rotation of the samples did not result in extinction of the birefringent effect. [54] This strongly suggests that the morphology is oriented in the radial direction of the sample.

While XRD analysis of the processed samples did not directly provide evidence of a mesophase formation, the resulting assessment of crystallinity provided a potential mechanism of the mesophase formation. Based on the results of this study, it was hypothesized that processing PLA under various pressure-temperature profiles could result in a liquid crystal morphology. The mechanism of this formation was hypothesized to be related to crystal formation. It was theorized that pressure-temperature treatment could result in a decreased crystal size and increased crystal

concentration. These changes in crystallinity could then be attributed to a more restricted environment which causes the amorphous region to orient.[54] However, to test this hypothesis and more accurately characterized the nature of the morphological changes within PLA under these conditions, further analysis must be conducted.

Herein we seek to build on this work and analyze the induced pressure-temperature morphology of both PLA and PCL using modulated differential scanning calorimetry, x-ray diffraction, hot-stage x-ray diffraction, x-ray peak deconvolution, polarized light microscopy, and hot-stage polarized light microscopy.

Differential and Modulated Differential Scanning Calorimetry

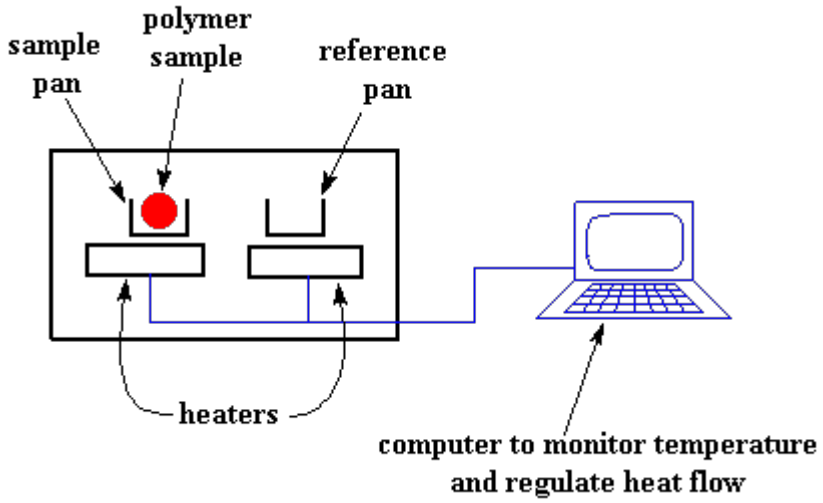

FIGURE 3 SCHEMATIC REPRESENTATION OF DSC (IMAGE TAKEN FROM HTTP://PSLC.WS/MACROG/DSC.HTM)

Differential Scanning Calorimetry (DSC) is an analytical method which utilizes the measurement of heat flow into or out of a sample as a function of temperature or time. To accomplish this measurement, a sample is placed in an aluminum sample pan which is then placed in the DSC's sample compartment. Conversely, an empty reference pan is placed in the reference

compartment for comparison upon heating and cooling. By heating or cooling both compartments simultaneously while monitoring the thermocouples, the differential heat flows of each sample can be calculated. Using this data, the DSC software can calculate the materials glass transition temperature, melting temperature, as well as additional thermal properties such as specific heat capacity and heat of fusion.[55]

DSC techniques are widely employed to measure the enthalpy change of amorphous polymers as a function of temperature. Figure 4 shows a typical DSC scan of an aged (first heat) and quenched (second heat) PLA specimen upon heating and reheating.

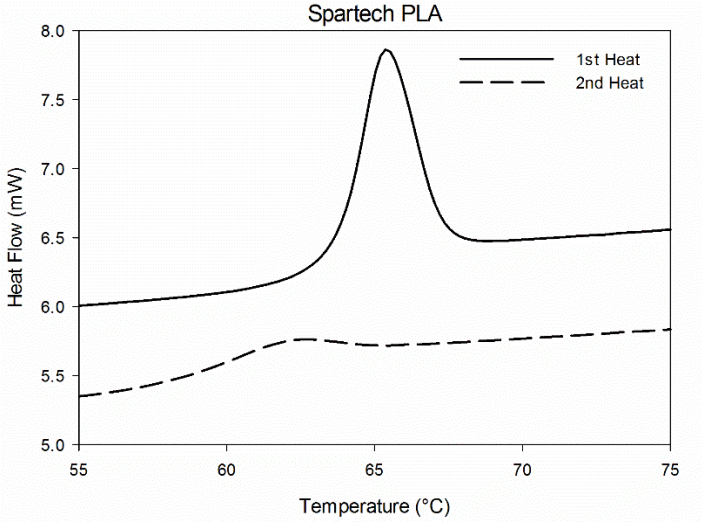

FIGURE 4 DSC TRACE OF AGED (1ST HEAT) AND QUENCHED (2ND HEAT) SPARTECH PLA[54]

The first heating of the PLA specimen shows the thermal history of the aged sample, as received from Spartech Packaging Technology. Upon heating above the melt, and cooling at a rate of 10 °C/min, the sample was reheated to display the typical thermal history of a quenched sample. For the quenched specimen during the second heat, the heat flow increased upon heating due to gradual increase of the specific heat capacity from the glassy heat capacity to the rubbery heat

capacity. In comparison, the aged specimen during the first heating showed an endothermic overshoot, caused by enthalpy loss from structural relaxation during the aging period. Structural relaxation plays an important role in the performance of polymers. The structure of an amorphous polymer is unable to rearrange towards an equilibrium state instantaneously at temperatures near the glass transition. Thus, longer aging times result in a more sluggish structure (since it is closer to the equilibrium state), which is represented by an increase in density and viscosity, and a decrease in enthalpy and mobility.

Further structural details can be obtained through a method known as Modulated Differential Scanning Calorimetry (MDSC). This method allows for the separate analysis of changes in specific heat, such as the glass transition, from kinetically-controlled processes such as crystallization. MDSC accomplished this separation through a step wise temperature profile in which the temperature is raised at a specific rate then held constant in a cyclic manner. The heat flow response from this temperature profile can then be split into two separate curves. The response during the heating step is associated with the specific heat of the material, while the response where the temperature is held constant is associated with the slower kinetic processes. In other words:

$$\frac{dq}{dt} = C_p(T) \cdot \beta + \frac{dq}{dt}(T, t)$$

Where, $\frac{dq}{dt}$ is the total heat flow, $C_p(T)$ is the specific heat, β is the scan rate, and $\frac{dq}{dt}(T, t)$ is the heat flow from the kinetic processes.[56]

Overall, the thermal properties obtained by DSC and MDSC methods can be strong indicators into the nature of a polymer's structural morphology.

X-RAY DIFFRACTION

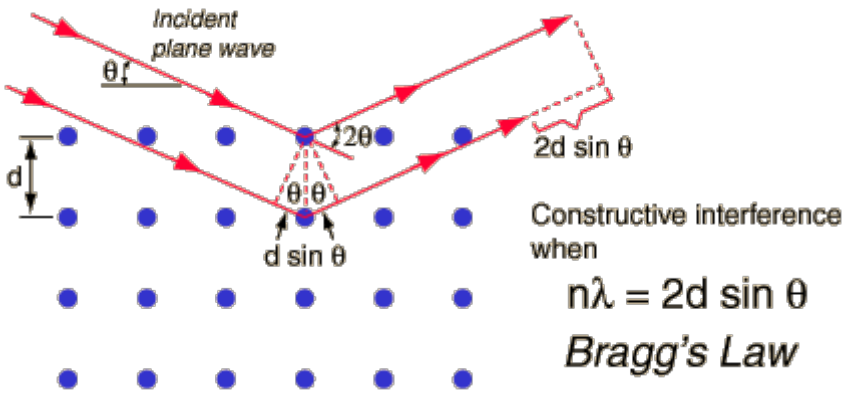

FIGURE 5 DEPICTION OF BRAGG'S LAW USED IN XRD (IMAGE TAKEN FROM HTTP://HYPERPHYSICS.PHY-ASTR.GSU.EDU/HBASE/QUANTUM/BRAGG.HTML)

XRD uses the concept of x-ray diffraction and scattering upon encountering an obstacle to elucidate or provide its user with details of the materials atomic spacing and molecular structure. These details include a materials crystal structure and size. This technique exploits the use of x-rays are a type of electromagnetic radiation possessing high energies with short wavelengths on the order of the inter-atomic spacing within solids. Thus, when two x-ray beams diffract off of a material, the scattered waves either reinforce (constructively interfere) or destructively interfere with one another. When the scattered waves remain in phase, the resulting wave from adding the two together is twice the amplitude of the original. If the scattered waves are out of phase, the resulting wave has an amplitude of zero. The resulting phase relationship can also be an intermediate between these two extreme. This phenomenon is best modeled by Bragg's Law.[57]

Since amorphous materials do not possess uniform atomic spacing (variable "d" seen in the Bragg's Law Equation of Figure 5) the x-ray diffractogram will record a broad peak corresponding to the waves scattering in many directions. Conversely, high intensity narrower peaks are indicative of crystalline order.

POLARIZED OPTICAL LIGHT MICROSCOPY

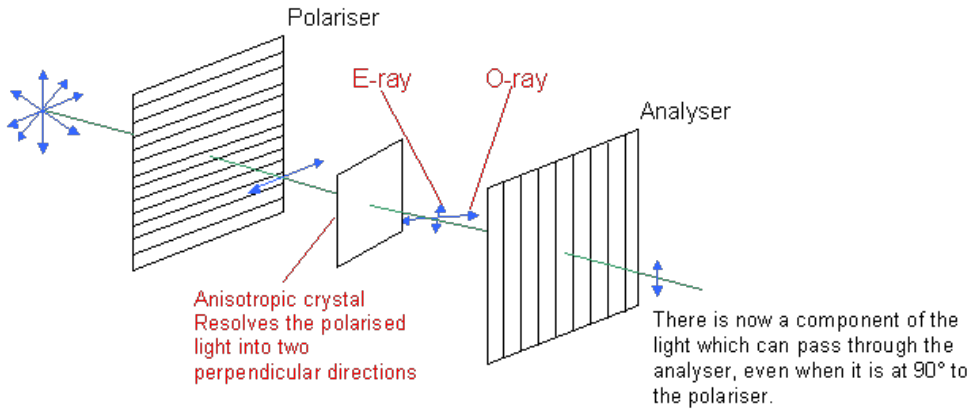

FIGURE 6 SCHEMATIC REPRESENTATION OF BIREFRINGENCE (IMAGE TAKEN FROM HTTP://WWW.ICBL.HW.AC.UK/LEARNEM/DOITPOMS/OPTICALMICROSCOPY/PMICROSCOPY.HTM)

Some mesophase morphologies are characterized by an optical property called birefringence. Birefringence is defined as the decomposition of a ray of light into two rays, upon passing through a material with dependence on the polarization of the light. This phenomenon can be explained by the anisotropic orientation inherent in birefringent materials. As light passes through a material that has structural orientation in a single direction, the passing light will also align in the direction of the orientation axis. This effect is known as single refraction. Consequently, as light passes through a material possessing multiple indices of refraction, it is broken down into a variety of different directionalities and can be observed as a colorful birefringent effect. [58]

The detection of birefringence is a simple process and can be accomplished using a microscope equipped with polarized filters. When a structurally oriented mesophase material is placed between two cross polarizing filters and exposed to a white light source, a display of birefringence can be seen.

Project 2:

Polymeric Nanoparticles Containing Biologic Drugs

Glucagon-Like Peptide-1 Receptor Agonists for the Treatment of Diabetes

Type 2 diabetes (T2D) has recently reached epidemic proportions in both developed and developing counties, and is intimately associated with the growing occurrence of obesity.[59] T2D is a chronic disease characterized by hyperglycemia due to defective insulin secretion and resistant to insulin action. In the treatment of diabetes, glucagon-like peptide-1 receptor agonists (GLP-1 RAs) are the only class of glucose lowering agents associated with weight loss. Other agents such as metformin, DPP-4 inhibitors, and basal insulin are regarded as being either weight neutral or weighting gaining.[60] GLP-1 RAs stimulate insulin secretion after an oral glucose load via the incretin effect. In type 2 diabetes, this process can become blunted or even be absent; however, the utilization of pharmacological levels of GLP-1 can revive insulin excretion.[61]

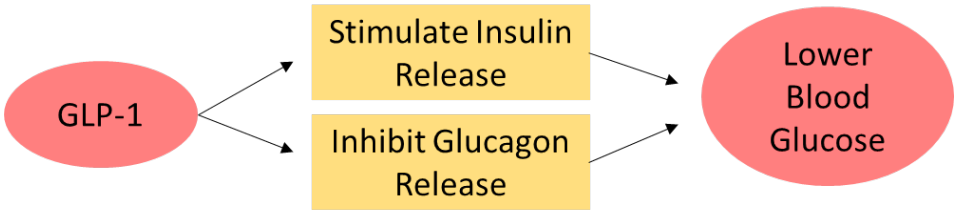

FIGURE 7 BLOOD GLUCOSE LOWERING MECHANISM OF GLP-1

Therapy with GLP-1 RAs is typically based on self-administration by subcutaneous injection using a pen device or syringe. Examples of GLP-1 RAs that are currently approved for diabetes treatment include: twice-daily exenatide BID (Byetta , BMS), once-daily lixisenatide (Lyxumia, Sanofi/Zealand), once-daily liraglutide (Victoza, Novo Nordisk) and once-weekly

exenatide LAR (Bydureon, BMS). Current optimization of GLP-1 RAs aim to improve efficacy, tolerability, patient compliance, frequency of dosages, and ease of administration. [59]

POLYMER NANOPARTICLES FOR BIOLOGIC DRUG DELIVERY

One of the major challenges in the field of peptide and protein drugs is their delivery to the site of action. Due to their high molecular weight and susceptibility to degradation by both enzymes and extreme pH values, peptides and proteins usually display poor absorption across epithelial membranes and exhibit low oral bioavailability. For this reason, the majority of peptide and protein therapeutics are currently administered by injection. In some cases, even upon injection, these molecules are rapidly metabolized and cleared from circulation and therefore can require multiple injections to be administered daily.[41] Thus, from the perspective of both the pharmaceutical industry and patients alike, the ability to reduce the frequency of injections or convert an approved injectable peptide or protein into a non-injected formulation would represent a major advance in treatment. A leading approach in this effort has been through the utilization of biodegradable polymeric nanoparticles. However, there are many complexities associated with the production of these formulations and there have been many cases in which products have failed to reach clinical success.[38,39,41,62–65]

CHALLENGES OF CONVENTIONAL NANOPARTICLE PREPARATION

Solvent evaporation is one of the most commonly utilized method for preparing drug loaded polymeric particles. Typically in the solvent evaporation process, high-energy homogenization or sonication is used to produce an emulsion between a polymer-drug solution and an aqueous phase containing a surfactant, typically PVA. The resulting oil-in-water (o/w) emulsion is stirred and stabilized to allow for the evaporation of the organic solvent and

precipitation of polymeric particles. Upon precipitating, the polymer may entrap the drug that was present in each droplet, resulting in the formation of drug loaded polymeric particles. These particles may then be collected through centrifugation, filtration or dialysis.

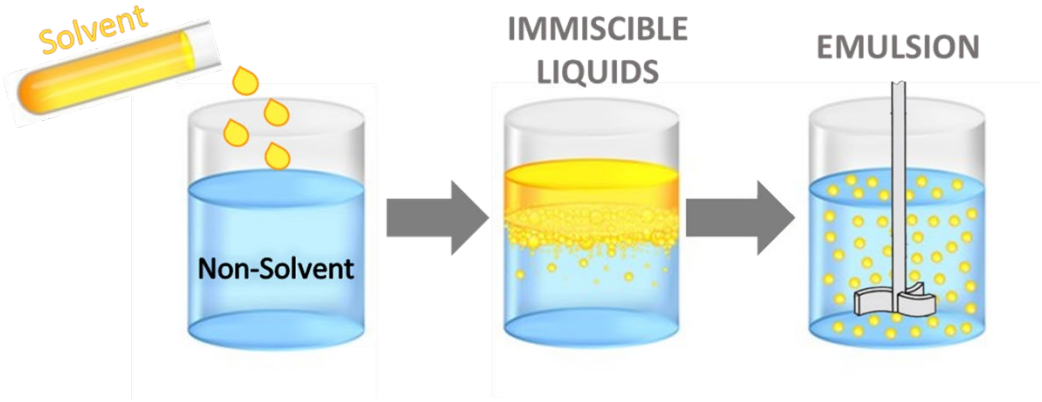

FIGURE 8 EXAMPLE OF IMMISCIBLE SOLVENT BEHAVIOR IN EMULSION NANOPARTICLE PRODUCTION TECHNIQUES

While these techniques may be suitable for small molecule drug formulations, many large biologic drugs with secondary and tertiary structures are likely to denature as a result of both the high shear environment and oil-water interface formed during the emulsification process. [42–44] These emulsion processes may also be riddled with low encapsulation efficiencies, due to the use of an aqueous phase in which the drug is soluble. [33] The loss of drug bioactivity in these instances is primarily problematic due to the high cost of many protein therapeutics, which may result in these formulations failing to achieve economic viability. Interestingly, despite these disadvantages, solvent evaporation has remained a mainstay for biologic drug encapsulation by polymeric particles.

PHASE INVERSION NANOENCAPSULATION

Unlike traditional encapsulation techniques, such as solvent evaporation, the process of Phase Inversion Nanoencapsulation (PIN) involves the spontaneous formation of particle from a

continuous phase. In other words, the addition of a dilute polymer solution to a miscible non-solvent results in the formation of precipitation nuclei or particles. An attractive benefit of the PIN processes is that is occurs in a single instantaneous step and utilizes a miscible solvent and non-solvent which removes many of the challenges associated with the step of emulsification. In addition, the particle size and properties may be governed by the polymer concentration and viscosity rather than the high sheer mixing which is necessary to control size in solvent evaporation techniques. [45,66]

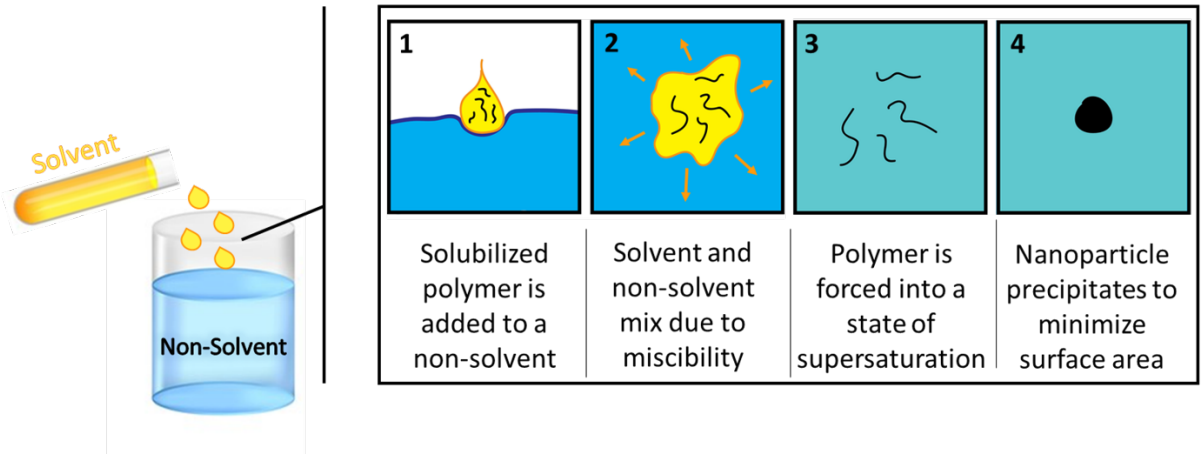

FIGURE 9 SCHEMATIC REPRESENTATION OF PHASE INVERSION NANOENCAPSULATION PROCESS

SCANNING ELECTRON MICROSCOPY

Scanning electron microscopy (SEM) is a common method for the analysis of nanomaterials, as it provides direct visualization of surface morphology, geometry, and size distribution at a nanoscale resolution. Unlike optical microscopy, SEM resolution is not limited by the diffraction limit of light. In characterization using SEM, nanoparticles in a dry powder form are mounted to a sample holder and sputter coated with a conductive metal, such as gold. Images may then be obtained by scanning the sample with a fine and focused electron beam, under high

vacuum conditions. Typically, the electron beam is emitted from an electron gun fitted with a high melting point tungsten filament cathode.[67] In some instances, the electron beam can damage the polymer, thus electron beam voltages ranging from 1 to 30 kV are typically used.[45] The images are then constructed from the obtained secondary and back scattering electrons emitted from the sample surface onto a detector.[67]

DYNAMIC LIGHT SCATTERING

Dynamic light scattering (DLS) is another commonly used technique for the analysis of nanoparticle size. In the application of DLS, a laser beam is illuminated onto a sample of suspended particles in a non-solvent. When the laser beam encounters the nanoparticle suspension, light scatters in all directions as a function of size and shape of the particles. Particularly, the intensity of fluctuations of the light scattered from the particles is dependent on the Brownian motion of the particles in the non-solvent. Thus DLS is used to determine the velocity of the Brownian motion movement, also called the translation diffusion coefficient. From this measurement, size of the particles can be inferred. The larger the particle, the slower the velocity will be. The Stokes-Einstein relationship is a commonly used equation to calculate the relationship between light scattering and size.

$$D_t = \frac{k_B T}{6\pi\eta R_h}$$

Where D_t is the translational diffusion coefficient, k_B is Boltzmann constant, T is temperature, η is viscosity of the medium, and R_h is the hydrodynamic radius. [68]

CHAPTER 1

THE EFFECT OF TEMPERATURE AND PRESSURE ON POLYCAPROLACTONE MORPHOLOGY

Cameron Baptista, Aharon Azagury, Hyeseon Shin, Christopher M. Baker, Eileen Ly, Rachel Lee, and Edith Mathiowitz‡‖

Department of Molecular Pharmacology, Physiology and Biotechnology
Center of Biomedical Engineering
Brown University, Providence, RI 02912, USA
‡‖ Edith_Mathiowitz@Brown.edu

The following manuscript has been published in the journal POLYMER
Elsevier: Polymer Volume 191, 16 March 2020, 122227
DOI: 10.1016/j.polymer.2020.122227

ABSTRACT

The morphology and melting behavior of poly(ϵ-caprolactone) (PCL) processed at varying pressure-temperature-time conditions (2,000-20,000 lb_f, 22-70 ºC, and 5-15 min) were studied using polarized light microscopy (PLM), differential scanning calorimetry (DSC), and X-Ray diffraction (XRD). Samples processed well below the melting region at 22 ºC displayed minimal to no birefringent properties, with broadened crystalline XRD scattering patterns, indicative of plastic crystal mesophase morphology. Plastic crystal quantity was shown to gradually increase from 16% to 30% with processing pressure increasing from 2,000 lb_f to 20,000 lb_f. The mechanism of this formation is thought to be the result of crystal disorganization upon plastic deformation, related to the low-energy barrier slip-planes in the crystalline structure. With sufficient chain mobility achieved at higher processing temperatures (50 ºC and 60 ºC), samples displayed broad birefringent strokes under PLM and were characterized by XRD scattering patterns of broad anisotropic arcs around the equator of the 2D azimuthal pattern, which are indicative of condis crystal mesophase orientation. As opposed to plastic crystal, the condis crystal quantities showed no correlation with increased pressure, ranging between 28% and 40% as processing pressure increased. The additional chain mobility at these temperatures is thought to enable the mesophase to orient radially (normal to the direction of the external load), allowing the transition from plastic crystal to condis crystal. Thus, this paper reports the formation of four distinct morphologies upon processing PCL namely; crystalline, condis crystal mesophase, plastic crystal mesophase, and amorphous.

INTRODUCTION

In polymers, the application of external stress or strain can result in molecular chain orientation. This orientation results in an anisotropic scattering of light, termed birefringence. Birefringence can be frozen into a polymer by applying stress or strain to the material while it is heated to its stress-annealing temperature, then cooled while the external force is maintained. Thus, upon cooling, the molecular chain orientation will exist within the material even after the external load is removed. Generally, this frozen birefringence is referred to as residual stress and is of significant interest in many polymer manufacturing processes, as this residual stress can impart both desired and undesired mechanical characteristics.[54,58,69–73] In some instances the residual stresses from processing are desirable, such as for polymer fibers, as orientation formed by tensile drawing has shown the ability to increase the tensile strength in the direction of the orientation.[69,74,75] While in other instances, the formation of residual stresses can cause an imbalance in the structural stability, resulting in fatigue and spontaneous breakage.[69] To assess residual stress, a method termed photoelasticity is often used, which utilizes cross polarized filters to characterize the magnitude of residual stress stored in a material based on the material's birefringent optical properties.[58,71–73]

In recent years, it has been observed that the polymer chain orientation arising from residual stress from processing such as extrusion, tensile drawing, and rolling can manifest as a mesophase.[3,76–81] The term mesophase refers to a state of matter with intermediate order, falling between the complete disorder of the amorphous phase and the complete order of the crystalline phase. Mesophases have been broadly categorized as liquid crystals, plastic crystals, and conformationally disorder crystals (condis crystals) based on their varying positional, orientational, and conformational orientation.[48] These mesophases, being distinct from the

crystalline and amorphous phases, are of interest as they often give rise to distinct thermal and mechanical properties.[3,76–81]

Particularly, significant focus has been directed towards the ability to induce a mesophase in poly(lactic acid) (PLA) via mechanical processing.[54,75,78–80] PLA is a biodegradable polymer with promising properties to serve as an environmentally friendly and biocompatible alternative to petroleum-based plastics. However, PLA along with most other biocompatible polymers fail to compete with the thermal and mechanical properties of many commercialized petroleum-based polymers.[82] Our lab has previously demonstrated the ability to induce a liquid crystal like anisotropy in PLA through the application of hydraulic compression. Most significantly, it was found by DSC that multiple glass transitions were present through the glass transition region of pressure-temperature treated samples, suggesting the formation of multiple morphologies during processing. These results analyzed in tandem with the anisotropic birefringent properties of the sample under PLM suggested that the induced glass transitions correspond to a liquid crystal like mesophase in processed PLA.[54] Similarly, a mesophase of PLA has also been demonstrated as the result of residual tensile stress in the production of PLA fibers and films. [75–79] This mesophase of PLA was characterized by a post glass transition endotherm and increased cold crystallization kinetics.[12] In concordance, it has also been shown that increasing mesophase content can directly affect the strength of PLA fibers, measured by stress and strain at the breaking point.[75] Therefore, it is apparent that the mechanically induced mesophase of PLA serves as a new route for optimizing the material properties.

This ability to induce mesophase orientation through residual stress has inspired us to analyze similar biodegradable thermoplastic semi-crystalline polymers, specifically PCL. PCL is a polyester which possess many properties that make it useful for a broad range of applications.

These properties include customizable degradation, ease of manufacturing and addition of functional groups for enhancement of hydrophobicity and biocompatibility.[83,84] PCL's physical properties usually consist of a glass transition temperature (T_g) of -65 to -60 °C and a melting temperature (T_m) of 56-65 °C with dependence on the materials morphology.[83,85–87] PCL's physical characteristics such as degradability are greatly affected by the materials molecular weight and crystallinity.[88–92] PCL's molecular weight typically varies between 3-80 kg/mol. PCL is capable of reaching a crystallinity content as high as 69%.[86,87] PCL's degradation profile is usually quite slow, taking 2-4 years to degrade through hydrolytic cleavage and enzymatic fragmentation with dependence on the materials crystallinity, making it an ideal applicant for long term biodegradable use in many fields. [89,91,93] Additionally, PCL's ease of miscibility with other polymers as well as various small molecules makes it a very popular choice for biomedical applications such as long-term implant and oral drug delivery devices.[84,91,94]

Thus, the aim of this paper is to study the morphological changes that occur in PCL under the application of pressure at various temperatures and time periods, via DSC, hot-stage PLM, and XRD. Particularly, we seek to answer the question: can mesophases be induced by the temperature-pressure processing of PCL?

MATERIALS AND METHODS

Preparation of Polycaprolactone Pellets

CAPA 640 PCL was received from Perstorp Holding AB (Perstorp, Sweden) for scientific use with molecular weight (MW) of 37 kg/mol. PCL pellets, as received, were processed by melting 4 granules weighing (≈100 mg) on a hot plate at a temperature of about 65 °C. Pellets produced in this manner were found to have a thickness of 0.071 in with a diameter of 0.409 in. All samples were then placed in individual containers and stored on the benchtop at room

temperature. These pellets were used as an unaltered control throughout this paper. In addition, a solvent casted control sample was prepared by dissolving the CAPA 640 PCL in HPLC grade Tetrahydroflurane (THF, by Fisher Scientific, Pittsburgh, Pennsylvania) and pipetting onto a glass slide. This served as a representative example of semi-crystalline PCL under PLM.

Processing of PCL samples

Each pellet containing 100 mg of PCL was processed using the method described previously by Baker et. al.[54] In summary, samples were placed between two 4" x 4" stainless steel plates. Then, a Carver Auto Series Hydraulic Press (Carver, Wabash, Indiana) equipped with a heating/cooling system was used to expose the pellets to desired stress, temperature, and time profiles. Specifically, pressures of 2,000, 5,000, 10,000, 15,000, and 20,000 lb_f at temperatures of 22, 50, 60, and 70 °C over three periods of time: 5, 10 and 15 min were implemented. These targeted temperatures were chosen to be both below and above PCL's melting temperature (T_m) of 60 °C.[87] Upon elapse of the allotted time under pressure and temperature, samples were cooled under pressure, maintained at 22 °C over a 5 min time period, and then released from the press for analysis. In total, 60 different processing conditions were characterized. Once sample processing was complete, their physical dimensions were recorded (see Table. 1S).

Size Exclusion Gel Permeation Chromatography

A Gel Permeation Chromatography (GPC) system configured for size exclusion (Perkin Elmer Flexar Ultra High Performance Liquid Chromatography system Totalchrom WS MI software V 6.2 Perkin Elmer, Shelton, Connecticut) was used to determine molecular weight (MW = 37 kg/mol). PCL granules were dissolved in THF, filtered with a 0.22 μm filter and run through two serially connected Waters HR 4 & HR 5E Columns (Waters, Milford, Massachusetts) at a flowrate of 1 mL/min. The GPC was calibrated using a monodisperse polystyrene standards.

Polarized Light Microscopy (PLM)

PLM was performed using an Olympus Model BX-60 (Olympus, Center Valley, Pennsylvania) microscope equipped with polarized filters, 10X, and 50X objectives. For hot-stage analysis, the microscope stage was replaced with a Linkam Scientific Model THMS600 Hot Stage (Linkam Scientific Instruments, Tadworth, United Kingdom) which was operated with a TMS 94 temperature controller running Linksys32 Ver.2.2 software (Linkam Scientific Instruments, Tadworth, United Kingdom). Small pieces cut from the PCL samples were placed on an optically transparent quartz dish and heated for the purposes of optical analysis at a rate of 10°C/min from room temperature until full melt (determined by the clearance point). Images were captured at a rate of 1 image every 10 sec, utilizing a PixeLINK (PixeLINK, Ottawa, Canada) model PL-E421CU color enabled camera running PixeLINK Capture OEM Software Version 2.3.5.0 (PixeLINK, Ottawa, Canada).

Observations of birefringence upon melting allowed for a visual estimation of the clearance point, in which the sample became entirely amorphous. The melting range (ΔT) was defined as the change in temperature between the onset of the melt and the final temperature at the clearance point. The onset of the melt was considered as the first temperature in which the sample displayed a visually noticeable change in morphology (such as darkening under polarized light). The final clearance point was considered as the temperature in which the sample became entirely amorphous, displaying a black image under polarized light.

XRD Structural Analysis

XRD was performed using a Bruker D-8 Advance X-Ray Powder Diffraction system running DaVinci Software and a Cu X-Ray tube operating at 40 kV and 40 mA equipped with a Bruker Vantec-500 Xe-CO_2 gas filled detector with a 13.5 cm diameter window set at 20 cm from the goniometer center. System wavelength was 0.15418 nm. The system optics consisted of a polycap with an output beam divergence of 0.25° for Cu and a spot diameter of less than 4.0 mm and a 79 mm long 0.3 mm collimator on the incident beam path (Bruker, Billerica, Massachusetts). Scans were run at 2θ angle from 15°- 70° with a virtual step size of 0.02° and a counting time of 30 s per step. Upon completion of the scan, data was analyzed using the Bruker Diffrac-Eva software package (Bruker, Billerica, Massachusetts). All samples were scanned using a zero-diffraction plate between the aluminum stage and sample.

In addition, hot-stage XRD was performed to analyze structural evolution through the melt. A Bruker TC-DOME Modular Temperature Stage was used to heat the samples prior to each scan. Various temperatures were chosen between ambient conditions and the melting temperature. Prior to each scan, samples were heated to the desired temperature at a rate of 50 °C/min and maintained for 5 min. Upon completion of the scan, data was analyzed using the Bruker Diffract-Eva software package (Bruker, Billerica, Massachusetts).

XRD Phase Content Calculation

The phase content of each sample was calculated from the obtained XRD scattering profiles by peak deconvolution using the PeakFit v4.12 software. The fitting method used was developed by Stoclet et al. in which Gaussian profiles were assumed for all scattering peaks and halos.[78] Particularly, the amorphous halo parameters were determined by the unaltered PCL which displayed the halo peak at a 2θ value of approximately 21°. In addition, the intensity of the

amorphous halo was limited to 2,000 counts maximum based on the intensity of the pure amorphous PCL when heated to a molten state at 70 ºC. Upon establishing a best fit amorphous halo, the (110), (111), and (200) orthorhombic crystalline face peaks were established. Finally, mesophase peaks were fit to a R^2 value of at least 0.99 when comparing the computed model to the experimental data. The content of each phase (amorphous, mesophase, and crystalline) was calculated by the area under the diffraction peaks, using the ratio from one phase to the total scattering peaks.

DSC Thermal Analysis

A DSC (DSC 8500 with Pyris software, Perkin Elmer, Shelton, CT) was used to analyze PCL samples under a dry nitrogen purge. The DSC was calibrated with a pure indium standard at a heating rate of 10 °C/min. Samples (3-5 mg) were cut from the processed pellets with a razor blade and weighed on a microbalance (Microbalance AD.4, Perkin Elmer, Shelton, CT). Samples were cooled to -60°C and held for a period of one minute prior to commencing the DSC cycle. To analyze the first and second heating, samples were cycled from -60 °C to 100 °C, cooled back to -60 °C, and reheated to 100°C. All runs were conducted with a heating/cooling rate of 10°C/min. Melting temperature (T_m) and enthalpy of crystallization (ΔH_f) were then calculated using Pyris software (Perkin Elmer, Shelton, CT).

RESULTS AND DISCUSSION

Fabrication of the PCL

Samples were fabricated as described in the materials and methods. The temperatures were chosen to be below the T_m of PCL (57 °C) at 22 °C and 50 °C, and both near and above the T_m at 60 °C and 70 °C. All samples were in effect, processed above the glass transition given PCL's low T_g of -60 °C. Upon lapse of 5 min, 10 min, and 15 min processing time, the samples were cooled to room temperature (≈22 °C), while the pressure was maintained, using cold water jackets around the plates. Once cooled to room temperature (≈5 min), the pressure was released, and the sample was ready for further analysis. In total, 60 different processing conditions were characterized. Once sample processing was complete, their physical dimensions were recorded (see Table. 1S). Analysis of the unaltered material by FTIR, DSC, and XRD is presented in Fig 1S.

PLM Analysis of Processed PCL Morphology

The morphology of each processed sample was first analyzed for its birefringent properties using PLM. The birefringent properties of solvent casted, melt casted, and unaltered PCL samples, are depicted in Fig. 2S. These samples were used to provide a visual reference of the known semi-crystalline PCL morphology.[95] Briefly, Fig. 2S depicts a clearly defined spherulitic crystalline structure in all three references.

Fig. 1 depicts a representative PLM collage of the morphological changes in the PCL samples at a fixed time interval of 15 min. It should be noted that time showed the least prominent effect on birefringent properties, hence a duration of 15 min was used to represent the effect of processing pressure and temperature throughout this paper. Nevertheless, PLM collages for samples processed at time intervals of 5 min and 10 min are provided in Fig. 2S and Fig. 3S. In

Fig. 1, each column moving from left to right is representative of increasing processing pressure from 2,000 - 20,000 lb_f while each ascending row is representative of increasing processing temperature from 22 - 70 °C.

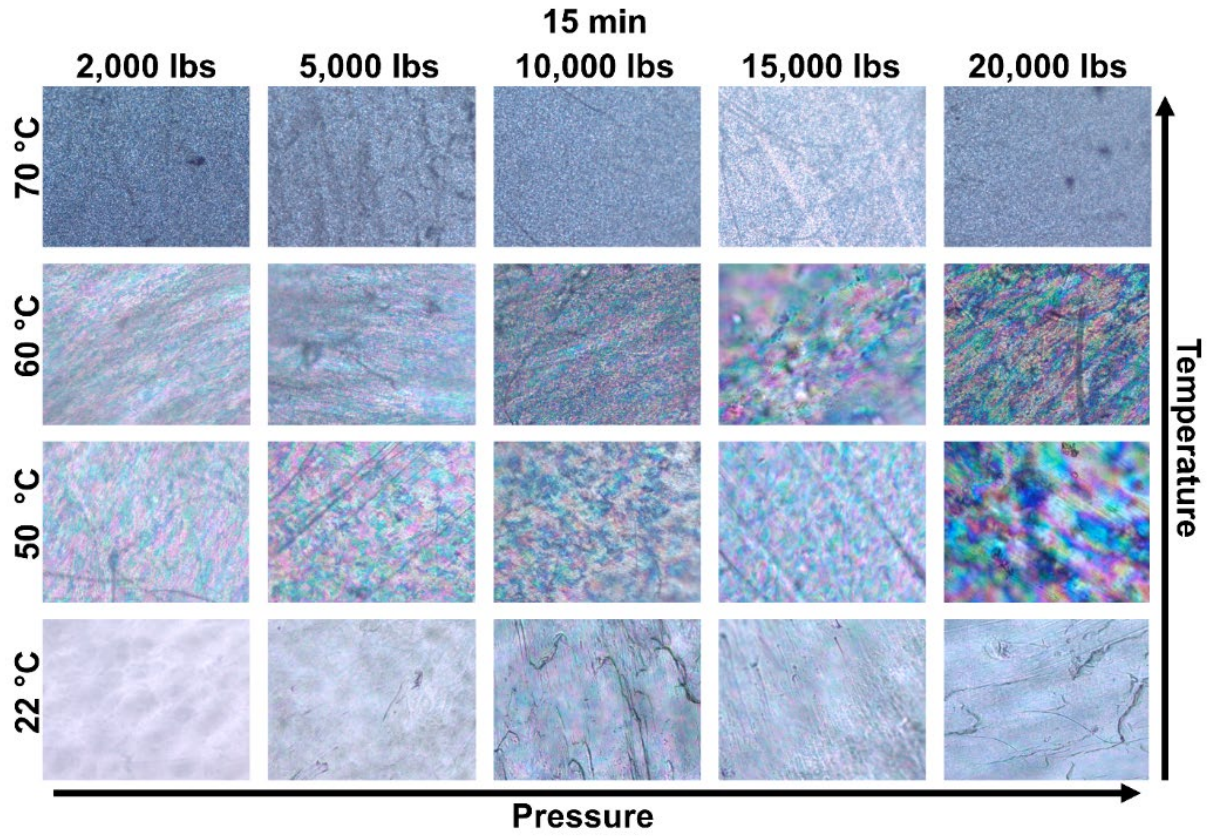

FIGURE 1 PLM IMAGES AFTER 15 MIN OF PROCESSING THE PCL UNDER TEMPERATURE CONDITIONS OF 22 °C, 50 °C, 60 °C, AND 70 °C AND PRESSURE CONDITIONS OF 2,000 LB_F, 5,000 LB_F, 10,000 LB_F, 15,000 LB_F, AND 20,000 LB_F.

It becomes evident from Fig. 1 that a wide array of birefringent populations were induced by the various processing conditions used in this study. These birefringent populations could be divided into three general groups based on processing temperature. First, the samples at processing temperatures significantly below the melting region (at 22 °C) but above the glass transition, show minimal to no birefringence suggesting some processing induced anisotropy, but to a lesser degree compared to samples pressed at 50-60 °C. This is likely due to the plastic deformation upon

compression and the low kinetic energy the molecules possess. When applying pressures above 5000 lb_f it seemed to induce slightly more birefringence, suggesting that for this set up, pressures above 5000 lb_f provide enough energy to orient the PCL morphology at 22 °C.

The most prominent birefringence in PCL post treatment is seen at processing temperatures of 50 °C and 60 °C where the material is close to the T_m (between the onset and offset of the full crystalline melting region, approximately 50-65 °C). The birefringence in these samples is generally seen to increase in intensity as the pressure is increased from 2,000 to 20,000 lb_f. This development of birefringence seen in Fig. 1 follows the general behavior described by Zoetelief et. al. in their outline of the principles of residual stress formation.[70] This induced birefringence is thought to form as the PCL cools through the thermal transition from a fluid to a solid state while under pressure. In the case of PCL, the glass transition is approximately -60 °C which means the amorphous regions of PCL are in a rubbery state at ambient conditions (25 °C).[83] However, due to the semi-crystalline nature of PCL, the bulk material is a brittle and rigid solid below the melt and a liquid above the melt. Thus, upon heating to a temperature close to the melting point (50 °C and 60 °C) the mechanism of this residual stress formation starts with tensile stresses introduced at the outer layers of the sample (in contact with the plates), due to non-slip conditions at the hydraulic press platen as the sample is compressed. Upon cooling, compressive stress is then introduced as pressure is maintained on the rigid outer layers while the cooling front moves inward to the melt. In turn, this explains why much less birefringence is observed when treating PCL at 22 °C (bottom row of Fig. 1) compared to the broad birefringent strokes seen in the samples processed at 50 °C and 60 °C (second and third rows of Fig. 1). Overall, these varying degrees of optical anisotropy seen in Fig. 1 are indicative of the processing induced morphology. The mechanism of these

phenomena will be discussed in more details in the following sections. Please note that no spherulites or crystalline morphology was observed in samples processed at 50-60 ºC.

In the case of the samples processed at 70 °C (above Tm), birefringence was only observed from small tightly packed crystals. This is likely attributed to the free flowing nature of the compressed PCL samples. Upon reaching a fully molten state the sample becomes an incompressible liquid. Thus, without a mold to hinder the flow, the compressive force was translated to outward flow of the material in the direction normal to the compression. This resulted in a final processed sample film significantly thinner than samples processed below or near the melt (see Table. 2S). PCL is known to crystallize in orthorhombic dendritic spherulites, thus the tightly packed birefringent structures seen in the samples processed at 70 °C (top row of Fig. 1) are typical of semi-crystalline PCL, with the only difference being that no large spherulites are seen. This outward flow appears to have alleviated residual stress from the structure, showing only the small crystals and spherulites, similar to what was observed for the samples treated without pressure (Fig 2S).

Hot-Stage PLM Analysis of the Processing Induced Morphology Melting Behavior and Thermal Stability

The melting behavior and thermal stability of the morphologies observed were analyzed by hot-stage PLM (see figure 4s, 5s, and 6s). Fig. 2 was constructed from 6s and was focused on the direct transition before the onset of melting and the clearance point. Fig. 2 depicts representative processed samples with varying degrees of birefringence (specifically the set of samples processed for 15 min at 20,000 lb_f). These conditions were chosen as representatives based on the PLM images analyzed in the previous section, where the most prominent birefringence appeared at 20,000 lb_f. In addition, while time displayed the least prominent effect on birefringence

formation, varying the processing temperature appeared to have the most significant effect. In Fig. 2 the processing temperature is increased with ascending rows from the bottom. The hot stage temperature is increased with each column from left to right. Fig. 2 specifically depicts PLM images with a focus on the changes observed close to the melting point.

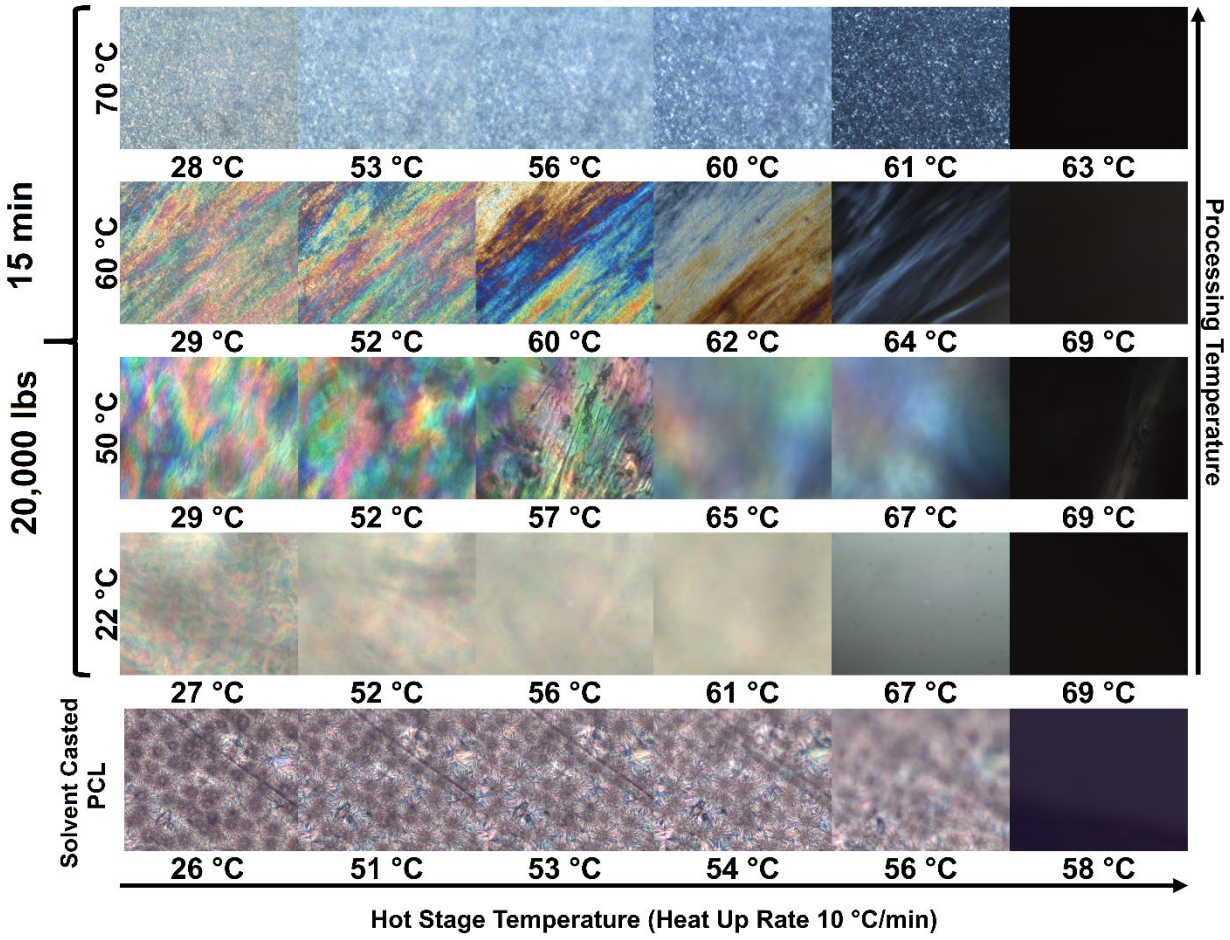

FIGURE 2 HOT STAGE PLM IMAGES TAKEN OF SOLVENT CASTED PCL AND THE SAMPLES PROCESSED UNDER 20,000 LB_F FOR 15 MIN AT TEMPERATURES OF 22 TO 70°C.

The solvent casted thin film PCL sample (bottom row of Fig. 2) displays a typical spherulite crystalline morphology which begins to melt from a spherulitic crystal structure to an amorphous phase at a hot-stage temperature of 56 ºC and reaches a clearance point around 58 ºC (PCL Tm = 57 ºC).

Conversely, the sample processed at 22 ºC (second row from the bottom of Fig. 2) that displayed faint birefringent anisotropy was found to have a much broader melting behavior, spanning about 13 ºC between the onset and offset of the melt. As the hot-stage temperature increased, the sample appeared to begin melting around 56 ºC and retained some structural order up to 69 ºC, where the clearance point was reached. Similarly, the sample processed at 50 ºC (third row from the bottom of Fig. 2) which displayed broad birefringent strokes also displayed a broadened melting behavior when compared to the solvent casted PCL, spanning for 12 ºC. As the hot-stage temperature increased, the sample began to melt around 57 ºC and retained structural order up to 69 ºC, where the clearance point was reached. Again, the sample processed near the Tm at 60 ºC (fourth row from the bottom of Fig. 2) which displayed a predominately anisotropic birefringent morphology also melted over a broadened range of temperatures, spanning about 9 ºC. This sample began to melt around 60 ºC and reached a clearance point around 69 ºC. Finally, the sample processed above the Tm at 70 ºC (which displayed a typical semi-crystalline morphology) melted over a narrower range similar to the solvent casted PCL, spanning only about 2 ºC. This sample began to melt around 61 ºC and reached a clearance point around 63 ºC.

Thus, it can be concluded that the processing induced anisotropy persists through the melting region, disappearing only at the clearance point when the sample is entirely amorphous. This is expressed most clearly by the melting behavior of samples processed at 50 ºC and 60 ºC, depicted in Fig. 2. This general trend of processing temperature effect on the melting behavior of processed PCL was consistent for all pressure and time conditions analyzed. Specifically, pressure and time did not affect the temperature at which the birefringence diminished (see Fig. 4S-6S). In other words, the anisotropy induced at all conditions was stable through the melt. In addition, the processing induced morphology appeared to affect both the onset and offset of the melting region,

as well as the clearance point at which the sample becomes entirely amorphous as observed by the hot-stage PLM. In both the solvent casted PCL and the sample processed at 70 ºC that displayed typical semi-crystalline morphology, the ΔT through the melt was narrow. In contrast, the samples processed at 22 ºC, 50 ºC, and 60 ºC that displayed varying degrees of the processing induced anisotropy, resulted in broadened melting spans. Further, increases in melting span and in clearance point were seen for samples processed at all varying pressures and time durations as well (see Fig. 7S and 8S).

As the different processing conditions induced varying degrees of orientation, crystal size, morphology content, and thermal stability, PLM analysis is not enough to fully comprehend these effects. Thus, to better understand these variations in PCL's morphology and thermal stability, XRD and DSC analyses were conducted.

Structural Analysis of the PCL Morphology by XRD

In conjunction with the PLM data in the previous sections, XRD was used to better characterize the effect of pressure, temperature, and time processing parameters on the structure and melting behavior of PCL. Representative XRD profiles of PCL processed at 20,000 lb_f for 15 min, at temperatures 22 ºC, 50 ºC, 60 ºC, and 70 ºC are shown in Fig. 3 and Fig. 4 (2D azimuthal scattering patterns and integrated 2D XRD profile, respectively). Again, these conditions were chosen as representatives based on the PLM images in which the most prominent birefringence appeared at 20,000 lb_f. In addition, these conditions were chosen to be the focus as time displayed the least prominent effect on birefringence formation, while varying temperature appeared to have the most significant effect.

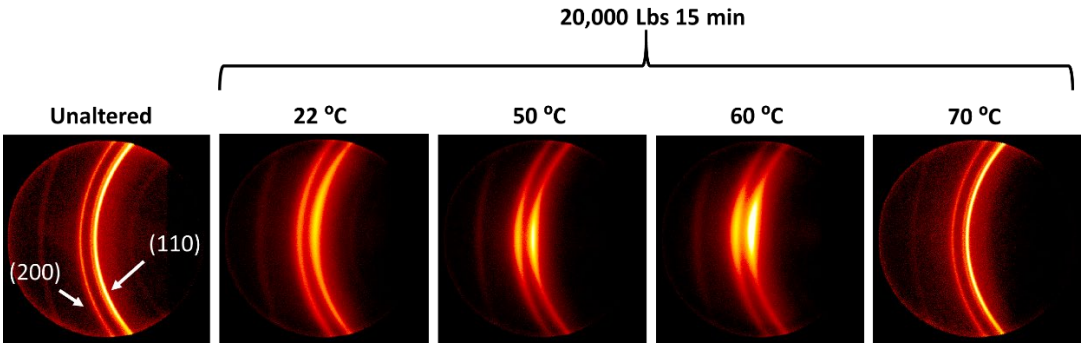

FIGURE 3 THE 2D AZIMUTHAL XRD PROFILES OF UNALTERED PCL AND PCL PROCESSED AT 20,000 LB_F FOR 15 MIN AT TEMPERATURES 22 ºC, 50 ºC, 60 ºC, AND 70 ºC. XRD SCANS WERE TAKEN AT ROOM TEMPERATURE. NOTE, THE COUNT INTENSITY OF THE DEPICTED XRD SCATTERING WAS ADJUSTED TO MINIMIZE THE BACKGROUND SCATTERING AND PREVENT WASHOUT OF THE ANISOTROPIC REGIONS.

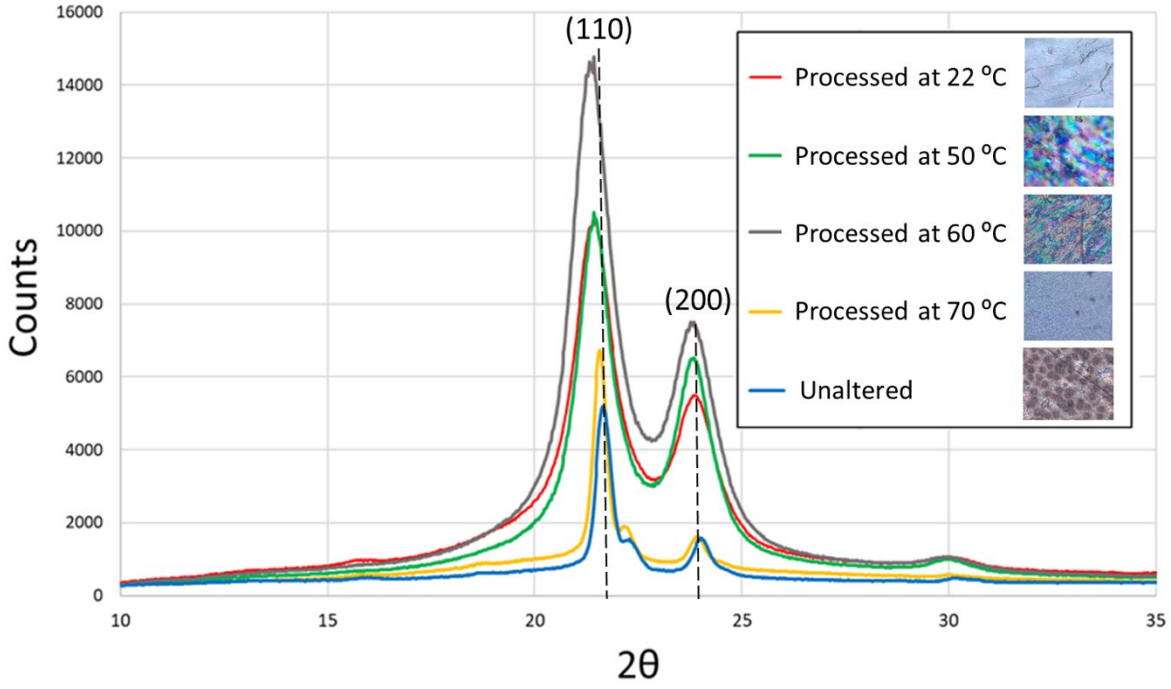

FIGURE 4 THE INTEGRATED XRD PROFILES OF UNALTERED PCL (BLUE) AND PCL PROCESSED AT 20,000 LB_F FOR 15 MIN AT TEMPERATURES 22 ºC, 50 ºC, 60 ºC, AND 70 ºC (RED, GREEN, GRAY, AND YELLOW RESPECTIVELY). THE FIGURE LEGEND ALSO DEPICTS THE CORRESPONDING PLM IMAGE OF EACH SAMPLE. XRD SCANS WERE TAKEN AT ROOM TEMPERATURE.

Two characteristic peaks of crystalline PCL at 2θ values of 21° and 24° are clearly observed in all processed samples (Figure 4). These diffractions are attributed to the (110) and (200) faces (respectively) associated with the well-known orthorhombic crystal lattice of PCL. An additional small peak can also be seen in many samples at a 2θ value of 22 °C, which has been associated with the (111) plane of the orthorhombic unit cell.[96] Distinct differences can be seen in peak intensities and peak widths among these orthorhombic unit cell diffractions as processing conditions change (Fig. 3 and 4).

As expected, the unaltered PCL sample displays an isotropic scattering profile characterized by a diffused amorphous halo and sharp (110), (111), and (200) crystalline peaks (Fig. 3 and 4). The amorphous phase of the unaltered PCL displays no positional, orientational, or conformational order, thus presenting a weak and diffused scattering ring. On the other hand, the crystalline phase of unaltered PCL displays the characteristic three levels of positional order associated with the (110), (111), and (200) orthorhombic crystal faces with their inherent conformational order. To clarify, this analysis adopts the definitions of orientational, positional, and conformational order set by Wunderlich.[48] In this instance, orientational order refers to the long range order of the polymer chains and can be observed by XRD as the uniformity of scattering of a given Debye-Scherrer ring (i.e. isotropic or anisotropic). Positional order refers to the intermolecular spacing, which is typically characteristic of the chain packing of a particular crystal structure, and can be observed by XRD at the 2θ value at which a given Debye-Scherrer ring occurs. As mentioned, there are three levels of positional order associated with the (110), (111), and (200) orthorhombic crystals faces of PCL. These three levels of positional order are associated with the lamellar folding and intermolecular spacing specific to each crystal face. Finally, conformational order refers to the rotational arrangement of the atoms in a single polymer chain

(i.e. gauche or anti conformation) and can be observed by XRD as the sharpness of a given Debye-Scherrer ring.

At a low processing temperature of 22 °C (well below the PCL melting region), the scattering patterns observed in Figs. 3 and 4 begin to broaden compared to the unaltered PCL. This broadening can be seen in Fig. 3 as the (110) and (200) face Debye-Scherrer rings thicken compared to the unaltered PCL scattering profile, also manifested in the integrated scattering profiles depicted in Fig. 4. Generally, the broadening of a crystalline peak can be primarily attributed to either decreasing crystal size or increasing structural disorder within the sample. Thus, it is likely that the plastic deformation from applying pressure well below the melting temperature results in a disordering of the initial orthorhombic crystal conformation. To this end, a comparison can be made between the morphology observed here in PCL and the plastic crystal mesophase.[48] Plastic crystals are defined as a type of mesophase in the "plastic" state with no birefringent properties, attributed to positional order with both conformational and orientational disorder. The mechanism of formation of plastic crystals is thought to be the deformation of crystallites, due to a large number of slip planes within the structure.[48] These criteria are also observed herein with the minimal to no birefringence seen by PLM (Fig. 1) and the broadened and primarily isotropic crystalline peaks observed by XRD (Fig. 3). However, it should be noted that the plastic crystal morphology was previously thought to be limited to small molecules only, particularly with spherical shaped mesogens.[48] This spherical shape of the small molecule mesogen is thought to minimize the energy barrier for their reorientation, allowing for this plastic crystal mesophase to form. Since long chain macromolecules such as polymers are inherently non-spherical, it was previously regarded that this plastic crystal reorientation could not occur in these materials.[97,98] A recent publication by Claudio et. al. was the first to demonstrate the ability to

induce a plastic crystal like structure in a long chain macromolecule, by stretching fibers of an ethylene-norbornene copolymer.[98] This morphology was identified by positional order with orientational and conformational disorder observed by XRD, similar to that seen here for PCL (Fig. 4). In the case of ethylene-norbornene, the ability to form a plastic crystal morphology was attributed to the pseudo-spherical norbornene units along the polymer chain, which are thought to minimize the energy barrier of the crystalline slip-planes. [98] In the case of PCL, it is well known that long chain hydrocarbon crystals of orthorhombic structure can form dislocations on either side of which the terminal methyl groups lie. In addition, several screw and edge dislocations can occur in these long chain hydrocarbon crystals. Any of these dislocations are noted to cause individual layers of the crystal to slip over one another.[99] Further, it should also be noted that while PCL is typically described as being similar to polyethylene, the carbonyl groups of PCL result in a slightly twisted chain formation of the unit cell. Thus, the disordering of the PCL crystal structure can also be attributed to irregularly located carbonyl groups along the chain direction. [96,100] These slip-planes coupled with irregularly spaced carbonyl groups are thought to allow for plastic crystal formation in PCL upon plastic deformation. Thus, these slip-planes are thought to allow for plastic-crystal formation in PCL upon plastic deformation.

With processing temperature increasing to 50 ºC and 60 ºC (between the on-set and off-set of the PCL melt), the scattering of the (110) and (200) orthorhombic faces develops into two broadened and anisotropic arcs around the equator (Fig. 3 and 4). As mentioned, the two scattered arcs on the equator are indicative of the orthorhombic face positional order and the conformational disorder of imperfect lamellae folds. The focus on the equator is owed to the orientation in the radial direction (perpendicular to the direction of the sample compression). This orientation is further identified by the change in peak ratios of these faces (Fig. 4) compared to the control PCL

sample (2:1 vs 4:1 respectively). These thickening arcs become brighter and more centralized at the equator compared to the 22 ºC sample. The morphology induced in these samples seems to meet the definition of condis crystal mesophase.[48] Condis crystals are defined as a type of mesophase in the solid state with birefringent properties attributed to positional and orientation order, and partial or full conformational disorder. [48,81] This induced morphology in PCL closely resembles that of the condis crystal morphology induced in polyethylene (PE) at high pressures.[81,101–103] Both PE and PCL are similar in that they form orthorhombic crystal structures, with planar zigzag chain conformation. [81,96,104] By compressing PE samples in a metal gasket, Basset et. al. discovered that PE forms an intermediate phase under high pressures at temperatures between the solid and melt. This phase also displayed anisotropy around the (110) and (200) faces of the PE orthorhombic XRD scattering pattern, similar to the patterns seen in Fig. 3 of PCL.[101,105] Later studies went on to identify this intermediate phase of PE as a condis crystal mesophase. [81,102,103] Similarly, a condis crystal mesophase was also identified in isotactic polypropylene (iPP). In this instance, the mesophase of iPP was identified by the broadened anisotropic peaks of the integrated crystalline XRD scattering, as is seen here in PCL (Fig. 4). [81,106]

At the highest processing temperature tested of 70°C, the scattering pattern seen in Fig. 3 and 4 appears similar to that of the unaltered PCL sample as was observed with the PLM analysis. A diffused amorphous halo and sharp (110), (111), and (200) crystalline peaks are seen for the sample processed at 70 °C, indicating a typical isotropic and semi-crystalline structure as was also observed by PLM.

Hot-Stage XRD Analysis of the Processing Induced Morphology Melting Behavior and Thermal Stability

To further investigate the structural evolution of the PCL morphology upon melting, hot-stage XRD was conducted to collect scattering profiles of representative samples at increasing temperatures through the melt. Each processed sample was scanned at 25 ºC, 35 ºC, 45 ºC, 55 ºC, 65 ºC, and 75 ºC. The hot-stage XRD profiles of unaltered PCL and representative processed PCL samples are presented in Fig. 5 and 6 (2D azimuthal scattering and integrated hot-stage XRD, respectively). Again, PCL processed at 20,000 lb_f for 15 min, at temperatures 22 ºC, 50 ºC, 60 ºC, and 70 ºC were chosen as representatives based on the PLM images in Figure 1, where the most prominent birefringence appeared at 20,000 lb_f. In Fig. 5, each row displays varying processing conditions and each column displays the structural evolution as the sample was heated through the melt. Fig. 6A-E depict the corresponding integrated scattering profiles.

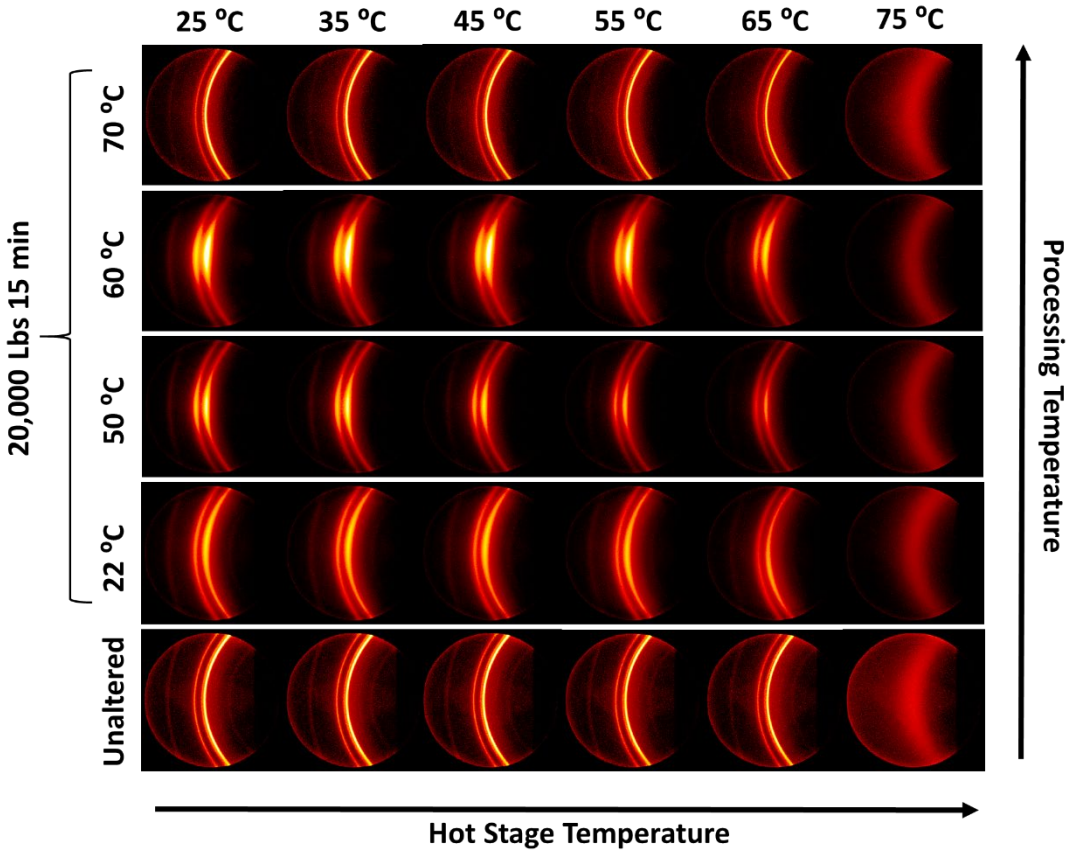

FIGURE 5 THE HOT-STAGE 2D AZIMUTHAL XRD PROFILES OF UNALTERED PCL (BOTTOM ROW) AND PCL PROCESSED AT 20,000LBS FOR 15 MIN AT TEMPERATURES 22 ºC, 50 ºC, 60 ºC, 70 ºC (ASCENDING ROWS). EACH ROW REPRESENTS THE PROCESSING CONDITIONS AND EACH COLUMN REPRESENTS THE HOT-STAGE XRD TEMPERATURE. NOTE, THE COUNT INTENSITY OF THE DEPICTED XRD SCATTERING WAS ADJUSTED TO MINIMIZE THE BACKGROUND SCATTERING AND PREVENT WASHOUT OF THE ANISOTROPIC REGIONS

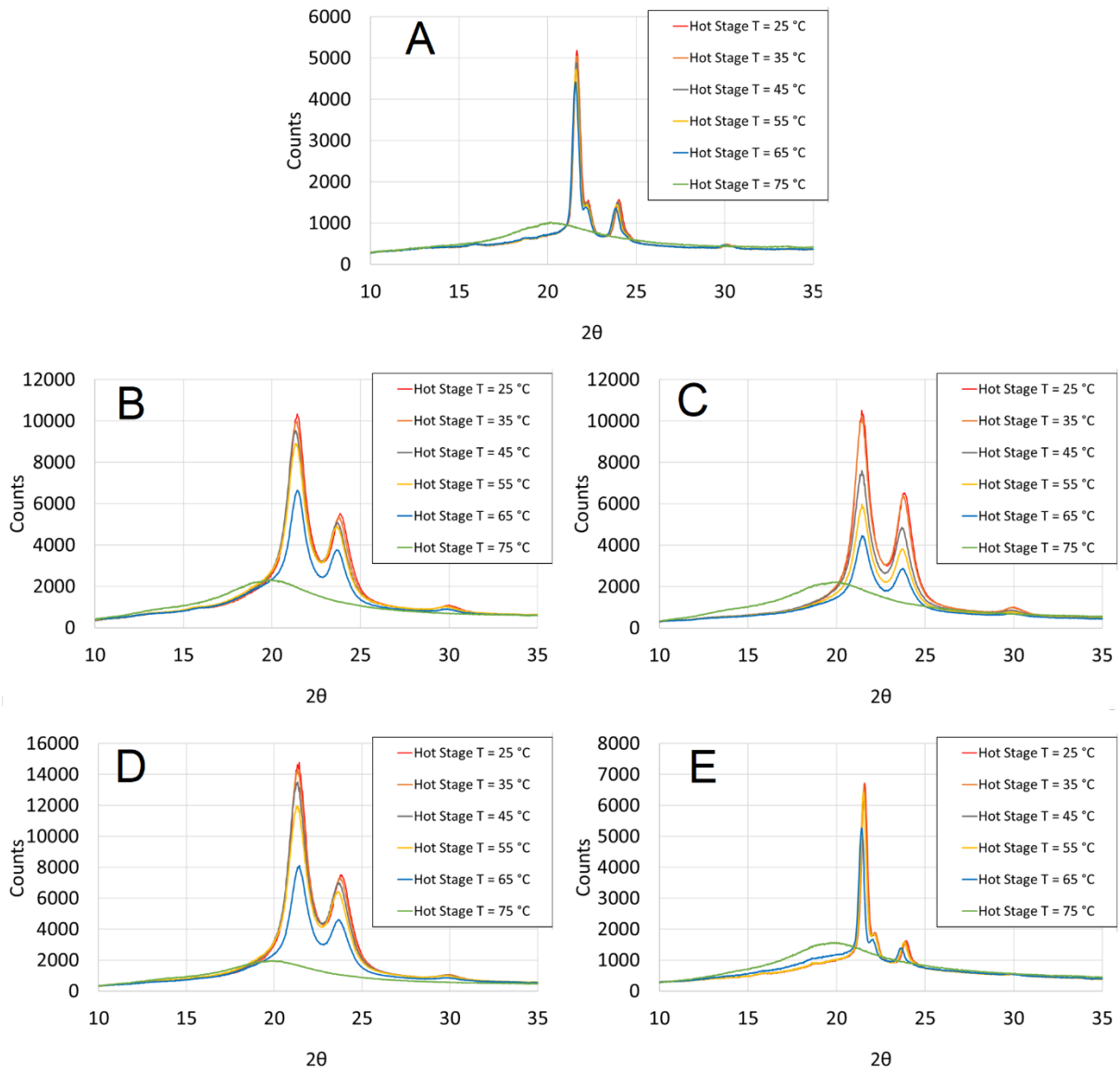

FIGURE 6 THE INTEGRATED HOT-STAGE XRD PROFILES OF (A) UNALTERED PCL AND PCL PROCESSED AT 20,000LBS FOR 15 MIN AT TEMPERATURES OF (B) 22ºC, (C) 50ºC, (D) 60ºC, AND (E) 70ºC. EACH SCATTERING PATTERN IS REPRESENTATIVE OF THE MORPHOLOGY OF THE SAMPLE AT VARIOUS TEMPERATURES THROUGH THE MELT, RANGING FROM 25 °C TO 75 °C

As seen in Fig. 5 (bottom row) and Fig. 6A, the unaltered PCL maintained a relatively similar XRD pattern upon heating. The sample displayed the characteristic (110), (111), and (200) reflections which decreased in intensity as the melting temperature was approached. Upon

surpassing the melting temperature at 75 ºC, the crystalline peaks disappeared entirely with only a broad amorphous halo remaining.

At the lowest processing temperature tested of 22 °C, a more prominent structural evolution can be seen through the melt (Fig. 5 and 6B). As a reminder, it was shown in Figures 3 and 4 that this sample displayed plastic crystal-like mesophase morphology, with broadened Debye-Scherrer rings indicating conformational disorder. It can be seen in Fig. 5 (second row from the bottom) that these broadened plastic crystal-like peaks begin to diminish upon heating the sample to 65 ºC. Upon heating from 55 ºC to 65 ºC, the intensity of the XRD scattering profile is decreased, but the crystalline rings still remain diffused in comparison to the typical sharp rings seen in the unaltered PCL. The dimming of these rings (seen in Fig. 5) can be seen more pronounced in Fig. 6B. It can be seen that this sample exhibits a narrowed amorphous halo and broadened crystalline peaks at ambient conditions. Upon heating to 65 ºC, the intensity of both the amorphous and crystalline contributions decrease. This decrease is associated to the decrease in intensity seen in Fig. 5. Upon further heating to 75 ºC, these crystalline rings melt, leaving only a diffuse and scattered amorphous halo.

XRD profiles of samples containing condis crystal-like mesophase morphology (i.e. samples processed at 50 ºC and 60 ºC) can be seen in the second and third rows of Fig. 5. Again, these samples displayed more prominent structural evolution through the melt when compared to the unaltered PCL. Upon heating, the two anisotropic mesophase arcs centered at the equator of the 2D azimuthal XRD profiles were observed to decrease in intensity. Upon reaching 65 ºC, the mesophase arcs were minimized leaving predominantly the (110) and (200) crystalline rings. The crystalline rings were then observed to diffuse at 75 ºC, leaving a broad amorphous halo remaining. The dimming of the two mesophase arcs (seen in Fig. 5) can also be seen in Fig. 6C and 6D. It can

be seen that the processed samples containing the condis crystal mesophase exhibit a narrowed amorphous halo at ambient conditions. Upon heating, a significant decrease in intensity can be seen as the halo broadens. This halo decrease is associated to the dimming of the mesophase arcs seen in Fig. 5.

The PCL sample processed above the melt at 70 ºC (shown to display a semi-crystalline morphology) behaved similarly to the unaltered PCL. This sample maintained a relatively constant XRD pattern upon heating. The sample displayed the characteristic (110), (111), and (200) reflections which decreased in intensity as the melting temperature was approached. Upon surpassing the melting temperature at 75 ºC, the crystalline peaks disappeared entirely with only a broad amorphous halo remaining (Fig. 5 and 6E).

Overall, it can be concluded from the XRD observed melting behavior depicted in Fig. 5 and 6 that the mesophase is stable through the melt (as was also observed in the PLM analysis, Fig. 2). It was also seen that the mesophase transitions directly from both the condis crystal-like and plastic crystal-like phase to the amorphous phase upon heating. This is indicated by the decrease in intensity of the mesophase arcs (Fig. 5) and mesophase peaks (Fig. 6) without a corresponding increase in the sharpness of the isotropic crystalline scattering. To emphasize this point, one can look to the condis crystal mesophase of iPP in comparison. [81] The melting behavior of the PCL mesophase seen here differs from the iPP mesophase, which was shown to first crystallize to the more stable monoclinic crystal prior to melting.[81,106] Unlike PCL, the broad mesophase XRD scattering peaks of iPP were seen to sharpen and transition to stable crystalline peaks upon heating. [106] In contrast, it becomes clear from Fig. 5 and 6 that this transition from mesophase to crystal does not occur in PCL. Rather, the mesophase transitions directly to an amorphous state upon melting. This difference in melting behavior between PCL and iPP is not

unexpected, as it has been noted that not all condis crystal mesophases anneal to the crystalline form upon heating. Thus, while the condis crystal mesophase is thought to be a precursor of crystallinity, not all condis crystals transition into a crystalline form upon melting. [81]

Phase Content of Processed PCL Calculated from XRD Scattering Profiles

To better understand the formation of the mesophases morphology in PCL as a function of the processing pressure and temperature, a quantitative structural analysis of the investigated samples was obtained by peak deconvolution of the integrated XRD scattering profiles. Specifically, the crystalline, amorphous, and mesophase phase content of each sample were calculated based on the peak area contribution to the total scattering area, using the methods described by Stoclet et. al.[75] Depicted in Fig. 7 are representative peak fitting analyses for unaltered PCL (without mesophase) and PCL processed at 20,000 lbs for 15 min at 50 ºC (with mesophase). These two samples serve as representatives to demonstrate the general peak fitting analysis for samples with and without mesophase morphology.

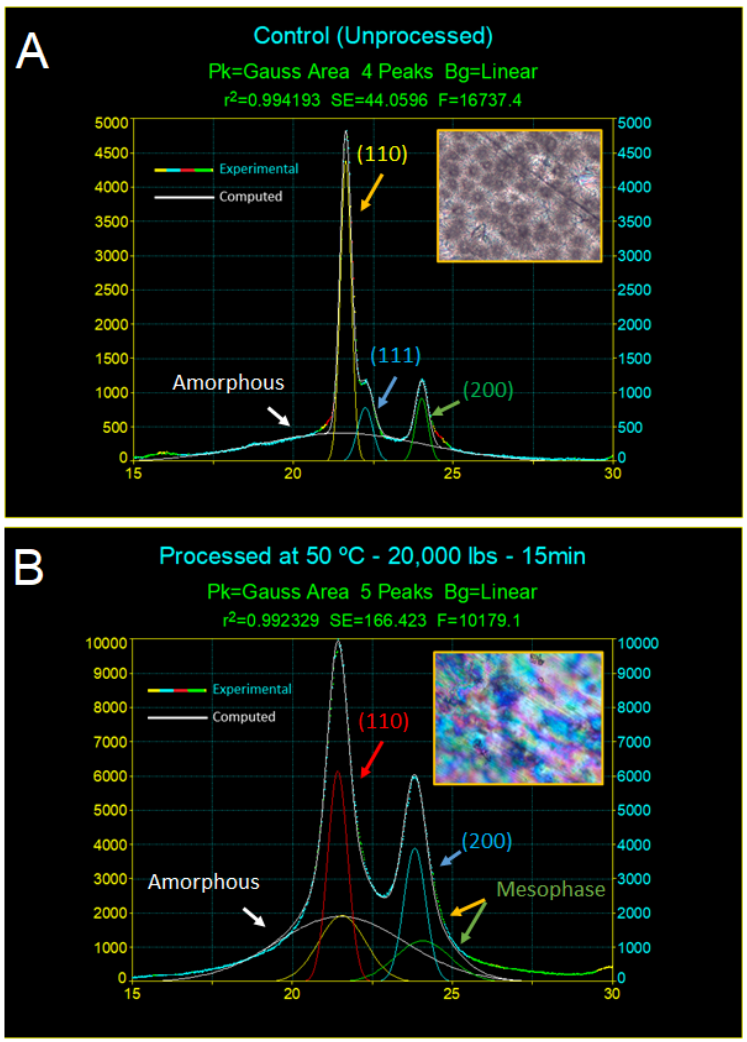

FIGURE 7 PEAK DECONVOLUTION OF THE INTEGRATED XRD SCATTERING PROFILES OF (A) UNALTERED PCL AND (B) PCL PROCESSED AT 20,000 LBS FOR 15 MIN, AT 50 ºC.

It can be seen in Fig. 7A that the scattering profile of unaltered PCL can be fitted using three sharp Gaussian peaks corresponding to the (110), (111), and (200) crystalline faces and a broad amorphous halo centered at a 2θ value of approximately 21°. Alternatively, peak fitting of the processed PCL containing mesophase morphology revealed that crystalline and amorphous contributions alone could not account for the whole XRD scattering (e.g., Fig. 7B). Rather, it was necessary to introduce two Gaussian mesophase peaks to achieve a statistically significant fit.

Further supporting the hypothesis that these additional two peaks are attributed to the mesophases stems from their intermediate full width at half max (FWHM). The mesophase peaks possessed a FWHM that falls between the broad amorphous halo FWHM and the sharp crystalline peak FWHM. Accordingly, the intermediate FWHM is due to the intermediate mesophase organization. In addition, the mesophase peaks were seen to overlap with both the (110) and (200) crystal faces, which is in agreement with the two mesomorphic arcs attributed to the plastic crystal and condis crystal structures seen in the 2D azimuthal patterns displayed in Fig. 5.

Fig. 8 and Table 1 present the induced crystalline, mesophase, and amorphous phase content of the treated PCL samples as a function of the processing pressure and temperature conditions. The top image in Fig. 8 depicts the 3D diagram of all three phases, amorphous (red), crystalline (green), and mesophase (blue). The bottom images of Fig. 8 depict 2D contour maps of each corresponding plane, with the colored legend representing percent phase content. As mentioned, treatment time showed the least prominent effect on the morphologies observed, thus 15 min is used to represent the effects of pressure and temperature. Figure 9 presents the change in phase content of the processed samples with respect to the unaltered PCL. The unaltered PCL displayed 49% amorphous and 51% crystalline phase content.

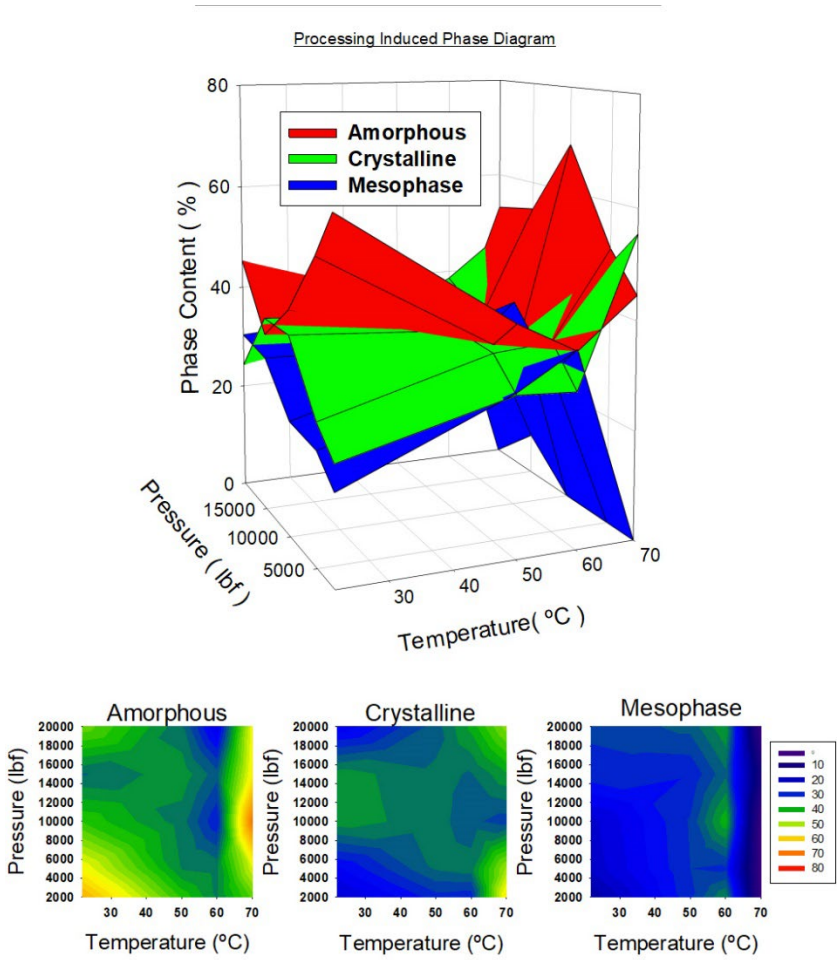

FIGURE 8 PROCESSING INDUCED PHASE DIAGRAM BASED ON THE QUANTITATIVE STRUCTURAL ANALYSIS OBTAINED BY PEAK DECONVOLUTION OF THE INTEGRATED XRD SCATTERING PROFILES. THE TOP IMAGE DEPICTS THE 3D DIAGRAM OF ALL THREE PHASES, AMORPHOUS (RED), CRYSTALLINE (GREEN), AND MESOPHASE (BLUE). THE BOTTOM IMAGES DEPICT 2D CONTOUR MAPS OF EACH CORRESPONDING PLANE, WITH THE COLORED LEGEND REPRESENTING PERCENT PHASE CONTENT.

Temperature	Pressure	Amorphous	Crystalline	Mesophase
Unaltered		49	51	0
22	2000	62	21	16
22	5000	54	26	21
22	10000	42	37	21
22	15000	34	37	29
22	20000	45	24	30
50	2000	41	29	29
50	5000	36	34	30
50	10000	35	35	30
50	15000	37	35	28
50	20000	34	33	33
60	2000	36	28	36
60	5000	35	35	29
60	10000	28	32	39
60	15000	33	34	33
60	20000	24	39	38
70	2000	45	55	0
70	5000	51	49	0
70	10000	69	31	0
70	15000	55	38	8
70	20000	53	47	0

TABLE 1 PROCESSING INDUCED PHASE CONTENT BASED ON THE QUANTITATIVE STRUCTURAL ANALYSIS OBTAINED BY PEAK DECONVOLUTION OF THE INTEGRATED XRD SCATTERING PROFILES.

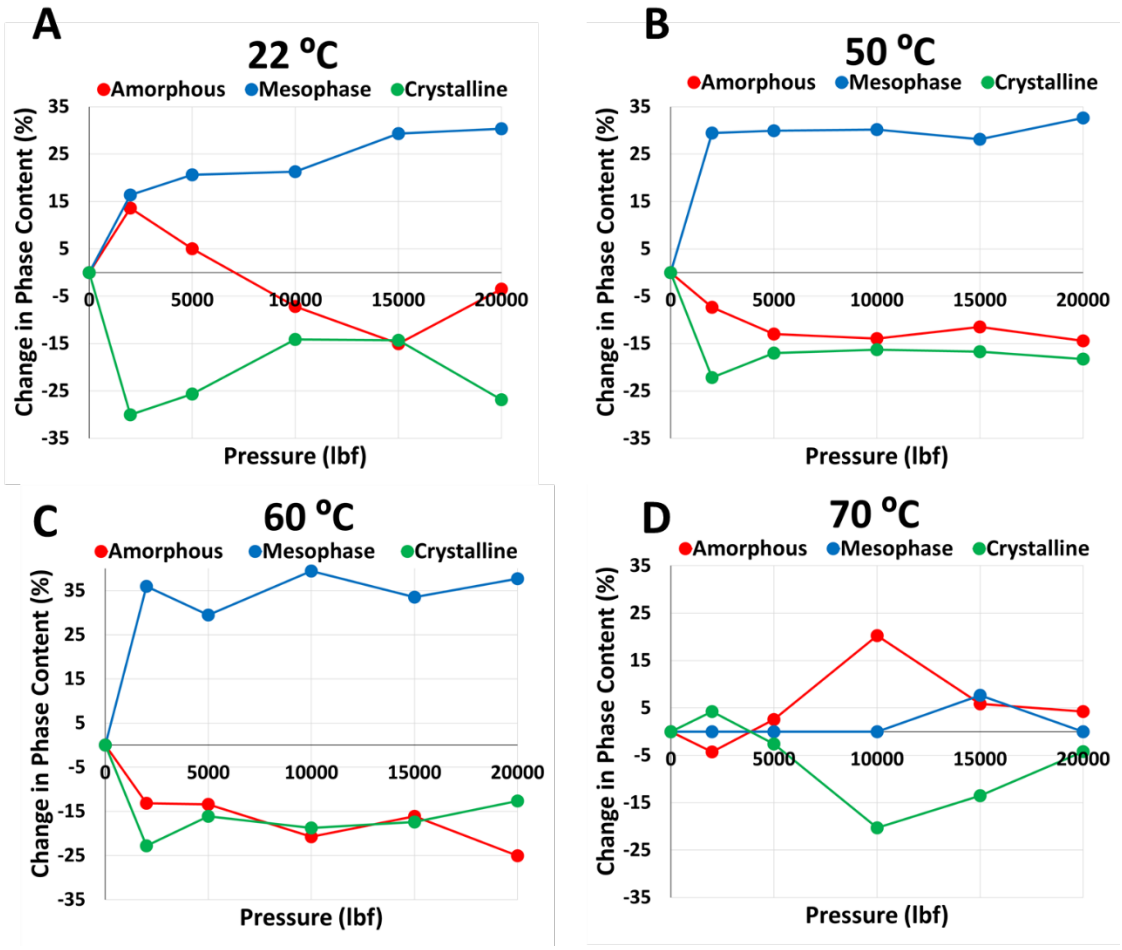

FIGURE 9 PERCENT CHANGE IN PHASE CONTENT COMPARED TO UNALTERED PCL AS A FUNCTION OF PROCESSING PRESSURE, FOR PROCESSING TEMPERATURES OF (A) 22 ºC, (B) 50 ºC, (C) 60 ºC, AND (D) 70 ºC.

Looking at the effects of processing pressure and temperature on mesophase formation, it can be seen in Fig. 8 and 9A that samples processed at 22 ºC showed a gradual increase in mesophase content from 16% to 30% as pressure increased from 2,000 lb_f to 20,000 lb_f, respectively. At low pressures of 2,000 lb_f and 5,000 lb_f, this gradual increase in mesophase content was solely at the expense of the crystalline phase, with percent crystallinity decreasing by 30% and 26% compared to unaltered PCL, respectively. This finding further supports the hypothesis that plastic crystals form as the resulted of deformed pre-existing crystals. However, upon

increasing pressure to 10,000 lb_f, 15,000 lb_f, and 20,000 lb_f, the samples processed at 22 ºC showed increasing mesophase formation at the expense of both the amorphous and crystalline phases, with amorphous content decreasing by 7%, 15%, and 4% and the crystalline content decreasing by 14%, 14%, and 27% respectively.

Upon increasing the processing temperature to 50 ºC and 60 ºC, the processing pressure did not display any discernable trend on mesophase formation (Fig. 8, 9B, and 9C). At 50 ºC, the mesophase content remained relatively constant (28-33 %) at all pressures. Similarly, at 60 ºC the mesophase content also displayed no trend with increasing pressure, fluctuating between 30% and 40%. In addition, the formation of mesophase in all 50 ºC and 60 ºC samples came at the expense of both the amorphous and crystalline phases. At 50 ºC, the crystalline content decreased by 16% to 22% and the amorphous content decreased by 7% to 14% compared to the unaltered PCL. At 60 ºC, the crystalline content decreased by 13% to 23% and the amorphous content decreased by 13% to 25%, compared to the unaltered PCL.

Thus, a mechanism of mesophase formation in PCL emerges. It appears that pressure displays the most predominate effect on the formation of the plastic crystal mesophase at processing temperatures below Tm (22 ºC). This effect of pressure on plastic crystal formation is likely due to the insufficient kinetic energy (i.e. temperature) of the polymer chains to orient to a favored position upon deformation at temperatures below Tm. As a result, the samples processed at 22 ºC and 2,000 – 5,000 lb_f form a plastic crystal mesophase solely at the expense of the crystalline phase. This would be expected, based on the mechanism of plastic crystal formation described by Claudio et. al. in which reorientation occurs as a result of low-energy barrier slip-planes within the crystal structure.[98] However, upon increasing the external load to 10,000 – 20,000 lb_f, sufficient energy can be achieved to also orient the morphology. As a result, these

samples show increased mesophase content, with contributions from both the amorphous and crystalline phases as orientation occurs. This trend also correlates directly to the PLM images observed in Figure 1, in which the samples processed at 22 ºC and pressures of 2,000 lb_f and 5,000 lb_f displayed no birefringence, but upon increasing pressure to 10,000 lb_f – 20,000 lb_f a faint birefringence was observed.

Accordingly, it appears that when sufficient chain mobility is achieved at increased temperatures of 50 ºC and 60 ºC, the effect of pressure on mesophase formation is reduced and another mesophase is created (i.e. condis crystal). Evidently, the samples at 50 ºC and 60 ºC formed relatively constant quantities of condis crystal mesophase at all pressures ranging from 2,000 – 20,000 lb_f, characterized by strong birefringence (Fig. 1) and anisotropic XRD scattering (Fig. 3). In addition, this condis crystal morphology formed at the expense of both the amorphous and crystalline phases. Thus, while the plastic crystal mesophase forms at temperatures below Tm (yet above Tg) as the result of low-energy barrier slip-planes within the crystalline phase, the condis crystals mesophase is thought to form by a similar mechanism yet with sufficient chain mobility to achieve orientational order at the expense of the amorphous phase.

To this end, it should be noted that upon surpassing the melt at 70 ºC mesophase content was not detected. All samples processed at 70 ºC displayed 0% mesophase, with the exception of one sample processed at 15,000 lb_f which displayed about 8% mesophase. A similar trend was seen by Cheng et. al. in their quantification of the PE mesophase, which at the time was termed as an intermediate phase.[103] It was shown that the intermediate phase content of PE gradually increased with temperatures towards the melt, reaching a maximum right before the Tm. However, upon surpassing the Tm they also saw a significant drop in mesophase formation.[103] This drop is likely attributed to the formation of crystals when sufficient thermal energy is maintained in the

system above the melt. This is supported in PCL by the maxima in crystalline content seen at 70 ºC (Fig. 8).

Melting Behavior and Thermal Stability of the PCL Morphology as Observed by DSC

DSC was used to further characterize the effect of pressure and temperature on the morphology and melting behavior of PCL. The T_m, ΔH_f, and % crystallinity were calculated from the DSC curves depicted in Fig. 10 (Table 2S). In Fig. 10 each individual graph contains 4 DSC heating curves, representing the melting behavior of samples at each processing temperature (22 °C, 50 °C, 60 °C, 70 °C). Each sample was cycled from -60°C to 100°C with a heating rate of 10°C/min. Each graph from left to right corresponds to increasing processing pressure from 2,000 lb_f to 20,000 lb_f. These conditions were chosen as representatives as explained previously.

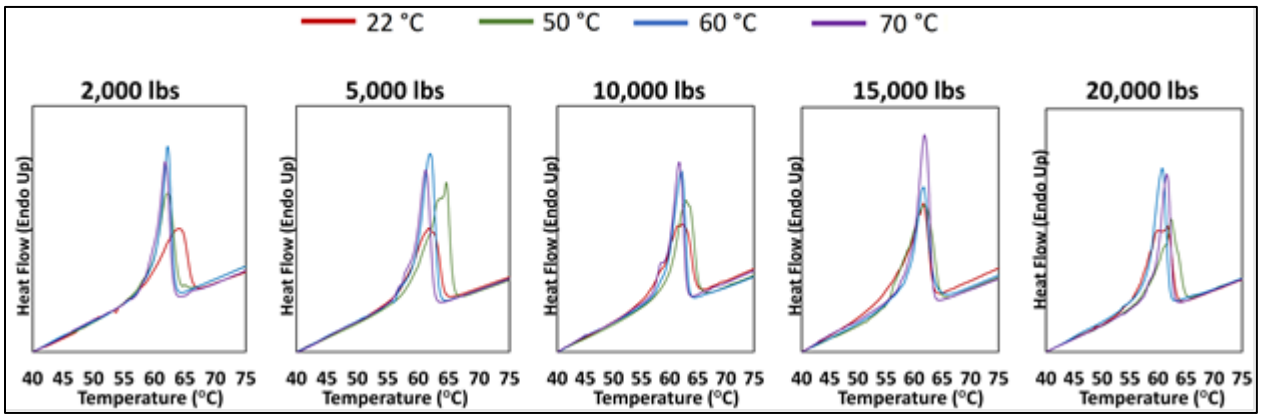

FIGURE 10 EFFECTS OF PROCESSING TEMPERATURE AND PRESSURE ON THE DSC MELTING ENDOTHERM OF PCL PROCESSED AT PRESSURES RANGING FROM 2,000 LBS – 20,000 LBS, AT TEMPERATURES RANGING FROM 22 °C – 70 °C, FOR A DURATION OF 15 MIN. FOR INTERPRETATION OF THE REFERENCES TO COLOR IN THIS FIGURE LEGEND, THE READER IS REFERRED TO THE WEB VERSION OF THE ARTICLE.

A general trend is observed in the broadness of the melting peak determined by the DSC heating curves in Fig. 10. Samples processed at 22 °C (red curves) and lower pressures (2,000-10,000 lb_f), which contain 16-21% (by XRD) mesophase content, display consistently broader

melting profiles compared to equivalent samples processed at higher temperatures. However, samples pressed at higher pressures (15,000 – 20,000 lb_f) where the mesophase content increased to 29- 30%, showed a melting behavior more in-line with those of the samples processed at 50 ºC. Samples processed at 50 ºC (green curves), which contain between 28% and 32.63% condis crystal mesophase, show melting peaks with an intermediate broadness when compared to the samples processed at 22 ºC and lower pressures (2,000-10,000 lb_f) and the highly crystalline samples processed at 70 ºC. Similarly, samples processed at 60 ºC (blue curves), which contain between 30% to 38% mesophase (by XRD), also show melting peaks with an intermediate broadness. In-line with this correlation, the 70 ºC that consistently displayed a crystalline morphology, displayed narrower melting behavior compared to equivalent samples processed at lower temperatures. Thus, it appears that the preferential orientation present within the sample plays a critical role in the broadness of the DSC melting peak.

As a result, this broadening can be interpreted as variations of the ordered structures within the sample. Since each morphological structure possesses a different thermal stability and different ΔH_f, the variations in morphology result in a wider peak. When samples are processed at temperatures well below the Tm and above Tg (22 ºC), disorganization of the crystallites can occur, resulting in a plastic crystal mesophase. This was characterized by broadened (110) and (200) crystalline XRD scattering rings with a slight anisotropy and an opaque PLM image with faint birefringence. Thus, this broad distribution of the enthalpy change during the DSC melt could be attributed to the percentage of plastic crystal mesophase, forming less stable and more conformationally disordered crystallites within the sample. Likewise, samples processed under pressure and at temperatures close to Tm (50 ºC and 60 ºC) form the more oriented condis crystal mesophase (compared to plastic crystal) characterized by broad birefringent strokes under PLM

and strong anisotropic XRD scattering arcs. The strong anisotropy and orientational order in these samples appears to correlate with the melting peak narrowing. Similarly, samples under pressure processed above the melt (70 ºC), which form a semi-crystalline morphology characterized by small tightly packed crystallites under PLM and sharp XRD scattering rings displayed, display a narrowed melting behavior. A study by Zhuravlev et. al. showed that a double melting behavior of PCL correlated to the different populations of crystals with varying stability.[107] Another study by Liu et. al. showed that a broad double melting in a PCL DSC heating curve can arise when both randomly oriented and preferentially oriented crystals exist within the PCL sample morphology.[108] Thus, the narrowing of the melt perceived by the mesophase and crystalline morphologies may be explained by the increasing preferential orientation within these samples.

CONCLUSION

The morphology and melting behavior of PCL processed by varying pressure-temperature conditions were analyzed using PLM, DSC, and XRD. Processing the PCL samples above the Tm (approximately 57ºC) at 70ºC resulted in a semi-crystalline morphology consisting of small tightly packed crystals, as observed by PLM, and characterized by sharp isotropic crystalline XRD peaks. Samples processed at lower temperatures yet still within the region of the melt at 50 ºC and 60 ºC displayed broad birefringent strokes under PLM and were characterized by XRD scattering patterns indicative of condis crystal mesophase orientation, with broad anisotropic arcs around the equator of the 2D azimuthal pattern. Samples processed well below the melting region at 22 ºC displayed minimal to no birefringent properties, and were determined by XRD to possess a plastic crystal mesophase morphology, with broadened crystalline scattering patterns.

As mentioned, plastic crystals were shown to form at the lowest temperature tested of 22 ºC, and gradually increased in quantity with increasing pressure. The mechanism of this formation

is thought to be the result of crystal disorganization upon plastic deformation, related to the low-energy barrier slip-planes in the crystalline structure. This mechanism was also supported by the significant decrease in crystallinity upon formation of plastic crystal morphology. With sufficient chain mobility achieved at higher processing temperatures (50 ºC and 60 ºC), the mesophase formation appeared to transition from plastic crystal to condis crystal. As opposed to plastic crystal, the condis crystal quantities were not affected by pressure. The additional chain mobility at these temperatures enabled this mesophase to orient radially (normal to the direction of the external load). In orientating to the condis crystal phase, this phase was observed to form at the expense of both the crystalline and amorphous phases. Analyzing these mesophases by hot-stage PLM and hot-stage XRD, revealed that they are stable through the melt, transitioning directly from the condis or plastic crystal states to amorphous when heated above the Tm. Finally, it was seen by both hot-stage PLM and DSC that the induced morphologies had a significant effect on the melting range ΔT observed by hot-stage PLM and the ΔH_f of the melting peak observed by DSC. The semi-crystalline morphologies of the samples processed at 70 °C displayed melting behavior over a narrower range of temperatures under hot-stage PLM with a sharper melting peak seen by DSC, when compared to the other induced morphologies. The samples that were processed at lower temperatures (60 °C, 50 °C, and 22 °C) displayed larger melting range ΔT under hot-stage PLM compared to the samples processed at 70 °C, with the ΔH_f more broadly distributed through the melting peak observed by DSC. This broadening of the PLM melting range and the DSC melting peak appears to correlate with the mesophase content.

We believe that this type of characterization will help further the understanding of polymer morphology and in future work we intend to apply this approach to analyze both erodible and non-

erodible polymer. The findings shown here further suggest that mesophase formation in PCL may serve as a new route for tailoring the material properties.

SUPPLEMENTAL MATERIALS

Processing Conditions			Radius	Height	Volume	Surface Area	Δ Height	Δ Surface Area
Press (lbs)	Time (min)	Temp (°C)	(in)	(in)	(in^3)	(in^2)	(in)	(in^2)
Unaltered			0.205	0.071	0.009	0.354	N/A	N/A
2,000	5	22	0.260	0.039	0.008	0.488	-0.032	0.134
		50	0.351	0.023	0.009	0.823	-0.048	0.469
		60	0.651	0.002	0.003	2.667	-0.069	2.313
		70	1.141	0.002	0.008	8.194	-0.069	7.840
	10	22	0.327	0.035	0.012	0.744	-0.036	0.390
		50	0.520	0.009	0.008	1.728	-0.062	1.374
		60	0.643	0.006	0.008	2.622	-0.065	2.268
		70	1.081	0.001	0.004	7.349	-0.070	6.995
	15	22	0.255	0.045	0.009	0.479	-0.026	0.125
		50	0.478	0.010	0.007	1.463	-0.061	1.109
		60	0.576	0.009	0.009	2.114	-0.062	1.760
		70	1.196	0.001	0.004	8.995	-0.070	8.641
5,000	5	22	0.305	0.033	0.010	0.646	-0.038	0.292
		50	0.491	0.010	0.008	1.546	-0.061	1.192
		60	0.640	0.008	0.010	2.602	-0.063	2.248
		70	1.100	0.001	0.004	7.610	-0.070	7.256
	10	22	0.295	0.027	0.007	0.597	-0.044	0.243
		50	0.482	0.011	0.008	1.493	-0.060	1.139
		60	0.629	0.006	0.007	2.510	-0.065	2.156
		70	0.956	0.003	0.009	5.754	-0.068	5.400
	15	22	0.320	0.027	0.009	0.698	-0.044	0.344
		50	0.408	0.010	0.005	1.072	-0.061	0.718
		60	0.656	0.007	0.009	2.729	-0.064	2.375
		70	0.978	0.001	0.003	6.016	-0.070	5.662
10,000	5	22	0.323	0.029	0.009	0.712	-0.042	0.358
		50	0.466	0.012	0.008	1.400	-0.059	1.046
		60	0.583	0.005	0.005	2.150	-0.066	1.796
		70	1.340	0.001	0.006	11.282	-0.070	10.928
	10	22	0.324	0.025	0.008	0.708	-0.046	0.354
		50	0.542	0.008	0.007	1.873	-0.063	1.519
		60	0.615	0.007	0.008	2.400	-0.064	2.046
		70	0.986	0.003	0.009	6.121	-0.068	5.767
	15	22	0.338	0.021	0.008	0.762	-0.050	0.408
		50	0.493	0.008	0.006	1.552	-0.063	1.198
		60	0.695	0.003	0.005	3.044	-0.068	2.690
		70	1.074	0.001	0.004	7.248	-0.070	6.894
15,000	5	22	0.377	0.022	0.010	0.943	-0.049	0.589
		50	0.529	0.006	0.005	1.775	-0.065	1.421
		60	0.649	0.003	0.004	2.655	-0.068	2.301
		70	1.142	0.002	0.008	8.201	-0.069	7.847
	10	22	0.344	0.017	0.006	0.778	-0.054	0.424
		50	0.552	0.004	0.004	1.925	-0.067	1.571
		60	0.635	0.004	0.005	2.549	-0.067	2.196
		70	0.947	0.001	0.003	5.641	-0.070	5.287
	15	22	0.369	0.024	0.010	0.909	-0.047	0.555
		50	0.418	0.012	0.007	1.129	-0.059	0.775
		60	0.483	0.012	0.009	1.502	-0.059	1.148
		70	0.933	0.001	0.003	5.475	-0.070	5.121
20,000	5	22	0.355	0.018	0.007	0.832	-0.053	0.478
		50	0.468	0.005	0.003	1.388	-0.066	1.034
		60	0.678	0.003	0.004	2.897	-0.068	2.543
		70	0.877	0.002	0.005	4.838	-0.069	4.484
	10	22	0.366	0.017	0.007	0.878	-0.054	0.524
		50	0.526	0.008	0.007	1.762	-0.063	1.408
		60	0.666	0.007	0.010	2.816	-0.064	2.462
		70	0.890	0.002	0.005	4.988	-0.069	4.634
	15	22	0.419	0.019	0.010	1.153	-0.052	0.799
		50	0.485	0.013	0.010	1.514	-0.058	1.160
		60	0.606	0.007	0.008	2.334	-0.064	1.980
		70	0.781	0.002	0.004	3.842	-0.069	3.488
(Surface Area=$2\pi rh+2\pi r^2$)								

TABLE. 1S. PHYSICAL DIMENSIONS OF ALL PROCESSED SAMPLES.

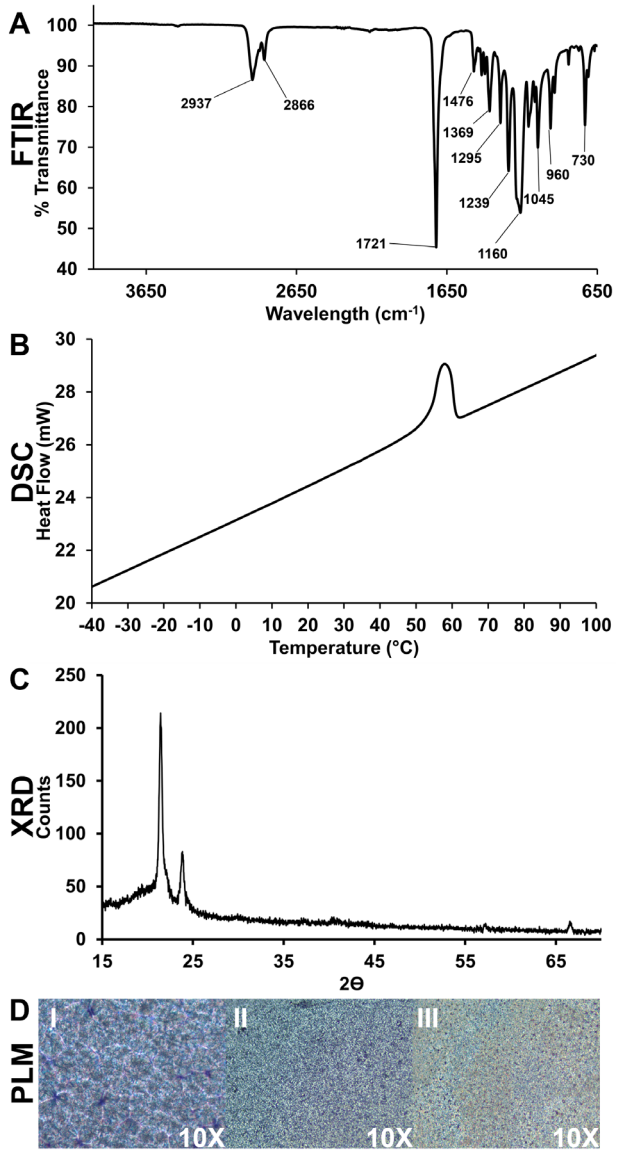

FIGURE. 1S. UNALTERED PCL ANALYSIS. FTIR INTERFEROGRAM OF PCL (A). DSC PROFILE OF PCL. (B) XRD PROFILE. (C) PLM IMAGES (D) UNALTERED (D-I), SOLVENT CASTED (D-II), MELT CASTED (D-III) PCL.

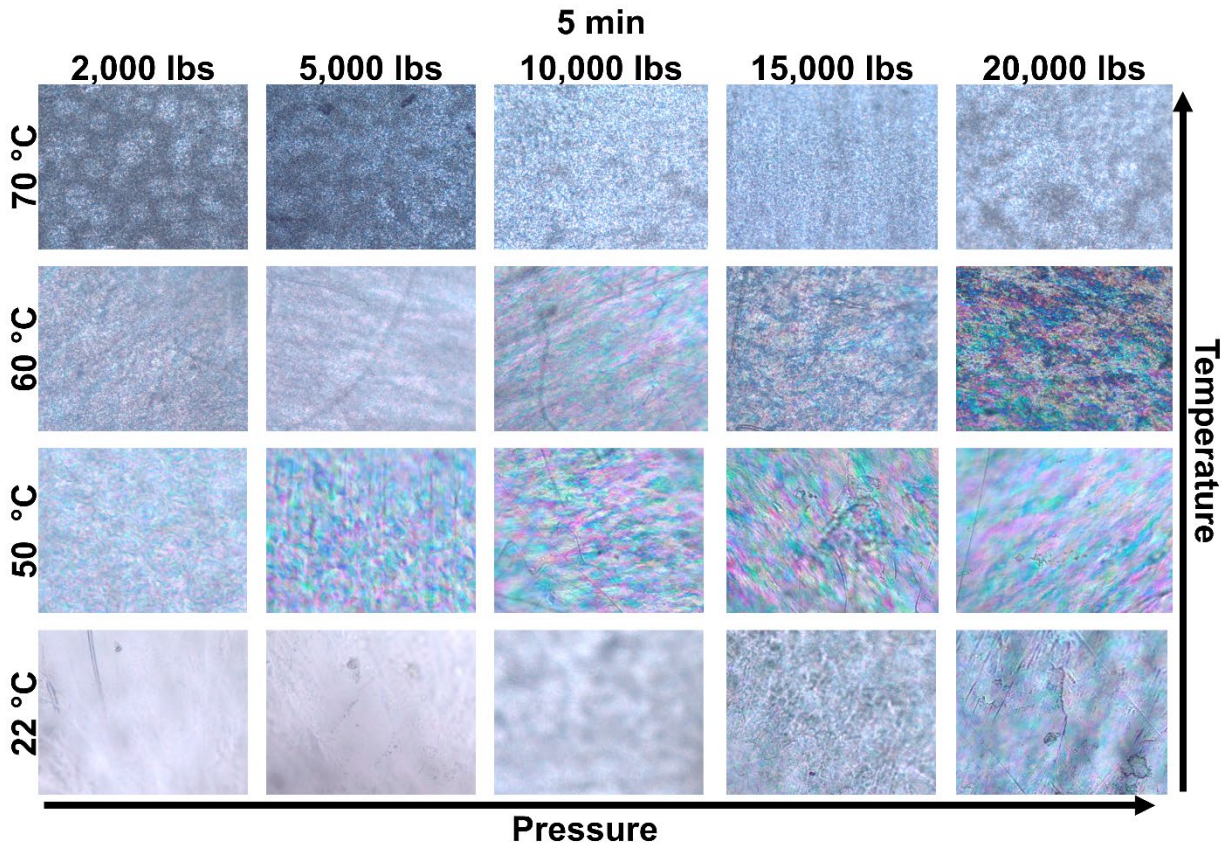

FIGURE 2S CROSSED POLARIZED MICROSCOPY IMAGES AFTER PROCESSING THE PCL FOR 5 MIN UNDER ALL TEMPERATURE CONDITIONS (22 °C, 50 °C, 60 °C, 70 °C) AND PRESSURE CONDITIONS (2,000 LBS, 5,000 LBS, 10,000 LBS, 15,000 LBS, 20,000 LBS)

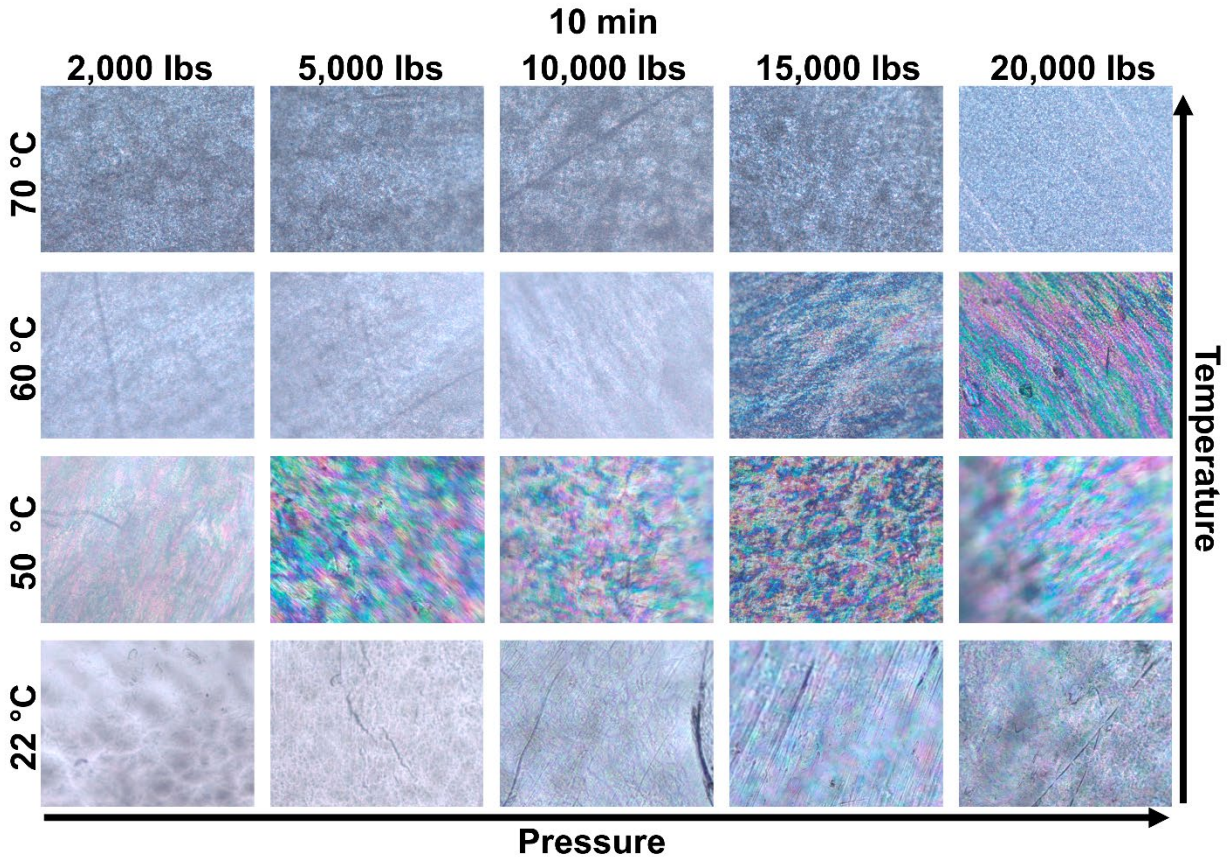

FIGURE 3S CROSSED POLARIZED MICROSCOPY IMAGES AFTER PROCESSING THE PCL FOR 10 MIN UNDER ALL TEMPERATURE CONDITIONS (22 °C, 50 °C, 60 °C, 70 °C) AND PRESSURE CONDITIONS (2,000 LBS, 5,000 LBS, 10,000 LBS, 15,000 LBS, 20,000 LBS)

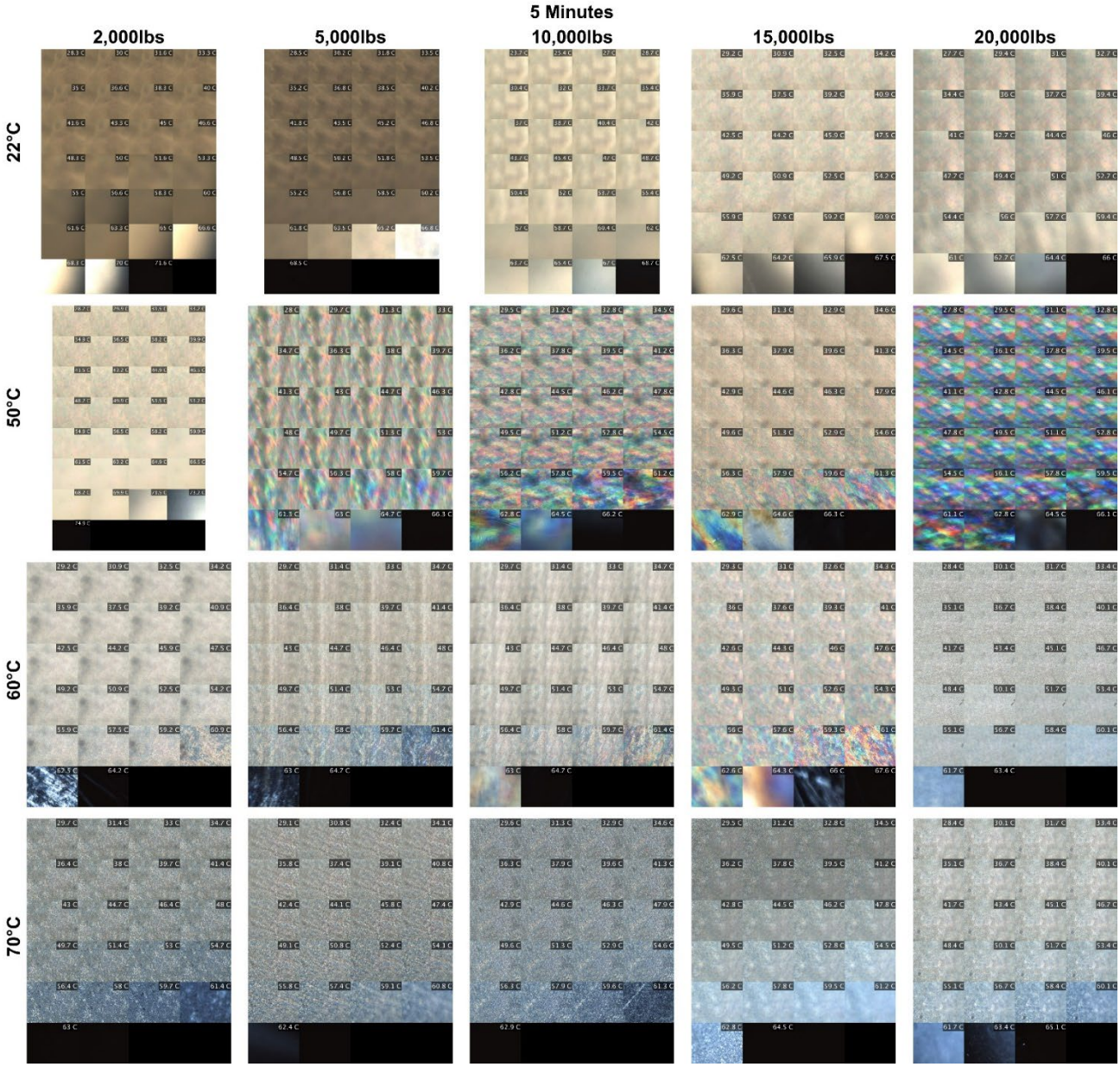

FIGURE 4S HOT-STAGE CROSSED POLARIZED MICROSCOPY IMAGES AFTER PROCESSING THE PCL FOR 5 MIN UNDER ALL TEMPERATURE CONDITIONS (22 °C, 50 °C, 60 °C, 70 °C) AND PRESSURE CONDITIONS (2,000 LBS, 5,000 LBS, 10,000 LBS, 15,000 LBS, 20,000 LBS). THE TEMPERATURE IN THE TOP RIGHT CORNER OF EACH IMAGE REPRESENTS THE HOT-STAGE TEMPERATURE

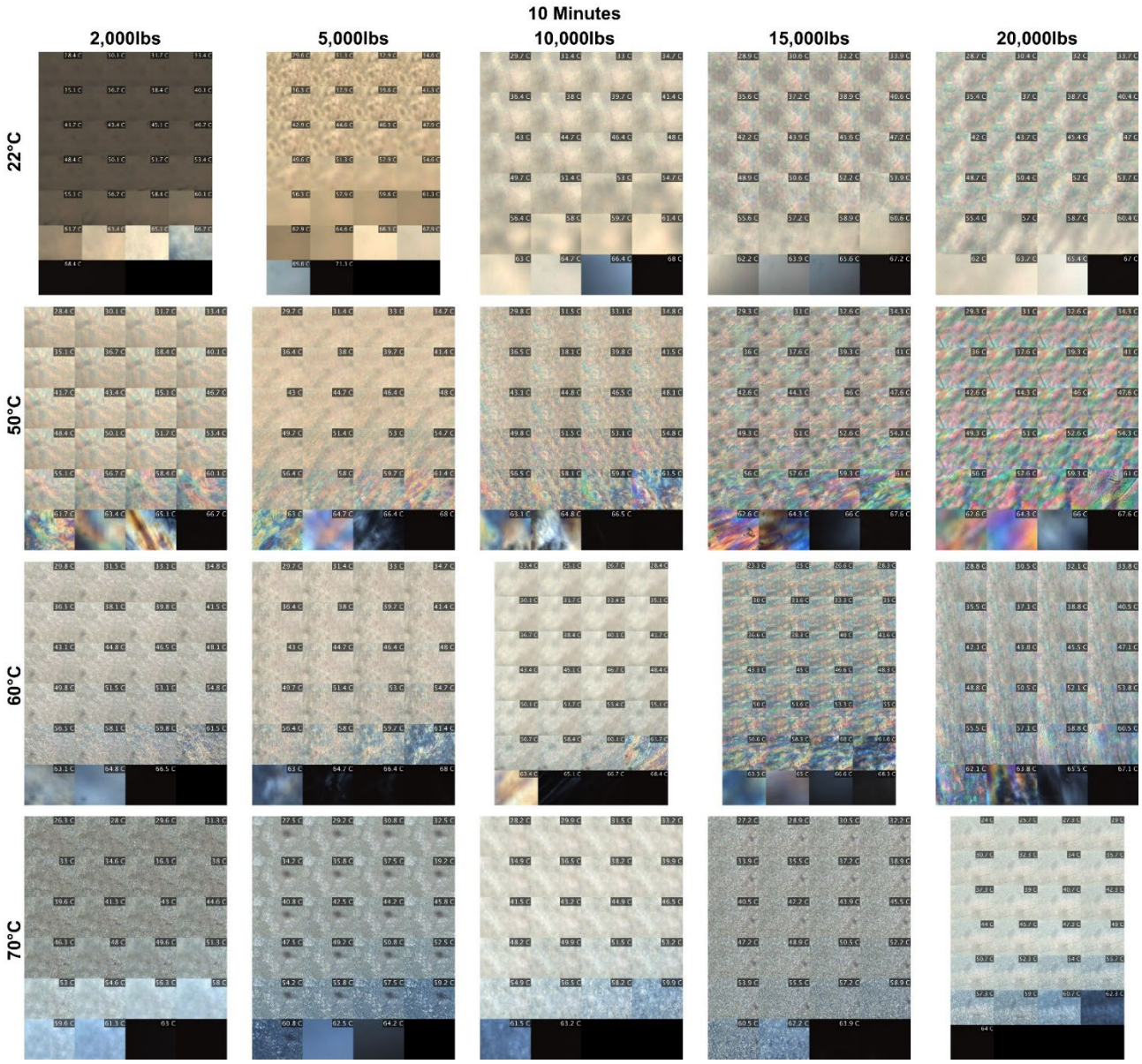

FIGURE 5S HOT-STAGE CROSSED POLARIZED MICROSCOPY IMAGES AFTER PROCESSING THE PCL FOR 10 MIN UNDER ALL TEMPERATURE CONDITIONS (22 °C, 50 °C, 60 °C, 70 °C) AND PRESSURE CONDITIONS (2,000 LBS, 5,000 LBS, 10,000 LBS, 15,000 LBS, 20,000 LBS). THE TEMPERATURE IN THE TOP RIGHT CORNER OF EACH IMAGE REPRESENTS THE HOT-STAGE TEMPERATURE

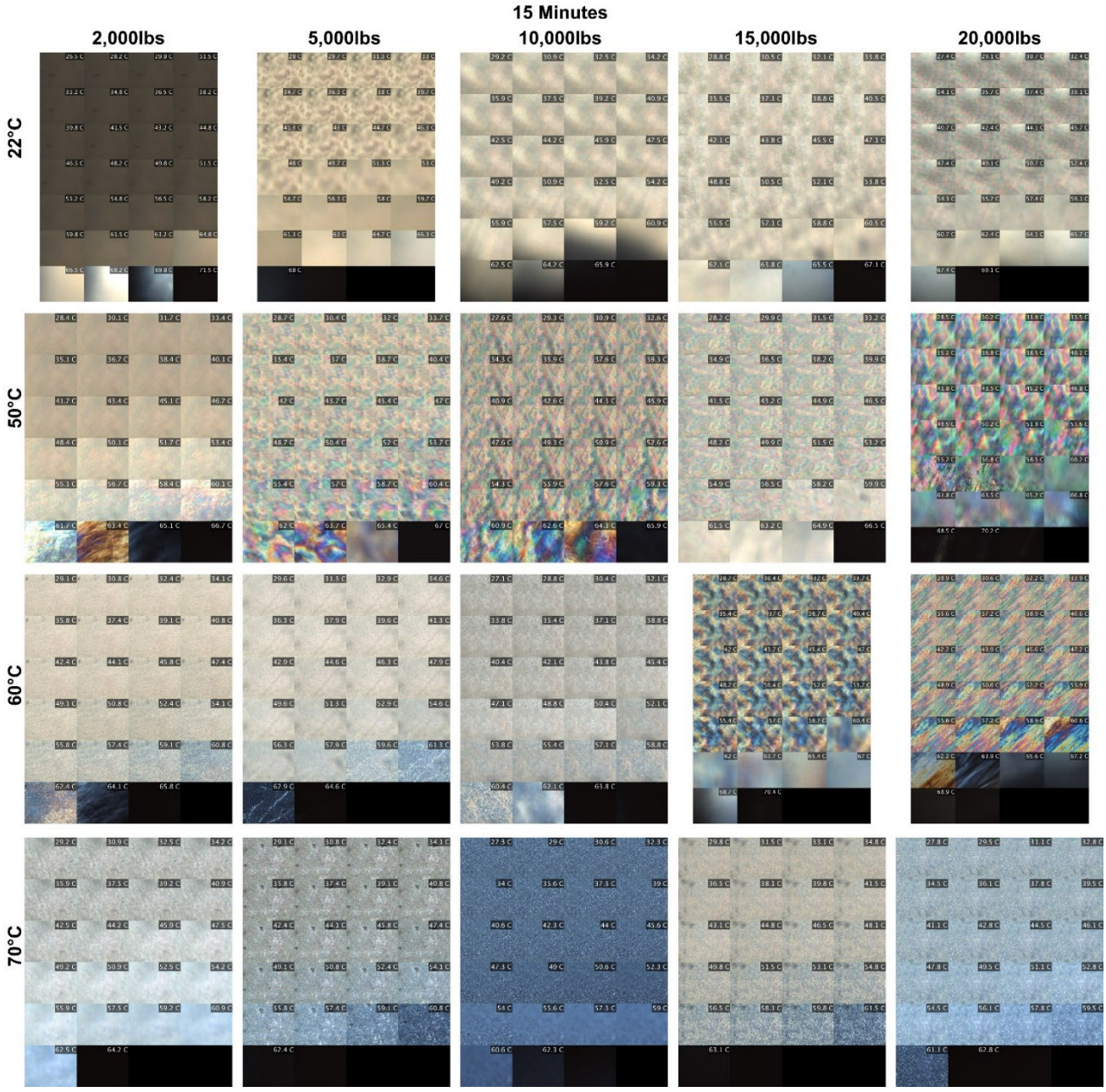

FIGURE 6S HOT-STAGE CROSSED POLARIZED MICROSCOPY IMAGES AFTER PROCESSING THE PCL FOR 15 MIN UNDER ALL TEMPERATURE CONDITIONS (22 °C, 50 °C, 60 °C, 70 °C) AND PRESSURE CONDITIONS (2,000 LBS, 5,000 LBS, 10,000 LBS, 15,000 LBS, 20,000 LBS). THE TEMPERATURE IN THE TOP RIGHT CORNER OF EACH IMAGE REPRESENTS THE HOT-STAGE TEMPERATURE

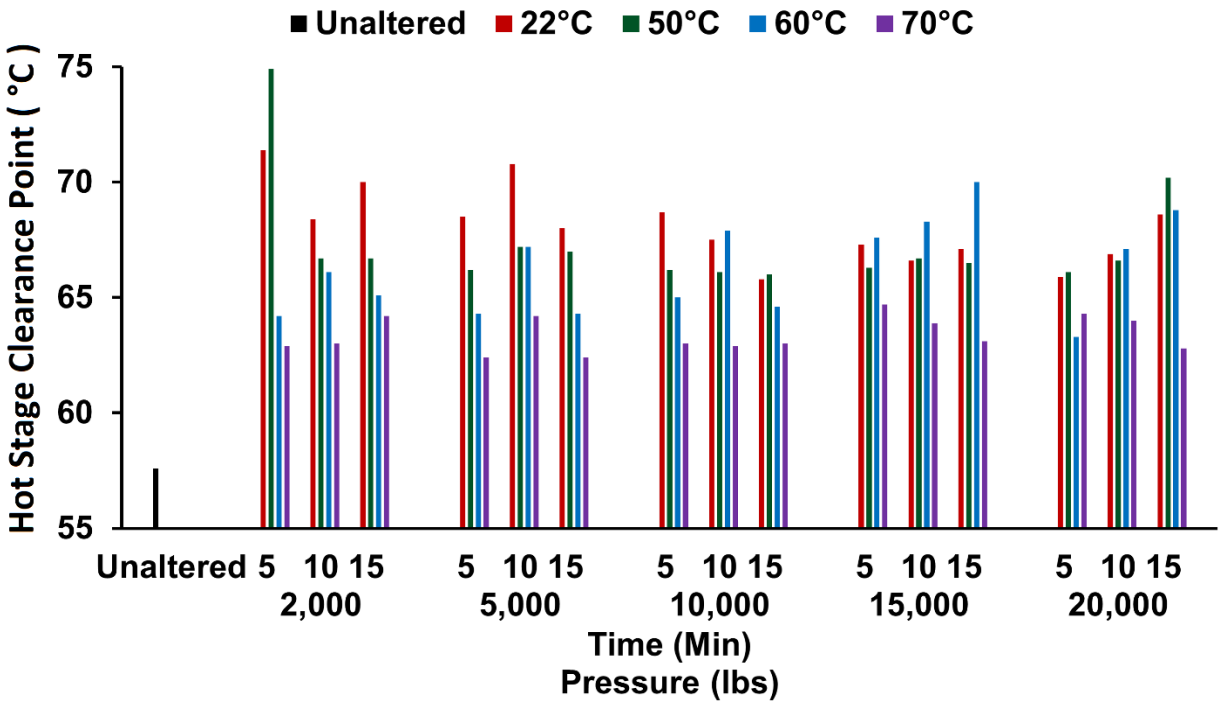

FIGURE 7S CLEARANCE POINT OBSERVED BY HOT STAGE PLM. THE CLEARANCE POINT WAS DETERMINED BY THE TEMPERATURE AT WHICH THE SAMPLE BECAME ENTIRELY AMORPHOUS, DISPLAYING A BLACK IMAGE UNDER POLARIZED LIGHT.

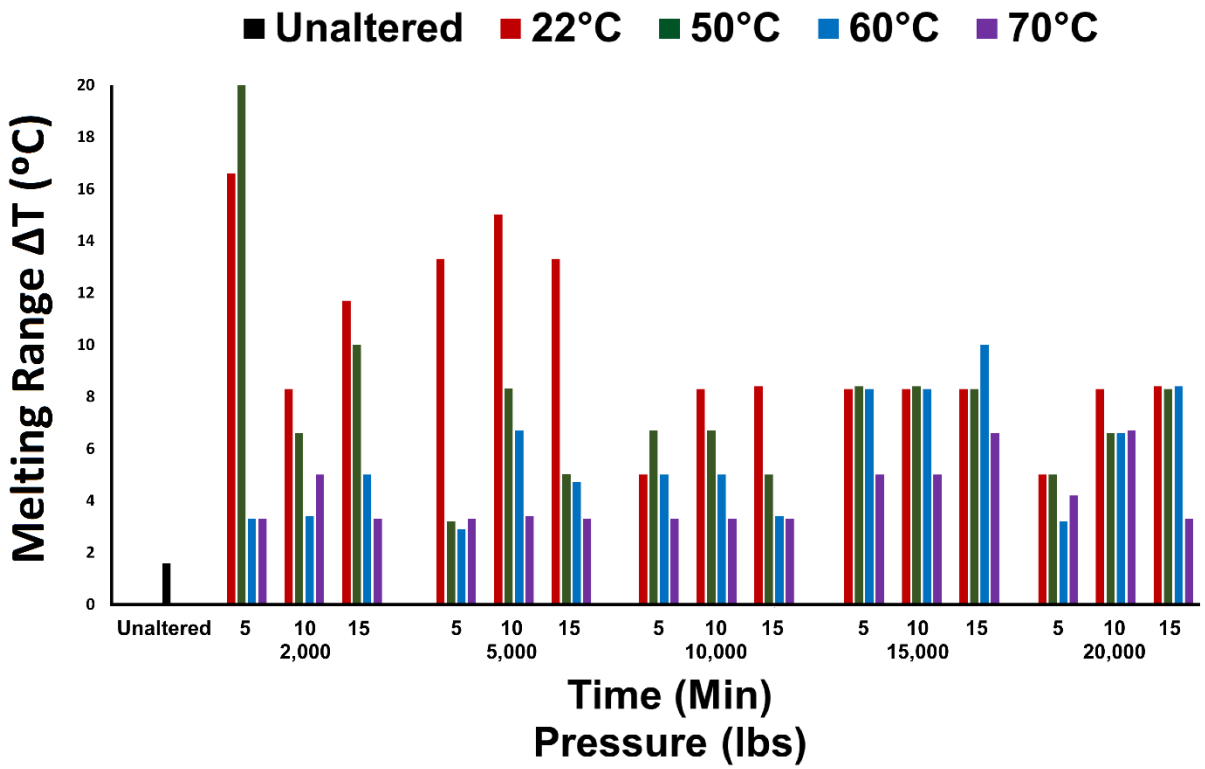

FIGURE 8S MELTING RANGE OBSERVED BY HOT STAGE PLM. THE MELTING RANGE ΔT WAS DETERMINED BY THE CHANGE IN TEMPERATURE BETWEEN THE ONSET OF THE MELT AND THE FINAL CLEARANCE POINT. THE ONSET OF THE MELT WAS CONSIDERED AS THE FIRST TEMPERATURE IN WHICH THE SAMPLE DISPLAYED A VISUALLY NOTICEABLE CHANGE IN MORPHOLOGY (SUCH AS DARKENING OR BLURRING UNDER POLARIZED LIGHT). THE FINAL CLEARANCE POINT WAS CONSIDERED AS THE TEMPERATURE IN WHICH THE SAMPLE BECAME ENTIRELY AMORPHOUS, DISPLAYING A BLACK IMAGE UNDER POLARIZED LIGHT.

Processing Condtions			DSC	ΔH (J/g)	Hot Stage	DSC % Crys	XRD
Press (lbs)	Time (Min)	Temp (°C)	T_m (°C)		T_m (°C)	ΔH/139.5 (J/g)	% Crys
Unaltered			57.73	17.8351	57.73	12.79%	24.85%
2,000	5	22	60.83	25.7582	71.40	18.46%	18.13%
		50	61.37	30.5136	74.90	21.87%	25.25%
		60	62.33	30.6591	64.20	21.98%	34.34%
		70	61.65	31.6741	62.90	22.71%	27.69%
	10	22	62.76	28.5836	68.40	20.49%	20.41%
		50	62.45	30.0635	66.70	21.55%	28.90%
		60	62.03	31.0028	66.10	22.22%	30.97%
		70	61.54	30.4632	63.00	21.84%	31.72%
	15	22	63.85	29.6617	70.00	21.26%	18.19%
		50	62.08	29.2408	66.70	20.96%	27.54%
		60	62.17	29.7445	65.10	21.32%	32.58%
		70	61.77	31.2198	64.20	22.38%	28.35%
5,000	5	22	61.90	30.5651	68.50	21.91%	24.75%
		50	63.00	29.8566	66.20	21.40%	37.10%
		60	62.18	30.7761	64.30	22.06%	29.46%
		70	61.18	30.4830	62.40	21.85%	27.78%
	10	22	62.58	28.6597	70.80	20.54%	17.30%
		50	61.78	29.3238	67.20	21.02%	36.37%
		60	62.08	29.4613	67.20	21.12%	31.04%
		70	61.10	31.5923	64.20	22.65%	27.62%
	15	22	61.66	31.7214	68.00	22.74%	21.95%
		50	64.59	32.7501	67.00	23.48%	39.01%
		60	61.93	32.1270	64.30	23.03%	30.20%
		70	61.21	32.6190	62.40	23.38%	28.08%
10,000	5	22	60.97	31.7188	68.70	22.74%	17.84%
		50	63.34	32.8006	66.20	23.51%	37.84%
		60	62.89	31.7932	65.00	22.79%	30.15%
		70	61.29	34.0963	63.00	24.44%	21.50%
	10	22	60.83	31.1485	67.50	22.33%	24.91%
		50	62.41	32.9268	66.10	23.60%	37.05%
		60	62.04	31.5283	67.90	22.60%	33.99%
		70	61.42	31.7718	62.90	22.78%	27.22%
	15	22	61.40	29.0005	65.80	20.79%	20.96%
		50	62.90	31.9336	66.00	22.89%	31.91%
		60	62.08	32.1475	64.60	23.04%	35.53%
		70	61.69	31.8219	63.00	22.81%	22.79%
15,000	5	22	60.90	30.8659	67.30	22.13%	12.20%
		50	62.01	31.4791	66.30	22.57%	40.94%
		60	62.52	32.2562	67.60	23.12%	45.01%
		70	61.18	32.2138	64.70	23.09%	29.66%
	10	22	61.21	30.6228	66.60	21.95%	25.47%
		50	62.54	31.5901	66.70	22.65%	40.64%
		60	62.75	31.9243	68.30	22.88%	33.35%
		70	60.96	30.1758	63.90	21.63%	25.42%
	15	22	61.61	31.1623	67.10	22.34%	22.79%
		50	61.73	31.5907	66.50	22.65%	27.52%
		60	61.64	32.0554	70.00	22.98%	37.87%
		70	61.81	30.8747	63.10	22.13%	25.88%
20,000	5	22	61.65	30.5718	65.90	21.92%	13.26%
		50	61.54	30.8482	66.10	22.11%	38.22%
		60	61.06	30.4229	63.30	21.81%	31.14%
		70	60.10	30.7628	64.30	22.05%	29.13%
	10	22	61.14	31.1457	66.90	22.33%	29.13%
		50	61.16	30.5574	66.60	21.90%	35.70%
		60	61.52	30.7932	67.10	22.07%	43.36%
		70	60.70	30.8127	64.00	22.09%	24.40%
	15	22	61.61	30.2809	68.60	21.71%	21.68%
		50	62.30	30.5333	70.20	21.89%	26.97%
		60	60.73	30.3275	68.80	21.74%	24.58%
		70	61.54	32.0635	62.80	22.98%	23.43%

TABLE. 2S CALCULATED DSC T_M, ΔH, HOT STAGE T_M, DSC ΔH DERIVED % CRYSTALLINITY, AND XRD DERIVED % CRYSTALLINITY VALUES OF THE MATERIAL BEFORE AND AFTER PROCESSING BETWEEN 2,000 LBS-20,000 LBS WHILE EXPOSED TO TEMPERATURES BELOW AND ABOVE THE T_M OVER 5-15 MIN.

CHAPTER 2

THE CHARACTERIZATION AND QUANTIFICATION OF THE INDUCED MESOPHASES OF POLY-L-LACTIC ACID

Cameron Baptista, Aharon Azagury, Christopher M. Baker, and Edith Mathiowitz[†‡]

Department of Molecular Pharmacology, Physiology and Biotechnology
Center of Biomedical Engineering
Brown University, Providence, RI 02912, USA
‡‡ Edith_Mathiowitz@Brown.edu

The following manuscript has been published in the journal POLYMER
Elsevier: Polymer Volume 226, 4 June 2021, 123822
DOI: 10.1016/j.polymer.2021.123822

ABSTRACT

The pressure-temperature induced mesophases of poly-l-lactic acid (PLA) were studied upon processing at 20,000 lb_f, for 15 min, at varying temperatures from 40 – 120 ºC. The morphology and melting behavior of the processed samples were analyzed by x-ray diffraction (XRD), polarized light microscopy (PLM), and differential scanning calorimetry (DSC). Samples processed near and below the glass transition temperature at 52 °C and 63 °C displayed a nematic-like mesophase, characterized by orientational order of the amorphous XRD scattering, birefringence by PLM, and a post-Tg endotherm by DSC. The nematic-like mesophase quantity in these samples was determined to be 8.7% to 20.5%, respectively, based on hot-stage XRD and peak deconvolution. This nematic-like state was shown to disorder upon heating around the glass transition at 65 °C. Samples processing above the glass transition temperature at 74 °C, 85 ºC, and 120 ºC, displayed a condis crystal-like mesophase, characterized by crystalline reflections of the mesophase XRD scattering, birefringence by PLM, and an increased melting endotherm by DSC. The total quantity of mesophase in these samples was shown to be betweeen 8.8% and 15.8%. Thus, this paper reports the characterization and quantification of two distinct PLA mesophases upon pressure-temperature processing: a nematic-like mesophase formed at temperatures below the glass transition and a condis crystal-like mesophase formed at temperatures above the glass transition.

INTRODUCTION

A complete understanding of morphology as a function of processing conditions is of great importance for the control of thermal and mechanical properties of a material, particularly for polymers. Compared with metals and other inorganic materials, polymers exhibit very complicated

morphological structures: varieties of molecular composition and molecular weight, supramolecular structures, molecular orientation, and phase morphology.[1,47] As a result, this complexity of polymer morphology provides opportunities to produce versatile materials with a wide range of properties.

In terms of morphology polymers are generally classified into two categories: amorphous and semi-crystalline. Amorphous polymers have a randomly oriented isotropic structure, and are characterized as having a glass transition temperature but no melting temperature. Semi-crystalline polymers consist of both amorphous regions and crystalline regions, and are characterized as having both a glass transition temperature and a melting temperature. The crystalline regions of polymers commonly form a spherulite morphology. Spherulites are radially-oriented lamellar crystals which are connected by an interlamellar amorphous phase.[1]

Due to the long chain nature of polymers, the amorphous phase can be oriented to obtain anisotropic properties. In orienting, the structural units of the material preferentially align along an orientation axis. This orientation of the polymer structure can be considered a mesophase (derived from the Greek word "meso" meaning "in the middle").[47,48] The term mesophase was first coined in 1922 by Georges Friedel, and is used to describe morphology that is an intermediate between the conventional amorphous and crystalline phases. Generally, three types of mesophases have been classified: liquid crystals, plastic crystals, and conformationally disordered (condis) crystals. These three types of mesophases have been defined by Wunderlich based on varying degrees of positional, conformational, and orientational order.[48]

This phenomenon of orientation is most notably seen in liquid crystal polymers. Due to their oriented fluid phase, liquid crystalline polymers are often used as precursors to high-performance solids, such as fibers, films, and injection molded products. The most notable

example of liquid crystal orientation is Kevlar, which is a material made from polymeric fibers spun from a polyamide liquid crystal. Due to the high degree of orientation in the molten liquid phase, upon cooling Kevlar maintains this orientation and forms highly durable fibers. The large number of van der Waals forces that result from Kevlar's oriented structure can provide strength in tension up to 200 MPa, which is 10 times that of steel. This oriented structure also endows Kevlar with a high impact toughness, allowing for its application in bulletproof vests. Kevlar is also a superior insulator, with a thermal conductivity of 0.0482 W/mK, similar to that of fiber glass insulation.[49,50]

It is well established that the oriented nature of mesomorphic polymers can allow for applicational benefits such as increased tensile strength and impact toughness, decreased rate of degradation, increased shelf life, decreased permeability to gases, and increased thermal conductivity with low electrical conductivity compared to that of conventional amorphous and semicrystalline polymers.[3,49,51] However, despite these attractive properties, very few biocompatible or eco-friendly mesogenic polymers have been commercialized. This low commercialization may be owed to the fact that for a polymer to naturally display mesomorphic properties, it must contain mesogenic moieties within the polymer chain. Mesogens are rigid and linear regions of a polymer backbone that cause it to spontaneously align in the molten phase. Typically, these mesogens have exotic and complex molecular structures when compared to commonly used polymers and are not susceptible to biodegradation. [7,52,53]

To this end, various techniques have been used to induce orientation into biodegradable polymers that do not naturally display this morphology under typical molten conditions. These techniques can be generally classified as stretching techniques [5–7,109,110] and flow techniques [8–11]. To this end, particular interest has been directed towards the mesophases of polylactic acid (PLA).

[76–78,109–112] Stoclet et al. have demonstrated via differential scanning calorimetry (DSC) and x-ray diffraction (XRD analysis) the ability to induce a mesophase by tensile drawing PLA at temperatures of 70°C and below (most favorably at 10°C above the Tg).[75,78] This mesophase of PLA has been further characterized by Wang et al. in PLA films, and shown to improve the crystallization kinetics upon annealing. [109,110]

Recent work published by our lab suggests that polymer mesophases may also be induced in non-mesogenic polymers via temperature controlled hydraulic compression.[54,113] The compression method includes the steps of (1) heating the polymer to a desired temperature (2) exposing the polymer to a set pressure for time periods varying between 5 and 15 min, while maintaining the temperature; and (3) cooling the polymer while maintaining the elevated pressure. These studies have utilized DSC, XRD, and polarized light microscopy (PLM) to analyze the morphological changes occurring in biodegradable thermoplastic polymers, such as PLA and polycaprolactone (PCL), under various temperature-pressure-time profiles. Most significantly, in the case of PLA, it was found by DSC that multiple glass transition endotherms were present through the glass transition region of the pressure-temperature treated samples.[54] These findings suggested the formation of multiple morphologies during the temperature controlled hydraulic compression processing. These results analyzed in tandem with the anisotropic birefringent properties of the sample under PLM suggested that the change in the glass transition region corresponds to a liquid-crystal like mesophase present in the PLA.[54] Thus, this paper aims to provide further characterization and quantification of the pressure-temperature induced mesophase of PLA. These aims will be addressed through analysis by hot-stage XRD, hot-stage PLM, and modulated DSC (MDSC).

MATERIALS AND METHODS

Processing of Poly-L-Lactic Acid samples

The PLA used in this experiment was donated from Spartech Packaging Technologies (Spartech, Kohler, Wisconsin) for academic research. The PLA was received in sheets, measured to be 0.08 cm thick. For DSC analysis, squares with the dimensions of 1.27 cm x 1.27 cm x 0.05 cm were cut from the bulk material. For XRD analysis, 2.54 cm x 2.54 cm x 0.08 cm squares were cut from the bulk material. The samples were individually subjected to pressure-temperature-time profiles using the method described by Baker et. al.[54] In an effort to balance the scope of this research and build upon prior findings, the effect of pressure and time variability was not analyzed. Thus, a pressure of 20,000 lb_f and a time period of 15 min was used for all processing profiles in this study. The primary variable analyzed was temperature, with parameters ranging from room temperature (approximately 25°C) to 120°C used in processing. This range ensured that the effect of chain mobility on mesophase formation could be analyzed, with temperatures chosen below, through and above the glass transition of approximately 64°C.

In processing the PLA, the samples were placed between two 10.16 cm x 10.16 cm stainless steel plates and inserted into a heating/cooling capable Carver Auto Series Hydraulic Press (Carver, Wabash, Indiana). The hydraulic press was first heated to the desired processing temperature and maintained for 5 min to ensure thorough heating of the sample prior to applying stress. Upon reaching the desired temperature set point, a pressure of 20,000 lb_f was applied immediately for a duration of 15 min. Following, a water mediated cooling system was used to quench the samples back to room temperature while maintaining the 20,000 lb_f stress. It should be noted that the cooling rate was variable, depending on the temperature of the flowing water. However, the cooling process for all samples was on the order of about 5 min.

To provide a set of controls for this study, parallel samples were processed with temperature-time profiles alone, in the absence of external pressure. These control reference samples are defined as follows:

As Received Sample: This sample represents the morphological state of the PLA that was received from Spartech Packaging Technologies. The As Received material was a direct precursor to each processed sample.

Unprocessed Sample: This sample demonstrates a typical semi-crystalline PLA. The thermal history was removed from the As Received sample by melt casted a sample of approximately 2.54 cm inch x 2.54 cm on a hot plate by heating to the melting point (approximately 165°C) for 10 minutes and then removing to ambient conditions.

DSC Temperature Only Controls: In addition, a set of 6 control samples were processed directly in a Perkin Elmer DSC 7 with Pyris Software (Perkin Elmer, Shelton, CT). As Received PLA samples of 3-8 mg weight were heated to desired temperatures ranging from 25°C to 120°C at a rate of 50°C/min and held for 15 min, then subsequently cooled back down to room temperature at a rate of 50°C/min. These controls were designed to provide a reference point for the effect of temperature alone on the DSC heating behavior of the PLA.

Structural Analysis

Hot-stage XRD was performed using a Bruker D-8 Advance X-Ray Diffraction system running DaVinci Software and a Cu X-Ray tube operating at 40 kV and 40 mA equipped with a Bruker Vantec-500 Xe-CO_2 gas filled detector with a 5.32 inch diameter window set at 7.87 inch from the goniometer center. The system optics consisted of a polycap with an output beam divergence of 0.25° for CU and a spot diameter of less than 0.16 inch and a 3 inch long 0.012 inch collimator on the incident beam path (Bruker, Billerica, Massachusetts). Scan were run from 10°

to 90° 2θ with a virtual step size of 0.02° and a counting time of 30 s per step. A Bruker TC-DOME Modular Temperature Stage was used to heat the samples prior to each scan. Various temperatures were chosen between ambient conditions and the melting temperature. Prior to each scan, samples were heated to the desired temperature at a rate of 50°C/min and maintained for 5 min. Upon completion of the scan, data was analyzed using the Bruker Diffract-Eva software package (Bruker, Billerica, Massachusetts).

Polarized Light Microscopy

PLM was performed using an Olympus Model BX-60 (Olympus, Center Valley, Pennsylvania) microscope equipped with polarized filters, 10X, and 50X objectives. For hot-stage analysis, the microscope stage was replaced with a Linkam Scientific Model THMS600 Hot Stage (Linkam Scientific Instruments, Tadworth, United Kingdom) which was operated with a TMS 94 temperature controller running Linksys32 V2.2 software (Linkam Scientific Instruments, Tadworth, United Kingdom). Small pieces cut from the PLA samples were placed on an optically transparent quartz dish and heated for the purposes of optical analysis at a rate of 10˚C/min from room temperature until full melt (determined by the clearance point). Images were captured at a rate of 1 image every 10 s, utilizing a PixeLINK (PixeLINK, Ottawa, Canada) model PL-E421CU color enabled camera running PixeLINK Capture OEM Software Version 2.3.5.0 (PixeLINK, Ottawa, Canada).

Observations of birefringence upon melting allowed for a visual estimation of the clearance point, in which the sample became entirely amorphous. The melting range (ΔT) was defined as the difference in temperature between the onset of the melt and the final temperature at the clearance point. The onset of the melt was considered as the first temperature in which the sample displayed a visually noticeable change in morphology (such as darkening under polarized light). The final

clearance point was considered as the temperature in which the sample became entirely amorphous, displaying a black image under polarized light.

Phase Content Calculation

A quantitative assessment of the weight fractions of each phase (amorphous, mesophases, and crystalline) was conducted from the obtained XRD scattering profiles, by peak deconvolution using the Fityk 1.3.1 software. The fitting method used was developed by Stoclet et al. in which Gaussian profiles were assumed for all scattering peaks and halos.[75,78] Particularly, the amorphous halo parameters were determined by both the unprocessed PLA and previously cited literature reports, with two halo peaks occurring at 2θ values of approximately 15.5° and 21.5°. Upon establishing a best fit amorphous halo, the (110)(200), (203), and (015) crystalline face peaks were established at 2θ value of approximately 16.5°, 18.8° and 22.3°. Finally, mesophases peaks were fit to a R^2 value of at least 0.99 when comparing the computed model to the experimental data. The content of each phase (amorphous, mesophase, and crystalline) was calculated by the area under the diffraction peaks, using the ratio from one phase to the total scattering peaks.

Thermal Analysis

The Perkin Elmer DSC 7 used for thermal analysis was calibrated with a pure indium standard at a heating rate of 10°C/min. Samples of approximately 3-8 mg were cut from the processed PLA and weighed on a Perkin Elmer AD.4 Microbalance (Perkin Elmer. Shelton, CT). To account for inhomogeneity within each processed sample, eight separate DSC runs were conducted. Each run was conducted on either an outer, middle, center, or corner region of the sample. Two separate runs were conducted from each of these areas to test reproducibility and analyze trends within the sample based on location.

The DSC was programed to first cool the sample to -10°C and hold the sample for a period of one minute prior to heating, in order to equilibrate the thermocouple. A StepScan cycle was then used to modulate the temperature in a stepwise manner from -10°C to 170°C. The StepScan parameters were set to have a heating rate of 10°C/min with a step size of 2°C. A one second time resolution was used between points. The isothermal temperature equilibrium was set to hold for a maximum of 1 min with a criteria parameter set to 0.05. The reversing and non-reversing components were then extracted using the Pyris software and displayed as a function of heat flow and time. The Tg, change in specific heat capacity, and enthalpy of relaxation, cold crystallization, and melt were calculated.

RESULTS AND DISCUSSION

Processing of PLA Samples

Samples were processed at four temperatures (40°C, 63°C, 85°C, and 120°C) under 20,000 lb_f for a duration of 15 min. The first temperature of 40°C was chosen as it fell well below the glass transition of the As Received PLA (about 65°C). This temperature represents the polymer in the glassy state, in which chain mobility is at a minimum. The second temperature of 63°C was chosen to obtain a better understanding of how the polymer would behave when processed in the glass transition region. This temperature represents the polymer in an intermediate phase between glassy and rubbery, in which chain mobility is mildly restricted. The third and fourth temperatures of 85°C and 120°C were chosen to obtain a better understanding of how the polymer would behave when processed in the rubbery state (between Tg and Tm) with different driving forces of crystallization. Table 1 provides a detailed account of the dimensional changes that occurred upon processing each PLA sample.

TABLE 1 DIMENSIONAL CHANGES OF PLA SAMPLES UPON PROCESSING

Processing Conditions			Length (cm)	Width (cm)	Thickness (cm)	Surface Area (cm^2)	ΔThickness (cm)	ΔSurface Area (cm^2)
Pressure (lbs)	Time (min)	Temperature (°C)						
As Received			1.27	1.27	0.08	1.61	N/A	N/A
20,000	15	40	1.57	1.57	0.05	2.35	0.03	-0.84
		63	2.03	1.85	0.04	3.74	0.03	-2.13
		85	2.06	2.13	0.04	4.39	0.04	-2.77
		120	2.34	2.31	0.03	5.35	0.05	-3.74

Structural Analysis by XRD

Hot-stage XRD patterns were collected of all PLA samples processed under the conditions described in the previous section. The results are presented in Figure 1S and highlight the structural changes of each sample upon melting on the hot-stage. Correspondingly, each XRD pattern is presented as both a 2D azimuthal scattering pattern and an integrated 2D XRD profile. The changes in amorphous, crystalline, and mesophase content both below and above the glass transition (Tg≈65°C) were calculated by peak deconvolution and can be seen in Table 2. Representative XRD profiles of unprocessed PLA, and PLA processed at 63°C and 85°C were chosen to demonstrate the note-worthy influences of pressure-temperature processing on the structure of PLA (Figures 1, 2, and 3 respectively).

TABLE 2. CALCULATED PHASE CONTENT UPON HEATING, BASED ON HOT-STAGE XRD PEAK DECONVOLUTION. TO ASSESS THE THERMAL STABILITY OF EACH PHASE, PHASE CONTENT WAS CALCULATED FOR SAMPLES PROCESSED BOTH BELOW THE GLASS TRANSITION AT 25°C AND ABOVE AT 85°C.

Processing Conditions			Hot-Stage Temperature	Phase Content		
Pressure (lbf)	Time (min)	Temperature (°C)		% Crystalline	% Amorphous	% Mesophase
20,000 lbf	15 min	As Received	25 °C	0.54	99.46	0.00
			85 °C	0.92	99.08	0.00
		Unprocessed	25 °C	25.22	74.78	0.00
			85 °C	24.56	75.44	0.00
		52 °C	25 °C	0.00	91.29	8.71
			85 °C	0.00	100.00	0.00
		63 °C	25 °C	0.00	79.50	20.50
			85 °C	0.00	100.00	0.00
		74 °C	25 °C	9.04	75.13	15.83
			85 °C	11.12	88.88	0.00
		85 °C	25 °C	18.63	71.79	9.58
			85 °C	24.66	67.98	7.36
		120 °C	25 °C	24.12	67.10	8.79
			85 °C	21.26	70.38	8.36

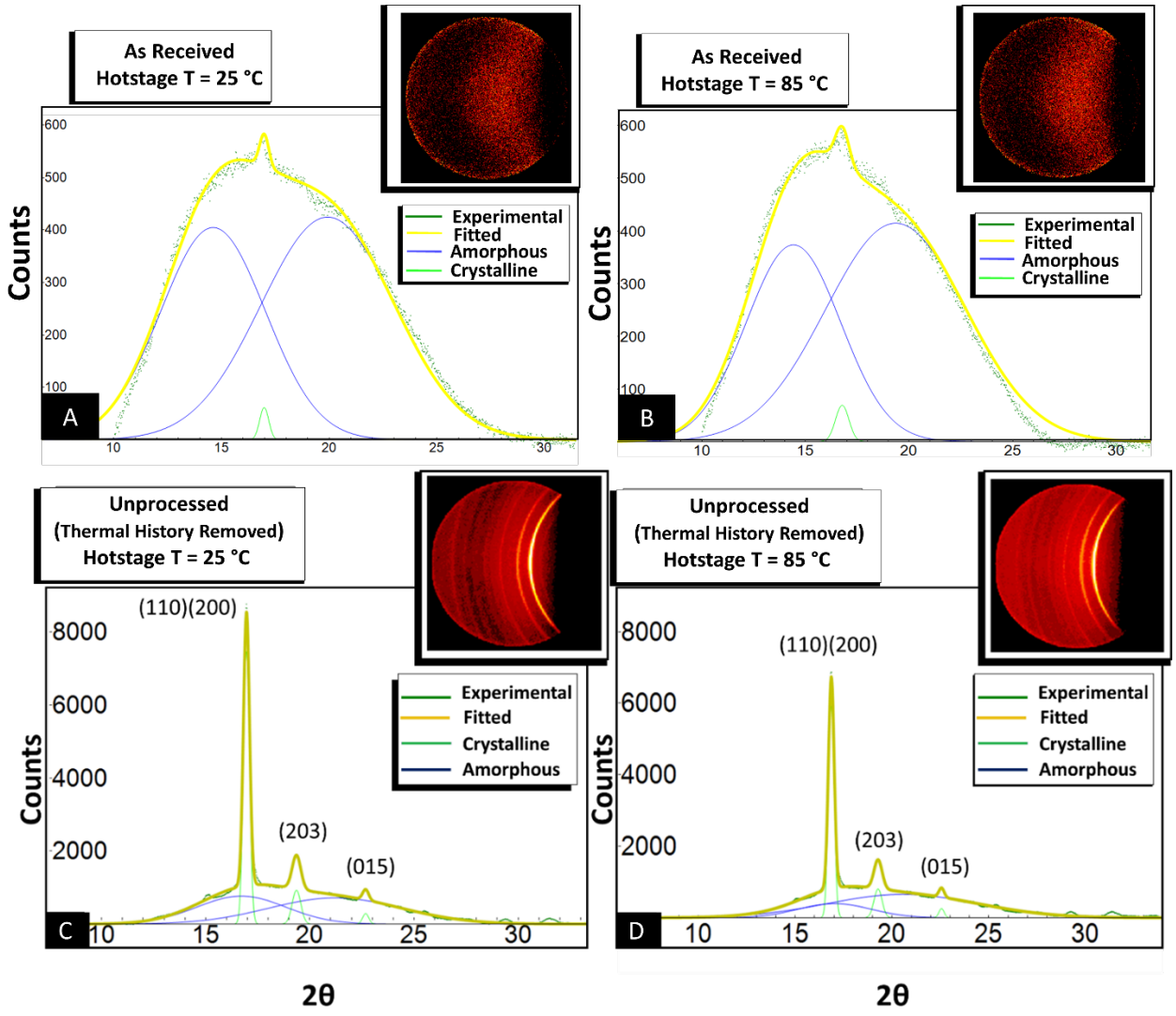

FIGURE 1. HOT-STAGE XRD PATTERNS OF AS RECEIVED PLA BOTH (A) BELOW TG WITH HOT-STAGE TEMPERATURE = 25 °C AND (B) ABOVE TG WITH HOT-STAGE TEMPERATURE = 85 °C. UNPROCESSED PLA WITH THE THERMAL HISTORY REMOVED BOTH (C) BELOW TG WITH HOT-STAGE TEMPERATURE = 25 °C AND (B) ABOVE TG WITH HOT-STAGE TEMPERATURE = 85 °C.

It can be seen in Figures 1a and 1b, that the initial As Received sample from Spartech PLA was predominantly amorphous, displaying broad amorphous halos by XRD. As expected of semi-crystalline PLA, upon removing the thermal history in the unprocessed sample (Figures 1c and 1d) the material displays an isotropic integrated XRD profile consisting of broad amorphous peaks and

sharp crystalline peaks. Specifically, upon deconvolution of the XRD profile, three characteristic peaks of crystalline PLA can be seen in the unprocessed PLA diffractogram. The high intensity crystal peak which falls at a 2θ value of approximately 16.5° has been noted as the (110) and (200) lattice plane reflections of the α and α' crystalline structures of PLA, respectively. While the lower intensity crystal peaks which fall at 2θ values of approximately 18.8° and 22.3° have been assigned to the reflections from the (203) and (015) lattice planes, respectively. [75,78,111,114] In addition to the crystalline peaks, two broad amorphous halos appear at 2θ values of approximately 15.5° and 21.5°. These halos are consistent with previous reports on PLA and are noted to arise from the two characteristic inter-chain spacings within the amorphous region. [75,77,78,111,114]

The 2D azimuthal scattering patterns (top right corner of Fig. 1) represent the respective unprocessed PLA profiles as diffused amorphous rings overlapped by sharp crystalline rings of uniform intensity. This typical semi-crystalline scattering pattern may best be defined and interpreted by the associated positional, orientational, and conformational order. In this instance, orientational order refers to the long-range order of the polymer chains and can be observed by the azimuthal scattering as the focusing of intensity of a given Debye-Scherrer ring (i.e. isotropic or anisotropic). Thus, the uniform intensity and lack of focusing of the amorphous halo and crystalline rings observed in Figure 1 indicate an isotropic structure with no orientation order. Positional order refers to the inter-atomic spacing, which is typically characteristic of the atomic packing of a particular crystal structure and can be observed by XRD at the 2θ value at which given Debye-Scherrer rings occurs. As mentioned, there are three levels of positional order associated with (110), (200), (203), and (015) faces of the α and α' crystalline structures of PLA. Thus, multiple crystalline rings appearing at defined 2θ values of approximately 16.5°, 18.8° and 22.3° indicates positional order arising from these respective crystalline faces. Finally,

conformational order refers to the rotational arrangement of the atoms in a single polymer chain (i.e. gauche or anti conformation) and is associated with the lamellar folding and intermolecular spacing associated with crystal formation. This conformational order can be observed by XRD as the sharpness of a given Debye-Scherrer ring. Thus, the sharpness of the crystalline peaks observed in Figure 1c and 1d represents conformational order within the crystalline phase. To summarize, the semi-crystalline morphology of the unprocessed PLA was identified by XRD though the corresponding positional and conformational order with orientational disorder.

It should be noted that upon heating the unprocessed PLA through the glass transition (from Fig.1c at 25 °C to 1d at 85 °C), the amorphous and crystalline content was shown to remain relatively constant. As recorded in Table 2, the percent crystallinity at 25 °C (Fig 1a) was 25.2% and the percent crystallinity when heated to 85 °C (Fig 1b) was 24.6%. This finding is expected, as PLA is not typically regarded to cold crystallize until temperatures of 100 °C to 140°C are reached (this will be discussed in more detail in the following sections). To this end, while the phase content of each morphology remains the same, the overall intensity of the scattering decreases upon heating from 25 °C (Fig 1a) to 85 °C (Fig 1b). This change in intensity with consistent morphology can be attributed to the thermal expansion and deviations in thickness of the sample as the amorphous region transitions from the glassy to rubbery state.

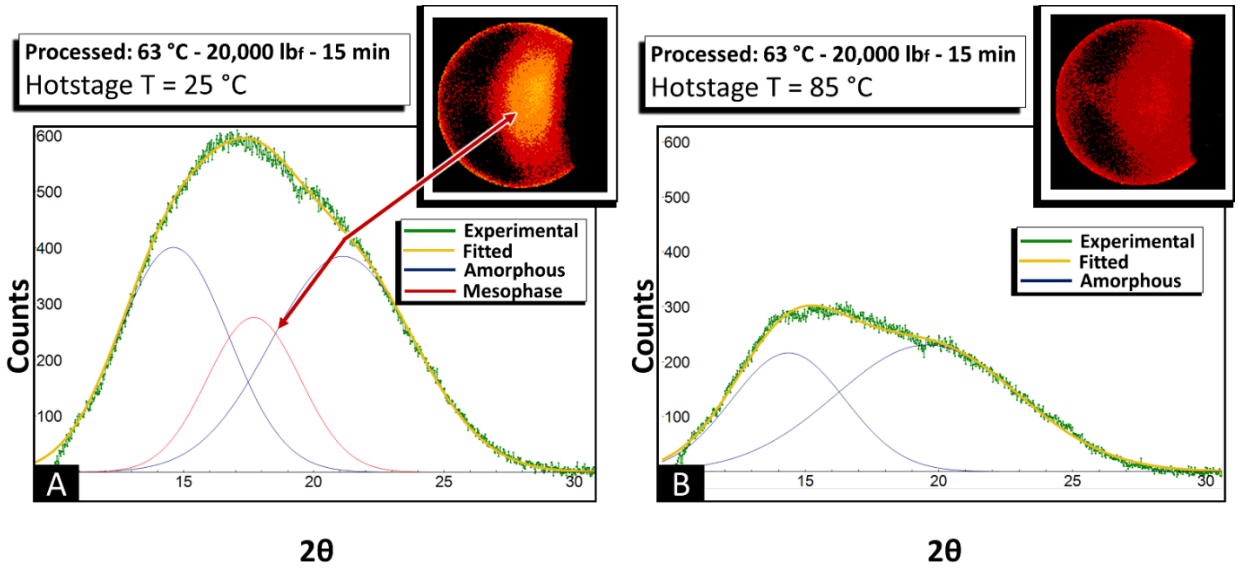

FIGURE 2. HOT-STAGE XRD PATTERNS OF PLA PROCESSED AT 63 °C, UNDER PRESSURE OF 20,000 LB_F FOR A DURATION OF 15 MIN. XRD PATTERNS ARE SHOWN (A) BELOW TG WITH HOT-STAGE TEMPERATURE = 25 °C AND (B) ABOVE TG WITH HOT-STAGE TEMPERATURE = 85 °C

Figure 2 depicts the hot-stage XRD diffraction patterns of PLA processed within the glass transition region at 63°C and the corresponding peak deconvolutions. It should be noted that similar morphology was observed in samples processed at both 52 °C and 63 °C (Figure 1S). It can be seen in Figure 2 that upon processing at 63 °C this sample also displays the characteristic amorphous halos around 2θ = 15.0° and 2θ = 21.0°. However, in addition to these amorphous peaks, a third Gaussian peak located around 2θ = 17.0° is introduced (Fig. 2a). As indicated by the red arrows in Fig. 2a, this Gaussian peak at 2θ = 17.0° is associated with the focusing of the amorphous region around the equator of the azimuthal scattering. This anisotropic scattering is indicative of orientational order within the sample. Specifically, the orientational order seen here in combination with positional and conformational disorder, indicates the presence of a nematic liquid crystal-like mesophase of PLA.[115] It has been defined by Wunderlich that liquid crystal-like mesophases are the subclass of mesophase which are most similar to the amorphous phase, with

the primary distinction between the two phases being orientational order.[48] Moreover, several reports on strain induced oriented PLA fibers have also noted the need for a peak at this approximate location to account for this type of nematic-like mesomorphic form. [75,77,78,111,116,117] In addition, this result is in agreement with previous reports which indicate that this mesophase forms at temperatures close to the glass transition temperature.[78]

The mechanism of this mesophase formation is thought to relate to the limited degrees of freedom of the polymer chains at near-Tg temperatures. It is generally regarded that the frozen glassy structure of a polymer below Tg is limited only to vibrational motion, while heating to the glass transition allows for limited rotational and translational motion to be achieved as the polymer approaches the rubbery state. It is not until the glass transition region is surpassed that full rotational and translational motion can be achieved. Thus, when subjected to external stress and temperature, this limited rotational and translational motion near the Tg is suspected to result in nematic-like orientation as the polymer plastically deforms. It has also been suggested by Na et al that the mesophases of PLA may form naturally, to some degree, upon aging.[118]

Upon heating the PLA processed at 63°C through the glass transition region (from Fig.2a at 25°C to 2b at 85°C), the nematic-like orientation disappears. As recorded in Table 2, the initial phase content of the PLA processed at 63°C was 20.5% mesomorphic and 79.5% amorphous. Upon heating this sample through the glass transition, only amorphous content was detected. This transition can be seen in the 2D azimuthal scattering patterns (top right corners of Fig. 2a and 2b) as the anisotropic focusing of the amorphous region around the equator at 25°C transitions to an isotropic amorphous halo with uniform intensity at 85°C. In addition, a broadening of the corresponding integrated XRD profiles can also be seen as the sample is heated through the glass transition. As a result, the mesomorphic Gaussian peak at $2\theta = 17.0°$ is no longer needed in the

deconvolution of the sample at 85°C. Upon heating to 85°C, only the two characteristic amorphous halos around 2θ = 15.0° and 2θ = 21.0° are seen.

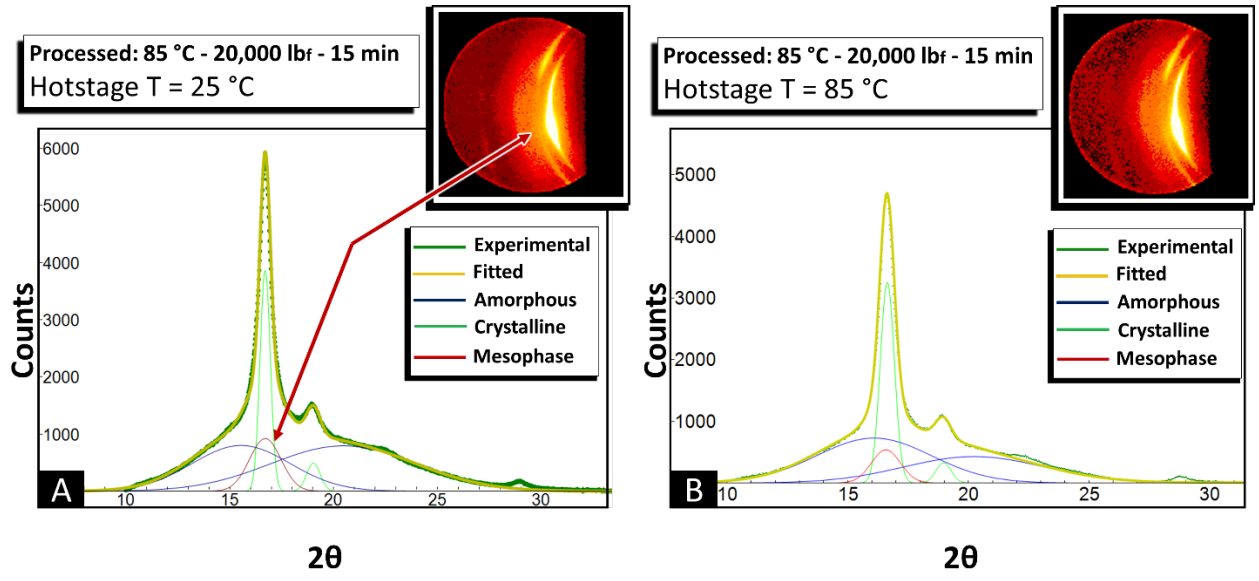

FIGURE 3. HOT-STAGE XRD PATTERNS OF PLA PROCESSED AT 85 °C, UNDER PRESSURE OF 20,000 LB_F FOR A DURATION OF 15 MIN. XRD PATTERNS ARE SHOWN (A) BELOW TG WITH HOT-STAGE TEMPERATURE = 25 °C AND (B) ABOVE TG WITH HOT-STAGE TEMPERATURE = 85 °C

Figure 3 depicts the hot-stage XRD diffraction patterns of PLA processed above the glass transition region at 85°C and the corresponding peak deconvolutions. It should be noted that similar morphology was observed in samples processed at both 74 °C, 85 °C, and 120 °C (Figure 1S). Unlike to the sample shown in Figure 2, processed at 63°C, it is seen here that the elevated processing temperature gives rise to the (110), (200), and (203) crystalline peaks at 2θ values of approximately 16.5° and 18.8° respectively. This increase in crystalline content is expected due to the onset of crystallization which can occur when maintained well above the glass transition. However, it should be noted that cold crystallization is typically expected to occur in PLA at approximately 110-115°C. Thus, the crystallization seen here suggests that processing under 20,000 lb_f pressure may reduce the thermal threshold for crystallization. Further, in addition to the

crystalline formation, it can be seen in the integrated XRD profiles that the Guassian peak located around $2\theta = 17.0°$ was introduced again to account for the orientational order of the mesomorphic form, similar to the sample processed at 63°C. However, in this instance the mesomorphic peak is shown to overlap with the (110) and (200) crystalline peaks. This overlap is marked by the red arrows in Fig. 3a, and can also be seen in the 2D azimuthal scattering as the (110) and (200) Debye-Scherrer ring focuses in intensity near the equator. Interestingly, unlike the mesomorphic form seen in Fig. 2, the morphology seen here is thermally stable and does not disorient upon surpassing the glass transition (from Fig. 3a at 25°C to 3b at 85°C). Rather, this mesomorphic form persists upon heating until the melting point of the crystalline phase is reached (Fig. 1S). Similar thermal stability findings upon tensile drawing of PLA fibers above the glass transition have been shown.[78,116] Stoclet et al. have also reported the surprising distinction that these mesomorphic crystalline reflections do not disorient after heating through the glass transition, unlike the nematic-like mesophase formed at lower temperatures.[78]

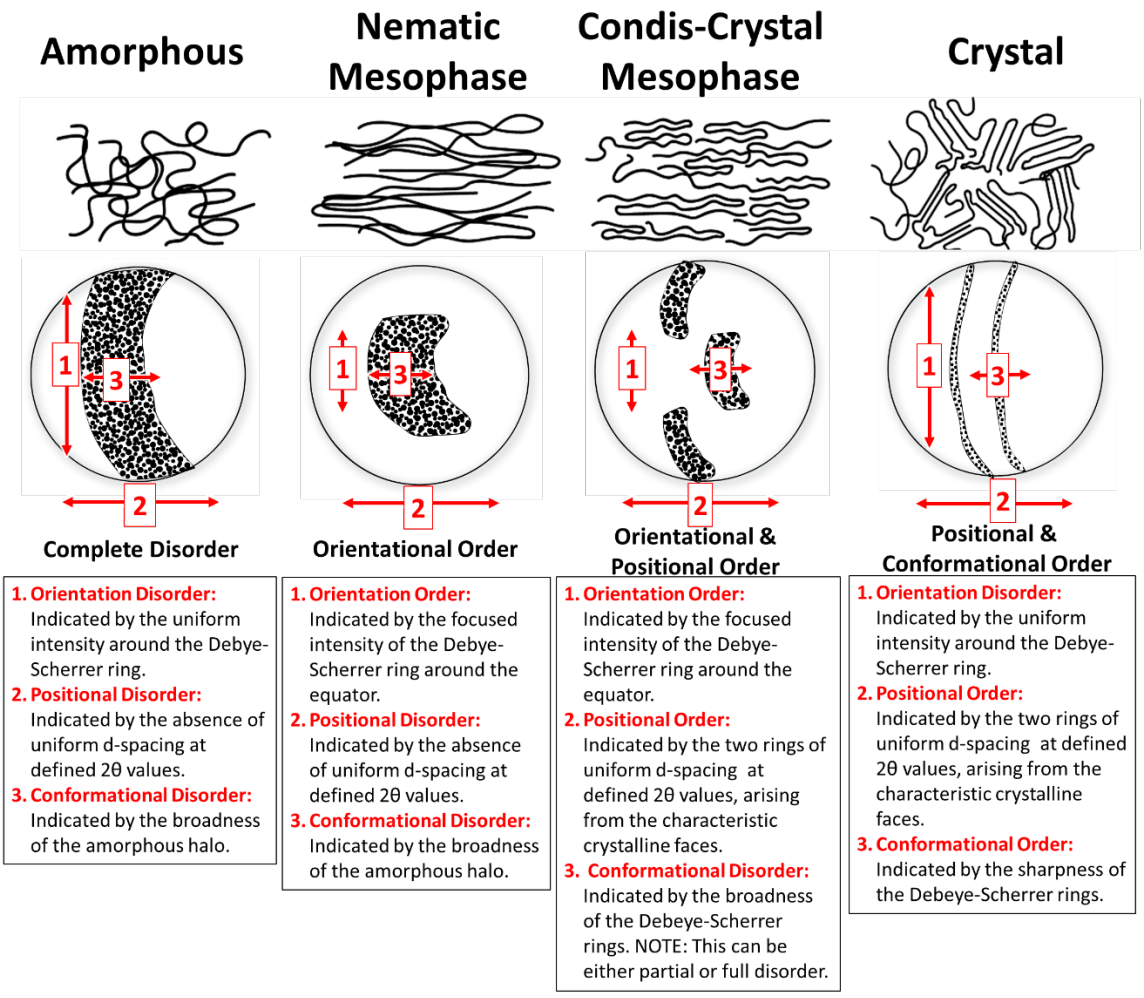

FIGURE 4. (TOP) SCHEMATIC REPRESENTATION OF MOLECULAR ORDER WITHIN THE AMORPHOUS, MESOPHASES, AND CRYSTALLINE MORPHOLOGIES. (BOTTOM) SCHEMATIC REPRESENTATION OF 2D XRD SCATTERING FOR EACH RESPECTIVE MORPHOLOGY, AS WELL AS A DETAILED LIST OF THE INTERPRETED ORIENTATIONAL, POSITIONAL, AND CONFORMATION ORDER.

To this end, the mesophase morphology seen in Fig. 3 displays both positional order as seen by the (110) and (200) crystalline reflection, and also orientational order as seen by the focusing of intensity at the equator of the 2D azimuthal scattering. Thus, these crystalline reflections of the mesophase may be considered more specifically as a condis crystal mesophase. Condis crystals are defined as a type of mesophase closer in structure to the crystalline form than

that of the nematic mesophase (seen in Fig. 2). In the case of condis crystal mesophases, the structure contains both orientational and positional order, whereas nematic mesophases contain only orientational order.[48] A schematic representation of these phases, along with their varying degrees of order are presented in Figure 4.

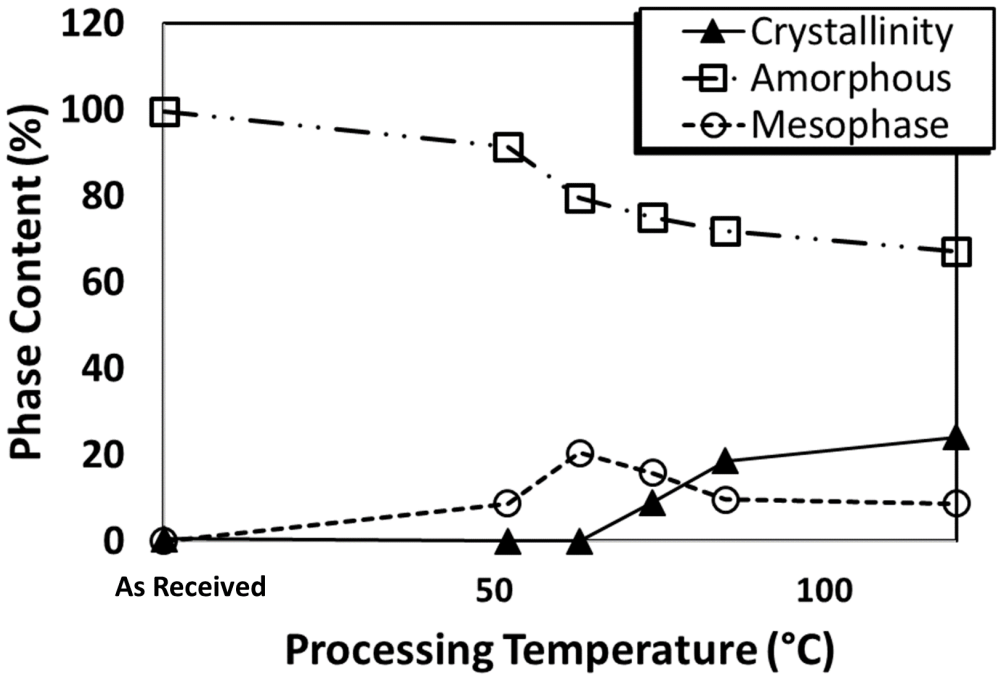

FIGURE 5. CALCULATED PHASE COMPOSITION AS A FUNCTION OF PROCESSING TEMPERATURE, CALCULATED BY XRD PEAK DECONVOLUTION.

A quantitative summary of the processing-induced phase content can be seen in Figure 5. Upon processing at 20,000 lb_f for 15 min at increasing temperatures from 52-120°C, distinct shifts in morphology were identified. Namely, transitions of the semi-crystalline PLA to a nematic-like and condis crystal-like mesophase were seen. At processing temperatures near and below the glass transition region (T = 52 °C and 63 °C), a nematic-like mesophases was observed, defined by orientational order and both positional and conformational disorder (Fig.2). The occurrence of this nematic-like mesophases was seen to reach a maximum (20.5% mesophases content) when

processed near the Tg at 63 °C (Figure 5). At increased processing temperatures, above the glass transition region (T = 74 °C, 85°C, and 120 °C), a condis crystal-like mesophases was observed, defined by orientational and positional order with conformational disorder (Fig. 3).

Birefringence Analysis by PLM

Corroborating the mesophase characterizations in the previous section, each processed sample displayed varying levels of birefringent intensity when analyzed under cross polarized light. This analysis of birefringence was used in parallel with the XRD scattering to further confirm the long range structural orientation within the mesomorphic PLA samples (Fig. 6). In addition, the structural origin and thermal stability of the nematic and condis crystal orientation was further assessed by melting the samples on a hot-stage enabled cross PLM (Fig. 7).

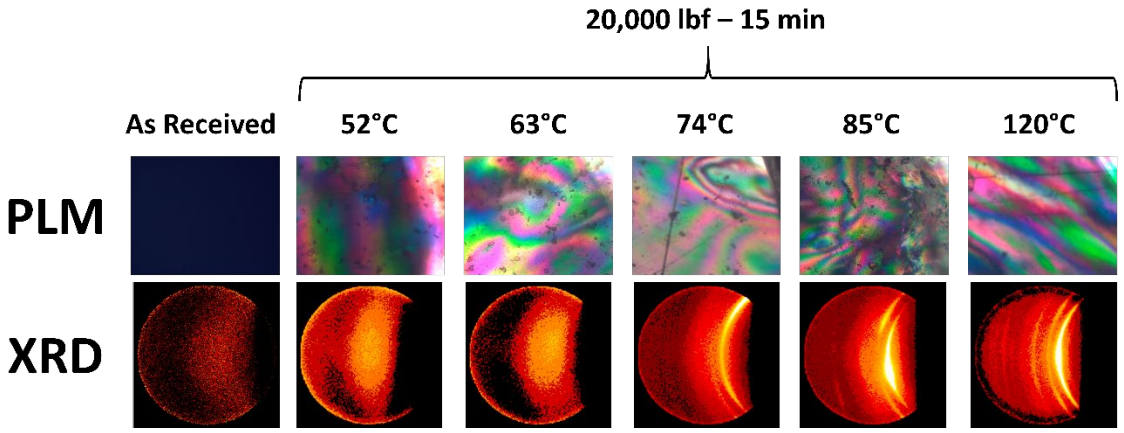

FIGURE 6. ORIENTATIONAL ORDER OF PROCESSED SAMPLES, OBSERVED BY (TOP) BIREFRINGENCE BY PLM AND (BOTTOM) FOCUSING OF XRD SCATTERING

Fig. 6 depicts the analysis of structural orientation within the unprocessed and processed samples. The top row displays the birefringent properties of each sample as observed by PLM, and the bottom row displays the 2D azimuthal XRD scattering. From left to right, each column displays

a typical example of the birefringence and XRD scattering of samples processed under increasing processing temperatures, starting with an unprocessed sample on the left.

First, it should be noticed that the As Received PLA sample does not display birefringence under cross polarized light, and correspondingly shows an isotropic amorphous scattering profile by XRD. This uniform scattering and lack of birefringence thus indicating that orientational order is not naturally present in the As Received sample. However, upon processing at 20,000 lb_f for 15 min at increasing processing temperatures from 52-120°C, each sample displayed some birefringent intensity. This birefringence seen in the processed samples is indicative of long range orientational order. Further, this characterization of birefringence is important for understanding the structural nature of the orientation observed by XRD (Fig. 2 and Fig. 3). As noted in the previous section, this orientational focusing of the XRD scattering is seen primarily in the amorphous region for those samples processed at 52 °C and 63 °C (suggesting a nematic-like mesophase). Whereas the samples processed at 74°C, 85°C, and 120°C begin to show this orientation in the (110) and (200) crystalline reflection (suggesting a condis crystal-like mesophase). It has been defined by Wunderlich. that the long range orientational order of both nematic and condis crystal mesophases should be observed by a manifestation of birefringence under cross polarized light.[48] Thus the findings displayed here in Figure 6 further support the XRD characterization of a nematic-like mesophase at 52°C and 63°C and a condis crystal-like mesophase at 74°C, 85°C, and 120°C.

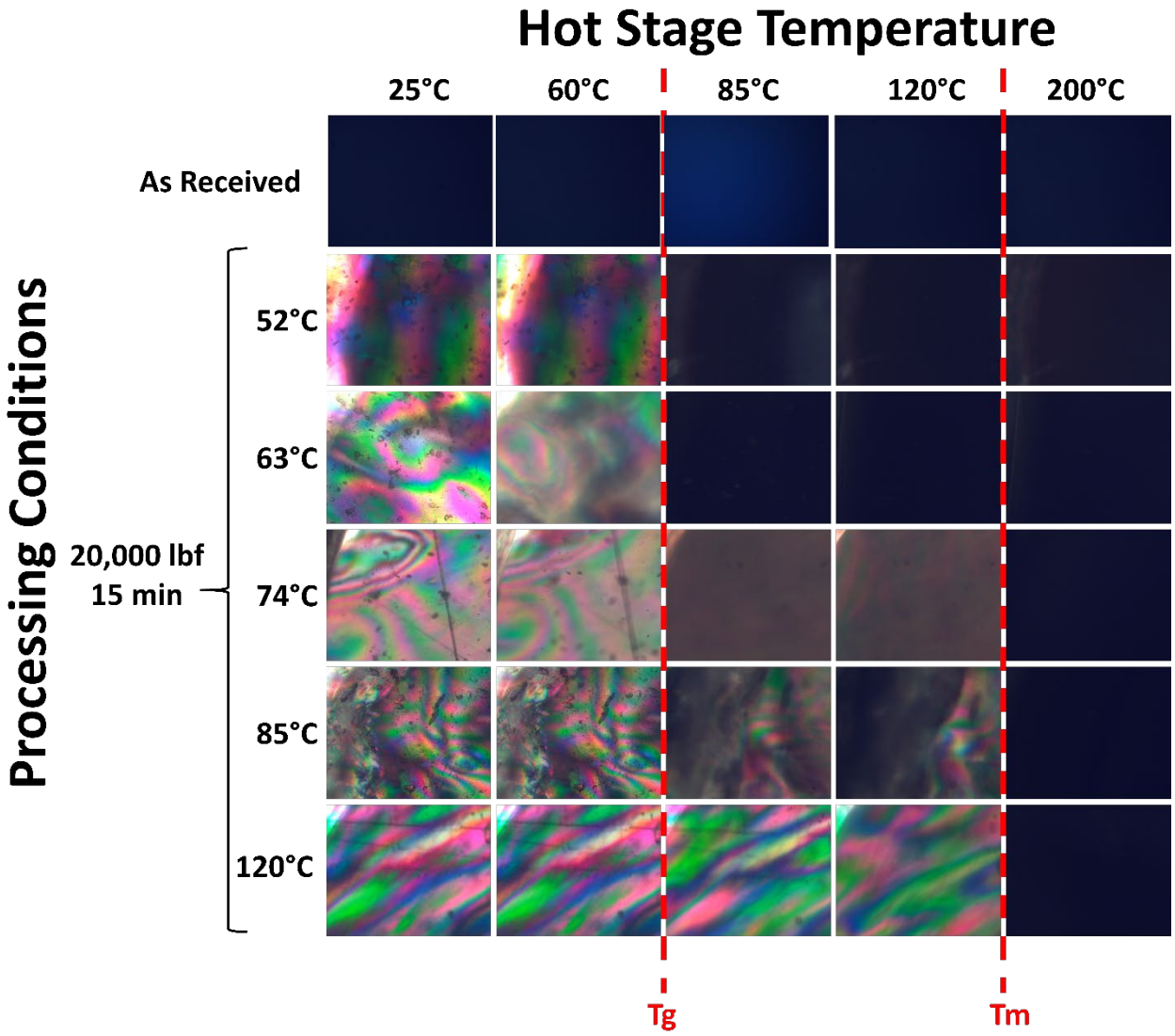

FIGURE 7. THERMAL STABILITY OF BIREFRINGENCE OBSERVED BY HOT-STAGE PLM

To this end, the structural nature and thermal stability of the birefringent orientation identified in Figure 6 was further characterized by hot-stage PLM (Figure 7). From top to bottom, each row in Figure 7 displays the melting behavior and the birefringent thermal stability of samples processed at increasing temperatures, starting with an As Received sample on the top.

Correspondingly, each column in Figure 7 displays the cross polarized image of that sample at increasing hot-stage temperatures.

The As Received sample (top row of Fig. 7) does not show any birefringence, but rather appears transparent below the glass transition at 25°C and 60°C (Tg ≈ 65°C). Upon heating above the glass transition, this sample remains completely transparent through to the melting point (Tm ≈ 160°C). This sample was shown by XRD to be predominately amorphous with the majority of the phase content being about 99% amorphous (Table 2). Further, it was also shown in the previous section that the amorphous and crystalline phase content remained relatively constant upon heating through the glass transition (Table 2 and Fig. 1). Thus, this persistent transparency observed by PLM upon heating is a characteristic of an amorphous and isotropic morphology.

Similarly, the samples processed at 52°C and 63°C (second and third rows of Fig. 7) also reached a clearance point upon surpassing the glass transition. However, in these instances both samples showed an initial display of birefringence. The structural origin of this birefringence is suggested to be the result of a nematic-like orientation of the amorphous phase, as observed by XRD (Fig. 2 and Fig. 6). Further supporting this assessment, it can be seen both here in Fig. 7 and also in Fig. 2 that the birefringence observed by PLM and the orientation of the amorphous halo observed by XRD both reach a clearance point above the glass transition. This coinciding disorganization of both the birefringence and XRD scattering provides further evidence that these phenomena arise from the same structural origin, namely a nematic-like mesophase. To this end, it should be noted that liquid crystal mesophases such as the nematic type defined here are amongst the class of mesophases considered closest to that of the amorphous state. In others words, they contain only long range orientational order but lack both the positional and conformational order typically found in the crystalline phase. As the nematic structure does not contain the thermally

stable lamellar folds, which are characteristic of the polymer melt, this mesophase is expected to transition from a glass state to a rubbery state upon heating. Thus, the disappearance of birefringence (Fig. 7) and orientational XRD scattering (Fig. 2) upon heating through the glass transition suggests that the nematic mesophase may have a glass transition close to that of the amorphous phase.

Unlike the samples processed at 52°C and 63°C, the samples processed at 74°C, 85°C, and 120°C maintained some thermal stability upon heating to the melting point (bottom three rows of Fig. 7). This persistence of birefringence upon heating to the melting point coincides with the orientation of the (110) and (200) crystal reflection which was also seen to be stable until the melting point was reached (Fig. 3). Thus, the birefringence seen here is suggested to be the result of a condis crystal-like mesophase, as observed by XRD (Fig. 3 and Fig. 6). This thermal stability of orientation up until the melting point further indicates that this orientation originated from lamellar folding. To this end, condis crystal mesophases are defined as a class of mesophase closer to the crystalline structure than that of liquid crystal (nematic) mesophase. In addition to the long range orientational order of these mesophases, condis crystals also display positional order indicative of the inter-chain spacings of the crystalline lamellar folds. This additional degree of positional order could be attributed to the observed increased thermal stability of the condis crystal mesophase, similar to that of the crystalline phase. Thus, the persistence of birefringence (Fig. 7 rows 4-6) and orientational XRD scattering (Fig. 3) upon heating through the glass transition and up until the melt (Fig. 1S) indicates that the condis crystal mesophases seen here behaves similar to the crystalline phase with a similar melting temperature.

Thermal Analysis by DSC

The thermal behavior of the processed PLA was investigated by Perkin Elmer's StepScan MDSC, as a function of processing temperature and pressure. To account for the inhomogeneity of the morphology within each sample as a result of processing, heating traces were analyzed from the center, middle, outer, and corner regions of each sample. A representative image of these regions can be seen in Figure 2S. The MDSC heating traces of all samples processed at 40°C, 63°C, °C 85°C, and 120°C are depicted in Figure 3S, 4S, 5S, and 6S. Additionally, heating traces from control samples can be seen in Figure 7S, in which the effect of temperature on sample morphology was analyzed in the absence of external pressure. Quantified values from the glass transition, cold crystallization, and melting are displayed in Tables 1S and 2S.

Upon heating, the pressure-temperature treated PLA samples showed four note-worthy thermal transitions that are characteristic of the processing induced morphology:

1. The appearance of an exotherm just before the glass transition when processed at 40 °C.
2. An increasing endothermic peak just above the glass transition when processed at 63 – 85 °C .
3. A broad cold crystallization exotherm shifting to low temperature when processed at 63 – 85 °C .
4. An increasing melting endotherm when processed at 85 – 120 °C.

The following sections will discuss each one of these transitions.

Pre-Tg Exotherm

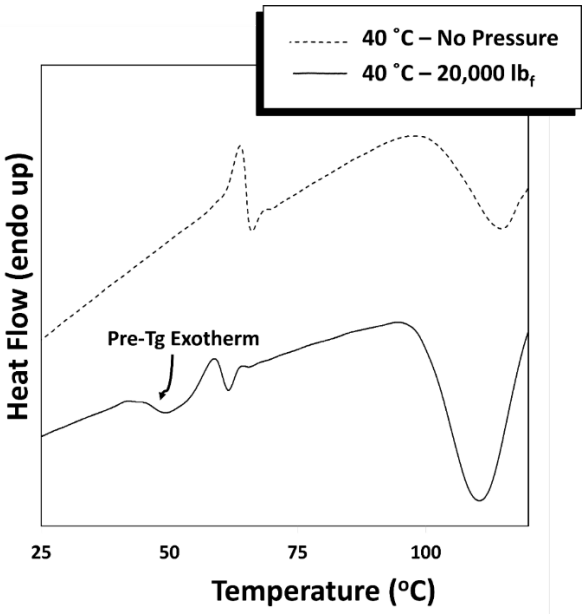

FIGURE 8. A REPRESENTATIVE NON-REVERSING STEPSCAN DSC CURVE DISPLAYING THE PRE-TG EXOTHERM OVERSERVED IN SAMPLES PROCESSED BELOW THE GLASS TRANSITION, AT 40 °C. THE DOTTED LINE DEPICTS A CONTROL SAMPLE TREATED WITH TEMPERATURE ALONE, AND THE SOLID LINE DEPICTS AN EQUIVALENT SAMPLE PROCESSED WITH A PRESSURE OF 20,000 LBF

A representative image of the pre-Tg exotherm found in the non-reversing MDSC curves can be seen in Figure 8. It should first be noted that this exotherm is entirely absent from the dotted line which depicts the control sample processed with at the same temperature (T = 40 °C) in the absence of external pressure. Thus, the origin of this exotherm could only stem from a pressure induced effect. In observing the full array of MDSC scans collected for all samples (Figures 3S-7S), it becomes readily apparent that this exotherm is predominantly displayed when PLA is processed under the glass transition at 40°C. It can be seen in Figure 3S that this exotherm is homogenously present in all regions of the sample, including the center, middle, outer, and corners. However, when the processing temperature was increased to a temperature near the Tg, this exotherm was not as homogenously displayed. This becomes apparent when observing Figure 4S,

which depicts the heating traces obtained from PLA processed at 63°C. In this sample, the exotherm can been seen in both the center and middle regions but is absent in both the outer and corner regions. Further, in observing Figures 5S and 6S, it can be seen that this exotherm is entirely absent when PLA is processed above the glass transition at both 85 °C and 120 °C.

Regarding the nature of this pre-Tg exotherm, it should first be noticed that it appears in the non-reversing curve of the MDSC runs. The appearance of this exotherm in the non-reversing curve indicates that this thermal transition is occurring while the temperature is maintained constant, as opposed to the reversing curve which displays transitions occurring during the heating step. Transitions in the non-reversing curve are associated with slower kinetic processes related to the rotational and translational movement of the polymer chains, while transitions that appear in the reversing curve are associated with faster kinetic processes, such as vibrational motion, and are directly related to the heat capacity of the material. Thus, it can be concluded that this exotherm may be the result of morphological changes related to slower kinetic processes, such as rotational and translational motion of the polymer chains. This finding is in line with previously reported literature on fiber drawn PLA, which have attributed this exotherm to the increased free volume of the material as the result of plastic defects.[75,78] The resulting increased free volume from these defects is thus thought to allow for early activation of molecular mobility.[11,119,120] It should be noted that the nature of plastic defects in compressed samples is likely different than that of the microvoids and cavities referenced in fiber drawn PLA. While prior studies on fiber drawn PLA were done with conventional DSC, the MDSC findings in this study strongly agree with the presented theory that the pre-Tg exotherm originating from plastic defects, since this transition is expected to be a slower kinetic process related to the rotational and translational shifting of the polymer chains upon heating. Further supporting the theory that this transition is the result of

plastic defects, is the observation that the exotherm occurred predominately when samples were processed below or near the Tg. It was seen that the exotherm appeared homogenously throughout the 40 °C processed sample, and it appeared only in the center and middle of the 65 °C processed sample. In addition, this exotherm was entirely absent in both the 85 °C and 120 °C processed samples. Considering that the PLA is in a rubbery state above its Tg of 64 °C, it would not be expected to see plastic defects in the 85 °C and 120 °C processed samples, since the amorphous phase of PLA is malleable and free flowing at these processing temperatures. These findings are significant because they suggest the hydraulic compression method used in this study can cause plastic defects within the polymer structure. It has been noted in the literature that the development of plastic defects can greatly reduce the mechanical strength of the material and can have detrimental effects on the performance of the product.[7,121,122] Thus, further consideration should be taken on the effect of processing conditions on the mechanical properties of products produced by this method.

Post-Tg Endotherm

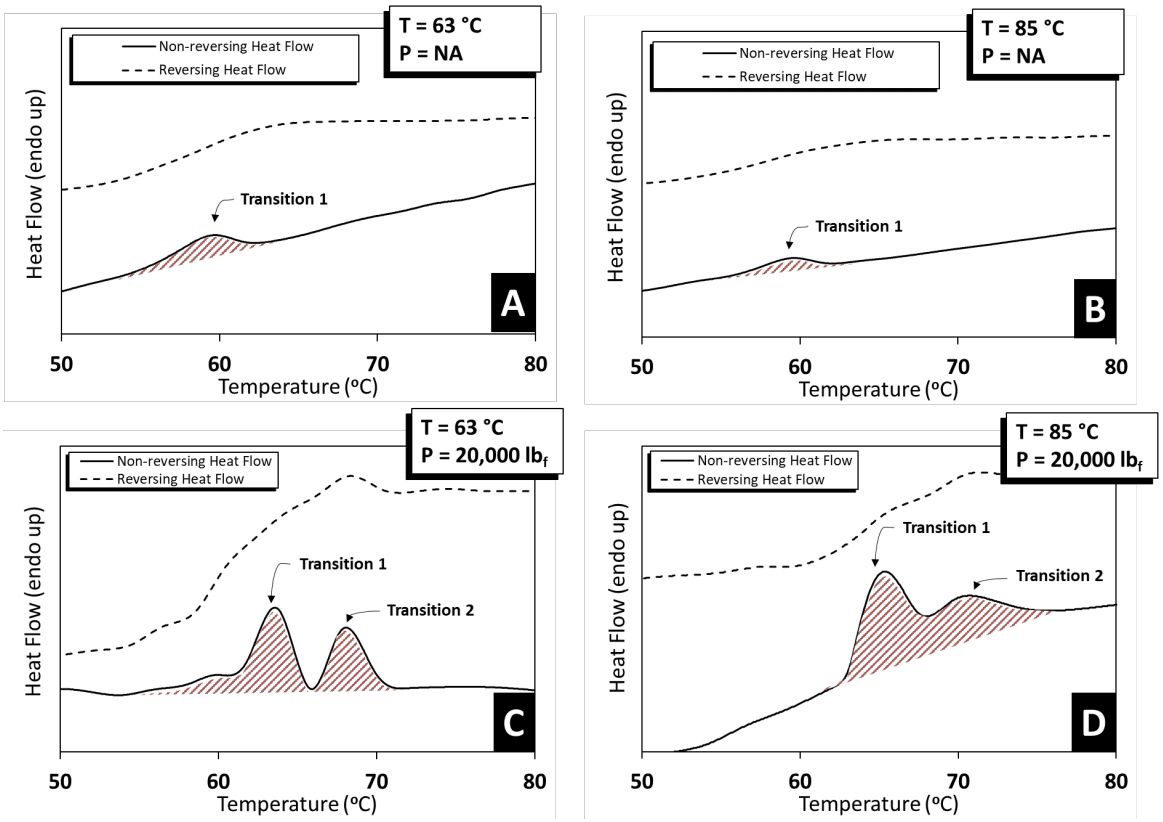

FIGURE 9. REPRESENTATIVE REVERSING (DOTTED LINE) AND NON-REVERSING (SOLID LINE) STEPSCAN DSC CURVES DISPLAYING THE POST-TG ENDOTHERM OVERSERVED IN SAMPLES PROCESSED NEAR AND ABOVE THE GLASS TRANSITION, AT 63 °C AND 85 °C. A AND B DEPICT CONTROL SAMPLES PROCESSED AT 63 °C AND 85 °C, RESPECTIVELY, IN THE ABSENCE OF PRESSURE. C AND D DEPICT SAMPLES PROCESSED AT 63 °C AND 85 °C WITH A PRESSURE OF 20,000 LB_F

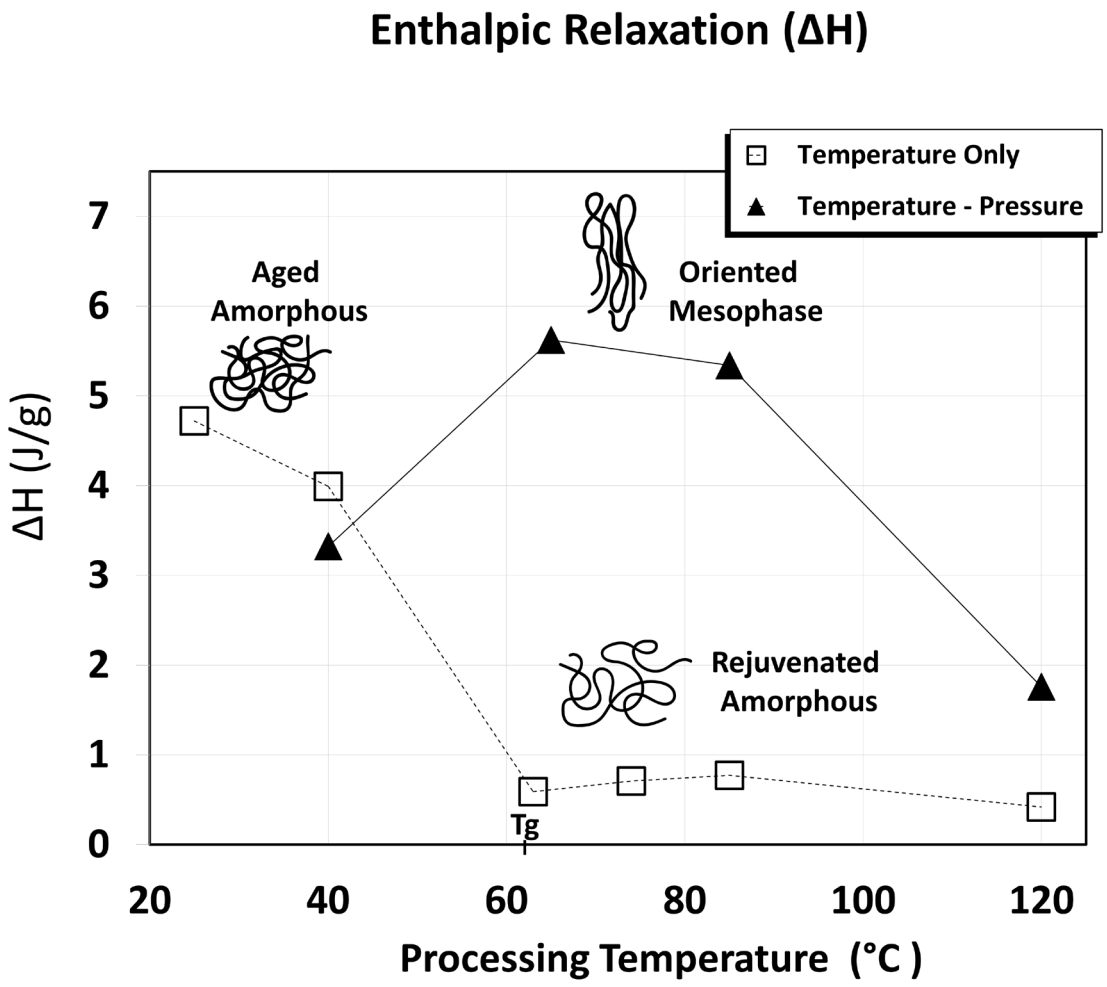

FIGURE 10. ENTHALPIC RELAXATION THROUGH THE GLASS TRANSITION AS A FUNCTION OF PROCESSING TEMPERATURE. THE SQUARE-DOTTED LINE DEPICTS CONTROL SAMPLES PROCESSED WITH TEMPERATURE ONLY AND THE TRIANGLE-SOLID LINE DEPICTS REPRESENTATIVE SAMPLES PROCESSED WITH TEMPERATURE AND A FIXED PRESSURE OF 20,000 LB_F

Representative images of the post-Tg endotherm can be seen in Figure 9. To start, analysis of the control samples in Figures 9a and 9b, which were processed in the absence of pressure, is necessary for the understanding of the post-Tg endotherm seen in the temperature-pressure processed samples, displayed in Figures 9c and 9d. It should be noted that the control PLA samples (Fig. 9a and Fig 9b), which were processed at 63°C and 85°C in the absence of pressure, each displayed a single endotherm in the non-reversing MDSC curve associated with the physical aging

of the polymer (enthalpic relaxation). This endotherm associated with physical aging is caused by an enthalpy loss from structural relaxation. The amorphous nature of a polymer structure is considered a thermodynamically high energy state.[123] Thus, over time the polymer chains begin to creep closer towards an equilibrated state, maximizing the number of secondary bonds between the molecules. This is represented by an increase in density and viscosity, and a decrease in enthalpy and mobility. As a result, the heating of the more stable aged sample results in an endotherm which appears in the non-reversing curve of the MDSC heating profile. This is because the transition from glassy to rubbery state in aged samples requires an increased heat flow towards the rotational and translation motion of the polymer chains.

Figure 10 shows the total enthalpic relaxation through the glass transition as a function of processing temperature, calculated based on the area under the MDSC endotherm. Continuing to analyze the control PLA (processed with temperature only), it can be seen in Figure 10 that the samples treated at 25 °C and 40 °C (without external pressure) display a larger degree of enthalpic relaxation through the glass transition region than the samples treated at 65 °C, 75 °C, 85 °C, and 120 °C (without external pressure). Note, the control sample maintained at 25 °C represents the unaltered PLA material, as received from Spartech Packaging Technologies. The 25 °C control sample displays the largest degree of physical aging, with an enthalpic relaxation (ΔH_{ER}) value of 4.72 J/g. This initial enthalpic relaxation is maintained in the sample processed at 40 °C , with a ΔH_{ER} value of 3.99 J/g. However, upon heating to temperatures near the glass transition and beyond, the 65 °C, 75 °C, 85 °C, and 120 °C control samples display a significant decrease in aging (enthalpic relaxation) with ΔH_{ER} values ranging from 0.420 J/g to 0.773 J/g. This phenomenon of decreasing the enthalpic relaxation and reversing the physical aging of the polymer by heating the sample above the glass transition is referred to as thermal rejuvenation. [120,124,125]

Upon heating above the glass transition, the aged polymer structure can regain chain mobility. Then, upon quenching, the structure is maintained in a thermally rejuvenated state. [126–128] From Figure 10, it can be seen that maintaining temperatures above Tg for 15 min is substantial for thermally rejuvenating the aged PLA samples.

It can be seen that the samples processed under 20,000 lbf at 65 °C and 85 °C contain either a distinct formation of a second endotherm in the non-reversing curve after the Tg or display a tailing of the typical enthalpic relaxation endotherm that appears to be two merging peaks (Figure 9c and 9d). This post-Tg endotherm then does not exists when processed above the cold crystallization temperature at 120 °C (Figure 6S). There are features of this pressure-temperature induced post-Tg endotherm that suggest it originates from the melting of an ordered mesophase rather than from a common aging-induced enthalpy relaxation. First, the observation that the pressure-temperature induced post-Tg endotherm is in some cases an entirely separate peak from that of the typical aging induced endotherm suggests that on a molecular level this transition results from fundamentally different kinetic motions. Second, this post-Tg endotherm appears slightly above the glass transition, which suggests is arises from a more thermally stable morphology. Thus, the manifestation of a post-Tg separate endotherm in these pressure-temperature processed samples suggests that the material is not purely amorphous and may originate from varying degrees of orientation within the polymer structure.

Stoclet et al. noted a similar processing induced post-Tg endotherm to the one seen in Figures 9c and 9d, as the result of tensile stretching of PLA fibers. This endotherm is commonly attributed to the generation of a mesomorphic phase, with local chain ordering [78,129–132] The increased secondary bonding between the chains that results from the orientation is thought to make the phase more stable, thus displaying an endotherm through the glass transition.[118,133–135]

According to Na et al. this post-Tg endotherm can then be thought of as the "melting" of the ordered mesophase.[135] Interestingly, it is worth noting that the peak temperature of the endotherm of the 85 ºC sample is higher than that of the 65 ºC sample, indicating that it forms a more stable morphology.

In support of this idea that the post-Tg endotherm originated from the mesophases of PLA, a quantitative analysis of the ΔH through the glass transition for the pressure-temperature processed samples can be seen in Figure 10. Upon comparing the samples processed under both pressure and temperature to the control samples processed in the absence of pressure, it becomes apparent that the samples processed with pressure were not thermally rejuvenated. As the processing temperature approaches the glass transition region the ΔH_{ER} value is higher for the samples processed under pressure compared to those treated with temperature alone. At the processing temperature of 65 °C, the representative PLA sample processed under pressure displayed a ΔH_{ER} value of 5.62 J/g through the glass transition, whereas the control sample processed with temperature alone displays 0.59 J/g. Upon heating well above the glass transition, the representative 85 °C sample processed under pressure showed a similar ΔH_{ER} value of 5.34 J/g, also maintaining a higher ΔH_{ER} value than the equivalent control sample, with a ΔH_{ER} value of 0.773 J/g. Further, upon heating beyond the cold crystallization point the samples processed under pressure and the control samples both converge towards thermal rejuvenation with ΔH_{ER} values of 1.76 J/g and 0.42 J/g respectively. Thus, it has been shown that maintaining temperatures above Tg for 15 min is substantial for thermally rejuvenating the aged PLA samples. However, it appears that processing under both temperature and pressure results in a more equilibrated state during the same 15 min duration. These observations provide strong evidence for the formation of more stable oriented mesophase induced by the pressure-temperature processing condition. To this

end, when corroborated with the XRD and PLM data described in the previous sections, this post-Tg endotherm is likely the result of a nematic-like mesophases structure. The nematic-like XRD scattering (Figure 2) and associated PLM birefringence (Figure 7) were both seen to disappear and disorient upon heating to the temperature at which this post-Tg endotherm is seen by MDSC.

Shifting Cold Crystallization

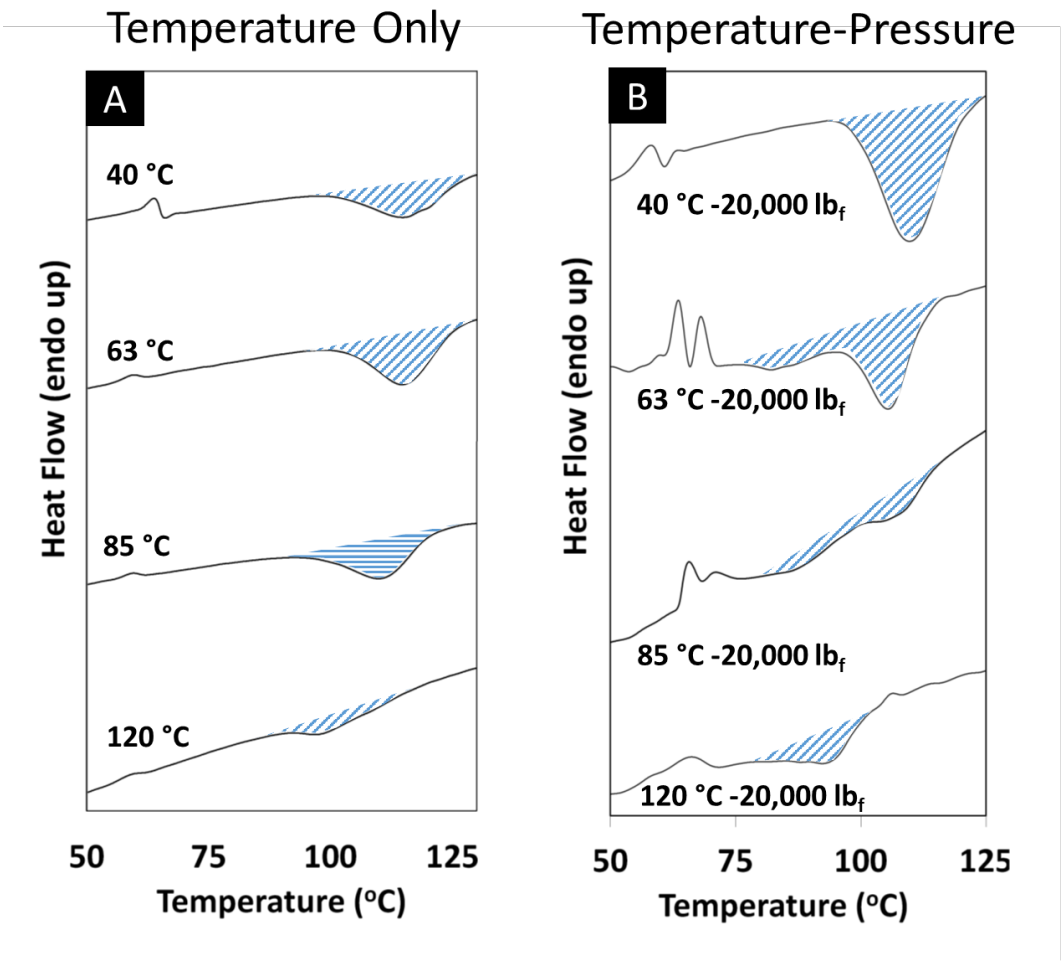

FIGURE 11. REPRESENTATIVE NON-REVERSING STEPSCAN DSC CURVES DISPLAYING THE SHIFTING COLD CRYSTALLIZATION OVERSERVED IN PROCESSED SAMPLES. A) DEPICTS CONTROL SAMPLES PROCESSED AT 40 °C TO 120 °C IN THE ABSENCE OF PRESSURE. B) DEPICTS SAMPLES PROCESSED AT EQUIVALENT TEMPERATURES WITH A FIXED PRESSURE OF 20,000 LB_F

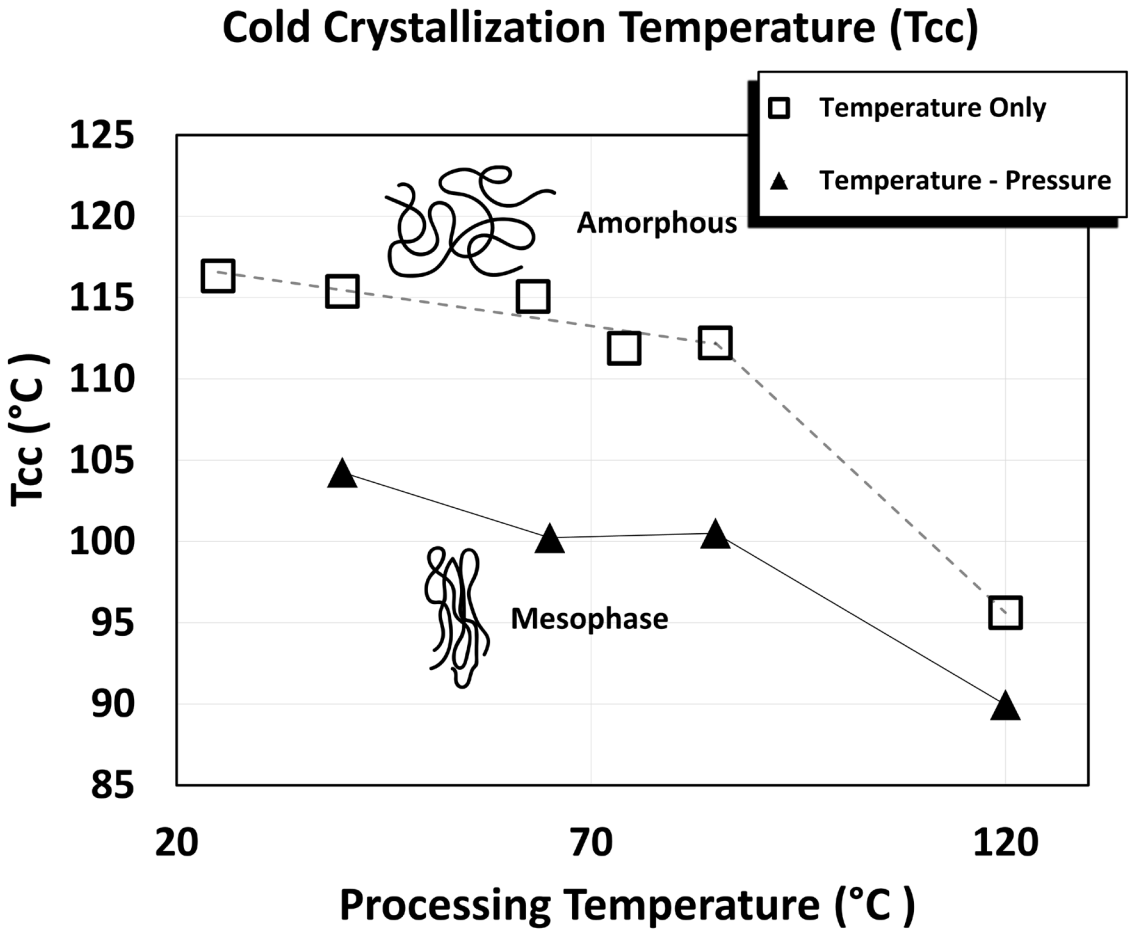

FIGURE 12. COLD CRYSTALLIZATION TEMPERATURE AS A FUNCTION OF PROCESSING TEMPERATURE. THE SQUARE-DOTTED LINE DEPICTS CONTROL SAMPLES PROCESSED WITH TEMPERATURE ONLY AND THE TRIANGLE-SOLID LINE DEPICTS SAMPLES PROCESSED WITH TEMPERATURE AND A FIXED PRESSURE OF 20,000 LB_F

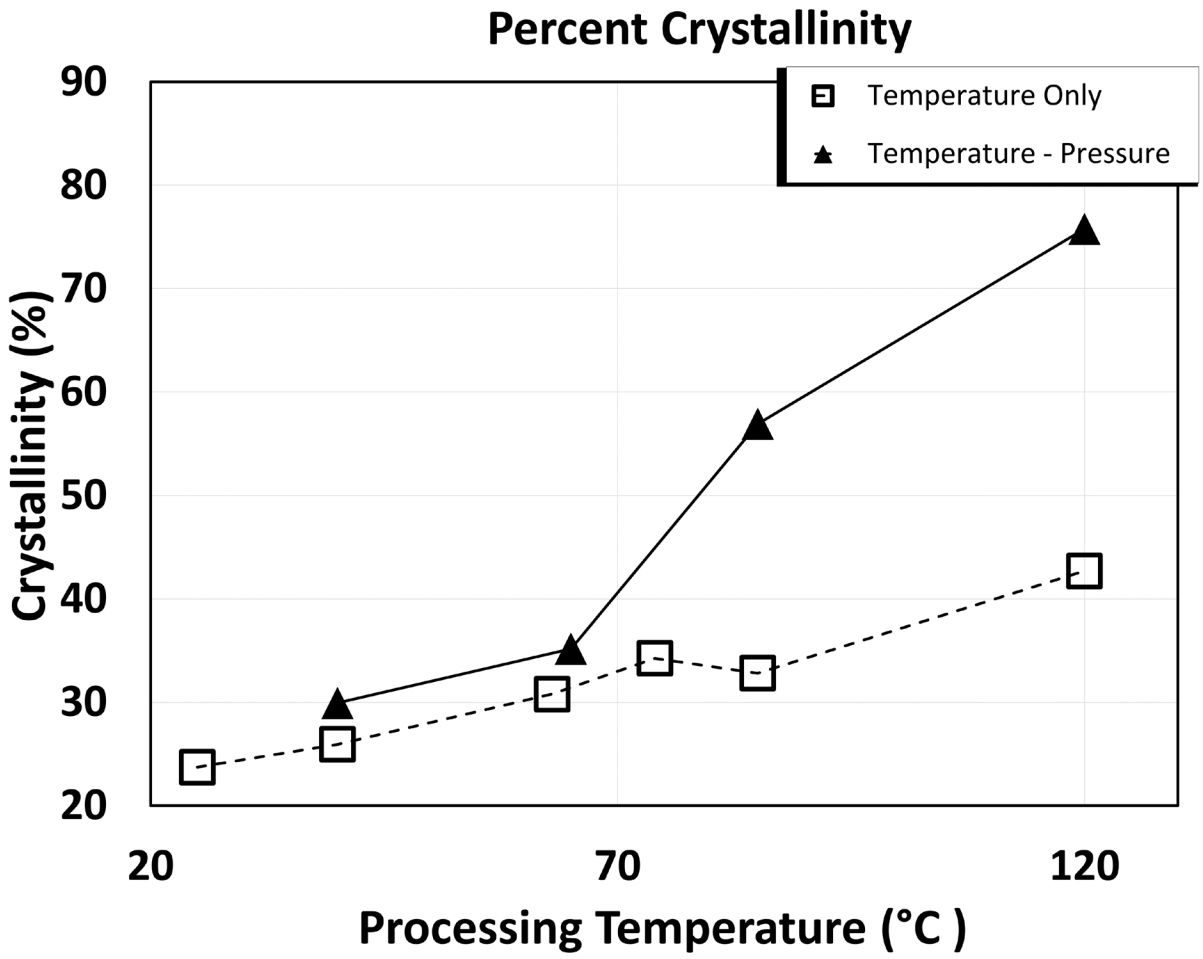

FIGURE 13. PERCENT CRYSTALLINITY AS A FUNCTION OF PROCESSING TEMPERATURE. THE SQUARE-DOTTED LINE DEPICTS CONTROL SAMPLES PROCESSED WITH TEMPERATURE ONLY AND THE TRIANGLE-SOLID LINE DEPICTS SAMPLES PROCESSED WITH TEMPERATURE AND A FIXED PRESSURE OF 20,000 LB_F

A representative image of the changes in the cold crystallization exotherm can be seen in Figures 11a and 11b. For comparison, cold crystallization temperature as a function of processing temperature was plotted for both the control and processed samples. To start, it should be noted that the cold crystallization temperatures of the control PLA show a slight downward trend when processed below the cold crystallization temperature of about 115 °C (shown in Figure 11a). With

control processing temperatures ranging from 25 °C to 85 °C, the cold crystallization temperature ranges from 111.89 °C to 116.34 °C. Upon processing above the initial cold crystallization temperature, at 120 °C, a significant decrease in the cold crystallization temperature can be seen at 95.61 °C. This trend of the cold crystallization exotherm shifting toward lower temperatures in the control PLA can be attributed to the initial crystallinity in the sample. In other words, crystals within the polymer sample act as nucleation centers for cold crystallization and enables crystal growth at lower temperatures. Thus, when processing the control samples at 25 °C to 85 °C the crystallinity of the samples was not significantly changed since the processing was done below the initial cold crystallization temperature of 116 °C (see Figure 13). Therefore, for control PLA samples the cold crystallization temperature was maintained relatively constant, with only a slight downward trend, since the number of nucleation centers was relatively the same between each sample. However, upon processing the control PLA at 120 °C, this processing temperature exceeded the initial cold crystallization of 116 °C and therefore greatly increased the number of crystal nuclei in the sample (shown again in Figure 13 of the following section). Therefore, upon reheating this sample, the crystallization rate was enhanced and a significant decrease in the cold crystallization temperature can be seen.

This analysis of the control PLA samples, processed with temperature alone, is significant for the understanding of the combined effects of both pressure and temperature processing on the cold crystallization of PLA. It can be seen in Figure 11b that the cold crystallization peak of the pressure-temperature processed samples shifts substantially toward lower temperatures and even presents the formation of two separate exotherms when compared to that of the control PLA. It is suspected that the local structural orientation from the pressure-temperature induced mesophases

(seen in Figure 9c and 9d as the post-Tg endotherm) enhance the crystallization kinetics of the PLA, thus decreasing the cold crystallization temperature.

It can be seen in Figure 13 that the percent crystallinity is similar in both the pressure-temperature processed PLA samples and the control PLA processed at between 40 °C to 63 °C. This suggests that processing with and without pressure both have similar effects on the crystallinity of PLA, at these temperatures near and below the Tg, meaning it is a purely thermal effect. From this observation alone, it would be expected that the cold crystallization temperature would be similar for both the pressure-temperature processed samples and the control samples. Based on the logic described above, both processed samples and control samples have similar degrees of crystallinity, therefore the number of nucleation points should also be similar. This should theoretically result in equivalent cold crystallization temperatures. However, upon observing Figures 11 and 12, it becomes apparent that the cold crystallization kinetics differ significantly between the processed and control samples at these temperatures.

While it was shown that both control and processed samples have similar percent crystallinities when processed between 40 °C and 63 °C, the cold crystallization temperature for the processed samples is significantly lower than that of the equivalent control sample (Figure 12). The representative processed PLA at these temperatures display cold crystallization temperatures of 104.25 °C and 100.22 °C respectively. Conversely, the control PLA samples processed at these temperatures display cold crystallization temperatures ranging from 115.38 °C to 115.08 °C. Since this decreased cold crystallization temperature of the processed samples cannot be attributed to the initial percent crystallinity, it is thought that the orientation of the mesophase acts as precursor for crystal formation. Similar results of the PLA mesophase resulting in increased crystallization kinetics have been reported by Wang et. al.[109,110]

Increasing Melting Endotherm

The percent crystallinity calculated by the MDSC curves is presented in Figure 13 as a function of processing temperature. It should first be noted that the crystallinity in the control PLA shows a gradual increase with increasing processing temperature. It can be seen in Figure 13, the percent crystallinity calculated from the melting endotherm ranges from about 24% when processed at 25 °C to 43% when processed at 120 °C. Accordingly, below the glass transition temperature the percent crystallinity was maintained relatively constant, with the 25 °C and 40 °C processed samples only differing in crystallinity by merely 2%. Upon heating near and above the glass transition temperature, the 63 °C, 74 °C, and 85 °C processed samples showed an increase in crystallinity due to the increased mobility. These three samples above the glass transition showed similar crystallinity with percent crystallinities of 31%, 34%, and 33% respectively. Finally, a drastic spike in crystallinity was seen in the 120 °C processed control sample that was above the cold crystallization temperature. This samples showed the largest increase in crystallinity, with a composition of 43%.

Observing the pressure-temperature processed samples in Figure 13, it can be seen that pressure-temperature processing above the glass transition (85 °C and 120 °C) results in increased crystallinity when compared to the control samples. It appears that increasing processing temperature shifts the morphology towards an ordered crystallized state. Thus, when the degrees of freedom are restricted near and below the glass transition, crystallization cannot be achieved. Rather, at these temperatures a maximum in mesophase morphology is reached, particular of the nematic-like form (Figures 5 and 13). However, when the glass transition temperature is surpassed and the degrees of freedom are less restricted, an increase in crystallinity is observed. In addition,

the mesomorphic form observed by XRD shifts from the nematic-like to condis crystal-like state (Figures 3, 5, and 13).

CONCLUSION

In the work presented here, hot-stage XRD, hot-stage PLM, and MDSC were used to provide insight towards the characterization and quantification of the oriented mesomorphic phases induced in non-mesogenic PLA through the application of hydraulic compression processing.

It was seen that pressure-temperature processing near and below the glass transition temperature (T = 40-63 °C) yielded a morphology containing orientational order, with positional and conformational disorder. Accordingly, this morphology was determined to be a nematic-like mesophase. This nematic-like mesophase was characterized by XRD through peak deconvolution and was shown to be associated with the focusing of the amorphous halo around the equator of the 2D azimuthal scattering. This long-range orientation order was further confirmed through the observation of birefringence under hot-stage PLM. Upon heating the nematic-like birefringence was observed to reach a clearance point shortly after the glass transition was surpassed. Further thermal characterization by MDSC showed that this extinction of birefringence was associated with a post-Tg endotherm and decreased cold crystallization kinetics. This endotherm is thus suggested to be the result of the disordering of the nematic-like state. Subsequently, the enhanced cold crystallization following the post-Tg endotherm suggests this mesophase is a precursor to the crystalline form, thus enhancing the crystallization kinetics.

Increased processing temperatures, above the glass transition (T = 74-120 °C) yielded a morphology containing orientational and positional order, with conformational disorder. This

morphology was determined to a be a condis crystal-like mesophases. The condis crystal-like form of PLA was characterized by XRD through peak deconvolution and was shown to be associated with the focusing and broadening of the (110) and (200) crystalline ring of the 2D azimuthal scattering. PLM was further used to confirm the long-range orientation of this mesophase, through the analysis of birefringence. Upon heating, the condis crystal-like birefringence was observed to reach a clearance point as the melting temperature was reached (unlike the nematic birefringence which reached a clearance slightly above the glass transition). Further thermal characterization by StepScan DSC showed that this extinction of birefringence was associated with an increased melting endotherm and percent crystallinity of the sample. This formation of a condis crystal-like mesophase and increased melting endotherm provides further evidence that the mesomorphic form of PLA is a precursor to the crystalline state.

This work demonstrates the ability of compression processing to induce mesophase morphology into non-mesogenic PLA. It is important to consider that other semi-crystalline or amorphous polymeric material might also exhibit mesophase behavior under conditions of temperature and compression processing. However, the structural and dynamic properties of more complex polymer morphologies, such as mesophases, have not fully been discussed or understood in the context of these conditions. Polymeric mesophases in non-mesogenic polymers may be more ubiquitous than previously thought, particularly since high pressure manufacturing such as hydraulic compression is common in industrial processing. We have shown that these mesophases can cause multiple phase transitions and impact the rate and temperature at which crystallization occurs.[54,113] Thus, if the energy needed to induce a mesophase is accidentally exceed by some manufacturing processes, these phase changes may have a considerable impact on the properties of polymeric products.

SUPPLEMENTAL MATERIALS

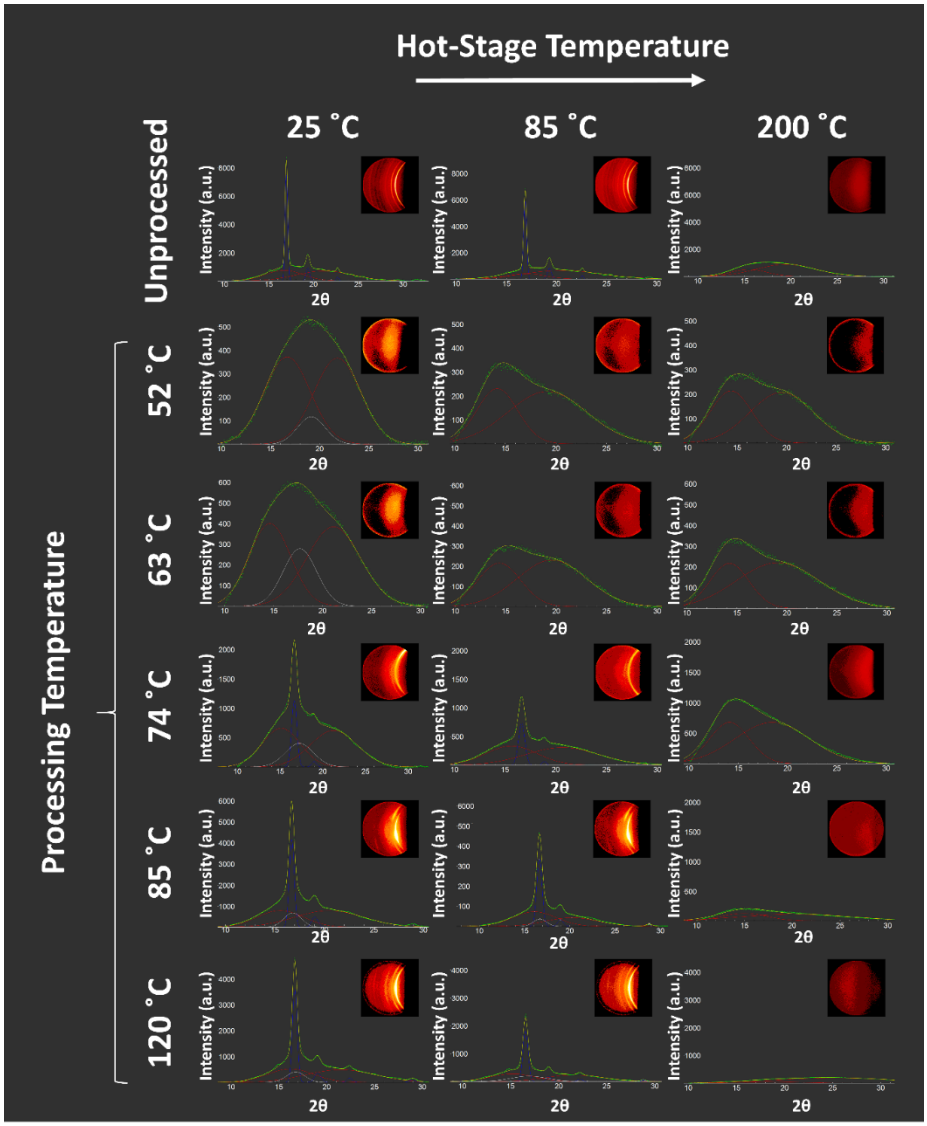

FIGURE 1S. HOT-STAGE XRD PATTERNS OF PLA SAMPLES PROCESSED AT 20,000 LB_F PRESSURE, FOR 15 MIN, AT VARYING TEMPERATURES FROM 52-120 °C. EACH ROW DEPICTS INDIVIDUAL SAMPLES AT THE VARYING PROCESSING CONDITIONS, WITH AN UNPROCESSED SAMPLE AT THE TOP. EACH COLUMN DEPICTS THE XRD PATTERN OF THE SAMPLES AS THE HOT-STAGE TEMPERATURE WAS INCREASED. IN EACH INDIVIDUAL FIGURE, THE INTEGRATED XRD PROFILE IS DEPICTED IN GREEN, WITH THE RESULTING PEAK DECONVOLUTIONS BELOW IN RED, BLUE, AND WHITE (CORRESPONDING TO AMORPHOUS, CRYSTALLINE, AND MESOPHASES RESPECTIVELY). IN ADDITION, EACH INDIVIDUAL FIGURE INCLUDES THE CORRESPONDING 2D AZIMUTHAL SCATTERING PATTERN IN THE TOP RIGHT CORNER.

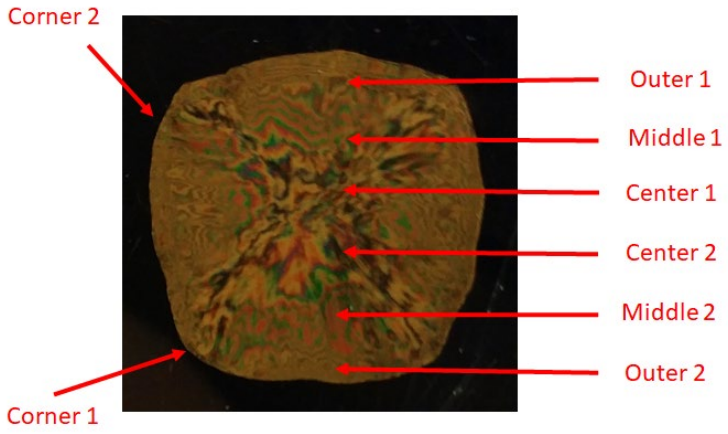

FIGURE 2S. REPRESENTATIVE IMAGE OF THE SAMPLE REGIONS TAKEN FOR DSC SCANS. TO ACCOUNT FOR THE INHOMOGENEITY OF THE MORPHOLOGY WITHIN EACH SAMPLE AS A RESULT OF PROCESSING, HEATING TRACES WERE ANALYZED FROM THE CENTER, MIDDLE, OUTER, AND CORNER REGIONS OF EACH SAMPLE.

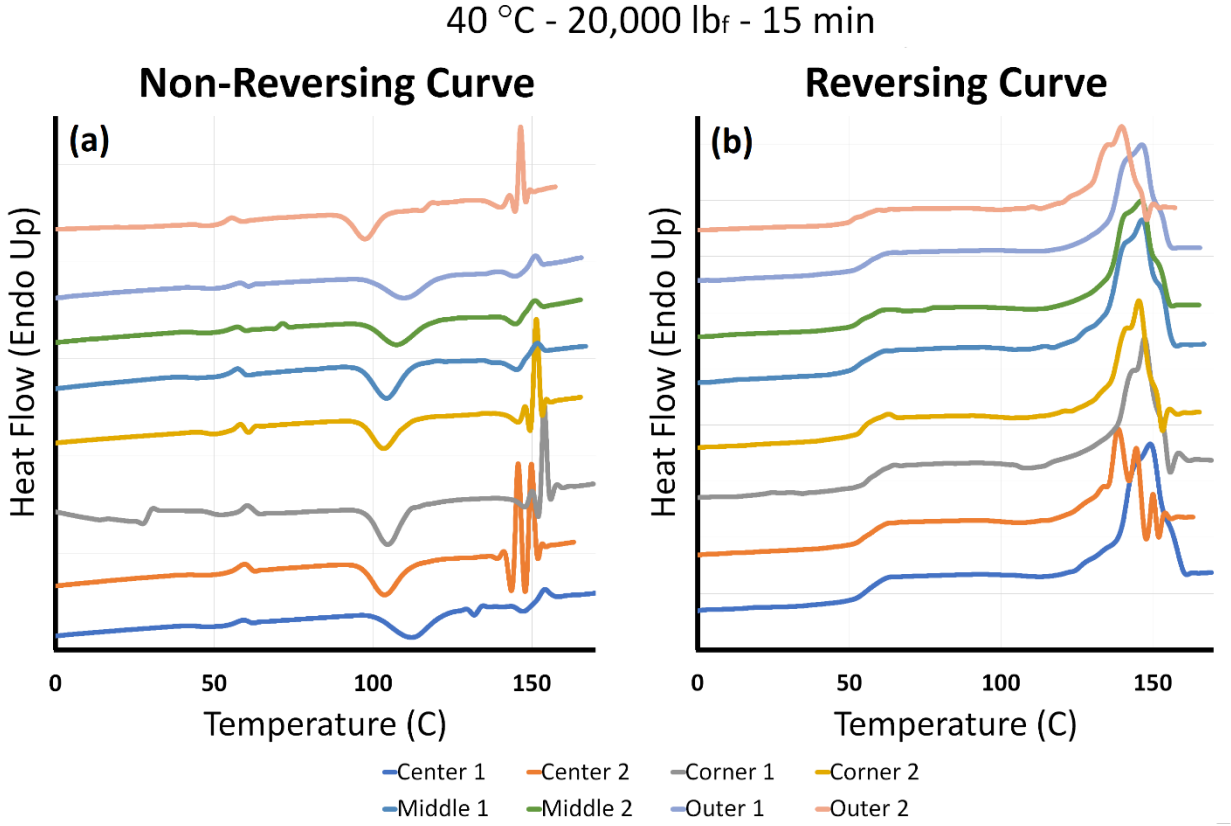

FIGURE 3S. STEPSCAN DSC HEATING TRACES OF PLA PROCESSED AT 40 °C, 20,000LBS, AND 15 MIN. CENTER, MIDDLE, CORNER, AND OUTER REGIONS ARE DEPICTED IN FIGURE 2S.

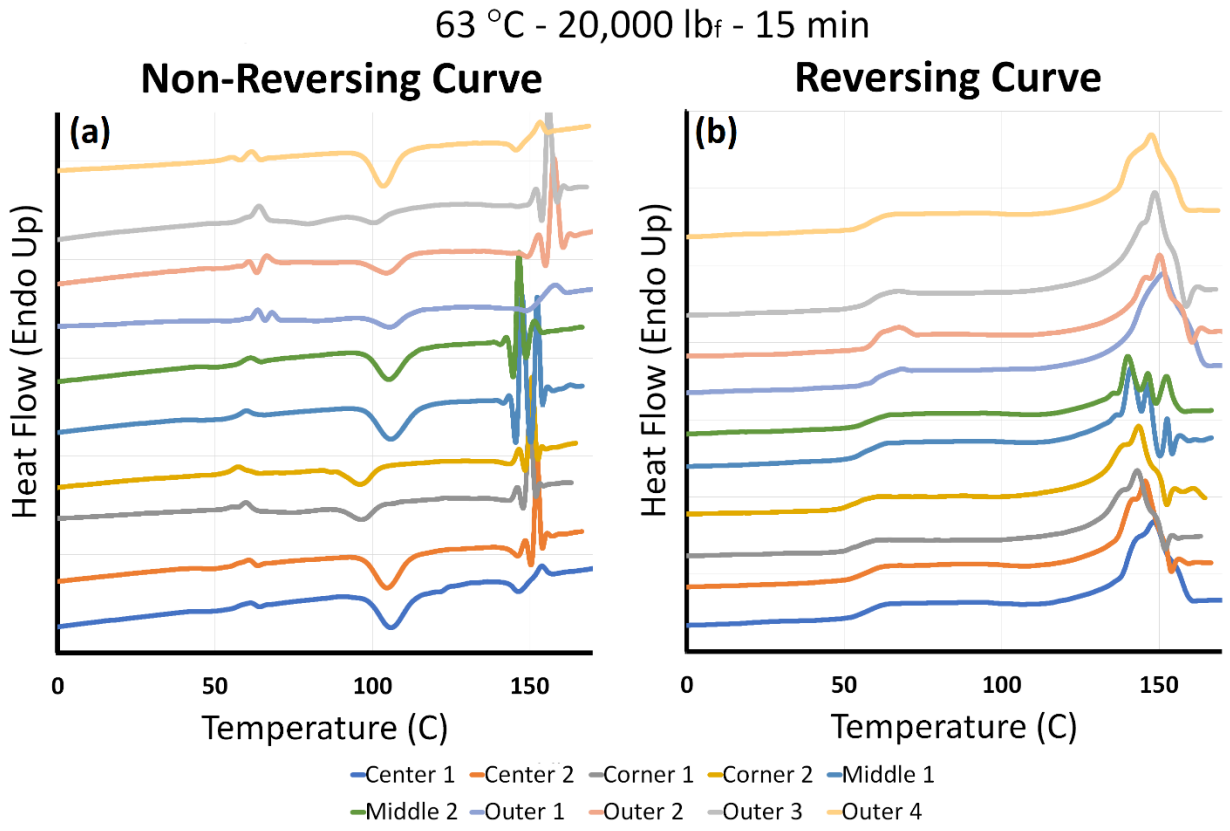

FIGURE 4S. STEPSCAN DSC HEATING TRACES OF PLA PROCESSED AT 63 °C, 20,000LBS, AND 15 MIN. CENTER, MIDDLE, CORNER, AND OUTER REGIONS ARE DEPICTED IN FIGURE 2S.

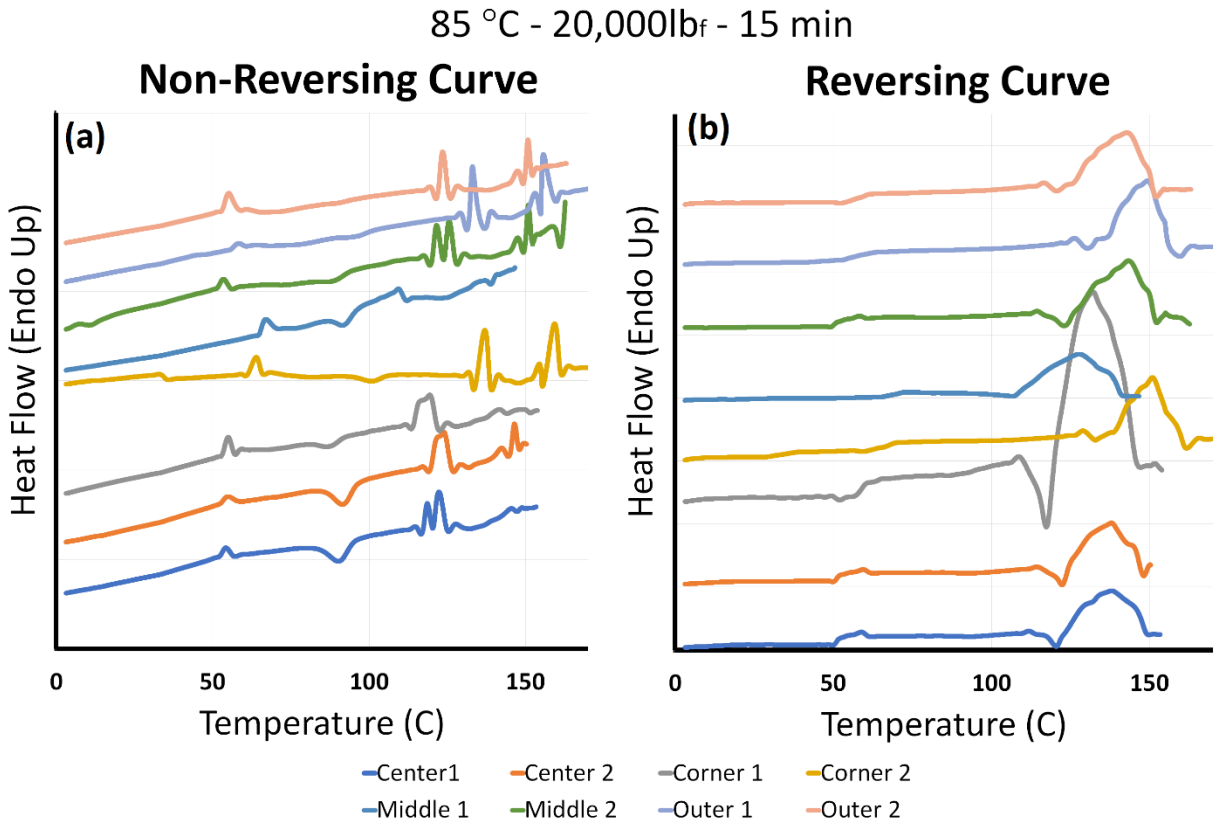

FIGURE 5S. STEPSCAN DSC HEATING TRACES OF PLA PROCESSED AT 85 °C, 20,000LBS, AND 15 MIN. CENTER, MIDDLE, CORNER, AND OUTER REGIONS ARE DEPICTED IN FIGURE 2S.

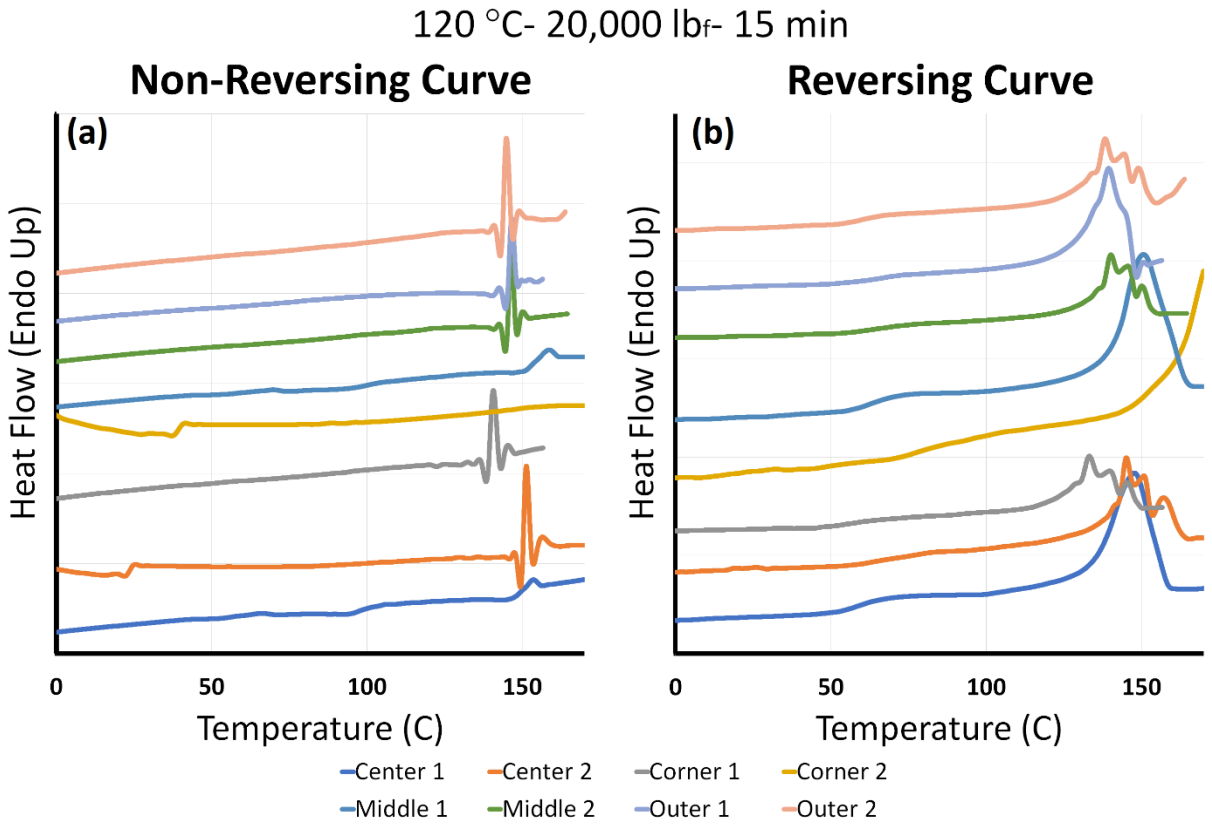

FIGURE 6S. STEPSCAN DSC HEATING TRACES OF PLA PROCESSED AT 120 °C, 20,000LBS, AND 15 MIN. CENTER, MIDDLE, CORNER, AND OUTER REGIONS ARE DEPICTED IN FIGURE 2S.

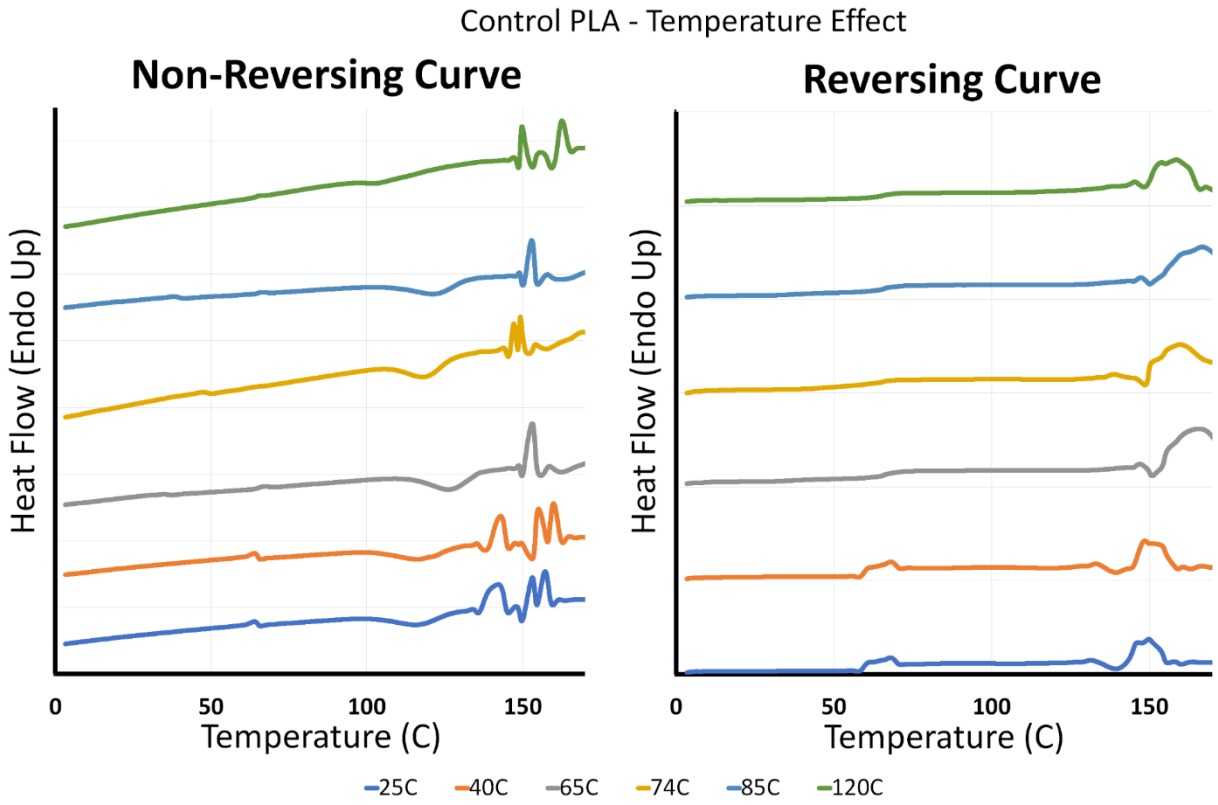

FIGURE 10S. STEPSCAN DSC HEATING TRACES OF CONTROL PLA PROCESSED AT VARYING TEMPERATURES FOR 15 MIN, IN THE ABSENCE OF PRESSURE.

Processing Conditions				Region	Tg (°C)			ΔCp (J/g°C)			Tm (°C)			Tcc (°C)		
Pressure (lbs)	Time (min)	Temperature (°C)				Average	STDEV		Average	STDEV		Average	STDEV		Average	STDEV
As Received - First Heat		0	0	n/a	57.58	57.435	0.205061	0.118	0.1115	0.00919239	151.89	152.555	0.940452	113.95	114.365	0.586899
As Received - Second Heat		0			57.29			0.105			153.22			114.78		
20,000	15	40	40	Center	58.99	58.435	1.090583	0.159	0.161375	0.01487027	149.69	147.06	2.618702	112.41	106.89	2.96854
		40		Center	59			0.168			141.29			106.35		
		40		Middle	57.07			0.16			149.03			107.65		
		40		Middle	57.06			0.153			149			110.06		
		40		Outer	59.15			0.188			146.85			105.16		
		40		Outer	59.91			0.135			146.88			104.5		
		40		Corner	57.41			0.166			146.86			104.25		
		40		Corner	58.89			0.162			146.88			104.74		
		65	65	Center	57.82	58.49875	0.704342	0.148	0.164	0.01894353	148.75	145.9063	2.95399	106	103.7988	2.384866
		65		Center	58.08			0.156			146.87			106		
		65		Middle	57.41			0.143			141.33			105.95		
		65		Middle	58.32			0.164			141.25			105.71		
		65		Outer	58.9			0.153			148.51			103		
		65		Outer	58.91			0.163			146.92			100.22		
		65		Corner	59.48			0.194			146.85			101.9		
		65		Corner	59.07			0.191			146.77			101.61		
		85	85	Center	58.05	63.56875	4.588833	0.186	0.14225	0.04305063	151.39	151.1688	0.480638	100.95	100.5488	1.990724
		85		Center	58.04			0.164			151.61			101.85		
		85		Middle	69.34			0.158			151.7			100.51		
		85		Middle	60.44			0.178			150.2			97.31		
		85		Outer	61.6			0.118			151.35			98.5		
		85		Outer	68.07			0.15			151.24			100.07		
		85		Corner	65.53			0.133			150.91			103.73		
		85		Corner	67.48			0.051			150.95			101.47		
		120	120	Center	60.26	63.18625	2.980613	0.116	0.096375	0.01947847	148.24	144.2863	3.612751	93.73	91.84	2.672864
		120		Center	66.24			0.095			141.1			-		
		120		Middle	61.08			0.099			148.17			89.95		
		120		Middle	63.89			0.102			141.07			-		
		120		Outer	68.66			0.088			145			-		
		120		Outer	62.79			0.089			141.07			-		
		120		Corner	62.29			0.123			141.03			-		
		120		Corner	60.28			0.059			148.61			-		
As Received - Processed with Temperature Only		25	25	n/a	59.47			0.195			149.88			116.34		
		40	40		59.54			0.22			146.37			115.38		
		63	63		58.52			0.125			152.01			115.08		
		74	74		57.48			0.207			151.22			111.89		
		85	85		57.94			0.146			150.99			112.22		
		120	120		60.39			0.136			154.78			95.61		

TABLE 1S. QUANTIFIED VALUES FROM THE STEPSCAN DSC CURVES OF THE GLASS TRANSITION (T_G) , CHANGE IN HEAT CAPACITY THROUGH T_G (ΔC_P), MELTING POINT (T_M), AND COLD CRYSTALLIZATION TEMPERATURE (T_{CC}).

Processing Conditions				Region	ΔH (J/g)									Calculations		
Pressure (lbs)	Time (min)	Temperature (°C)			Relaxation			Cold Crystallization			Crystal Perfection	Melting - NonReversing	Melting- Reversing	%Crystallinity		
					Individual	Average	STDEV	Individual	Average	STDEV				Individual	Average	STDEV
As Received - First Heat		0	0	n/a	2.149	1.363	1.111572	30.989	28.546	3.45492373	-3.674	3.471	54.363	24.88829	24.88829	
As Received - Second Heat		0			0.577			26.103			-4.188	3.594	60.922	36.76155		
20,000	15	40	40	Center	1.403	2.622125	0.682775	31.582	30.3915	5.62532366	-5.265		61.2	26.15789	22.79954	8.044103
		40		Center	3.165			26.768			17.149		25.624	17.19119		
		40		Middle	2.446			27.679			-9.23	3.656	60.319	29.07197		
		40		Middle	1.906			27.786			-5.578	3.707	56.883	29.24382		
		40		Outer	2.563			39.622			2.391		42.954	6.147154		
		40		Outer	3.001			38.333			6.077		52.525	21.77121		
		40		Corner	3.323			25.972			4.251		49.595	29.93985		
		40		Corner	3.17			25.39			3.064		43.621	22.87325		
		65	65	Center	2.398	3.4695	1.203223	34.245	23.238	7.19551865	-8.57	3.687	60.579	23.04082	29.23939	7.74087
		65		Center	2.987			28.364			5.344		47.908	26.73255		
		65		Middle	2.378			27.005			17.516		29.389	21.37487		
		65		Middle	2.26			26.629			10.546		36.767	22.21697		
		65		Outer	4.333			14.776			-14.723	3.166	67.012	43.69388		
		65		Outer	5.624			17.088			-7.142		56.983	35.18045		
		65		Corner	3.463			23.493			-1.945		51.664	28.16971		
		65		Corner	4.313			14.304			1.052		44.446	33.50591		
		85	85	Center	1.681	3.439875	1.822398	19.01	11.39475	8.54003964	0.322		52.783	36.62191	57.50443	16.47839
		85		Center	2.317			18.276			6.376		71.175	63.6681		
		85		Middle	5.34			23.627			6.07		83	70.29323		
		85		Middle	1.467			13.644			-5.075		50	33.59936		
		85		Outer	1.606			8.797			-7.374		70.078	57.90226		
		85		Outer	4.559			0.641			-11.095		71.2	63.87111		
		85		Corner	5.127			1.848			-9.487		59.49	51.72395		
		85		Corner	5.422			5.315			4.208		77.78	82.35553		
		120	120	Center	2.304	2.032	0.384666	5.591	1.056	2.087399	-9.871	3.343	77.948	70.70784	62.73563	9.69011
		120		Center	-			0			14.927		43.829	63.11063		
		120		Middle	1.76			2.857			-7.171	4.785	75.797	75.78303		
		120		Middle	-			0			7.166		40.959	51.69173		
		120		Outer	-			0			10.816		54.975	70.66702		
		120		Outer	-			0			15.882		36.265	56.01182		
		120		Corner	-			0			9.999		35.624	49.0043		
		120		Corner	-			0			-10.478	3.507	67.401	64.9087		
As Received - Processed with Temperature Only		25	25	n/a	4.72			20.039			19.626		22.489	23.71214		
		40	40		3.992			19.99			17.793		26.331	25.92266		
		63	63		0.589			21.676			1.527		48.819	30.79484		
		74	74		0.709			21.868			6.205		47.55	34.25027		
		85	85		0.773			20.23			3.206		47.58	32.82062		
		120	120		0.42			1.487			28.037		13.196	42.69173		

TABLE 2S. QUANTIFIED VALUES FROM THE STEPSCAN DSC CURVES OF THE CHANGE IN ENTHALPY (ΔH) OF THE GLASS TRANSITION ENDOTHERM (RELAXATION), COLD CRYSTALLIZATION EXOTHERM (COLD CRYSTALLIZATION), MELTING PEAKS (CRYSTAL PERFECTION, NONREVERSING MELT, REVERSING MELT), AND THE CALCULATED PERCENT CRYSTALLINITY (% CRYSTALLINITY).

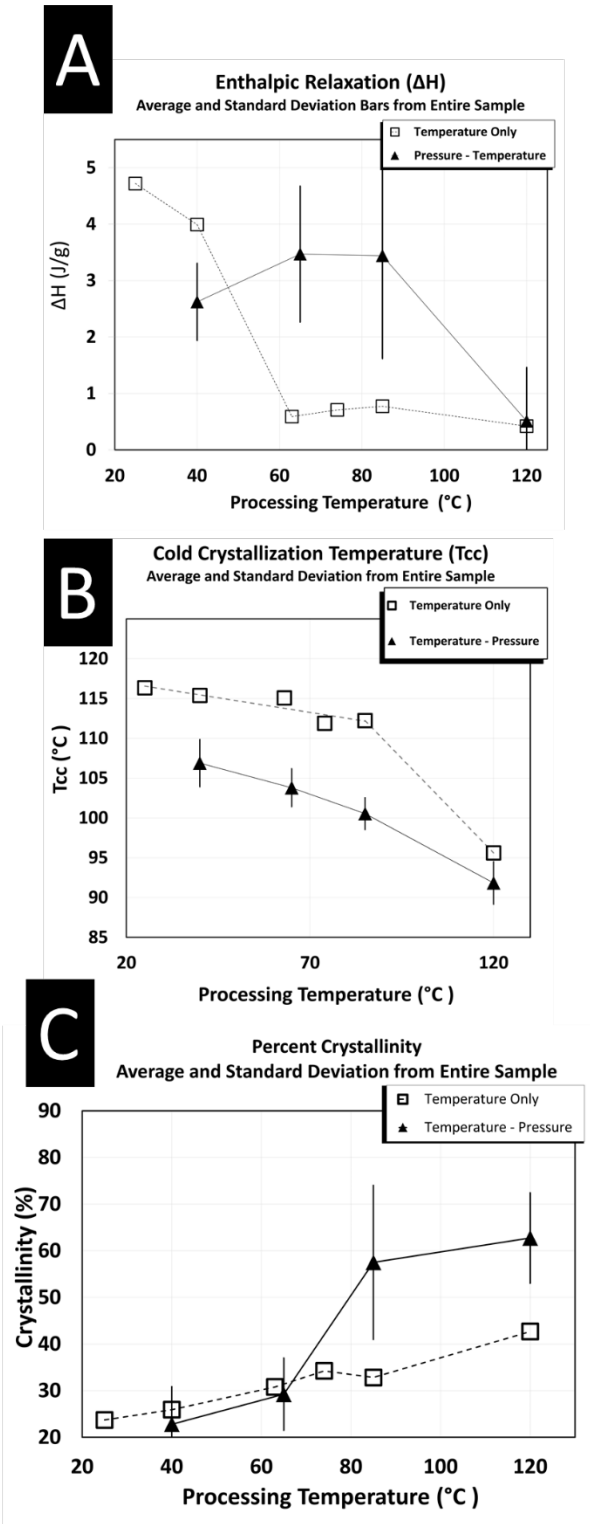

FIGURE 8S DSC ANALYSIS WITH AVERAGE VALUES FROM ALL REGIONS TESTED (CENTER, MIDDLE, OUTER, CORNERS). THE STANDARD DEVIATION REFLECTS THE INHOMOGENEITY OF SAMPLE MORPHOLOGY AS A FUNCTION OF PROCESSING.

CHAPTER 3

THE IMPACT OF PROCESSING-INDUCED POLYCAPROLACTONE MESOPHASES ON THE CONTROLLED RELEASE OF DEXAMETHASONE

Cameron Baptista, Anyaa Shah, El Hadji Arona Mbaye, Raj Sharan, Edith Mathiowitz[ll]

Department of Pathology and Laboratory Medicines
Center for Biomedical Engineering
Brown University, Providence, RI 02912, USA
[ll] Edith_Mathiowitz@Brown.edu

The following manuscript is in preparation for submission in the Journal of Controlled Release
2022

ABSTRACT

The work presented here demonstrates the ability to induce mesomorphic phases into non-mesogenic PCL containing small molecule drug, dexamethasone. Herein, the impact of these morphologies on the long-acting release behavior of dexamethasone is assessed. Controlling the release rate of small molecule drugs from a polymer matrix is often a major challenge in the development of long-acting drug delivery depots. To this end, optimum design may be achieved by tailoring the diffusion coefficient of the drug through the polymer network. Drug diffusion is thought to be intimately connected to the structure and morphology of the polymer matrix through which the diffusion takes place. Recent work by our lab has demonstrated that polymer mesophase morphology may be induced into non-mesogenic Polycaprolactone (PCL). It is demonstrated here that dexamethasone loaded PCL samples processed at 25 °C and 50 °C under hydraulic compression of 20,000 lb_f have a decreased diffusion flux and diffusion coefficient compared to those samples produced under lower loads (10,000 lb_f) in the restricted environment of a compression mold die. This decreased diffusion behavior was correlated to the processing-induced mesophase formation, which was estimated by peak deconvolution of the integrated XRD scattering profiles. The variable diffusion coefficient observed between samples processed under varying conditions is thought to be directly related to a decrease in free volume associated with mesophase formation.

INTRODUCTION

The successful treatment of chronic conditions is often dependent on adherence to medication.[136] To this end, conventional oral and injectable drug delivery has been regarded as suboptimal for chronic conditions due to challenges associated with maintaining therapeutic dosages in systemic circulation. Conventional drug delivery formulations have been associated with rapid fluctuations of drug plasma concentrations, high localized concentrations in the administered tissue, and erratic drug absorption which can result in undesirable side effects.[137] It has been demonstrated that long acting sustained drug release may improve treatment outcomes in some chronic conditions. The aim of long-acting delivery systems is to achieve slow release of a drug over an extended period of time from a single dosage. Successful long-acting formulations can help simplify dosing schedules, provide constant therapeutic concentration of drug, and in turn reduce patient side effects.[136]

Significant attention has been directed towards the modern design of long-acting sustained and controlled release systems for pharmaceutical applications.[138] In some instances, the preferred design is a matrix system where the drug is homogenously dispersed throughout a polymer. Compared to the alternative of a reservoir system, matrix systems remove the risk of rupture and toxic dosage dumping.[137] However, in some cases, a major challenge in the development of these matrix systems is the control of drug release rate.

Matrix systems which utilize non-degradable or very slow degrading polymers may release drug primarily by Fickian diffusion, in which the rate of release is directly correlated to the drug concentration gradient and the diffusion coefficient of the drug through the polymer matrix. Specifically, in these systems, challenges may arise when it is necessary to decrease or slow the rate of drug release to achieve optimum diffusion for therapeutic performance. A

common approach to speed up or slow down drug release is by tailoring the percent loading of drug in the polymer matrix. Here, an increase or decrease in loading would correspond to higher or lower concentration gradients and therefore faster or slower drug release, respectively. However, while decreasing drug loading might aid in controlling the release rate, this would inherently shorten the life span of the device. For some drugs, particularly those with high potency and low therapeutic dosages, slowing down release by decreasing the percent drug loading can be infeasible for practical long term applications. To this end, optimum design may be achieved by tailoring the diffusion coefficient of the drug through the polymer matrix.

Drug diffusion is thought to be intimately connected to the structure and morphology of the polymer matrix through which the diffusion takes place. [138,139] Generally, the rate of diffusion is regarded as being dependent on the free volume of the matrix (more free volume, faster diffusion).[14] Recent work by our lab has demonstrated that polymer mesophase morphology may be induced into non-mesogenic biodegradable polymers, Polycaprolactone (PCL) and Polylactic acid (PLA) via temperature controlled hydraulic compression. Specifically, it was observed in PCL that a plastic crystal and condis crystal type morphology may be induced depending on the processing temperature's proximity to the melt (PCL $T_m \approx$ 56-65 ºC) and the associated chain mobility at the processing temperature.[54,113,140] To this end, a change in free volume associated with the induced mesophase morphology may serve as a means for controlling the rate of drug diffusion.

The overarching goal of the work presented here is to induce mesomorphic phases into non-mesogenic PCL and assess the impact of these morphologies on the long-acting release behavior of a model small molecule hydrophobic drug, dexamethasone.

MATERIALS AND METHODS

Release Studies

Preparation of the DEX and blank PCL films

CAPA 640 PCL was received from Perstorp Holding AB (Perstorp, Sweden) for scientific use with a molecular weight (MW) of 37 kg/mol. Each film contained 250 mg of total material. Films containing the drug were loaded with 5%, 10% and 20% of DEX of the total mass. Nine films were made for each of the listed loading conditions, totaling 27 films containing the drug. Blank PCL films were only composed of the polymer and nine films were made in total. Films were made by weighing the appropriate amount of PCL and DEX and dissolving them in 2 mL of dichloromethane (DCM). Dissolution required a few rounds of sonication and vortex mixing. After the solution becomes completely clear, the contents were pipetted into a 62 mm petri dish and left in a hood overnight to allow the solvent to completely evaporate. The resulting thin film contained the drug dispersed within the polymer. The same procedure was followed for blank PCL films. These thin film samples are herein referred to as 'film cast' samples throughout this manuscript and serve as a control for the typical PCL behavior and morphology.

Processing of the DEX and blank PCL films

In a series of pressing steps, the 'film cast' samples described above were first pressed using a hand press and die. The press occurred at 10,000lbs_f and lasted for 5 min at room temperature. All films became cylindrical tablets. For each loading condition, three of those cylindrical tablets become our 'first press' tablets for the release studies. These are defined as such, as this process only reproduces standard techniques to produce a pill for medical administration. Three of the resulting tablets also became control samples for the Blank PCL films. The remaining tablets for each loading condition were then pressed using a Carver Auto Series Hydraulic Press (Carver, Wabash, Indiana) equipped with a heating/cooling system. Three of the remaining tablets

were placed between two 4" x 4" stainless steel plates and then heated at either 25 °C or 50 °C with the plates of the hydraulic press for 10 min. After heating time, the samples were pressed at 20,000lbs$_f$ for 5 mins and immediately after cooled until the plates of the hydraulic press returned to room temperature while still maintaining the pressure. This ensures that the induced morphology is maintained in the PCL after the pressure is removed. Blank PCL films also had triplicates of tablets that were pressed using the hydraulic press at 25 °C and 50 °C under 20,000lbs$_f$. Once processing was complete, final weight and physical dimensions for each tablet was recorded. Final amounts of drug and polymer in each tablet was calculated assuming that the initial loading remained the same after losses occurred during the solvent evaporation and pressing steps. Herein, these samples are referred to as 'Processed 25 °C' and 'Processed 50 °C' respectively.

Calibration curves for DEX and PCL

DEX was dissolved in phosphate buffer saline (PBS) with a pH of 7.4. Through serial dilutions, DEX standards with concentrations from 250 µg/ ml to 1µg/ ml were prepared. A Spectra max 384 Plus Ultraviolet Spectrophotometer (UV) was used to measure the absorbance of the DEX standard. Absorbance of the solutions was measured from 258nm to 262 nm, with maximum absorbance at 260 nm. With the measurements being repeated 5 times, choosing a range ensures that the wavelength chosen for the release studies provides the most consistent slope and r-squared for the linearity curve. DEX was found to obey the Beer-Lambert law in the concentration range of 1-50 µg/mL, allowing for the following calibration curve equation:

$$Absorbance\ (Au) = Concentration\ \left(\frac{ug}{mL}\right) * 0.0103 - 0.0177$$

Drug Release

Each tablet was placed in a scintillation vial containing 20mL of PBS to mimic sink conditions in a physiological environment. Release vials were incubated at 37 °C for the entirety

of the release experiment. Periodically, the PBS solutions for each sample would be collected and analyzed via UV spectroscopy in order to quantify the amount of drug released. Following the collection of PBS solutions, the release medium for each tablet would be subsequently changed with fresh PBS and then incubated again until the next time point. Drug concentrations were quantified using the absorbance values obtained from the SOFTmax PRO software 4.3.1 of the Spectra max 384 Plus Ultraviolet Spectrophotometer. Using the absorbance values and the calibration curves, concentrations were calculated for the different time points of the release studies. Solution concentrations usually fell outside the linearity region for DEX and hence, required dilutions. Following dilutions, new absorbance values were obtained and concentrations were once again calculated using the appropriate dilution factor.

Morphological studies

Preparation of 10% DEX tablets and blank PCL tablets

Morphological studies involved the use of separately produced 10% DEX tablets as well blank PCL tablets. 10% DEX tablets were made using the same protocol as the 25 ºC and 50 ºC tablets made for the release studies. There were eight 10% DEX tablets processed at 25 ºC and eight processed at 50 ºC. Blank PCL tablets were prepared following the exact same procedure except for the addition of DEX in those samples. Tablets were then placed into plastic falcon tubes with 20mL of PBS and incubated at 37 ºC. Tablets were taken out of the solution at specific time points (24h, 72h , 1 week, 2 weeks, 3 weeks , 1 month, 2 months, 3 months) and the solutions were discarded. Tablets were subsequently lyophilized and stored in a freezer until analysis by XRD.

XRD analysis

XRD was performed using a Bruker D-8 Advance X-Ray Powder Diffraction system running DaVinci Software and a Cu X-Ray tube operating at 40 kV and 40 mA (1600W) equipped

with a Bruker Vantec-500 Xe- CO_2 gas filled detector with a 13.5 cm diameter window set at 20 cm from the goniometer center. System wavelength was 0.15418 nm. The system optics consisted of a polycap with an output beam divergence of 0.25° for Cu and a spot diameter of less than 4.0 mm and a 79 mm long 0.3 mm collimator on the incident beam path. Scans were run at 2θ angle from 20° to 80° with a step size of 15° and a counting timestep of 60s (300s total). XRD scans are taken at 3 different spots in each tablet in order to display a more accurate picture of the polymer morphology and dispersion of the drug in the delivery system.

XRD phase content calculation

The phase content of each sample was calculated from the obtained XRD scattering profiles by peak deconvolution using the Fityk 1.3.1 software. The fitting method used was developed by Stoclet et al. in which Gaussian profiles were assumed for all scattering peaks and halos.[12] Particularly, the amorphous halo parameters were determined by the control film cast PCL which displayed the halo peak at a 2θ value of approximately 21°. Upon establishing a best fit amorphous halo, the (110), (111), and (200) orthorhombic crystalline face peaks were established. Finally, mesophase peaks were fit to a R^2 value of at least 0.98 when comparing the computed model to the experimental data. The content of each phase (amorphous, mesophase, and crystalline) was calculated by the area under the diffraction peaks, using the ratio from one phase to the total scattering peaks.

RESULTS AND DISCUSSION

In-vitro Release Studies

The dexamethasone loaded PCL tablets were evaluate for their in-vitro release kinetics to determine the impact of the processing history and induced morphology on the drug release behavior (Figure 1). Independent of processing conditions and drug loading, all PCL matrices showed sustained release over the 180 day duration of the experiment (6 months). However, the

increase of drug loading from 5%, 10% and 20% showed a gradual decrease in the cumulative percent release. This may in part be attributed to the low saturation solubility of dexamethasone in the aqueous release medium (approx. 0.1 mg/mL). Typically in instances where the drug concentration in the tablet is well below the saturation limit, an increase in drug loading would be expected to result in a direct increase in cumulative drug release. However, in the drug release presented here the concentration of dexamethasone in all tablets (5%, 10%, and 20% loading) is well above the saturation limit. Thus, regardless of the percent drug loading in each tablet, the total mass release may be limited due to the low saturation solubility, which may act as a rate limiting step.

While, PCL is subject to hydrolytic degradation, due to its hydrophobic nature its degradation times can be very slow (on the order of 2-4 years). In this study, there were no significant signs of tablet erosion observed over the duration of 6 months. This implies that the release of dexamethasone occurred primarily due to diffusion through the PCL matrix. To this end, the release profiles presented in Figure 1 are assumed to represent a time-dependent release based on Fick's law.

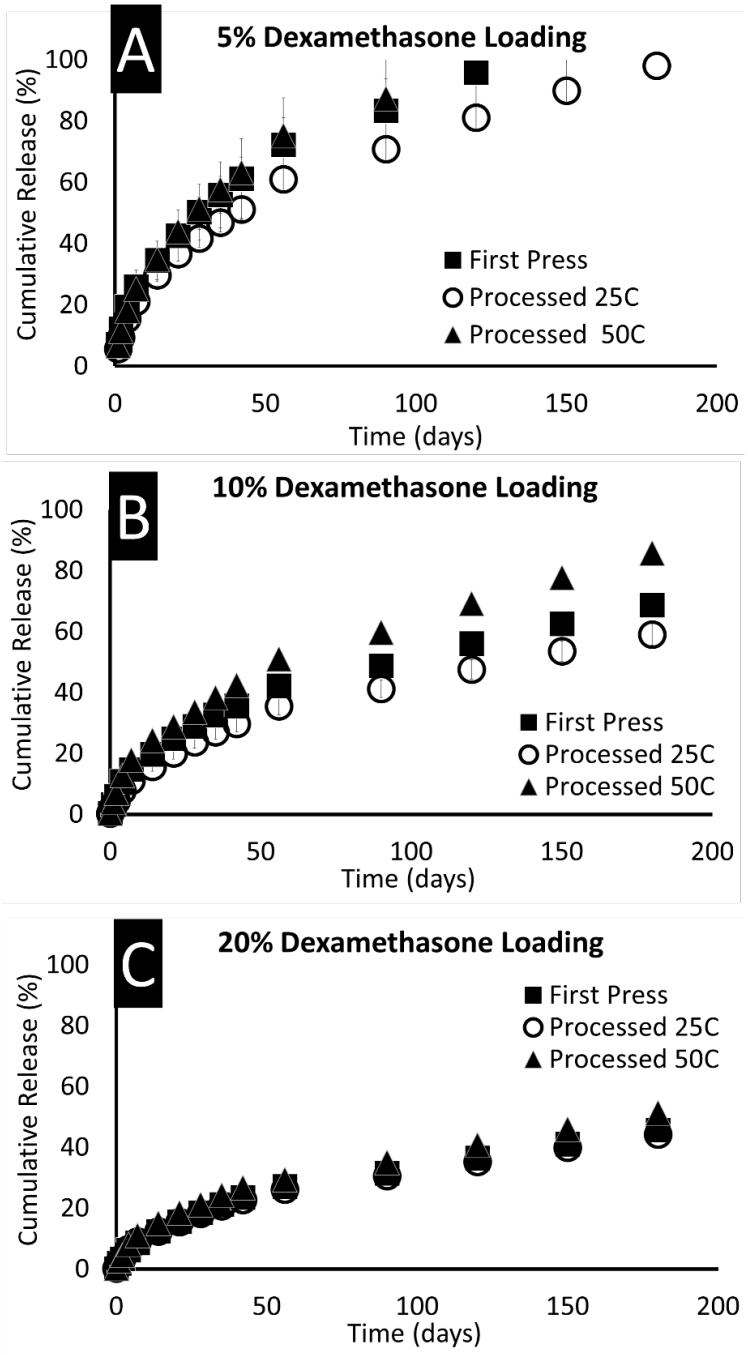

FIGURE 1 CUMULATIVE RELEASE PROFILES OF DEXAMETHASONE LOADED PCL TABLETS. A) 5% DEXAMETHASONE LOADING, B) 10% DEXAMETHASONE LOADING, AND C) 20% DEXAMETHASONE LOADING. EACH GRAPH DISPLAYS THE FIRST PRESS TABLETS (SQUARE CURVES) WHICH WERE HAND PRESSED AT 10,000 LB_F IN A TABLET DIE, AND THE HYDRAULICALLY PRESSED PROCESSED SAMPLES WHICH WERE COMPRESSED AT 20,000 LB_F AT BOTH 25 ^{O}C (CIRCLE CURVES) AND 50 ^{O}C (TRIANGLE CURVES).

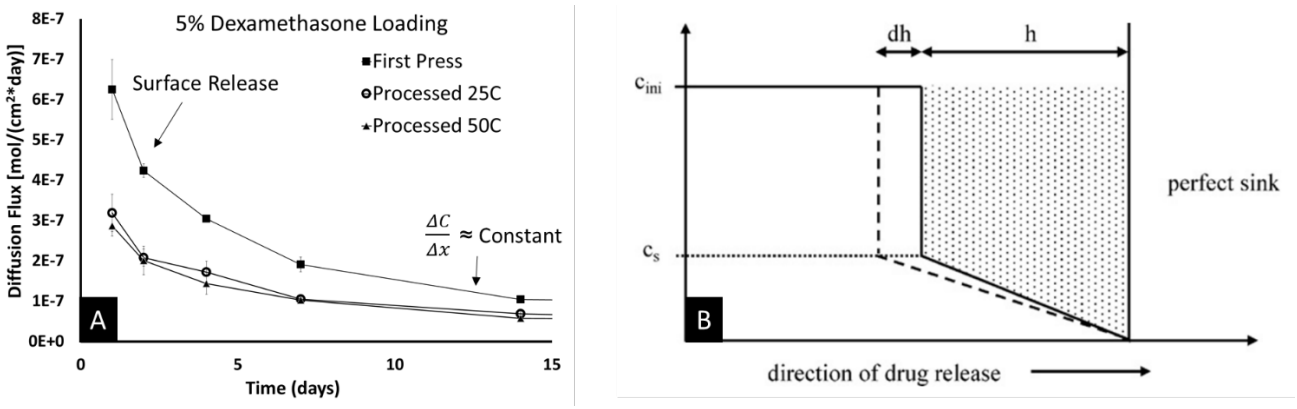

FIGURE 2 A) DIFFUSION FLUX AS A FUNCTION OF TIME FOR 5% DEXAMETHASONE LOADING PCL TABLETS. B) SCHEMATIC OF THE ASSUMED PSEUDO STEADY STATE DRUG CONCENTRATION–DISTANCE-PROFILE WITHIN THE PCL TABLETS AFTER EXPOSURE TO PERFECT SINK CONDITIONS AT TIME T (SOLID LINE) AND AT TIME T + DT (DASHED LINE). WHERE: CINI AND CS REPRESENT THE INITIAL DRUG CONCENTRATION WITHIN THE VOLUME OF THE PCL TABLET AND DRUG SATURATION SOLUBILITY, RESPECTIVELY; H REPRESENTS THE DISTANCE OF THE DIFFUSION FRONT AT TIME T; DH IS THE DISTANCE THIS FRONT MOVES INWARDS DURING THE TIME INTERVAL DT (FIG 2B ADAPTED FROM PEPPAS ET. AL).[138]

Figure 2a depicts the diffusion flux calculated between each time point on the 5% loading Dexamethasone the release curves, as a function of time. It can be seen in Figure 2a that the drug release rate is very high in the first week and continues to drop significantly up to 2 weeks. Beyond this time, the rate becomes slower and approaches a constant flux. To understand the release behavior depicted in Figures 1 and 2a, we adapt the Higuchi pseudo steady state model which describes drug release from thin films containing finely dispersed drug into sink conditions (Figure 2b). [138,141] In this scenario we make the following assumptions:

(1) Drug transport through the PCL is rate limiting, whereas drug transport to the release medium from the surface of the tablet is rapid.

(2) The release medium acts like a "perfect sink": The drug concentration in the surrounding PBS release medium can be considered negligible.

(3) The initial drug concentration in the PCL is much higher than the saturation solubility concentration of the drug in the release medium.

(4) The drug is finely dispersed within the PCL (the size of the drug particles is much smaller than the thickness of the film).

(5) The drug is initially homogeneously distributed throughout the PCL.

(6) The dissolution of drug particles is rapid compared to the diffusion of dissolved drug molecules through the PCL matrix.

(7) The diffusion coefficient of the drug through the PCL matrix is constant and does not depend on time or the position within the film.

(8) Edge effects are negligible: The surface of the PCL exposed to the release medium is large compared to its thickness. The mathematical description of drug diffusion can be restricted to one dimension.

(9) The PCL does not swell or dissolve during drug release.

In the context of these conditions, we may describe the release behavior in Figure 2a using the schematic in Figure 2b. Upon initial exposure to the perfect sink conditions, the dexamethasone in the PCL matrix begins to diffuse into the release medium. Initially, this occurs only close to the surface of the PCL. Thus, we see a rapid diffusion flux in the initial first week of release, where the surface concentration of the drug operates at saturation conditions. At these time points when the diffusion flux is rapid, we assume diffusion through the PCL has minimal impact on the release rate and dissolution from the surface is the governing step. Only when all drug particles located in the region next to the surface are finally dissolved does the

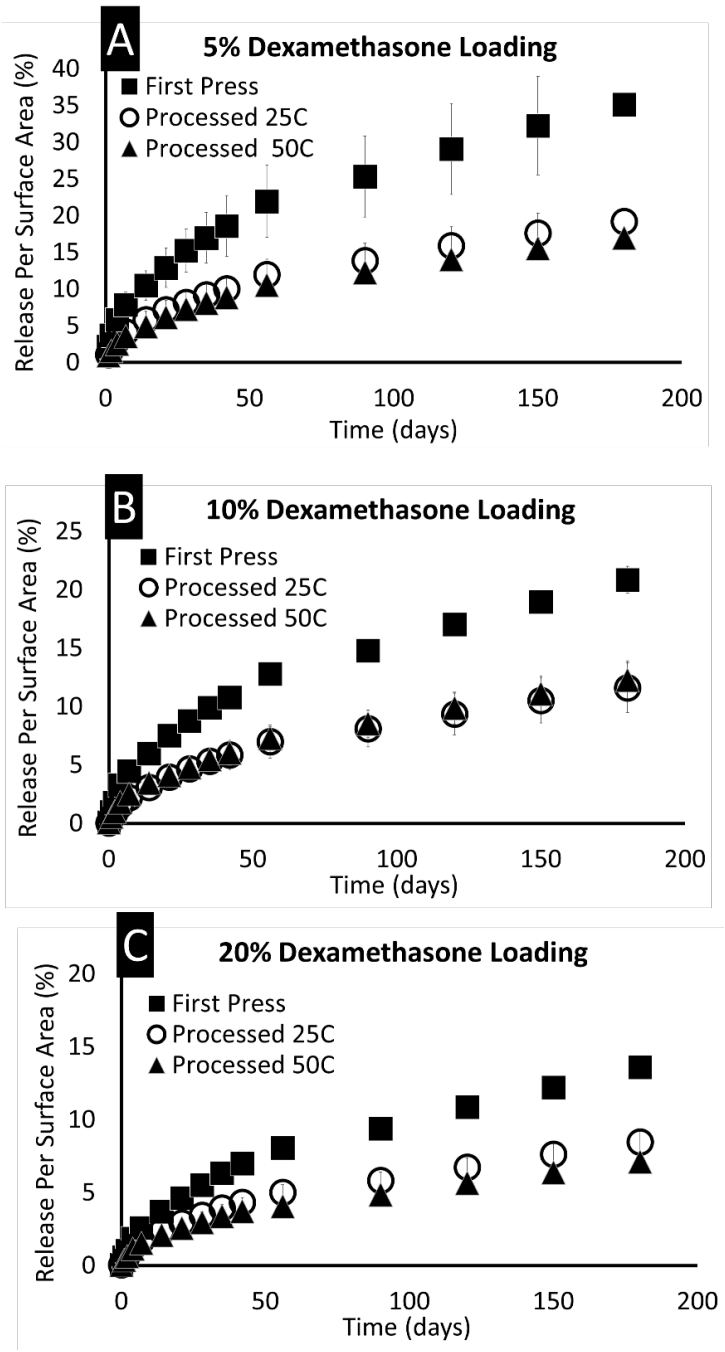

FIGURE 3 PERCENT RELEASE PER SURFACE AREA PROFILES OF DEXAMETHASONE LOADED PCL TABLETS. A) 5% DEXAMETHASONE LOADING, B) 10% DEXAMETHASONE LOADING, AND C) 20% DEXAMETHASONE LOADING. EACH GRAPH DISPLAYS THE FIRST PRESS TABLETS (SQUARE CURVES) WHICH WERE HAND PRESSED AT 10,000 LBF IN A TABLET DIE, AND THE HYDRAULICALLY PRESSED PROCESSED SAMPLES WHICH WERE COMPRESSED AT 20,000 LBF AT BOTH 25 OC (CIRCLE CURVES) AND 50 OC (TRIANGLE CURVES).

concentration of dissolved drug molecules at the surface fall below saturation concentration. At this point, the dissolved drug molecules located further away from the PCL surface begin to diffuse through the tablet matrix into the release medium, based on an inward moving concentration gradient. To simplify the release kinetics, the Higuchi model assumes pseudo steady state behavior in which the concentration gradient of dissolved drug remains at saturation concentration within the PCL at the moving diffusion front (due to rapid dissolution) and zero concentration at the surface (due to rapid release to sink conditions). Thus, in Figure 2a it can be seen that following the initial rapid release from the surface, the diffusion flux approaches constant. This can be attributed to the constant ΔC of the pseudo steady state gradient, and the small Δx of the PCL thickness, with the moving diffusion front having minimal effect on the gradient.

While the total cumulative release between the first press, and processed samples at 25 ºC and 50 ºC appear similar (Figure 1), an important attribute to note is the difference in the release per surface area of each sample (Figure 3). A constraint in this analysis between the different processing conditions, is the inherent change in surface area associated with each processing condition (Table 1S-3S in the supplemental materials demonstrates the dimensions of each sample). Typically, increased surface area to volume ratio of a release device is expected to result in an increase of the cumulative release (i.e. more surface drug contact with the release medium should be represented by higher rates of release). However, in the release demonstrated in Figure 1, the change in surface area does not appear to have a significant impact on cumulative release. This is curiously associated with a decrease in percent release per surface area (Figure 3). To further demonstrate this difference, the diffusion flux was approximated by analyzing each release curves in Figure 1 as shown in Figure 4, by assuming near constant

release rates in the first week, weeks 2-7 and weeks 8-26. The results of this analysis can then be seen in the Figure 5, which demonstrates that the diffusion flux of dexamethasone through the samples processed at 25 ºC and 50 ºC were consistently lower than the first press samples at all drug loadings.

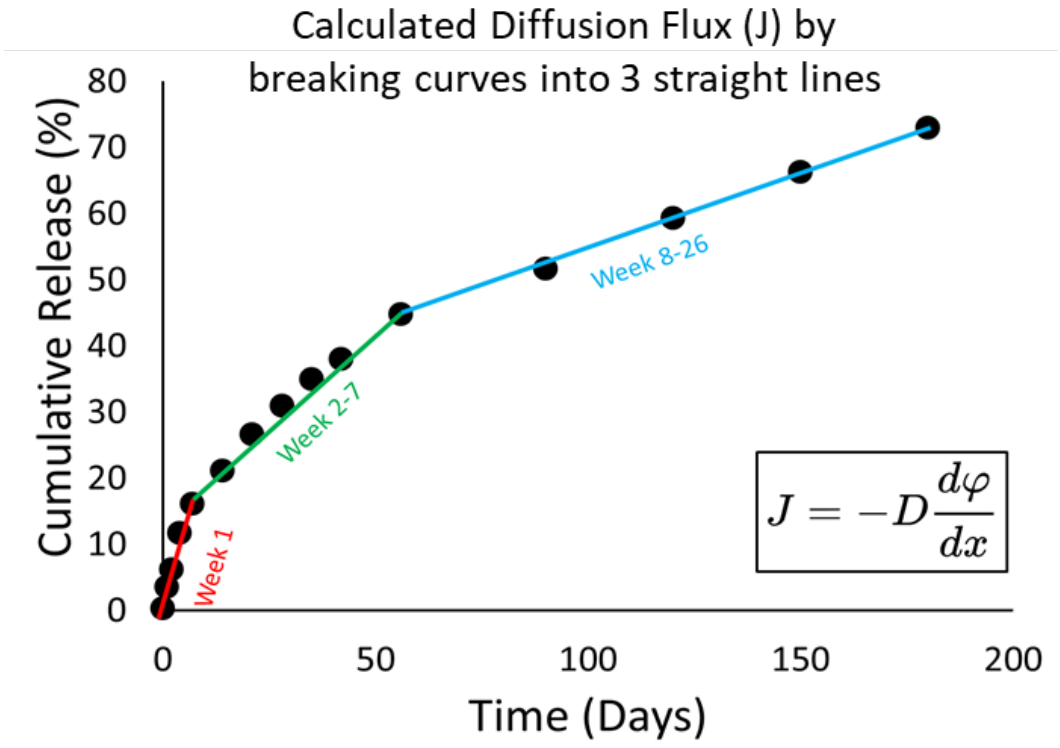

FIGURE 4 DIFFUSION FLUX WAS CALCULATED BY ASSUMING CONSTANT RELEASE RATES BETWEEN WEEK 1 (RED), WEEKS 2-7 (GREEN), AND WEEK 8-26 (BLUE).

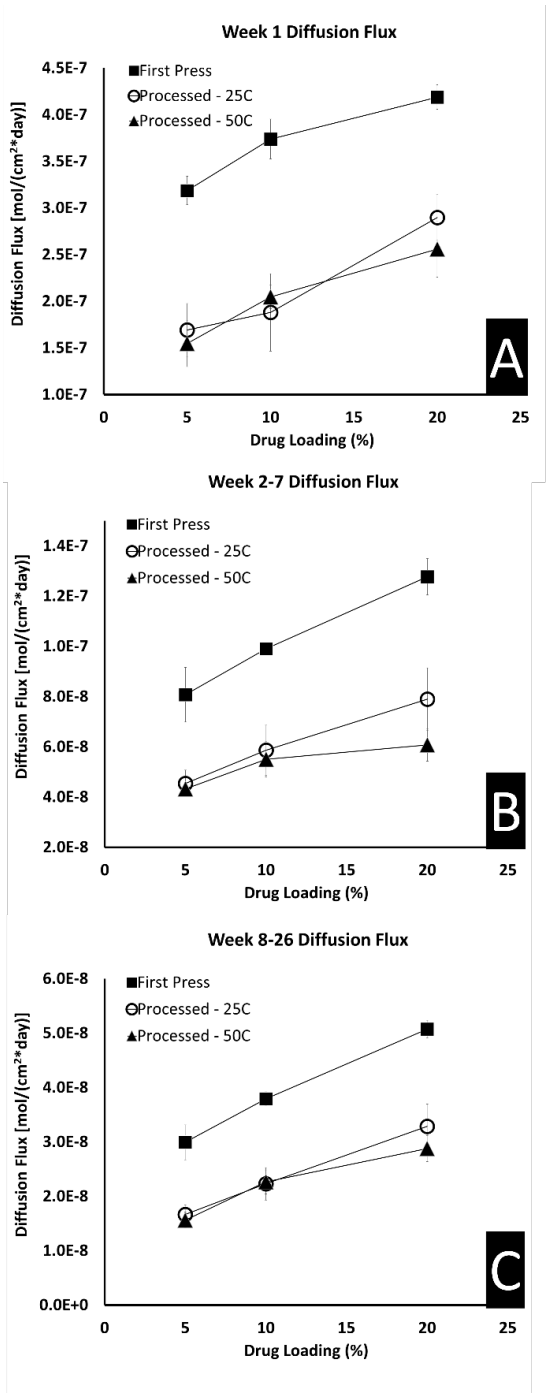

FIGURE 5 DIFFUSION FLUX OF DEXAMETHASONE LOADED PCL TABLETS IN A) WEEK 1, B) WEEKS 2-7, AND C) WEEKS 8-26. THE X-AXIS REPRESENT INCREASING DEXAMETHASONE LOADING, WHICH WAS INCREASED FROM 5% TO 20%. SQUARES: FIRST PRESS SAMPLES, CIRCLES: PROCESSED 25 ºC SAMPLES, AND TRIANGLES: PROCESSED 50 ºC SAMPLES.

The diffusion flux calculated in Figure 5 is assumed to follow Fick's first law of diffusion.

$$J = -D\frac{\Delta C}{\Delta x} \qquad (1)$$

Where J is the diffusion flux, D is the diffusion coefficient of dexamethasone through the PCL matrix, and ΔC/Δx is the concentration gradient of dexamethasone between the PCL surface and diffusion front. To this end, the behavior of the PCL systems presented here were already observed in Figure 2a to follow a pseudo steady state behavior, where it was seen that ΔC/Δx appears to approach a constant after the initial dissolution of the surface entrapped drug. Thus, this would suggest that the difference in diffusion flux observed between the first press, and processed samples at 25 °C and 50 °C is a consequence of a variable diffusion coefficient of dexamethasone through the PCL matrix in each sample.

To further explore the change in diffusion coefficient between each sample, each release profile was modeled using the Higuchi equation:

$$\frac{M_t}{A} = \sqrt{2Dc_{ini}c_s t} \qquad (2)$$

Where M_t is the cumulative mass of drug release at time t, A is the surface area of the PCL tablet, D is the diffusion coefficient of drug through the tablet, c_{ini} is the initial concentration of drug in the PCL tablet volume, and c_s is the saturation solubility limit of the drug in the release medium.

Specifically, the Higuchi equation was first rearranged to solve for the diffusion coefficient:

$$D = \left(\frac{M_t}{A\sqrt{2c_{ini}c_s t}}\right)^2 \qquad (3)$$

Then upon solving for the diffusion coefficient with the experimental data, the Higuchi modeled release could be obtained by:

$$M_t = A\sqrt{2Dc_{ini}c_s t} \quad (4)$$

Where area, diffusion coefficient, initial concentration and solubility concentration may be simplified into a constant, k, for each sample:

$$M_t = k\sqrt{t} \quad (5)$$

Figure 6 displays the Higuchi modeled release and the experimental release data for each first press sample with varying drug loading (5%, 10%, and 20%). It can be seen that the Higuchi modeled release fits the data relatively well with an $R^2 \approx 0.93$ for each sample. It can be noted that there appears to be slight deviations from the model towards the end of the release profile, particularly in the 5% and 10% loading samples (note that the last four experimental data points do not fall on the Higuchi modeled line). This may be attributed to the pseudo steady state assumption of a constant $\Delta C/\Delta x$ in the thin film behavior of the sample. In reality, this over simplification can be expected to cause a deviation of the model from the experimental data as the diffusion front moves inward. If we continue to assume ΔC is constant between the PCL surface and the inward moving diffusion front, then a significant increase in Δx as the depth of the diffusion front begins to deviate from thin film behavior would result in a decrease in the drug concentration gradient, no longer meeting the pseudo steady state criteria. Thus, this is why the Higuchi model only applies to relatively thin systems. Nonetheless, regardless of any small deviations, the Higuchi model appears to serve as an appropriate model for the experimental data shown here.

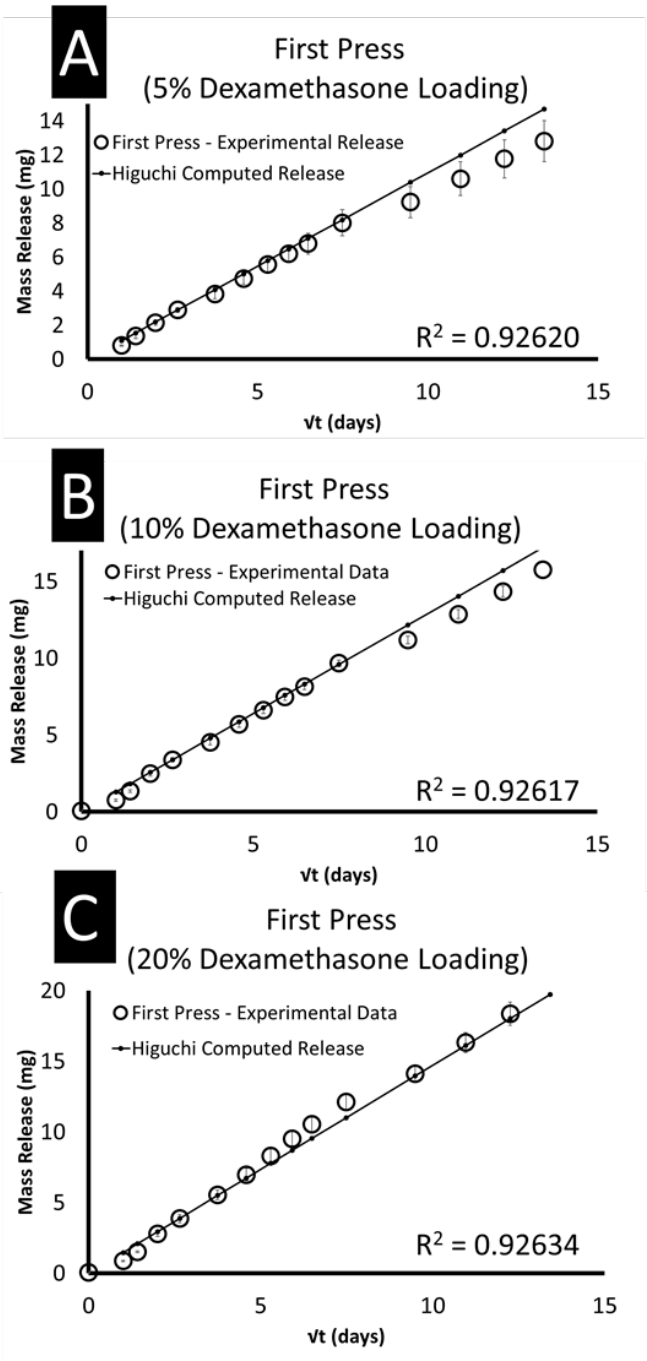

FIGURE 6 HIGUCHI MODELED AND EXPERIMENTAL RELEASE OF FIRST PRESS SAMPLES WITH A) 5% DEX LOADING, B) 10% DEX LOADING, AND C) 20% DEXLOADING. THE SOLID LINE IN EACH GRAPH IS THE HIGUCHI PSEUDO STEADY STATE MODEL WHICH DESCRIBES DRUG RELEASE FROM THIN FILMS CONTAINING FINELY DISPERSED DRUG INTO SINK CONDITIONS. THE DIFFUSION COEFFICIENT FOR EACH MODEL WAS SOLVED USING THE EXPERIMETNAL RELEASE. THE CIRCLES IN EACH GRAPH REPRESENT THE EXPERIMENTAL DATA COLLECTED FROM THE RELEASE STUDIES.

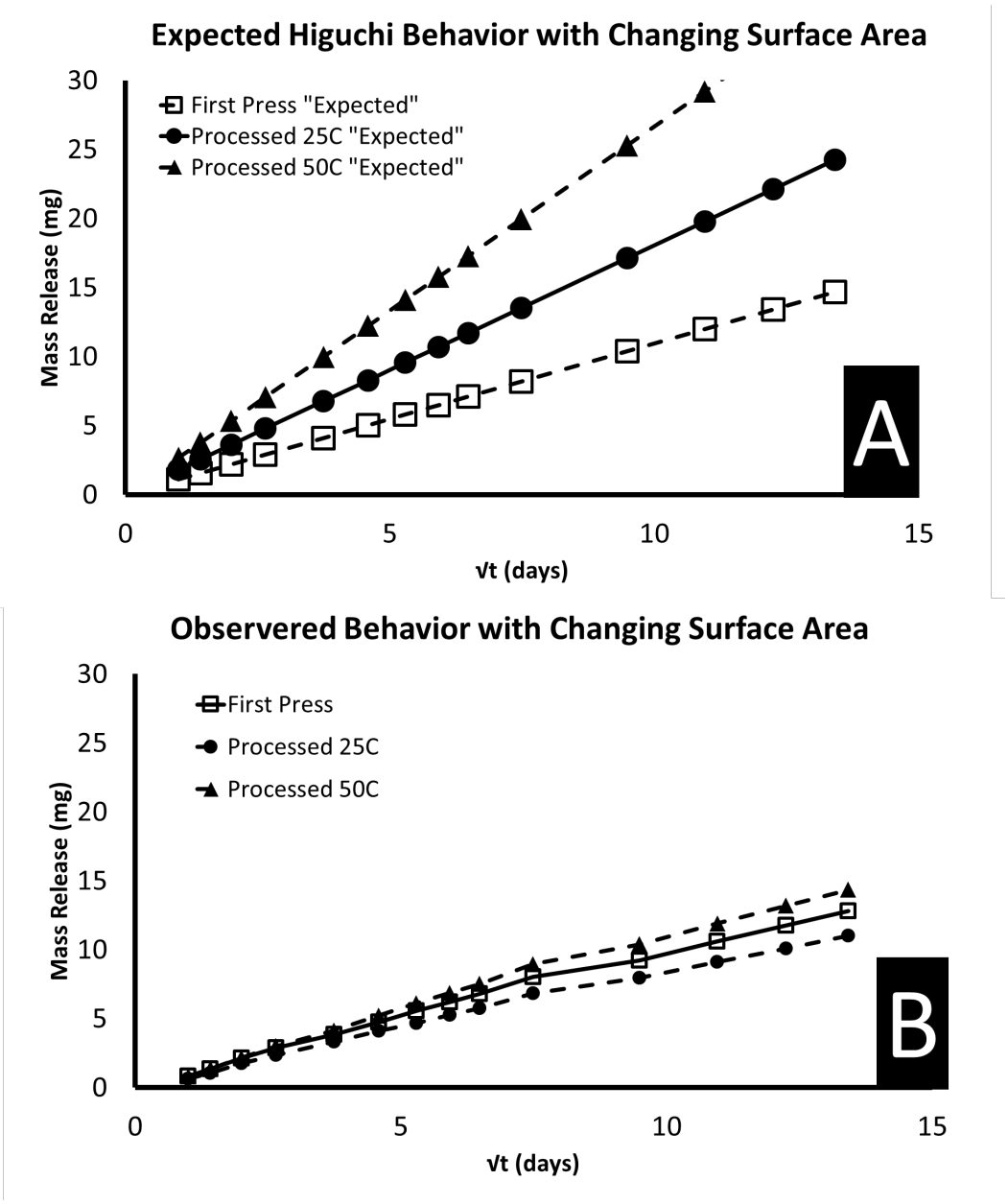

FIGURE 7 REPRESENTATIVE HIGUCHI MODELED AND OBSERVED EXPERIMENTAL RELEASE FOR SAMPLES WITH 5% DEX LOADING. A) HIGHUCHI MODELED RELEASE FOR FIRST PRESS, PROCESSED 25 ºC AND 50 ºC SAMPLES. THE DIFFUSION COEFFICIENT WAS ASSUMED TO BE CONSTANT BETWEEN ALL THREE SAMPLES, WITH SURFACE AREA BEING THE ONLY VARIABLE IN BEHAVIOR. B) THE OBSERVED EXPERIMENTAL RELEASE OF FIRST PRESS, PROCESSED 25 ºC AND 50 ºC SAMPLES. NOTE THAT A SIMILAR DIFFERENT BETWEEN EXPECTED AND OBSERVED RELEASE BEHAVIOR WAS ALSO SEEN FOR 10% AND 20% DEX LOADING.

To this end, Figure 7a displays representative Higuchi modeled curves of the 5% dexamethasone loading samples. In Figure 7a the diffusion coefficient between all three samples (first press, processed 25 ºC, and processed 50 ºC) were assumed to be the same. Thus the only variation between the modeled curves is the variation of surface area in each sample. It is clear from Figure 7a that as the surface area to volume ratio of the sample increases, a significant increase in cumulative mass release would be expected. However, in Figure 7b is it apparent that this expected behavior is not observed by our experimental data. Rather, the variation in surface area appears to have little to no impact on the cumulative mass release. Note this same trend between expected and observed behavior was also seen for the samples with 10% and 20% dexamethasone loading (see Figure 1S in the supplemental materials). To explain this, it is demonstrated in Figure 8 the need for a new diffusion coefficient to be calculated for each sample to accurately model the release with the Higuchi equation. In Figure 8, the dotted line represents the Higuchi model using the same diffusion coefficient as the first press sample (where surface area was the only variable between samples), and the solid line represents the Higuchi model using the new diffusion coefficient based on the release properties of the individual processed sample (calculated using Equation 3).

Finally, Figure 9 displays the average diffusion coefficients for each sample, computed by Equation 3. Here a clear trend emerges, with the processed samples at 25 ºC and 50 ºC displaying consistently lower dexamethasone diffusion coefficients, independent of drug loading, compared to the first press samples. In addition it appears that the first press samples show concentration dependent diffusion.

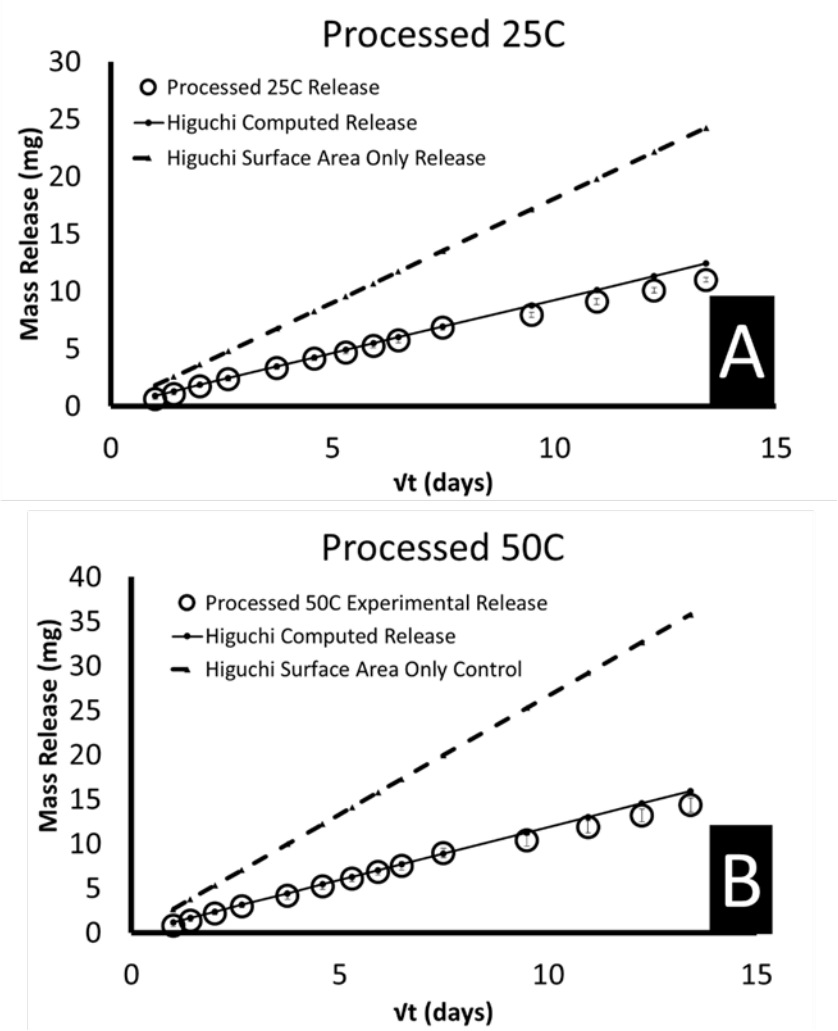

FIGURE 8 MODELS REPRESENTING THE VARIABLE DIFFUSION COEFFICIENTS IN 5% DEX LOADING SAMPLES A) PROCESSED 25 ºC AND B) PROCESSED 50 ºC SAMPLES COMPARED TO THE FIRST PRESS WITH EQUIVALENT LOADING. THE DOTTED LINE REPRESENTS THE HIGUCHI MODEL USING THE SAME DIFFUSION COEFFICIENT AS THE FIRST PRESS SAMPLE (WHERE SURFACE AREA WAS THE ONLY VARIABLE BETWEEN SAMPLES), AND THE SOLID LINE REPRESENTS THE HIGUCHI MODEL USING THE INDIVIDUAL DIFFUSION COEFFICIENT BASED ON THE RELEASE PROPERTIES TO THE INDIVIDUAL SAMPLE (CALCULATED USING EQUATION 3). CIRCLES IN EACH GRAPH REPRESENT THE EXPERIMENTAL RELASE DATA.

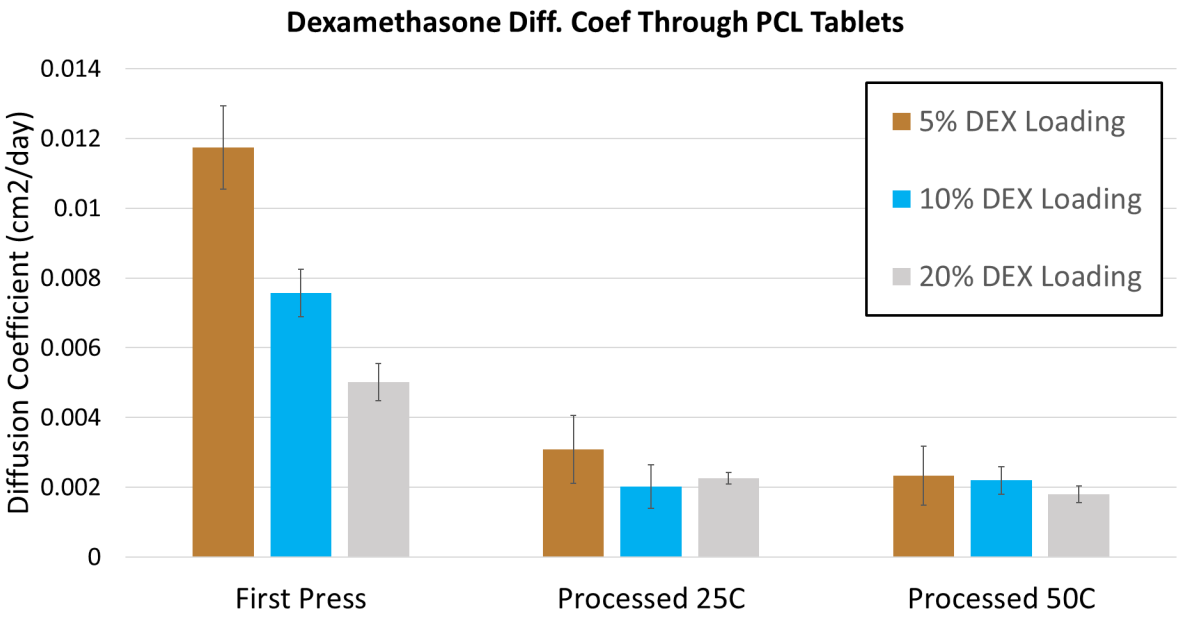

FIGURE 9 CALCULATED DIFFUSION COEFFICIENTS USING THE HIGUCHI EQUATION FOR FIRST PRESS, PROCESSED 25 ºC AND PROCESSED 50 ºC SAMPLES, WITH 5%, 10% AND 20% DEX LOADING.

Morphology Analysis

It is well regarded that diffusion-controlled release of small molecule drugs from a polymer is dependent on the structure of the polymer carrier. It has been shown that control of the solute diffusion coefficient may be achieved by controlling the degree of crystallinity, crosslinking, or branching within the polymer carrier. The mechanism of this controlled diffusion coefficient is attributed to the hindrance or enhancement of diffusion based on the free volume within the morphological structure. [139] To this end, the morphology of the film cast, first press, and processed PCL tablets used in this experiment were analyzed by XRD in an attempt to gain insight into the variable diffusion coefficient between samples.

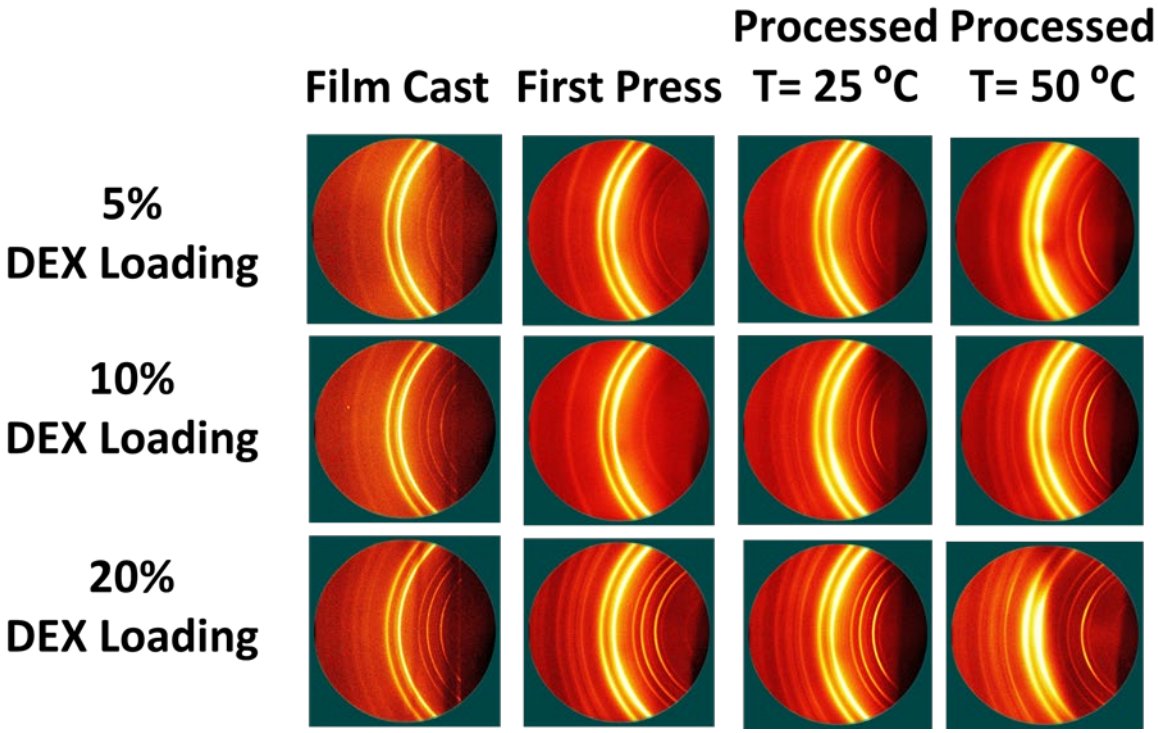

FIGURE 10 2D XRD AZIMUTHAL SCATTERING PATTERNS OF DEXAMETHASONE LOADED PCL TABLETS WITH 5%, 10%, AND 20% DRUG LOADING. THE FIRST COLUMN REPRESENTS FILM CAST PCL WITH TYPICAL SEMI-CRYSTALLINE MORPHOLOGY. THE SECOND, THIRD, AND FOURTH COLUMNS REPRESENT FIRST PRESS, PROCESSED 25 ºC AND PROCESSED 50 ºC SAMPLES RESPECTIVELY.

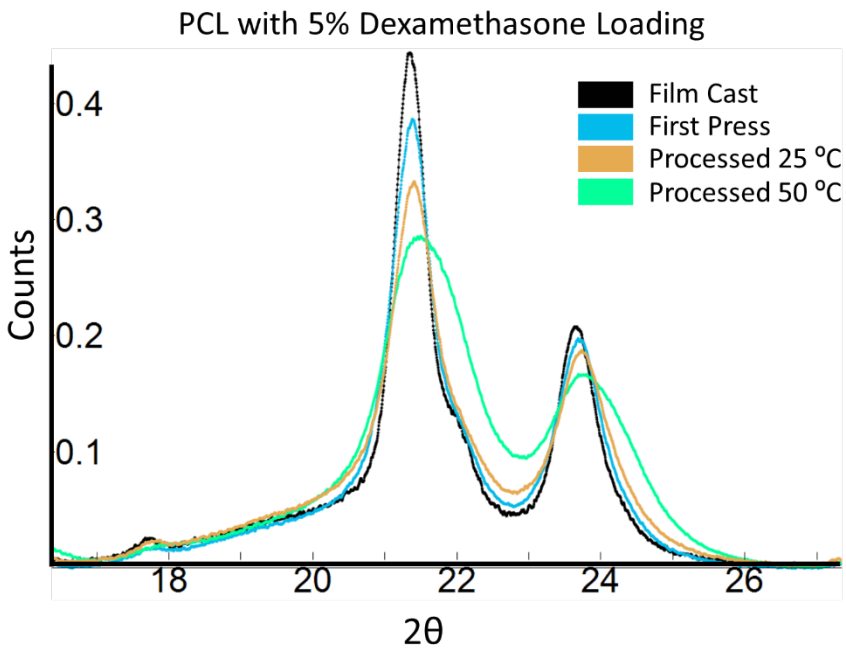

FIGURE 11 AREA NORMALIZED INTEGRATED XRD PROFILES OF 5% DEXAMETHASONE LOADING PCL TABLETS.

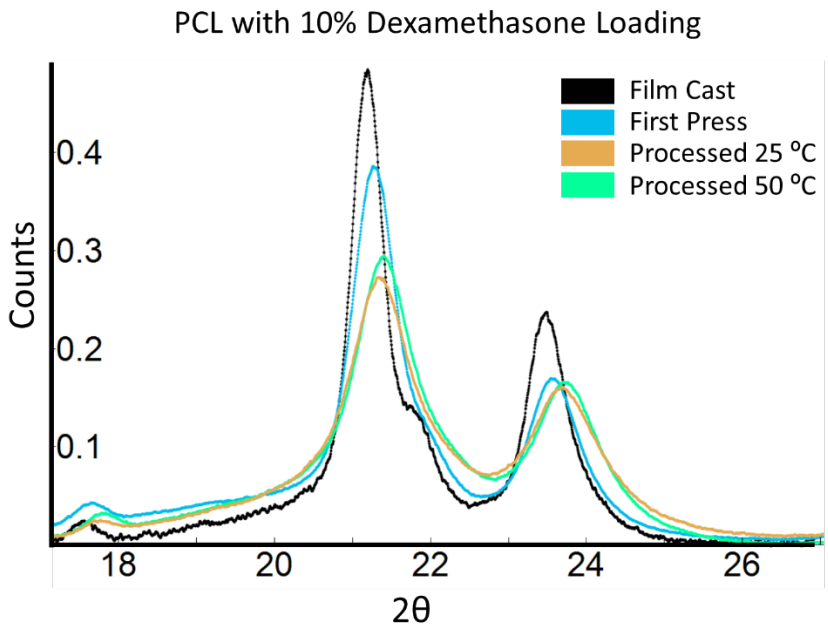

FIGURE 12 AREA NORMALIZED INTEGRATED XRD PROFILES OF 10% DEXAMETHASONE LOADING PCL TABLETS.

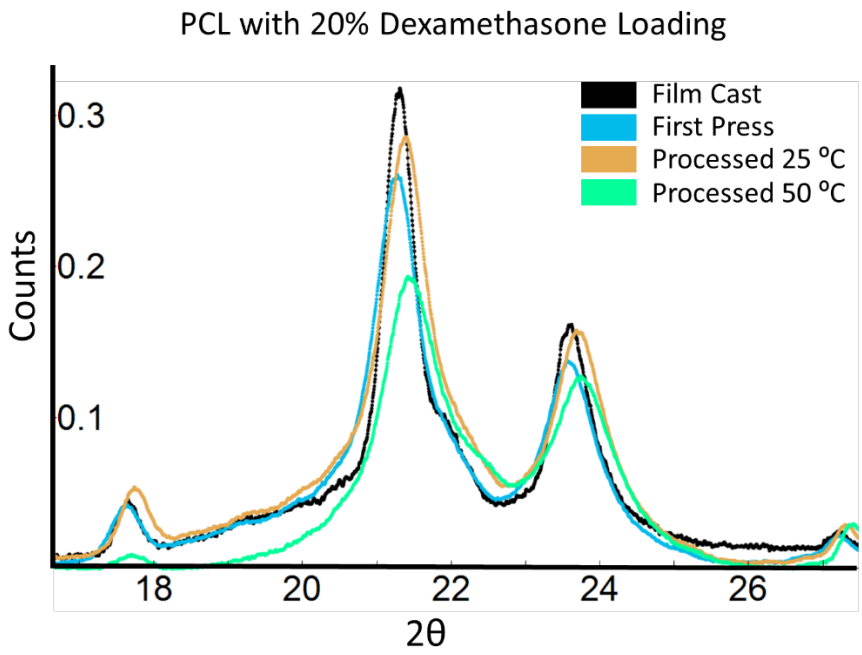

FIGURE 13 AREA NORMALIZED INTEGRATED XRD PROFILES OF 20% DEXAMETHASONE LOADING PCL TABLETS.

Figure 10 depicts XRD profiles of all dexamethasone loaded PCL tablets (2D azimuthal scattering patterns). The film cast PCL samples display a typical isotropic scattering profile characterized by a diffuse amorphous halo and sharp (110), (111), and (200) crystalline peaks (left most column of Figure 10). The amorphous phase of the film cast PCL displays no positional, orientational, or conformational order, thus presenting a weak and diffused scattering ring that underlies the crystal diffraction. The crystalline phase of the film cast PCL displays the characteristic three levels of positional order associated with the (110), (111), and (200) orthorhombic crystal faces with their inherent conformational order. To clarify, this analysis adopts the definitions of orientational, positional, and conformational order set by Wunderlich.[48]

In this instance, orientational order refers to the long range order of the polymer chains and can be observed by XRD as the uniformity of scattering of a given Debye-Scherrer ring (i.e.

isotropic or anisotropic). Positional order refers to the intermolecular spacing, which is typically characteristic of the packing of a particular crystal structure, and can be observed by XRD at the 2θ value at which a given Debye-Scherrer ring occurs. As mentioned, there are three levels of positional order associated with the (110), (111), and (200) orthorhombic crystals faces of PCL. These three levels of positional order are associated with the intermolecular spacing specific to each crystal face. Finally, conformational order refers to the rotational arrangement of the atoms in a single polymer chain (i.e. gauche or anti conformation) and can be observed by XRD as the sharpness of a given Debye-Scherrer ring.

In the first press, processed 25 °C and processed 50 °C samples, the scattering patterns observed in Figure 10 begin to broaden compared to the film cast PCL. This broadening can be seen in Figure 10 as the (110) and (200) face Debye-Scherrer rings thicken compared to the film cast PCL scattering profile. This broadening of the (110) and (200) face can be seen more clearly in the area normalized integrated scattering profiles depicted in Figures 11, 12, and 13. Generally, the broadening of a crystalline peak can be primarily attributed to either decreasing crystal size or increasing structural disorder within the sample. Since the processing temperature in all instances was below the T_m of PCL, it is most likely that the plastic deformation from applying pressure well below the melting temperature results in a disordering of the initial orthorhombic crystal conformation. To this end, a comparison can be made between the morphology observed here in PCL and the plastic crystal mesophase.[48,113] Plastic crystals are defined as a type of mesophase in the "plastic" state with positional order and both conformational and orientational disorder. The mechanism of formation of plastic crystals is thought to be the deformation of crystallites, due to a large number of slip planes within the structure.[48] In the case of PCL, it is known that long chain hydrocarbon crystals of orthorhombic structure can form dislocations on either side of which the

terminal methyl groups lie. In addition, several screw and edge dislocations can occur in these long chain hydrocarbon crystals. Any of these dislocations are noted to cause individual layers of the crystal to slip over one another.[99] Alternatively, the disordering of the PCL crystal structure may also be attributed to irregularly located carbonyl groups along the chain direction. [96,100] These slip-planes coupled with irregularly spaced carbonyl groups are thought to allow for plastic crystal formation in PCL upon plastic deformation. [113]

In addition, it was also previously reported that at processing temperatures around 50 ºC and 60 ºC (between the on-set and off-set of the PCL melt), the formation of a condis crystal mesophase could be seen.[113] Condis crystals are defined as a type of mesophase in the solid state with birefringent properties attributed to positional and orientation order, and partial or full conformational disorder. [48,81] Accordingly, it appeared that when sufficient chain mobility was achieved at increased temperatures of 50 ºC and 60 ºC, condis crystal mesophase is created based on a similar mechanism as the formation of the plastic crystal. Our lab has previously published a detailed review of this phenomenon in pure PCL films processed under similar conditions. [113]

A quantitative structural analysis of the dexamethasone loaded PCL samples were obtained by peak deconvolution of the integrated XRD scattering profiles (Figure 14). Specifically, the crystalline, amorphous, and mesophase phase content of each sample was calculated based on the peak area contribution to the total scattering area, using the methods described by Stoclet et. al.[75] Additional details of this method applied to PCL have been previously reported.[113] The deconvolution approach assumed Gaussian profiles for all scattering peaks and halos. Particularly, the amorphous halo parameters were determined by the film cast PCL which displayed the halo peak at a 2θ value of approximately 21°. Upon establishing a best fit amorphous halo, the (110), (111), and (200) orthorhombic crystalline face peaks were established. Finally, mesophase peaks

were fit to a R^2 value of at least 0.98 when comparing the computed model to the experimental data. The content of each phase (amorphous, mesophase, and crystalline) was calculated by the area under the diffraction peaks, using the ratio from one phase to the total scattering peaks (see Table 4S in the supplemental materials for deconvolution values).

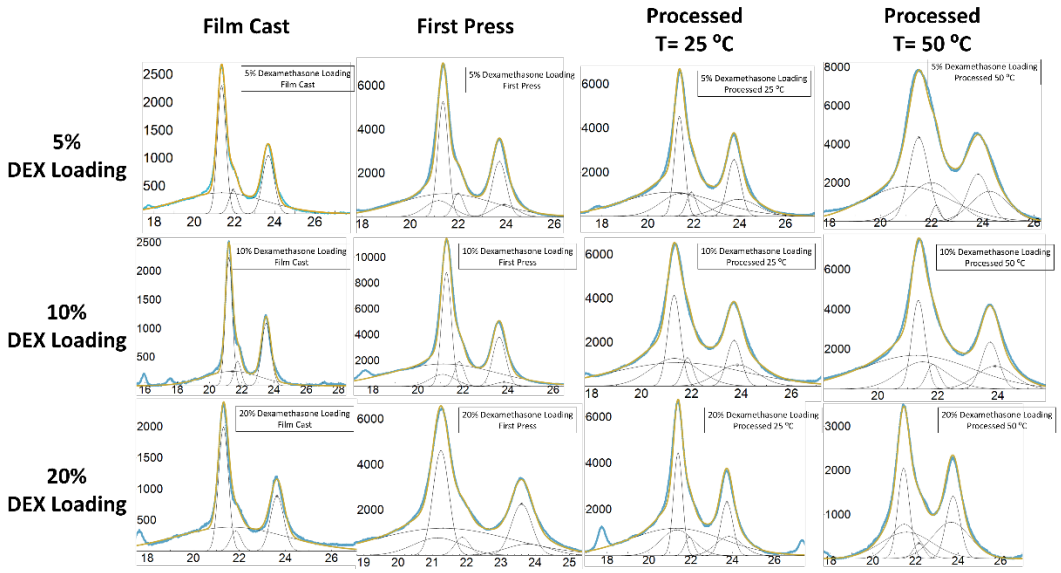

FIGURE 14 PEAK DECONVOLUTION ANALYSIS OF THE DEXAMETHASONE LOADED PCL SAMPLES, BASED ON THE INTEGRATED XRD SCATTERING PROFILES. TOP ROW: 5% DEX LOADING, MIDDLE ROW: 10% DEX LOADING, BOTTOM ROW: 20% DEX LOADING. THE COLUMNS FROM LEFT TO RIGHT REPRESENT FILM CAST, FIRST PRESS, AND PROCESSED 25 ºC AND 50 ºC SAMPLES RESPECTIVELY.

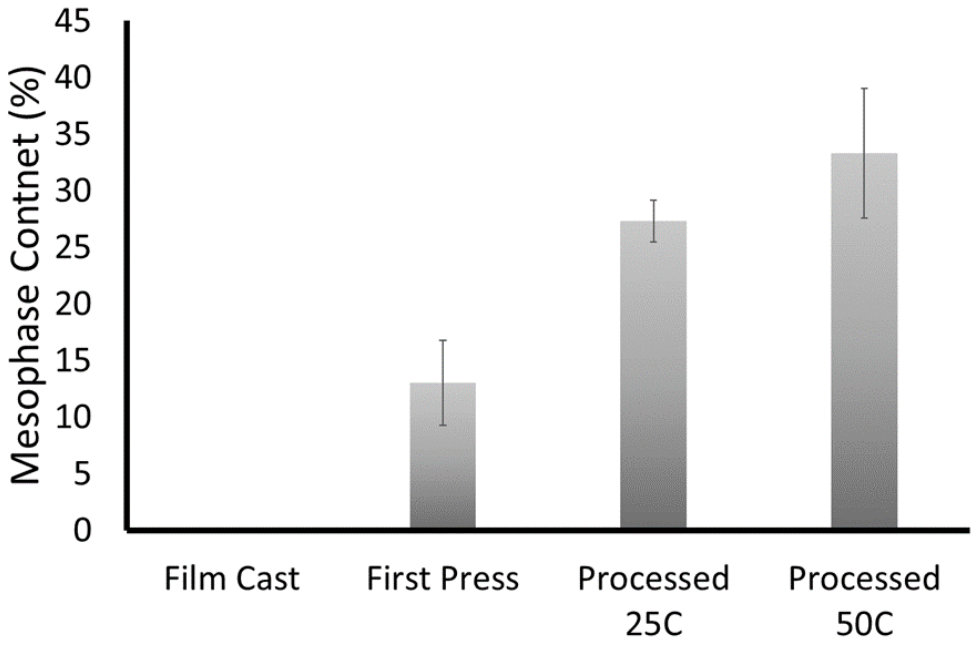

FIGURE 15 MESOPHASE CONTENT CALCULATED FROM THE XRD PEAK DECONVOLUTION ANALYSIS FOR FILM CAST, FIRST PRESS, AND PROCESSED DEXAMETHASONE LOADED PCL SAMPLES. NOTE THE STANDARD DEVIATION HERE REPRESENTS THE MESOPHASE VARIATION BETWEEN 5%, 10% AND 20% DRUG LOADING.

A general trend in mesophase content can be seen in Figure 15, in which increasing processing force, temperature, and plastic deformation correlate to an increase in mesophase formation. Specifically, it can be seen that the 'film cast' PCL samples displayed a typical semi-crystalline morphology, with no mesophase content detected. Here, these sample were produced via solvent cast from a DCM solution, with no external pressure or temperature applied in their processing history. The 'first press' samples were then produced from the 'film cast' samples by compressing into a tablet at 10,000 lb_f while constricted by a compression mold die. Here, it can be seen that upon initial application of pressure in the restricted environment of the compression mold, mesophase content begins to form (calculated on the order of 8-17%). Finally, the processed samples at 25 ºC and 50 ºC were produced from the 'first press' samples, by pressing in a temperature controlled hydraulic press under 20,000 lb_f. In these samples, the environment was

not restricted to a compression die, but rather upon application of force the samples were subject to plastic deformation and extruded flow between the plates of the hydraulic press. As a result, increased mesophase (calculated on the order of 25-40%) was estimated from the XRD deconvolution. This finding may be explained by the previously reported mechanism, in which mesophase formation was thought to be the result of crystal disorganization upon plastic deformation, related to the low-energy barrier slip-planes in the crystalline structure. In addition, the sufficient chain mobility achieved at higher processing temperatures (50 ºC) was shown to aid in the orientation and induction of these morphologies.

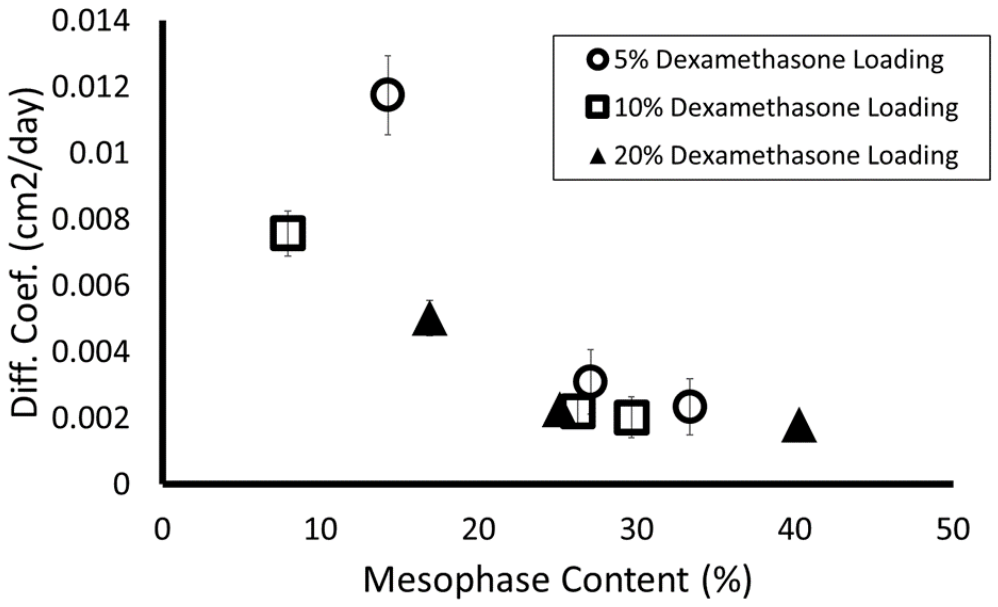

FIGURE 16 CORRELATION BETWEEN DIFFUSION COEFFICIENT CALCULATED BY THE HIGUCHI EQUATION AND THE MESOPHASE CONTENT ESTIMATED FROM XRD PEAK DECONVOLUTION. CIRCLES: 5% DEXAMETHASONE LOADING, SQUARES: 10% DEXAMETHSONE LOADING, AND TRIANGLES: 20% DEXAMETHASONE LOADING.

To this end, it can then be seen in Figure 16 that this formation of mesophase morphology within the PCL samples may in part describe the variable diffusion coefficient observed in the *in-vitro* release studies. A general trend can be seen in Figure 16, where the

samples with lower mesophase content (associated with the 'first press' processing) tend towards a higher diffusion coefficient (faster dexamethasone release). On the other hand, the samples with higher mesophase content (associated with the 'processed 25 °C' and 'processed 50 °C' samples) tend towards a lower diffusion coefficient (slower dexamethasone release).

Dexamethasone is thought to diffuse through the amorphous regions of the PCL network. Thus, an increase in density or decrease in free volume of the amorphous region of the network would be expected to result in a reduction of dexamethasone diffusion, as this would result in a direct decrease in the available area for the dexamethasone to travel through. It was previously shown by our lab that at low processing pressures, slight plastic crystal morphology could be observed, which formed primarily at the expense of the crystalline phase.[113] However, upon increasing the processing pressure and plastic deformation, mesophase formation was seen to form at the expense of both the amorphous and crystalline phases. In addition, it was shown that heating the samples nears the T_m to 50 °C may result in an anisotropic orientation of this morphology.[113] This mechanism of formation may explain the results observed in Figure 16, with the implication that the lower the diffusion coefficient observed is directly related to the decrease in free volume of the amorphous phase contribution to the plastic or condis crystal mesophase formation.

CONCLUSION

The work presented here has demonstrated the ability to achieve long-acting sustained release of dexamethasone from biodegradable PCL tablets, at loadings of 5%, 10%, and 20% w/w. Herein, it was observed that the release of dexamethasone appeared to occur primarily by the mechanism of Fickian diffusion, with negligible contributions from polymer degradation. This release behavior was successfully modeled using the Higuchi equation ($R^2 \approx 0.93$), suggesting the

tablets behave as a pseudo steady state system with finely dispersed drug. To this end, it was shown that to successfully model each sample using the Higuchi equation, a variable diffusion coefficient was needed based on the samples processing conditions. This variable diffusion coefficient was associated with a decreased diffusion flux, and a lower percent release per surface area of sample. First press samples (those processed under lower loads of 10,000 lb_f in the restricted environment of a compression molded die) appeared to have higher rates of release associated with a diffusion coefficient on the order of 5E-3 to 12E-3 cm^2/day. While samples processed under 20,000 lb_f in an unrestricted environment at temperatures of both 25 °C and 50 °C appeared to have lower rates of release associated with a diffusion coefficient on the order of 2E-3 to 3E-3 cm^2/day. Upon analysis by XRD, it was observed that processed samples with decreased diffusion behavior were correlated to the formation of processing induced mesophase morphology. It was estimated by peak deconvolution of the integrated XRD profiles that first press samples contained mesophase formation on the order of 8-17% of the total phase content, while samples processed under higher load and temperature contained an estimate of 25-40%. Thus, the variable diffusion coefficient observed between samples processed under varying conditions is thought to relate to the decrease in free volume associated with mesophase formation. These findings suggest that mesophase formation may impact the long-acting release behavior and may serve as a means for controlling the rate of drug diffusion.

SUPPLEMENTAL MATERIALS

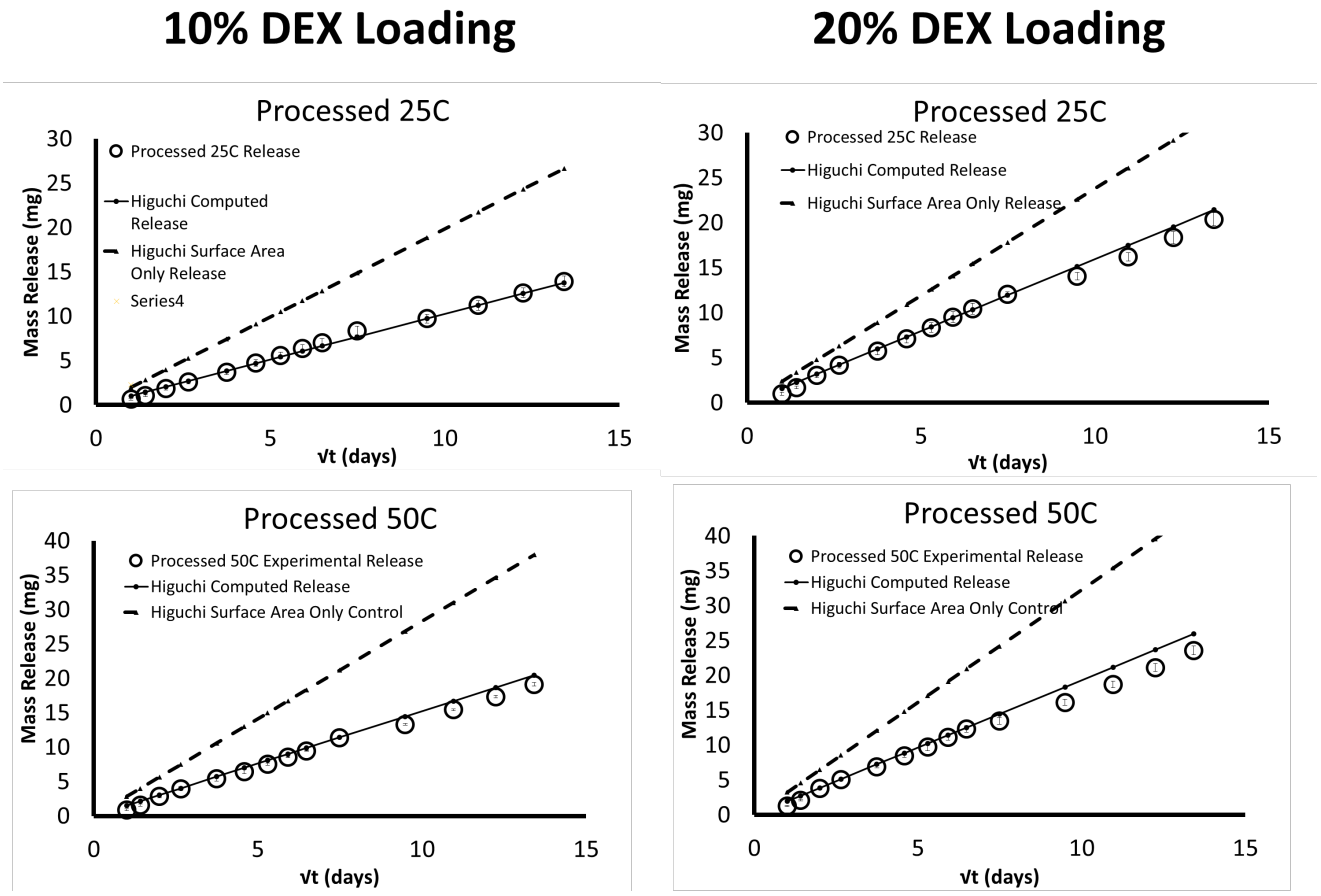

FIGURE 1S MODELS REPRESENTING THE VARIABLE DIFFUSION COEFFICIENTS IN 10% DEX LOADING (LEFT) AND 20% DEX LOADING (RIGHT). THE DOTTED LINE REPRESENTS THE HIGUCHI MODEL USING THE SAME DIFFUSION COEFFICIENT AS THE FIRST PRESS SAMPLE (WHERE SURFACE AREA WAS THE ONLY VARIABLE BETWEEN SAMPLES), AND THE SOLID LINE REPRESENTS THE HIGUCHI MODEL USING THE INDIVIDUAL DIFFUSION COEFFICIENT BASED ON THE RELEASE PROPERTIES TO THE INDIVIDUAL SAMPLE (CALCULATED USING EQUATION 3). CIRCLES IN EACH GRAPH REPRESENT THE EXPERIMENTAL RELASE DATA.

20% Dexamethasone Loading								
First Press (Tablets 1-3)			**Processed 25C (Tablets 4-5)**			**Processed 50C (Tablets 7-9)**		
Tablet 1			**Tablet 4**			**Tablet 7**		
Tablet mass after processing	224	mg	Tablet mass after processing	237.8	mg	Tablet mass after processing	225.6	mg
mass PCL after processing	179.2	mg	mass PCL after processing	190.24	mg	mass PCL after processing	180.48	mg
mass DEX after processing	44.8	mg	mass DEX after processing	47.56	mg	mass DEX after processing	45.12	mg
Radius	0.6485	cm	Radius	0.813	cm	Radius	1.1035	cm
Thickness	0.205	cm	Thickness	0.103	cm	Thickness	0.07	cm
Surface area	3.477710081	cm^2	Surface area	4.679138364	cm^2	Surface area	8.136456367	cm^2
Drug area density	12.88203989	mg/cm^2	Drug area density	10.16426451	mg/cm^2	Drug area density	5.545411659	mg/cm^2
Tablet 2			**Tablet 5**			**Tablet 8**		
Tablet mass after processing	214.6	mg	Tablet mass after processing	230.4	mg	Tablet mass after processing	229.7	mg
mass PCL after processing	171.68	mg	mass PCL after processing	184.32	mg	mass PCL after processing	183.76	mg
mass DEX after processing	42.92	mg	mass DEX after processing	46.08	mg	mass DEX after processing	45.94	mg
Radius	0.645	cm	Radius	0.823	cm	Radius	0.9805	cm
Thickness	0.164	cm	Thickness	0.105	cm	Thickness	0.07	cm
Surface area	3.278597509	cm^2	Surface area	4.798745079	cm^2	Surface area	6.471776685	cm^2
Drug area density	13.0909634	mg/cm^2	Drug area density	9.602510498	mg/cm^2	Drug area density	7.098514401	mg/cm^2
Tablet 3			**Tablet 6**			**Tablet 9**		
Tablet mass after processing	231.2	mg	Tablet mass after processing	221.8	mg	Tablet mass after processing	232.9	mg
mass PCL after processing	184.96	mg	mass PCL after processing	177.44	mg	mass PCL after processing	186.32	mg
mass DEX after processing	46.24	mg	mass DEX after processing	44.36	mg	mass DEX after processing	46.58	mg
Radius	0.65	cm	Radius	0.97	cm	Radius	1.037	cm
Thickness	0.169	cm	Thickness	0.086	cm	Thickness	0.067	cm
Surface area	3.344853698	cm^2	Surface area	6.435992374	cm^2	Surface area	7.193292133	cm^2
Drug area density	13.82422198	mg/cm^2	Drug area density	6.892487968	mg/cm^2	Drug area density	6.475477312	mg/cm^2

TABLE 1S DIMENSIONS AND MASS OF 20% DEXAETHASONE LOADING PCL TABLETS

10% Dexamethasone Loading								
First Press (Tablets 1-3)			**Processed 25C (Tablets 4-5)**			**Processed 50C (Tablets 7-9)**		
Tablet 1			**Tablet 4**			**Tablet 7**		
Tablet mass after processing	222.8	mg	Tablet mass after processing	231.2	mg	Tablet mass after processing	211.8	mg
mass PCL after processing	200.52	mg	mass PCL after processing	208.08	mg	mass PCL after processing	190.62	mg
mass DEX after processing	22.28	mg	mass DEX after processing	23.12	mg	mass DEX after processing	21.18	mg
Radius	0.639	cm	Radius	0.799	cm	Radius	0.9725	cm
Thickness	0.169	cm	Thickness	0.11	cm	Thickness	0.069	cm
Surface area	3.244083972	cm^2	Surface area	4.56342094	cm^2	Surface area	6.363979216	cm^2
Drug area density	6.86788634	mg/cm^2	Drug area density	5.066374613	mg/cm^2	Drug area density	3.328106406	mg/cm^2
Tablet 2			**Tablet 5**			**Tablet 8**		
Tablet mass after processing	230.6	mg	Tablet mass after processing	233.1	mg	Tablet mass after processing	225.7	mg
mass PCL after processing	207.54	mg	mass PCL after processing	209.79	mg	mass PCL after processing	203.13	mg
mass DEX after processing	23.06	mg	mass DEX after processing	23.31	mg	mass DEX after processing	22.57	mg
Radius	0.6435	cm	Radius	0.825	cm	Radius	0.993	cm
Thickness	0.184	cm	Thickness	0.105	cm	Thickness	0.078	cm
Surface area	3.345772614	cm^2	Surface area	4.820773927	cm^2	Surface area	6.682186424	cm^2
Drug area density	6.8922795	mg/cm^2	Drug area density	4.835323198	mg/cm^2	Drug area density	3.377636984	mg/cm^2
Tablet 3			**Tablet 6**			**Tablet 9**		
Tablet mass after processing	234.5	mg	Tablet mass after processing	243.6	mg	Tablet mass after processing	232.1	mg
mass PCL after processing	211.05	mg	mass PCL after processing	219.24	mg	mass PCL after processing	208.89	mg
mass DEX after processing	23.45	mg	mass DEX after processing	24.36	mg	mass DEX after processing	23.21	mg
Radius	0.6405	cm	Radius	0.9455	cm	Radius	1.124	cm
Thickness	0.182	cm	Thickness	0.111	cm	Thickness	0.05	cm
Surface area	3.310052706	cm^2	Surface area	6.276404179	cm^2	Surface area	8.291140535	cm^2
Drug area density	7.084479338	mg/cm^2	Drug area density	3.881203202	mg/cm^2	Drug area density	2.799373609	mg/cm^2

TABLE 2S DIMENSIONS AND MASS OF 10% DEXAETHASONE LOADING PCL TABLETS

5% Dexamethasone Loading								
First Press (Tablets 1-3)			**Processed 25C (Tablets 4-5)**			**Processed 50C (Tablets 7-9)**		
Tablet 1			**Tablet 4**			**Tablet 7**		
Tablet mass after processing	199.6	mg	Tablet mass after processing	221.4	mg	Tablet mass after processing	239.3	mg
mass PCL after processing	189.62	mg	mass PCL after processing	210.33	mg	mass PCL after processing	227.335	mg
mass DEX after processing	9.98	mg	mass DEX after processing	11.07	mg	mass DEX after processing	11.965	mg
Radius	0.6415	cm	Radius	0.813	cm	Radius	0.997	cm
Thickness	0.165	cm	Thickness	0.103	cm	Thickness	0.071	cm
Surface area	3.250730012	cm^2	Surface area	4.679138364	cm^2	Surface area	6.690310582	cm^2
Drug area density	3.070079633	mg/cm^2	Drug area density	2.365820187	mg/cm^2	Drug area density	1.788407257	mg/cm^2
Tablet 2			**Tablet 5**			**Tablet 8**		
Tablet mass after processing	237.6	mg	Tablet mass after processing	220.3	mg	Tablet mass after processing	238.7	mg
mass PCL after processing	225.72	mg	mass PCL after processing	209.285	mg	mass PCL after processing	226.765	mg
mass DEX after processing	11.88	mg	mass DEX after processing	11.015	mg	mass DEX after processing	11.935	mg
Radius	0.6435	cm	Radius	0.8335	cm	Radius	0.9605	cm
Thickness	0.198	cm	Thickness	0.099	cm	Thickness	0.074	cm
Surface area	3.402377831	cm^2	Surface area	4.883535094	cm^2	Surface area	6.24320697	cm^2
Drug area density	3.491675702	mg/cm^2	Drug area density	2.255538209	mg/cm^2	Drug area density	1.911677774	mg/cm^2
Tablet 3			**Tablet 6**			**Tablet 9**		
Tablet mass after processing	236.4	mg	Tablet mass after processing	232.1	mg	Tablet mass after processing	235.5	mg
mass PCL after processing	224.58	mg	mass PCL after processing	220.495	mg	mass PCL after processing	223.725	mg
mass DEX after processing	11.82	mg	mass DEX after processing	11.605	mg	mass DEX after processing	11.775	mg
Radius	0.626	cm	Radius	0.9375	cm	Radius	1.1545	cm
Thickness	0.202	cm	Thickness	0.08	cm	Thickness	0.043	cm
Surface area	3.256750874	cm^2	Surface area	5.993569734	cm^2	Surface area	8.686590081	cm^2
Drug area density	3.629384149	mg/cm^2	Drug area density	1.936241758	mg/cm^2	Drug area density	1.355537661	mg/cm^2

TABLE 3S DIMENSIONS AND MASS OF 5% DEXAETHASONE LOADING PCL TABLETS

5% DEX Loading					10% DEX Loading					20% DEX Loading				
	Film Cast	First Press	Processed 25C	Processed 50C		Film Cast	First Press	Processed 25C	Processed 50C		Film Cast	First Press	Processed 25C	Processed 50C
Crystalline	1230.92	2827.73	2427.46	4167.89	Crystalline	1197.07	4726.21	2635.87	2462.56	Crystalline	1067.08	2711.62	2301.01	1383.9
	758.529	1842.04	1855.2	2581.13		790.589	2757.82	1508.48	1715.97		643.687	1693.22	1560.59	1165.02
	230.783	591.914	580.667	324.309		232.284	1043.26	701.969	657.841		190.551	429.896	437.56	227.025
Amorphous	2056.87	5267.63	5648.13	7745.48	Amorphous	1095.94	10279	7045.13	7857.9	Amorphous	2317.08	5851.28	6584.18	1790.88
Mesophase	0	1055.13	1622.89	4574.71	Mesophase	0	1297.46	1967.88	2710.19	Mesophase	0	1369.7	2243.72	1272.06
	0	696.501	2280.37	2841.39		0	324.884	3045.57	1807.4		0	802.628	1410.31	1805.41
Mesophase Content (%)	0	14.26299849	27.07829783	33.35340837	Mesophase Content (%)	0	7.941519732	29.65678766	26.24695842	Mesophase Content (%)	0	16.89430614	25.13542683	40.25838877
Diffusion Coefficient		0.011743461	0.00308311	0.002328674	Diffusion Coefficient		0.00757655	0.00201952	0.002200246	Diffusion Coefficient		0.005015836	0.00225785	0.001795034

TABLE 4S XRD PEAK DECONVOLUTION VALUES OF DEXAMETHASONE LOADED PCL TABLETS

CHAPTER 4

PLGA NANOPARTICLES FOR LONG ACTING DELIVERY OF A NOVEL GLP-1 RECEPTOR AGONIST PEPTIDE IN THE TREATMENT OF TYPE 2 DIABETES

Cameron Baptista, Kosta Milovanovic, Aharon Azagury, and Edith Mathiowitz[‖]

Department of Molecular Pharmacology, Physiology and Biotechnology
Center of Biomedical Engineering
Brown University, Providence, RI 02912, USA
‖ Edith_Mathiowitz@Brown.edu

The following manuscript has been prepared for submission in the Journal of Controlled Release
2022

ABSTRACT

The preparation and characterization of PLGA nanoparticles loaded with a GLP-1 RA peptide is presented here. In this work, a process termed phase inversion nanoencapsulation was used to prepare GLP-1 RA and PLGA nanoparticles. Specifically, we provide evidence towards the mechanism of particle formation by supersaturation, nucleation, and growth upon adding a solubilized polymer or drug solution to a miscible non-solvent. Here, this mechanism is correlated to the Gibbs energy of mixing (ΔG_{Mix}) between the solvent and non-solvent used in the phase inversion process, calculated using the activity coefficients obtained from the UNIFAC method. By choosing the appropriate solvent and non-solvent pairs for the phase inversion process, it is demonstrated that particle size, encapsulation efficiency, and release profile can be optimized and tailored for a desired function. It was shown that the size of GLP-1 RA and PLGA particles tends to decrease with increasingly negative ΔG_{Mix} of the solvent and non-solvent pairs used to produce them. For example, solvent and non-solvent pair with a $\Delta G_{Mix}/RT$ value of -1.293 (dichloromethane and heptane) yielded PLGA particles with a number average size of 260 nm while those with a less negative $\Delta G_{Mix}/RT$ value of -0.205 (acetone and heptane) yielded particles with a comparatively larger number average size of 638 nm. To this end, it was also shown that the ΔG_{Mix} of solvent and non-solvent pairs used in the phase inversion process correlates to the GLP-1 RA encapsulation efficiency and release behavior of the drug from PLGA particles. It was shown that GLP-1 RA encapsulated using solvent and non-solvent pairs with $\Delta G_{Mix}/RT$ values (between approximately -1.4 and -0.6) displayed low burst release (0-20% of the theoretical loading) and released the majority of drug after an approximate 8 day (200 hour) lag period. On the other hand, GLP-1 RA encapsulation using solvent and non-solvent pairs with less negatives $\Delta G_{Mix}/RT$ values (between approximately -0.6 and -0.2) displayed a large burst release

(approximately 20-70% of the theoretical loading) with the majority of the drug being released by the 1 day (24 hour) time point (approximately 60-100% of the theoretical loading). Herein, we present this correlation between ΔG_{Mix} and particle size, encapsulation efficiency, and release profile through the mechanism of supersaturation, nucleation, and growth. It appears that more negative ΔG_{Mix} may increase the degree of polymer supersaturation which provides a decrease in particle size and increased affinity of the polymer to encapsulate the GLP-1 RA.

INTRODUCTION

The overarching goal of this research is to develop a polymer nanoparticle formulation containing a novel glucagon-like peptide-1 receptor agonist (GLP-1 RA) for its long acting delivery in the treatment of type 2 diabetes (T2D). The World Health Organization has estimated that 13% of the world's adult population is obese.[142] As a result of this global obesity epidemic, T2D has also recently reached epidemic proportions.[59,143] To this end, GLP-1 RAs have become an important treatment option for both glycemic control and body weight control in T2D patients.[59,144]

Generally, one of the major challenges in the field of peptide and protein therapeutics is their delivery to the site of action. Due to their high molecular weight and susceptibility to degradation by both enzymes and extreme pH values, peptides and proteins usually display poor absorption across epithelial membranes and exhibit low oral bioavailability.[30,41] For this reason, peptide therapeutics such as GLP-1 RAs are typically administered by subcutaneous injection.[41] In some cases, even upon injection, peptides can be rapidly metabolized and cleared from circulation and therefore require several injections to be administered daily.[41] Thus, from the perspective of both the pharmaceutical industry and patients alike, the ability to reduce the frequency of injections or convert an approved injectable peptide or protein into a non-injected

formulation would represent a major advance in treatment. A leading approach in this effort has been through the utilization of biodegradable poly (lactic-co-glycolic acid) PLGA nanoparticles. [15–27,38,41]

There are many unique challenges in the formulation of peptide and protein nanoparticle delivery systems that must be addressed to achieve consistent clinical performance. To start, a key barrier to clinical success is often the ability to achieve a tailored sustained release profile of the drug cargo from the nanoparticle delivery system.[30–33] Compounding this challenge, the size, surface charge, and shape of the nanoparticles must also be tailored as these factors have a key role in the biodistribution and fate of the drug *in vivo*.[34–39] To add, even in instances where successful therapeutic performance is achieved, formulations often face technical challenges associated with drug stability, drug loading efficiency, scale up feasibility, batch to batch consistency, and economic viability. [31,33,40,41]

There have been a number of studies which report the encapsulation of GLP-1 RAs in PLGA or polylactic acid (PLA) nanoparticles. [15–27] However, to our knowledge, AstraZeneca's Bydureon® is the only PLGA particle formulation to reach the market for the delivery of a GLP-1 RA.[28] To this end, Bydureon® is a relatively large particle formulation (particle size ~50 μm) and is currently limited to a once weekly subcutaneous injection.[28,29] Currently, the most common methods for producing polymeric nanoparticles require an initial step of emulsifying a polymer solvent in an aqueous non-solvent. [15–27] This emulsification step poses many challenges for the success of formulations containing peptide and protein drugs. Both the high sheer rate and oil-water interfaces formed during emulsification are prone to destroying the secondary and tertiary structures of the API.[42–44] These emulsion processes may also be riddled with low encapsulation efficiencies, due to the use of an aqueous phase in which the drug is soluble. In addition, the

emulsion droplet size is often a limiting factor on the ultimate size of the nanoparticles produced.[33] Our lab has previously developed and reported on a method termed phase inversion nanoencapsulation (PIN), which is designed to combat these issues.[45] The PIN process is based on the mechanism of precipitation by phase inversion and thus utilizes solvent and non-solvent pairs which are completely miscible, avoiding these key issues associated with emulsification. In the PIN process, nanoparticles spontaneously precipitate after the immersion of a solubilized polymer solution in a non-solvent. Upon addition, the mechanism of polymer phase inversion is thought to occur in three key steps: supersaturation, nucleation, and growth. [46]

To this end, it is suggested that the properties and mixing behavior of the solvent and non-solvent pairs used in the phase inversion process may impact the degree of supersaturation, nucleation and growth that occurs. Ultimately, these variations in mixing behavior may impact the size, shape, surface charge, drug loading efficiency, and drug release profile of the resulting nanoparticles. Our lab has previously published findings which established that the solvent and non-solvent used for phase inversion dictates the size and morphology of particles produced. It was shown that both concentration (% weight/volume) and the type of non-solvent used in phase inversion have a direct impact on the precipitation product.[45] Specifically, polystyrene was solubilized in dichloromethane at a concentrations of 1, 5, and 10 % and then precipitated into both petroleum ether and ethanol. At each concentration it was observed that the product precipitated into ethanol was substantially smaller than that of the product precipitated into petroleum ether. In the instance of the 1 and 5 % concentrations, the particles were on the order of 1-4 μm when precipitated into petroleum ether, where the equivalent particles precipitated into ethanol where below 100 nm.[45] However, beyond this study there is little to no in-depth or quantitative knowledge regarding this association, nor does a process exist which is designed to

specifically exploit the use of different solvent and non-solvent pairs for optimized drug encapsulation and release from polymeric nanoparticles. Thus, herein we seek to fill this gap in knowledge and further the understanding of how solvent choice impacts the PIN process upon encapsulating a GLP-1 RA peptide in PLGA nanoparticles.

MATERIALS AND METHODS

Preparation of micronized GLP-1RA, PLGA Nanoparticles, and GLP-1 RA loaded PLGA Nanoparticles

All nanoparticles in this work were prepared by phase inversion as described previously.[38,45] The phase inversion nanoencapsulation process includes the steps of first micronizing the drug and then encapsulating in a polymer nanoparticle. The drug is micronized by solubilizing in a good solvent and then adding the solution to a reservoir of non-solvent for the drug. A key factor in the process is that the solvent and non-solvent must be miscible with each other, which allows for the drug solvent to be extracted into the non-solvent and thus result in drug precipitation. Upon extraction of the solvent by the miscible non-solvent, the drug is thought to precipitate through the steps of supersaturation, nucleation and growth. The resulting product is micronized drug nanoparticles.

In the work presented here, we focus on the micronization and encapsulation of a single peptide drug (a novel GLP-1 receptor agonist peptide used to treat type 2 diabetes, provided curtesy of Sanofi S.A.). Various solvent and non-solvent combinations were analyzed during the GLP-1 RA micronization process. Both methanol and water were analyzed as solvents to solubilize the GLP-1 RA. In all instances the peptide was dissolved as a concentration of 20 mg/mL. From these solvents, the GLP-1 RA was then precipitated into different non-solvents: tert-butanol, 2-propanol,

acetonitrile, acetone, ethyl acetate, tetrahydrofuran, dichloromethane, and chloroform. In all instances, the ratio of solvent to non-solvent was 1 mL: 60 mL, in order to ensure reservoir conditions for the extraction of solvent.

In an effort to better our understanding of the phase inversion precipitation process, the work presented here also focused on phase inversion of pure PLGA particles (i.e. blank particles, not containing drug). In the analysis of blank PLGA particle formation, PLGA (75:25) with Mw = 4-15kDa was used (Resomer RG 752H, CAS 26780-50-7). The following polymer solvents were tested in the phase inversion process: dichloromethane, ethyl acetate, chloroform, acetone, acetonitrile, and tetrahydrofuran. Accordingly, the following non-solvents were tested: tert-butanol, 2-propanol, ethanol, heptane, and water. In all instances, the polymer was solubilized in each solvent at a concentration of 100 mg/mL. The solubilized polymer solution was then added to an excess of non-solvent to facilitate precipitation and particle formation. The ratio of solvent to nonsolvent was 1 mL: 60 mL, in order to ensure reservoir conditions for the extraction of solvent.

Finally, in the study of GLP-1 RA encapsulation and release from PLGA nanoparticles, three types of PLGA were used (PLGA (50:50) with Mw = 7-17kDa, Resomer 502H (CAS Number 26780-50-7), PLGA (75:25) with Mw = 4-15kDa Resomer 752H (CAS Number 26780-50-7), and PLGA (50:50) with Mw 2.3kDa, Evonik (XXXX). In this study, GLP-1 RA was micronized using methanol as the solvent in all instances. Upon solubilizing the drug in methanol, the solution was added to different nonsolvents to create the micronized drug product (nonsolvents: dichloromethane, chloroform, ethyl acetate, tetrahydrofuran, acetonitrile, and acetone). In each instance of micronization, the drug was solubilized at a concentration of 20 mg/mL and precipitated with a solvent:nonsolvent ratio of 1 mL: 60 mL. Upon precipitating the GLP-1 RA

peptide in various nonsolvents, the PLGA was then solubilized in each of the suspended micronized drug solution. It should again be noted here that the GLP-1 RA was micronized with nonsolvents of dichloromethane, chloroform, ethyl acetate, tetrahydrofuran, acetone, and acetonitrile. While these organic solvents are nonsolvents for the drug, they are solvents for the polymer. Thus, the PLGA was added to each micronized drug solution at a concentration of 100 mg/mL to produce a solution of solubilized polymer and suspended micronized drug. The final step in the phase inversion nanoencapsulation process was to add each solution to a nonsolvent for both the polymer and drug. In this study 2-propanol and heptane were used as nonsolvents for the final nanoparticle products. Upon phase inversion and precipitation, the particles were run through a positive pressure filtration column with a PTFE filter to collect the resulting particles and then lyophilized to remove residual solvents.

Size Measurements

The size of both the micronized GLP-1RA and blank PLGA NPs were determined using a Zetasizer Nano ZS Size Analyzer from Malvern Panalytical. Suspensions of 1 mg/mL were produced for all GLP-1 RA and PLGA NPs by brief vortex and sonication. Milli-Q water was used as a dispersant for PLGA and acetonitrile was used as a dispersant for GLP-1RA. Each suspension was placed in a quartz cuvette for size analysis. Scan were conducted in triplicates on each sample and the average particle sizes from each scan were compared.

Scanning Electron Microscopy

Particles were imaged with a ThermoScientifc ApreoVS SEM. Sample were prepared by applying the particles to a carbon-adhesive tab, mounted on an aluminum stub and sputter-coated with Au-Pd using a Polaron Sputter Coater. Samples were examined at 3 kV accelerating voltage.

Fourier Transform Infrared Spectroscopy

Following lyophilization of the micronized drug, 1.0±0.05 mg of each micronization was combined with 99.0±0.05 mg of FTIR-grade KBr and pressed into a pellet. First a background scan was conducted, and absorption spectra were recorded over 32 scans from 400 – 4000 cm -1 in 1 cm -1 steps. Using Spectragryph software, each spectrum was baseline corrected and normalized using the amide peak at 1650 cm -1. FITYK software was then used for the deconvolution and analysis.

UNIFAC Gibbs Energy Calculations

A major focus of this work was to understand the impact of solvent/non-solvent mixing behavior on the precipitation of GLP-1 RA and PLGA in the PIN process. To aid in this analysis, the Gibbs energy of mixing between solvents and non-solvents were calculated using the UNIFAC method.

Briefly, the Gibbs energy of mixing for an ideal mixture may be defined as:

$$\Delta G^{Ideal} = -RT\Sigma x_i Ln(x_i)$$

Where, R is the gas constant, T is temperature, and x_i is the mole fraction of each component.[145] However, mixtures of real fluids typically only behave close to ideal when each component has similar properties (as ideal behavior assumes the interactions between all components are the same). For example, in an ideal binary mixture of component A and component B, there is no distinguishing between A-A, B-B, and A-B interactions. For this reason, we adopt the UNIFAC method for estimating the non-ideal Gibbs energy of mixing between solvents used in the PIN process.

The UNIFAC method aids in describing deviations from ideal solution behavior through the calculation of excess functions. Excess functions contain activity coefficients that give a quantitative measure of interactions between individual components within a mixture (i.e. A-A, B-B, and A-B interactions). The non-ideal behavior of the Gibbs energy of mixing between real fluids may then be accounted for by an excess Gibbs energy term:

$$G_E = RT\Sigma x_i Ln(\gamma_i)$$

Where γ_i is the activity coefficient determined by the UNIFAC method. Thus, in this work the non-ideal Gibbs energy of mixing is calculated by:

$$\Delta G_{Mix} = \Delta G_{Ideal} + G_E = RT\Sigma x_i Ln(x_i * \gamma_i)$$

The UNIFAC method was first put forth in 1977 in a publication by Aage Fredenslund, Jürgen Gmehling, and Peter Rasmussen.[146] The UNIFAC method is a semi-empirical method based on the universal quasichemical (UNIQUAC) method for calculating activity coefficients. Accordingly, UNIFAC is an abbreviation for the UNIQUAC Function Group Activity Coefficents (UNIFAC) method. Through the analysis of each component's functional groups, the semi-empirical nature of the UNIFAC method allows for estimations of activity coefficients without any experimental data needed.

TABLE 3 LIST OF FUNCTIONAL GROUPS USED TO DESCRIBE EACH SOLVENT IN THE UNIFAC CALCULATIONS OF GIBBS ENERGY

Solvent	**Functional Groups**
Dichloromethane	1- CH2CL2
Chloroform	1- CCL3
Acetonitrile	1- CH3CN
Acetone	1- CH3, 1- CH3CO
Ethyl Acetate	1- CH3COO, 1- CH2, 1- CH3
Tert-Butanol	3- CH3, 1- OH
2-Propanol	1- (CH3)2CHOH
Ethanol	1- CH3, 1- CH2, 1- OH
Heptane	2- CH3, 5- CH2
Water	1- H2O

Table 1 displays the functional groups used to describe each solvent in our calculations. All Gibbs energy calculations were done using an excel sheet provided by Lira and Elliott as a digital supplement to the Introductory Chemical Engineering Thermodynamics textbook.[147] See reference 38 for the associated link to the excel file used in these calculations.[148]

Interaction Parameter Calculations

We would like to note here that the solvent and non-solvent interactions analyzed throughout this paper provide a simplified view of the PIN process. However, upon immersing the polymer/drug solution to a non-solvent there is a complex web of interactions that are anticipated

to have an impact on the resulting product. A complete understanding of this process would require consideration of not only solvent/non-solvent interactions, but also polymer/solvent, polymer/non-solvent, drug/solvent, drug/non-solvent, and polymer/drug interactions. For the bulk of this analysis, we assume the ΔG_{Mix} between these components to be negligible. This assumption is justified in part by the utilization of dilute polymer/drug solutions, which reduced their contribution to the total ΔG_{Mix}.

However, in some instances we consider the affinity of the polymer to the solvent using the Flory Huggins interaction parameter – dimensionless parameter X_{12}. Which can be approximated based on the Hildebrand solubility parameter:

$$X_{12} \approx \frac{v_1}{RT}(\delta_2 - \delta_2)^2$$

Where v_1 is the molar volume of the solvent and δ_1 and δ_2 are the solubility parameters of solvent and polymer respectively. The Flory Huggins interaction parameter accounts for the energies between polymer-polymer, polymer-solvent, and solvent-solvent. This equation is not regarded as being accurate for quantitative measurements, but rather serves as a qualitative guide when considering polymer solubility. The general notation is such that low X_{12} values indicate good solubility.

In-Vitro Release Studies

In-vitro drug release profiles were assessed by placing approximately 20mg of each nanoparticle formulation into a 1.5mL eppendorf tube containing phosphate buffer saline (PBS). At varying times points, the particles were spun down in a microcentrifuge at 8000 rpm for 10 minutes and the supernatant was collected for HPLC analysis. The particles were then resuspended in fresh PBS by brief vortex and sonication. Samples obtained from the release study were

analyzed against a standard curve by reverse phase chromatography (using a Phenomenex, Aeris 3.6µm Widepore XB-C18 column). A Waters 600 controller was used to maintain a flow rate of 0.5 mL/min of an acetonitrile and water mobile phase gradient containing 0.1% formic acid. A UV detection wavelength of 215nm was used to obtain the chromatograms.

RESULTS AND DISCUSSION

GLP-1 RA Micronization and Stability

Micronized Drug Particle Size

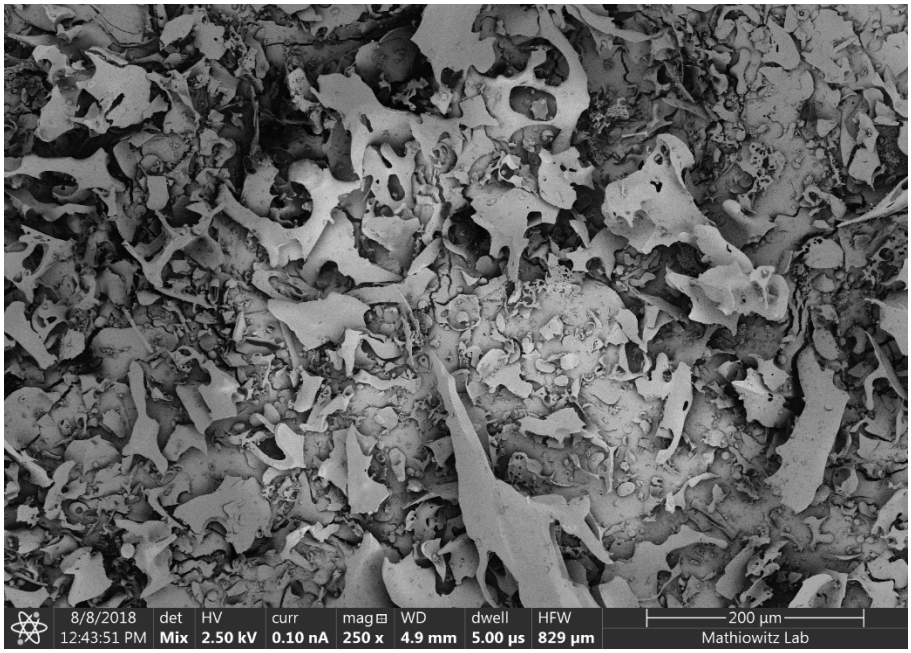

FIGURE 1. SEM IMAGE OF THE GLP-1 RA PEPTIDE AS RECEIVED FROM SANOFI S.A.

Depicted in Figure 1 is an SEM image of the GLP-1 RA peptide as it was received from Sanofi. Based on the SEM image, the peptide appeared to have arrived in the form of a lyophilized white powder, with large aggregates and sheets on the order of 50-200 µm. The first milestone set for this work was to achieve bioactive micronization of the GLP-1 RA peptide. Achieving sufficiently small micronization is a key aspect of the PIN process and is necessary for the

successful encapsulation and the subsequent long acting controlled release of the drug from phase inverted PLGA nanoparticles. When sufficiently small, the solid micronized GLP-1 RA particles are expected to act as a core nucleus in which the polymer in solution will precipitate around during the PIN process.

TABLE 4 GLP-1 RA MICRONIZATION TRIAL CONDITIONS WITH THE CORRESPONDING GIBBS ENERGY OF MIXING BETWEEN THE SOLVENT/NON-SOLVENT AND RESULTING MICRONIZED DRUG PARTICLE SIZE

Drug	Concentration	Solvent	Non-Solvent	Average Size (nm)	$\Delta G_{Mix}/RT$
GLP-1 RA peptide	20 mg/mL	Water	TBA	1304	-0.333
		Methanol	TBA	418	-0.658
			2-Propanol	324	-0.97
			Acetonitrile	302	-0.729
			Acetone	537	-0.443
			Dichloromethane	460	-0.506
			Chloroform	414	-0.553
			Ethyl Acetate	404	-0.486
			THF	381	-----

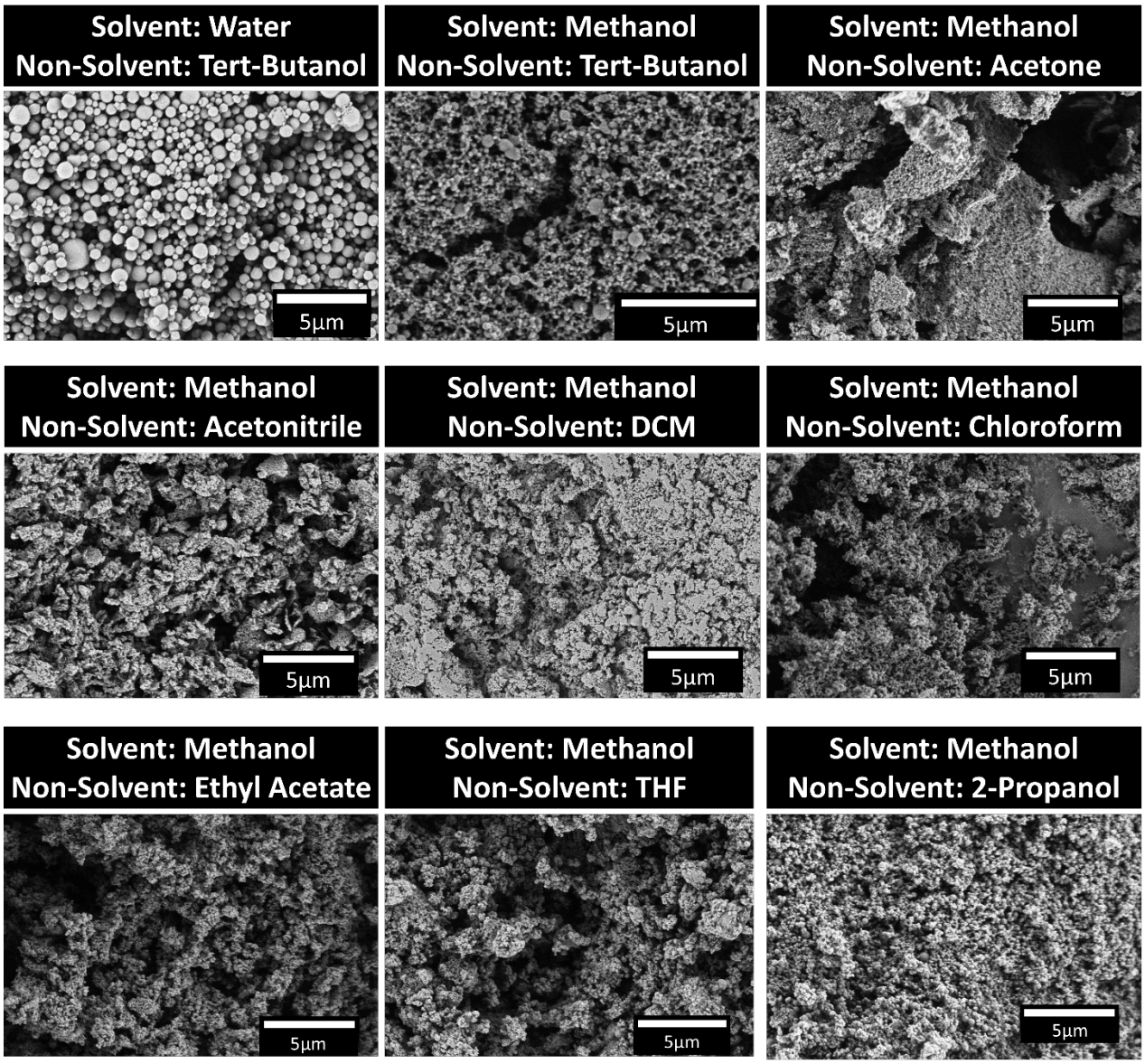

FIGURE 2. SEM COLLAGE OF MICRONIZED GLP-1 RA PRODUCED FROM PHASE INVERSION WITH VARYING SOLVENT AND NON-SOLVENTS.

Micronization trials of the GLP-1 RA were conducted under the conditions described in Table 2 and the resulting particle diameter was reported using a Malvern Zetasizer. In addition, corresponding SEM images of each GLP-1 RA micronization can be seen in the collage presented in Figure 2. Briefly, the GLP-1 RA was solubilized in either water or methanol at a concentration of 20 mg/mL and then precipitated into one of eight different non-solvents to produce a micronized particle (non-solvents: tert-butanol, 2-propanol, dichloromethane, chloroform, ethyl acetate, tetrahydrofuran, acetone, and acetonitrile). From the SEM images, it can be seen that each micronization process resulted in the formation of discrete spherical nanoparticles. Particle size analysis indicated that the particles produced with methanol as a solvent had an average particle diameter between 302-537nm, while the particles produced with water as the solvent were substantially larger with an average diameter of 1304 nm (Table 2).

The primary objective of these micronization trials was to understand the effect of varying solvent and non-solvent pairs on the formation of drug particles upon phase inversion. The solvents and non-solvents used for the micronization of the GLP-1 RA were miscible in all proportions. When two miscible fluids come into contact, there is an initial sharp interface in which diffusion of one liquid into the other occurs. Over time the fluids eventually mix creating a homogenous solution. Upon mixing, the precipitation of micronized drug particles is thought to occur in three general steps: supersaturation, nucleation, and growth.[46] Supersaturation occurs when the solution contains more dissolved solute than is thermodynamically stable. Thus, to gain thermodynamic stability, the solute begins to precipitate by nucleation and growth. Based on this mechanism, the rate at which the solvent and non-solvent mix is hypothesized to have some effect on the degree of supersaturation, nucleation, and growth of particles in the phase inversion process. For example, if the diffusion of solvent to nonsolvent is ‘fast’ then a high degree of supersaturation is expected,

resulting in more nucleation centers, less growth, and the formation of smaller nanoparticles. On the other hand, if the diffusion of solvent to nonsolvent is 'slow' then the GLP-1 RA peptide is expected to reach a lower degree of supersaturation, allowing for less nucleation and larger particles to form. Thus, here we seek to explore this hypothesis and gain insight into the relationship between solvent and nonsolvent mixing and the formation of nanoparticles upon phase inversion.

However, while diffusion of solid particles in liquid is a widely understood topic, there are relatively few data sets that describe the diffusion between two completely miscible liquids. This is in part due to the tedious, difficult, and expensive nature of this type of analysis.[149] As a result, many molecular theories have been developed to describe and model the complicated processes involved in miscible liquid-liquid mixing.[145] In this paper, we adopt the semi-empirical UNIFAC method for modeling non-ideal liquid mixtures as a means of describing the interactions between the solvents and non-solvents used for particle formation. Specifically, the UNIFAC interaction parameters were used to calculate the Gibbs energy of mixing (ΔG_{Mix}) for each solvent and non-solvent pair. The reason we use ΔG_{Mix} in this work is because we assume that it correlates to the rate at which the solvent diffuses into the nonsolvent. The conventional notation is such that a negative ΔG_{Mix} indicates favorable diffusion between the solvent and non-solvent. Accordingly, if ΔG_{Mix} is positive, the solvent and non-solvent will phase separate and a homogenous mixture will not spontaneously form. Thus, a comparative analysis of particle size and Gibbs energy of mixing was conducted (Figure 3).

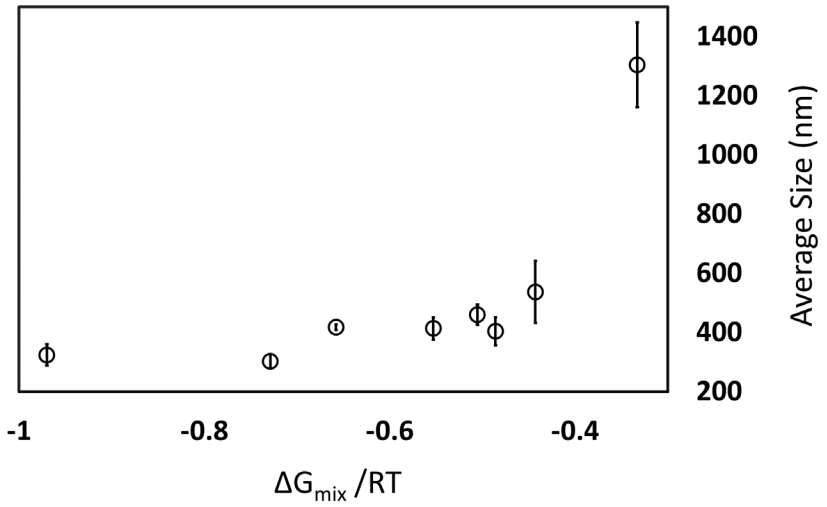

FIGURE 3. RELATIONSHIP BETWEEN GLP-1 RA MICRONIZATION HYDRODYNAMIC DIAMETER SIZE (Y-AXIS) AND THE GIBBS ENERGY OF MIXING BETWEEN SOLVENTS IN THE MICRONIZATION PROCESS (X-AXIS)

The Gibbs energy of mixing calculated by the UNIFAC method can be found in Table 2 for all solvent and non-solvent pairs used in the micronization process. Figure 3 demonstrates the relationship between ΔG_{Mix} and the resulting GLP-1 RA particle size. Generally, it can be seen that the largest particles (average diameter = 1304 nm) were formed from water and tert-butanol mixing, which also had the least negative ΔG_{Mix} ($\Delta G_{Mix}/RT$ = -0.333). However, it is interesting to note that all other solvent and non-solvents with increasingly negative ΔG_{Mix} (those produced from methanol as a solvent with $\Delta G_{Mix}/RT$ between -0.443 and -0.970) did not show a significant correlation with size (average diameters between 302 nm and 537 nm). This suggests that the particles formed may have reached a minimum critical size which is stable against dissolution.

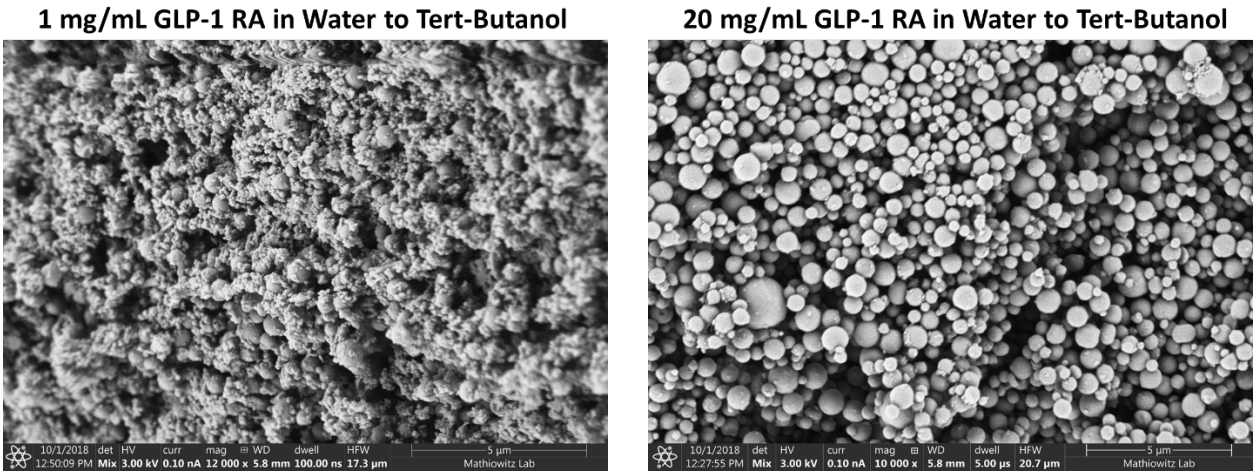

FIGURE 4. THE EFFECT OF VARYING GLP-1 RA CONCENTRATION ON MICRONIZATION PARTICLE SIZE

It has previously been shown that concentration of the solute in solvent is also a predominate factor in the resulting size of the precipitated nanoparticles.[45] This phenomenon is again demonstrated here in Figure 4 with the GLP-1 RA peptide precipitated from water to tert-butanol. In each instance of Figure 4, the GLP-1 RA was solubilized in water at either a concentration of 1 mg/mL (left) or 20 mg/mL (right). The peptide was then precipitated by immersing the soluble solution to a non-solvent (tert-butanol) with a solvent to non-solvent ratio of 1 mL:60 mL. It can be seen in Figure 4 that lower concentrations of drug in the solvent (1 mg/mL compared to 20 mg/mL) yield smaller particles upon phase inversion. Upon nucleation, particles are thought to grow as a result of condensation, in which the addition of single molecules collect on the nucleation surface to form a particle. It appears that the ability for this growth to occur is directly related to the concentration of drug in proximity to the primary nuclei. To this end, the trend seen in Figure 3 may also indicate that particles converge on a minimum size based on the constant 20 mg/mL concentration used, regardless of the ΔG_{Mix} between the solvent and non-solvent.

GLP-1 RA Stability Upon Micronization

In this section we provide some preliminary evidence to assess the feasibility of the GLP-1 RA peptide to retain its native bioactive structure upon micronization. However, it should be noted that a comprehensive analysis of the GLP-1 RA bioactivity was beyond the scope of this work.

Peptide and protein instability associated with process, storage, and delivery remains a major challenge in the formulation of biologic therapeutics. The GLP-1 RA peptide has a well-defined and unique folded state, in which the tertiary structure attributes to the native bioactive form.[150] Typically, the unfolding of this state is considered to denature the peptide and result in the loss of therapeutic bioactivity.[151] To this end, the use of organic solvents (such as those used for drug micronization in Table 1) have conventionally been thought to denature peptides from their native bioactive state. [44,152] However, this notion that organic solvents denature tertiary structure stems from examining aqueous-organic mixtures, not pure anhydrous organic solvents.[44] Studies over the past 15 year have established that many proteins can retain their native tertiary state in organic solvents, under the condition that they are anhydrous with little or no water content present.[44,153–159] To this end, in this section we explore the feasibility of retaining the native GLP-1 RA state upon micronization with organic solvents as described in the previous section.

Secondary Structure Analysis by FTIR

FTIR spectroscopy was used to provide evidence towards the GLP-1 RA conformation and stability upon micronization with various organic solvents. The Amide I band has been shown to be sensitive to protein secondary structure, with shifts in the frequency indicating structural change. In addition, due to the unique hydrogen bonding environments of the coil, α-helix, β-sheet, and amorphous secondary structures, the corresponding contributions can be approximated by

peak deconvolution.[160,161] Figure 5 depicts the full FTIR spectrograph of the GLP-1 RA as it was received from Sanofi. A peak deconvolution was performed on the Amide I band of the as-received GLP-1 RA FTIR spectrograph to achieve a curve fitting correlation of $R^2 > 0.99$. The deconvolution assignments of coils, α-helix, β-sheet, and amorphous secondary structures were based on those presented by Jackson et al.[161] The peak deconvolution obtained from the as-received GLP-1 RA FTIR was then applied to the Amide I FTIR spectra of each micronized GLP-1 RA that were subjected to organic solvent environments (depicted in Figure 6). Using an identical deconvolution profile, no significant shifts or changes in secondary structure conformation could be detected in the micronized drug, with each curve fitting correlation demonstrating an R^2 value greater than 0.99.

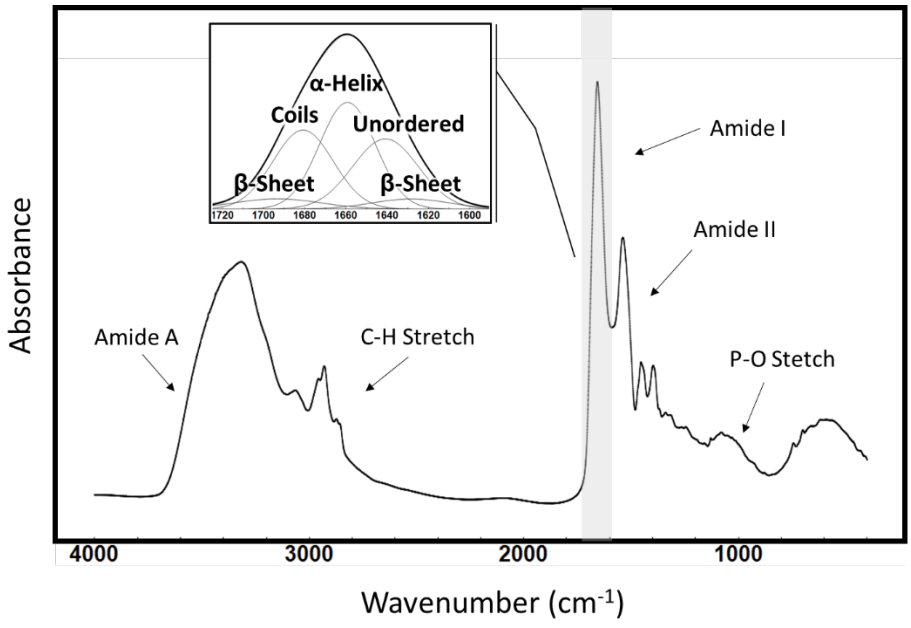

FIGURE 5. FTIR SPECTRUM OF THE GLP-1 RA PEPTIDE WITH LABELED AMIDE, C-H AND P-O BOND EXCITEMENTS. THE EXPANDED VIEW ILLUSTRATES THE DECONVOLUTION OF THE AMIDE I BASED ON SECONDARY STRUCTURE COMPONENTS.[160]

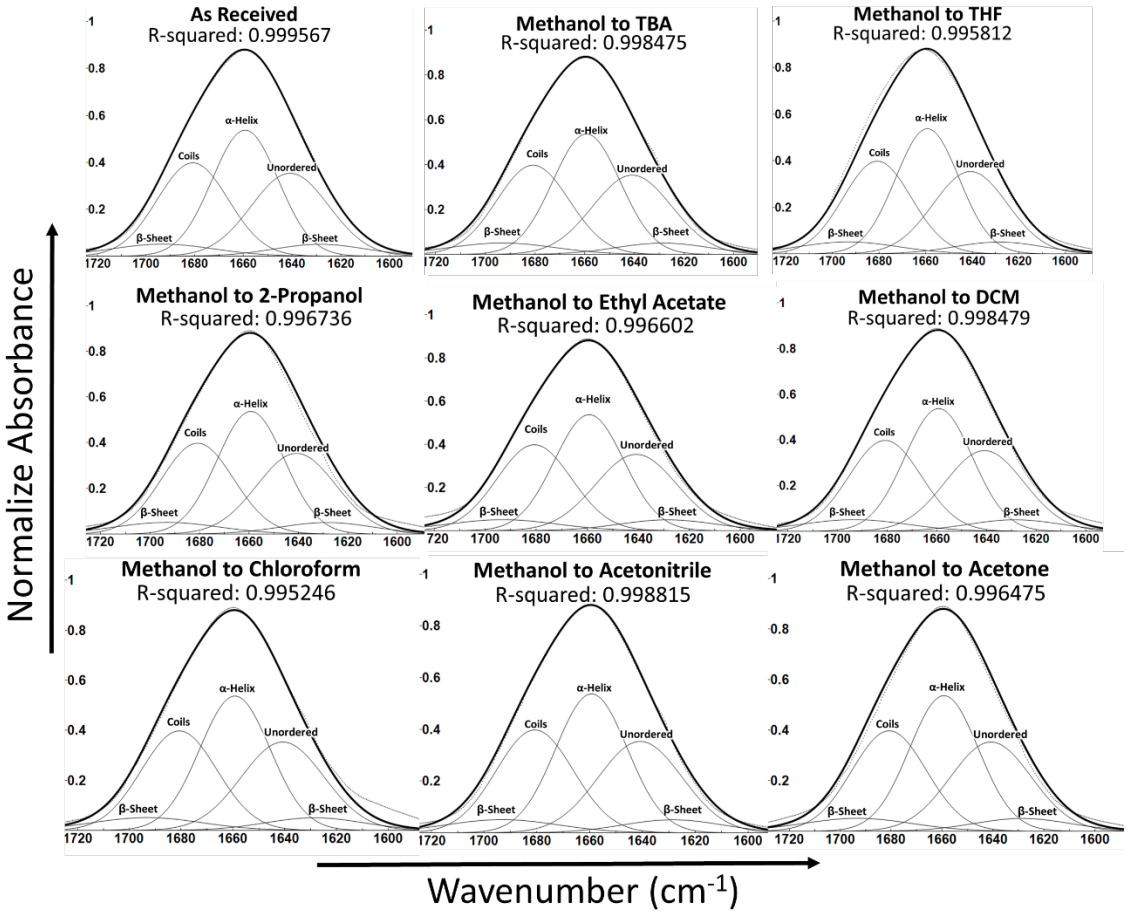

FIGURE 6. PEAK DECONVOLUTION COMPARISON OF THE FTIR SPECTRUM AMIDE I BAND OBSERVED FOR MICRONIZED GLP-1 RA PRODUCED FROM DIFFERING ORGANIC SOLVENTS

Size and Hydrophobicity Characterization by Reverse Phase HPLC

HPLC was used to compare the conformation of the micronized GLP-1 RA peptide to the drug as it was received from Sanofi, in order to give further insight to the stability of the peptide during the micronization process. Upon denaturation by organic solvent, peptide residues that are typically buried in the core of the folded native structure are thought to become exposed via unfolding and interact with the external solvent. As a result of this unfolding, denaturation

typically results in the peptide occupying a larger volume compared to the compact native state. In addition, denaturation is also expected to change the hydrophilic/hydrophobic nature of the peptide, as hydrophobic residues that were once buried become exposed to the solvent.[152] The HPLC method here utilized a reverse phase Phenomenex, Aeris 3.6µm Widepore XB-C18 (100 x 2.1 mm) column, which contained a hydrophobic stationary phase and allowed for peptide separation based on size and charge.

TABLE 5 REVERSE PHASE HPLC RETENTION TIMES OF GLP-1 RA MICRONIZED FROM VARIOUS SOLVENT AND NON-SOLVENT COMBINATIONS

Solvent	Nonsolvent	Retention Time
As Received		5.354
Methanol Only		5.316
Methanol	Tert-Butanol	5.331
	Dichloromethane	5.335
	Chloroform	5.396
	Ethyl Acetate	5.399
	Tetrahydrofuran	5.341
	Acetone	5.446
	Acetonitrile	5.303
	2-Propanol	5.311
Water	Tert-Butanol	5.331

HPLC chromatograms of eluted GLP-1 RA can be seen in Figure 1S of the supplemental materials. In addition, the retention time of each micronization is presented in Table 3. It can be seen in Table 3 that the as received GLP-1 RA peptide had a retention time of 5.354 min, while the micronizations with various solvent exposure had retention times ranging from 5.303 min to 5.446 min. The similarity of the retention times between the as received and micronized GLP-1

RA provides evidence towards the feasibility of the drug to retain the native state upon micronization, with no significant change in hydrophobicity or size.

However, while retention time was predominantly similar between the samples, it can be seen in Figure 1S that some micronizations showed the formation of a small secondary peak around a 6 min retention time. This secondary peak is seen most significantly in the micronizations with ethyl acetate, tetrahydrofuran, and acetone as the non-solvent. The formation of this peak indicates that some of the drug has undergone a conformational change with a variation in hydrophobicity or size compared to the native as received GLP-1 RA. As the retention time is longer (≈ 6 min) compared to the native state (≈ 5.3 min) this suggests the conformational change is more hydrophobic with a greater interaction to the hydrophobic stationary phase of the reverse phase HPLC column. When looking at the chemical structure of the organic solvents used in this experiment, ethyl acetate, tetrahydrofuran, and acetone are all aprotic solvents and contain highly electronegative oxygen species which can act as hydrogen bond 'acceptors'. Thus it is possible that these organic solvents may disrupt the intra-molecular bonds that stabilize the GLP-1 RA tertiary structure, resulting in buried hydrophobic residues being exposed to the surface.

To this end, future studies should account for this insight into the native and denatured state of the GLP-1 RA upon micronization. However, while some micronizations appeared to alter the native conformation in a portion of the GLP-1 RA, the majority of the drug appears to maintain the same size and hydrophobicity across all samples, warranting further study.

In-Vivo Bioactivity

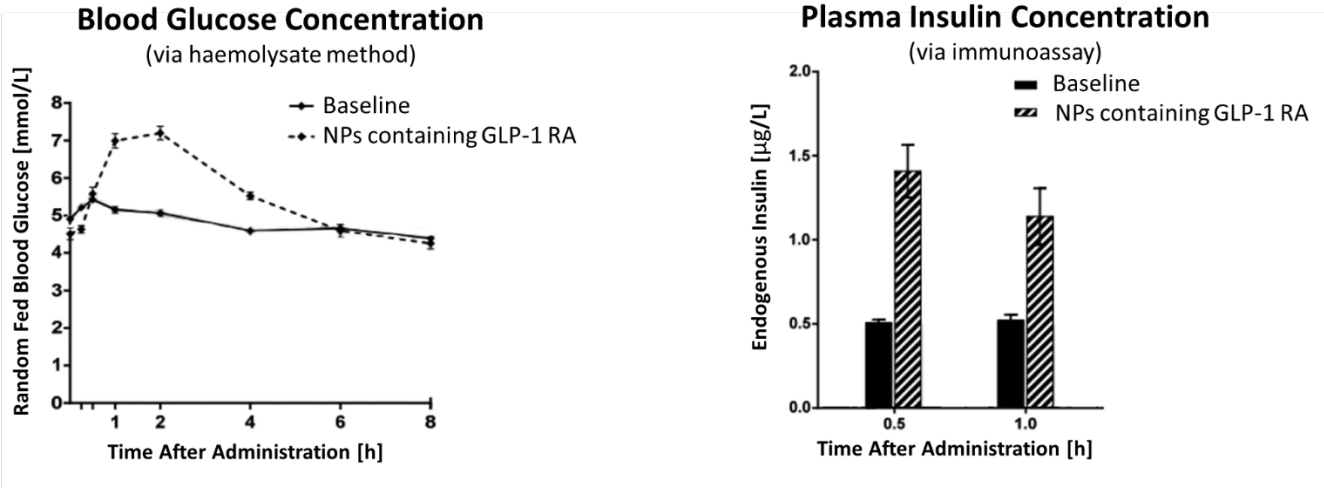

FIGURE 7 IN-VIVO GLP-1RA BIOACTIVITY AFTER ENCAPSULATION AND RELEASE FROM PLGA NANOPARTICLES. LEFT: BLOOD GLUCOSE CONCENTRATION OVER 8 HOURS. RIGHT: PLASMA INSULIN CONCENTRATION AT 0.5 AND 1 HOURS AFTER ADMINISTRATION.

Nanoparticles containing micronized GLP-1 RA (produced from solvent: water and non-solvent: tert-butanol) were subcutaneously administered to Wistar rats and serial blood samples were then drawn for blood glucose and insulin analysis. In the treatment of type 2 diabetes, GLP-1 RA is required for the production of insulin. In turn, insulin aids in preventing hyperglycemia by transporting glucose from the bloodstream into cells.[150] As expected, in rats administered with subcutaneous dosages of PLGA nanoparticles containing micronized GLP-1 RA, the blood glucose and plasma insulin concentrations were increased significantly as compared to baseline values. Noting that in rats there is a paradoxical impact on blood glucose due to activation of the sympathetic nervous system.[162]

While this analysis is not comprehensive of all micronized formulations, this in-vivo glucose and insulin response provides evidence towards the feasibility that the micronized GLP-1 RA remains in the native active state and again warrants future study

PLGA Nanoparticle Formation by Phase Inversion

TABLE 6 CONDITIONS USE TO PRODUCE PLGA NANOPARTICLES WITH CORRESPONDING GIBBS ENERGY OF MIXING BETWEEN EACH SOLVENT PAIR AND THE RESULTING AVERAGE SIZE OF THE NANOPARTICLES FORMED

Polymer	Concentration	Solvent	Non-Solvent	Average Size (nm)	$\Delta G_{Mix}/RT$
Resomer® RG 752 H, PLGA (75:25) 4-15 kDa	100 mg/mL	Dichloromethane	Tert-Butanol	386.87	-0.929
			2-Propanol	282.93	-1.161
			Ethanol	367.1	-0.71
			Heptane	260.17	-1.293
		Chloroform	Tert-Butanol	467.47	-0.666
			2-Propanol	259.3	-1.164
			Ethanol	430.1	-0.62
			Heptane	320.6	-0.63
		Ethyl Acetate	Tert-Butanol	372.17	-0.661
			2-Propanol	699.87	-0.297
			Ethanol	478.97	-0.565
			Heptane	373.43	-0.593
		Acetone	Tert-Butanol	477.8	-0.441
			2-Propanol	405.03	-0.627
			Ethanol	445	-0.464
			Heptane	638.53	-0.205
			Water	5201.67	-0.128
		Acetonitrile	Tert-Butanol	409.57	-0.539
			2-Propanol	353.7	-0.712
			Ethanol	370.8	-0.701
			Water	355.5	-0.473

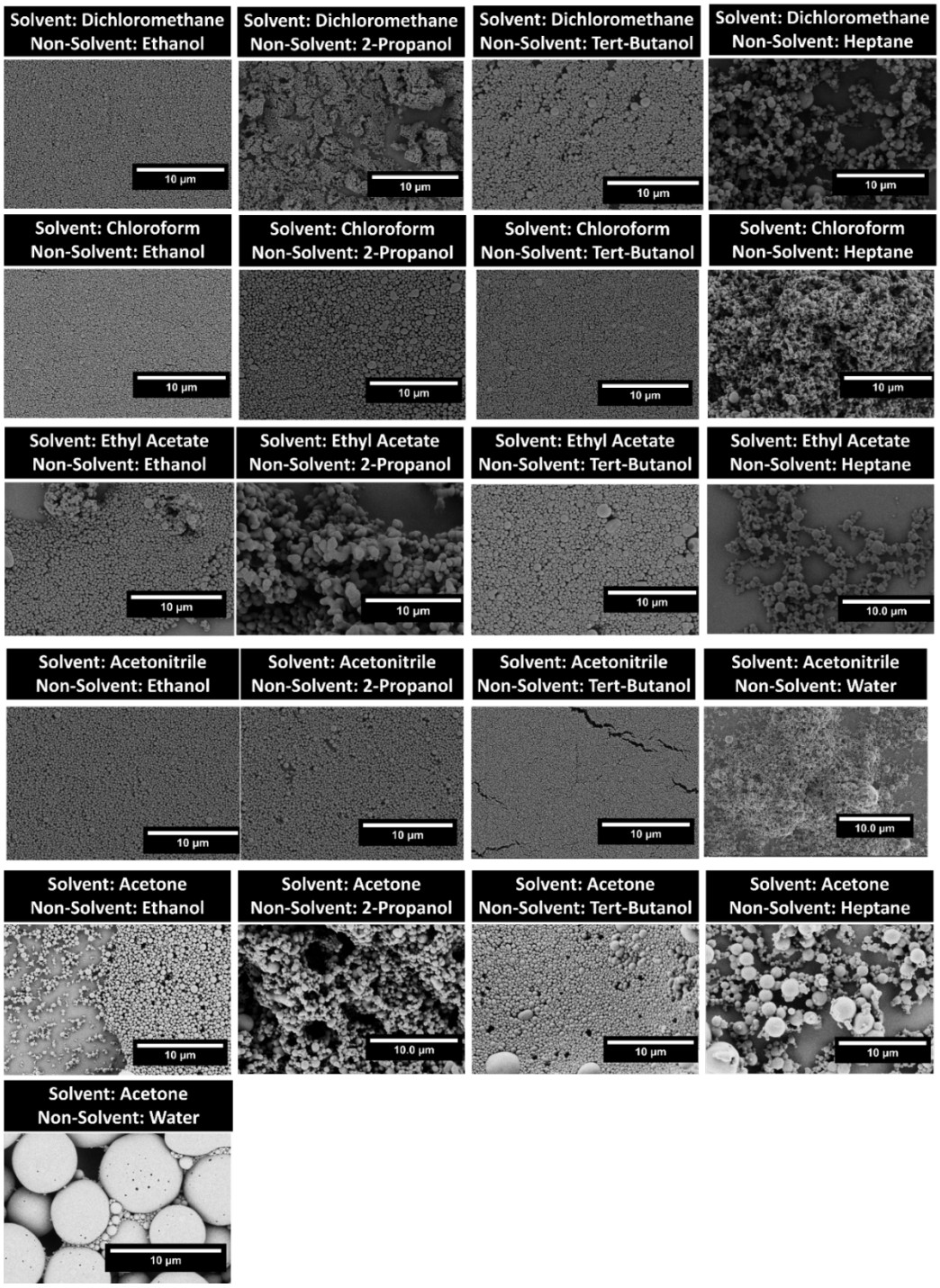

FIGURE 8. SEM COLLAGE OF PLGA NANOPARTICLES PRODUCED FROM PHASE INVERSION WITH VARYING SOLVENT AND NON-SOLVENTS.

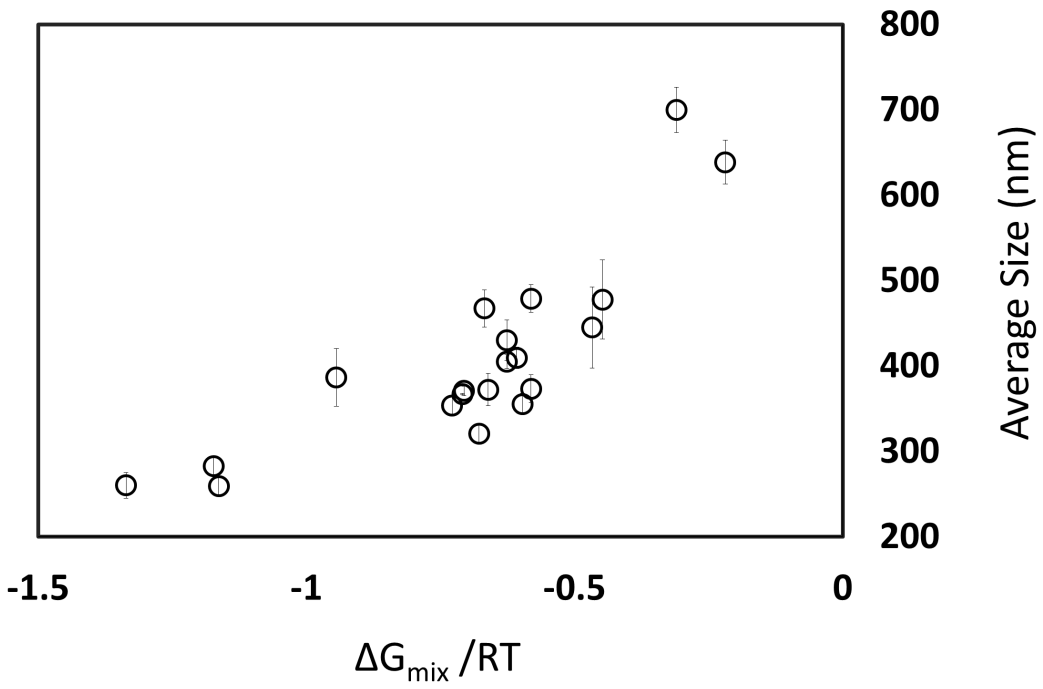

FIGURE 9. RELATIONSHIP BETWEEN PLGA NANOPARTICLE HYDRODYNAMIC DIAMETER SIZE (Y-AXIS) AND THE GIBBS ENERGY OF MIXING BETWEEN SOLVENTS IN THE PHASE INVERSION PROCESS (X-AXIS)

In an effort to better our understanding of the phase inversion precipitation process, this section explores the impact of solvent and non-solvent on the formation of pure PLGA nanoparticles by phase inversion (i.e. blank nanoparticles, not containing drug). In this study we focused on 4-15kDa PLGA (75:25). PLGA particles were produced by phase inversion under the conditions described in Table 4 and the resulting particle diameter was reported using a Malvern Zetasizer. In addition, corresponding SEM images of each PLGA nanoparticle production can be seen in the collage presented in Figure 7. From the SEM images, it can be seen that each precipitation process resulted in the formation of discrete particles.

Similar to the previous section, in which the correlation between ΔG_{Mix} of the solvents and resulting GLP-1 RA particle size was assessed, Figure 8 here shows the correlation of ΔG_{Mix} to the resulting PLGA nanoparticle size. Again, here we assume that ΔG_{Mix} is indicative to the rate

at which the solvent and non-solvent mix to create a homogenous solution. Thus, impacting the degree of supersaturation, nucleation, and growth of the PLGA nanoparticles upon phase inversion. It can be seen in Figure 8 that there is a general correlation between ΔG_{Mix} and PLGA nanoparticle size, with the least negative ΔG_{Mix} resulting in larger particles than those with the most negative ΔG_{Mix}. This correlation further confirms the impact of ΔG_{Mix} that was observed in in the previous section and suggests that Gibbs energy of mixing between solvent and non-solvent may be a useful indicator for predicting phase inverted nanoparticle size.

GLP-1 RA Encapsulation and In-Vitro Release from PLGA Nanoparticles

TABLE 7 GLP-1 RA LOADED PLGA NANOPARTICLES FORMULATIONS PRODUCED FOR IN-VITRO STUDIES ALONG WITH THE VARIOUS SOLVENTS AND NON-SOLVENTS USED TO PRODUCE THEM

PLGA type	GLP-1 RA	Concentration	PLGA Solvent /	PLGA and
2.3 kDa PLGA (50:50) Evonik	5 % (w/w)	100 mg/mL	Dichlormethane	2-Propanol Heptane
			Chloroform	2-Propanol Heptane
			Ethyl Acetate	2-Propanol Heptane
			Tetrahydrofuran	2-Propanol Heptane
			Acetone	2-Propanol Heptane
			Acetonitrile	2-Propanol
7-17 kDa PLGA (50:50), Resomer 502H	5 % (w/w)	100 mg/mL	Dichlormethane	2-Propanol Heptane
			Chloroform	2-Propanol Heptane
			Ethyl Acetate	2-Propanol Heptane
			Tetrahydrofuran	2-Propanol Heptane
			Acetone	2-Propanol Heptane
			Acetonitrile	2-Propanol
4-15 kDa PLGA (75:25), Resomer 752H	5 % (w/w)	100 mg/mL	Dichlormethane	2-Propanol Heptane
			Chloroform	2-Propanol Heptane
			Ethyl Acetate	2-Propanol Heptane
			Tetrahydrofuran	2-Propanol Heptane
			Acetone	2-Propanol Heptane
			Acetonitrile	2-Propanol

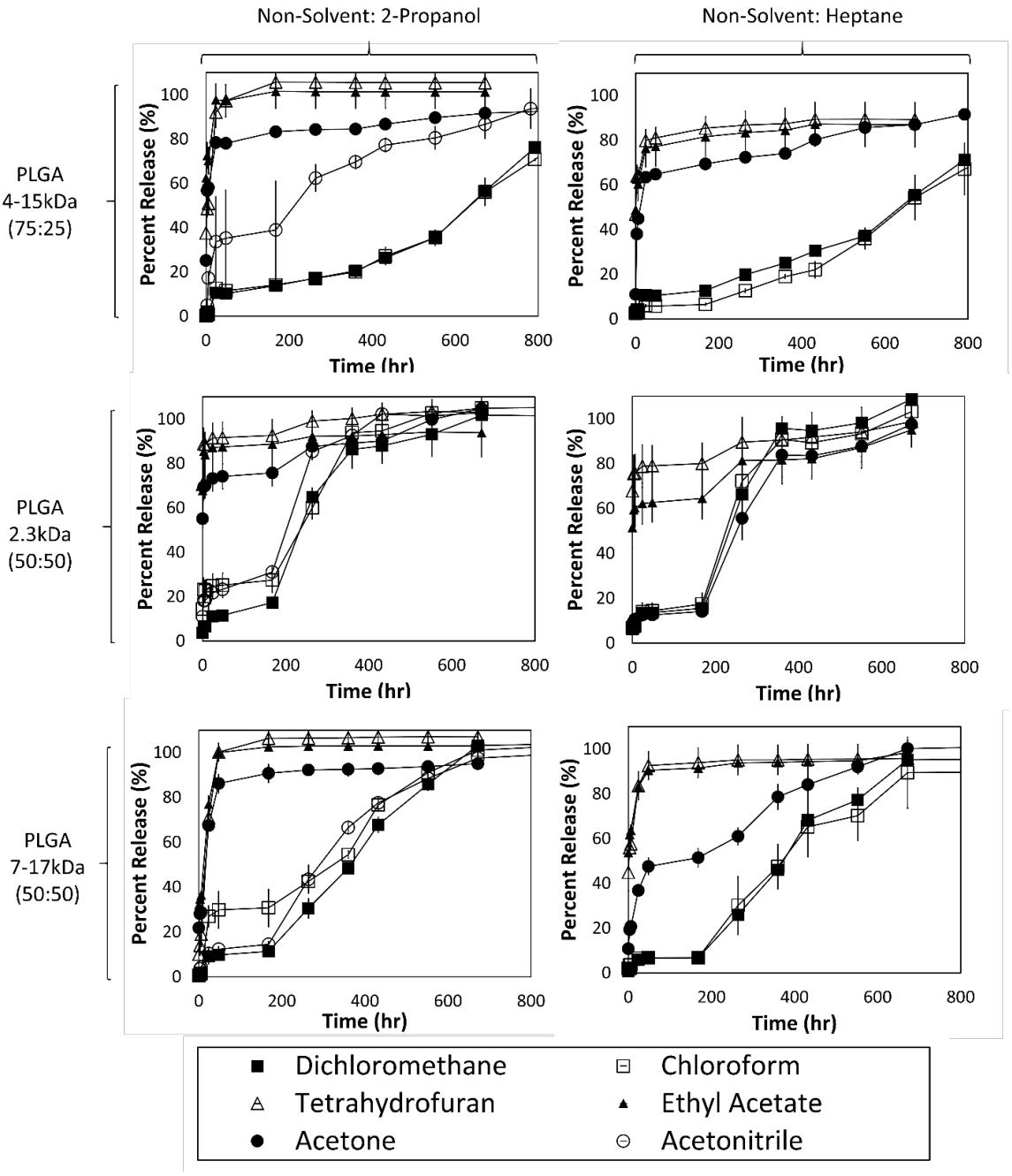

FIGURE 10. GLP-1 RA RELEASE CURVES FROM ALL NANOPARTICLE FORMULATIONS PRODUCED. EACH ROW PRESENTS A DIFFERENT TYPE OF PLGA USED: PLGA (75:25) 4-15 KDA (TOP), PLGA (50:50) 2.3 KDA (MIDDLE), AND PLGA (50:50) 7-17KDA (BOTTOM). EACH COLUMN PRESENTS A DIFFERENT PLGA/GLP-1 RA NON-SOLVENT USED: 2-PROPANOL (LEFT) AND HEPTANE (RIGHT). WITHIN EACH INDIVIDUAL GRAPH, THE CORRESPONDING CURVES REPRESENT FORMULATIONS PRODUCED WITH DIFFERENT PLGA SOLVENTS / GLP-1 RA NON-SOLVENTS (I.E. DICHLOROMETHANE, CHLOROFORM, TETRAHYDROFURAN, ETHYL ACETATE, ACETONE, AND ACETONITRILE).

In this section, we explore the effect of solvent/non-solvent choice in the PIN process on the resulting encapsulation and release of GLP-1 RA from PLGA nanoparticles. Table 5 displays all 33 nanoparticle formulations that were produced for the in-vitro release experiments. In this study, we used a fixed drug loading of 5% (w/w) GLP-1 RA in all nanoparticle formulations. The variables assed between formulations were (1) PLGA molecular weight and monomer ratio, (2) polymer solvent / drug non-solvent type, and (3) non-solvent type for both the polymer and drug in the encapsulation process.

To elaborate, three different types of PLGA were assessed in this study (2.3 kDa PLGA (50:50), 4-15kDa PLGA (50:50), and 7-17kDa PLGA (75:25)). These polymers were chosen to give insight into the impact of varying molecular weight and monomer ratio on the final product and to determine the robustness of the formulation between these variations. Several polymer solvent / drug non-solvent types were analyzed (dichloromethane, choloroform, acetonitrile, acetone, ethyl acetate, and tetrahydrofuran). It is important to note that the term "polymer solvent / drug non-solvent" refers to the process in which the GLP-1 RA is first micronized by precipitating into one of the above organic solvents. Upon precipitation, the PLGA polymer is then added to the suspension. In these instances the GLP-1 RA is not soluble but the PLGA is soluble. Thus we denote these organic solvents as "polymer solvent / drug non-solvent". The variations in these organic solvents were chosen to represent a full spectrum of polar/nonpolar and protic/aprotic solvents that are compatible with the PIN process. Finally, two types of non-solvent were assessed (heptane and 2-propanol). The term "non-solvent" here refers to the non-solvent for both the GLP-1 RA and the PLGA. Upon addition of the drug-polymer solution to the non-solvent, the polymer is precipitated to create the final formulation of encapsulated GLP-1 RA nanoparticles. Here we

explore heptane as a representative non-polar solvent and 2-propanol as a representative polar solvent.

In-vitro drug release experiments were conducted in a PBS medium and HPLC was used to quantify the release over time. The *in-vitro* drug release profiles for each formulation in Table 5 can be found in Figure 9. Briefly, Figure 9 is organized such that each individual graph displays the various release profiles obtained using different polymer solvents/drug non-solvents, with the graphs in the left column displaying the release profiles of particles precipitated into 2-propanol and the graphs in the right column displaying the release profiles of particles precipitated into heptane. Finally, each row of Figure 9 represents the particles formed from either PLGA (75:25) 4-15 kDa, PLGA (50:50) 7-17 kDa, or PLGA (50:50) 2.3 kDa.

The aim of this section was to determine the impact of solvent and non-solvent on the encapsulation and in-vitro release profile of GLP-1 RA from phase inverted PLGA nanoparticles. The running hypothesis here was that the solvent and non-solvent used in phase inversion may have an impact on the affinity for the polymer to encapsulate the peptide. In the PIN process, nanoparticles spontaneously precipitate after the addition of a solubilized polymer solution to a non-solvent. Upon precipitation, the presence of micronized GLP-1 RA particles are expected to act as a core nucleus in which the polymer in solution will precipitate around.

Evidence from the previous sections suggest that solvent choice can alter the size and morphology of particle formation by phase inversion. The proposed mechanism to explain these deviations between solvents is thought to arise from the degree of supersaturation that is achieved based on the ΔG_{Mix} of the solvent and non-solvent pairs. To this end, we seek to gain insight to how this mechanism may extend to the PIN process and the ultimate encapsulation and in-vitro release of the GLP-1 RA from PLGA nanoparticles.

Generally speaking, when analyzing Figure 9, drug release behavior from PLGA nanoparticles can be divided into four categories: burst release, diffusion release, lag time, and degradation release. The initial burst release refers to the poorly encapsulated drug on the surface of the nanoparticles, which is immediately released upon suspension of the particles. This burst is typically undesirable as it may result in a loss of drug content or toxic high dosages. Following the initial burst, large macromolecule drugs may diffuse from the polymer particle through a network of pores. While large molecules such as peptides and proteins may not directly diffuse through the polymer matrix, they may release through pores left behind by the surface encapsulated drug from the initial burst. Deeper encapsulated drug is thought to diffuse through the free volume of empty pores left behind by drug released closer to the surface, essentially diffusing though a network of pores. In the absence of this network of pores, large molecule drugs may remain encapsulated by the polymer and result in a lag time. The lag time refers to a period in which no drug release occurs, between the initial burst/diffusion and the onset of polymer degradation. In the case of PLGA, the polymer eventually begins to degrade by hydrolysis. Upon degradation a second phase of drug release may occur, in which the previously encapsulated drug is exposed as the polymer chains break down. [33]

Upon analyzing all 33 GLP-1 RA release profiles in Figure 9, several trends emerged and will be broken down and discussed in the following sections.

Variations Between Polymer Solvents / Drug Non-Solvents

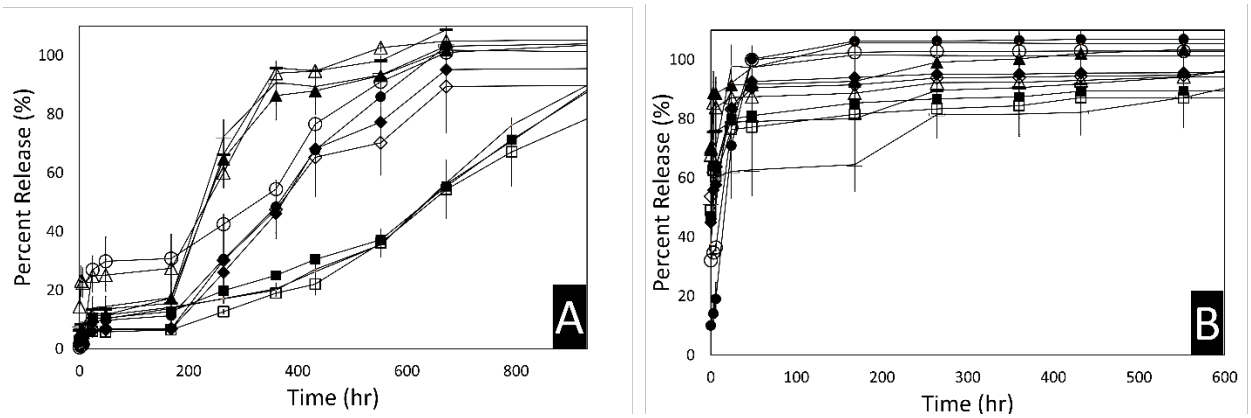

FIGURE 11. GLP-1 RA RELEASE CURVES FROM PLGA NANOPARTICLES PRODUCED WITH A) DICHLOROMETHANE AND CHLOROFORM OR B) ETHYL ACETATE AND TETRAHYDROFURAN

Figure 10a displays all formulations which utilized dichloromethane and chloroform as a drug nonsolvent and polymer solvent in the PIN process. Figure 10b displays all those which utilized ethyl acetate and tetrahydrofuran as a drug nonsolvent and polymer solvent. The release profile behavior of formulations produced with different polymer solvent / drug non-solvents can be generally broken down into two categories: those which release primarily by degradation (Figure 10a) and those which release primarily by burst and diffusion (Figure 10b). It can be seen in Figure 10a that across all three PLGA types and varying non-solvent type (2-propanol or heptane), these formulations consistently showed a low burst release (ranging from 0% to 14%), with the majority of drug releasing after a 200 hour lag time and upon the onset of polymer degradation. While on the other hand, formulations which utilized ethyl acetate and tetrahydrofuran showed higher burst release (ranging from 10% to 68%) with a majority of the drug being released at either the 0 hr time point or by diffusion within the first 6-24 hours.

In an attempt to understand the mechanism underlying the trend seen in Figure 10, we analyzed the release as function of ΔG_{Mix} between the solvents used in PIN and X_{12} (the interaction parameter between the polymer and solvent).

Encapsulation Efficiency and Release Profile as a Function of Solvent/Nonsolvent ΔG_{Mix}

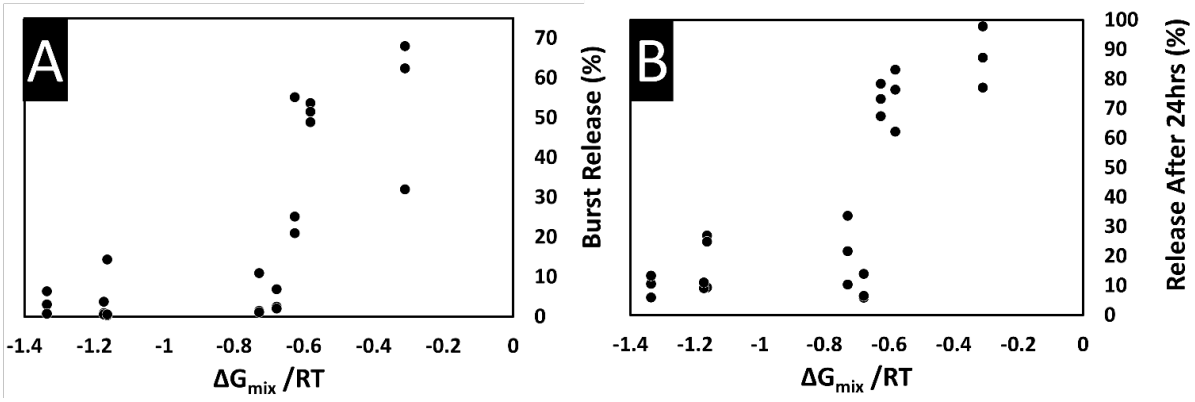

FIGURE 12. RELATIONSHIP BETWEEN GIBBS ENERGY OF MIXING BETWEEN THE SOLVENT AND NON-SOLVENT USED IN THE PIN PROCESS AND A) THE BURST RELEASE OF GLP-1 RA AT THE 0HR TIME POINT OR B) THE DIFFUSION RELEASE OF GLP-1 RA AFTER 24 HOURS

TABLE 8 GIBBS ENERGY OF MIXING BETWEEN THE SOLVENTS AND NON-SOLVENTS USED TO PRODUCE EACH PIN FORMULATION

ΔG_{mix} /RT		
Solvents	**Nonsolvents**	
	2-Propanol	Heptane
Dichloromethane	-1.173	-1.336
Chloroform	-1.163	-0.678
Ethyl Acetate	-0.31	-0.581
Acetone	-0.626	-0.219
Acetonitrile	-0.728	0.145

Figure 11 displays the relationship between GLP-1RA release from the PLGA nanoparticles and the solvent/non-solvent ΔG_{Mix}. Specifically, Figure 11a shows the GLP-1RA burst release at the 0hr time point as a function of the ΔG_{Mix} between the solvent/nonsolvent pair used to produce the particles. Accordingly, Figure 11b shows the GLP-1 RA release at the 24hr time point as a function of the ΔG_{Mix} between solvents used to produce the particles. To aid in this analysis, Table 6 displays the ΔG_{Mix} of each solvent/nonsolvent pair. Note that acetonitrile and heptane have a positive value of ΔG_{Mix} and are therefore not miscible. For this reason particles could not be produce and this formulation was excluded from this study (Table 6). Similarly, while acetone and heptane are miscible, they have low favorability of mixing with the least negative ΔG_{Mix}/RT value (Table 6), as a result particles from these solvents were observed to be substantially larger than the other formulations (see Figure 7). For this reason, the formulations produced from acetone and heptane were also excluded from his analysis.

Generally, it can be seen in Figure 11 that particles produced from solvents/nonsolvent pairs with more negative ΔG_{mix} also tend towards a lower GLP-1 RA burst release (Figure 11a) and lower diffusion within the first 24 hours (Figure 11b). Specifically, by utilizing Table 6 it can be seen that dichloromethane to 2-propanol, dichloromethane to heptane, chloroform to 2-propanol, chloroform to heptane, and acetonitrile to 2-propanol have comparatively low $\Delta G_{mix}/RT$ values ranging from -1.336 to -0.678. Correspondingly, Figure 11 shows these formulations to have minimal burst release (ranging from 0.33% to 14.4%) and 24 hour diffusion (ranging from 5.95% to 33.64%). To this end, it can be seen in the release curves from Figure 9 and 10a that these formulations predominantly retain the GLP-1 RA through a lag period of approximately 200 hours and show the majority of release upon the initiation of polymer degradation.

On the other hand, it can be seen in Table 6 that ethyl acetate and acetone had comparatively high ΔG_{mix} values with the non-solvent. The resulting particles formed from these solvent/nonsolvent pairs tended towards a larger GLP-1 RA burst release and 24 hour diffusion (Figure 11). Specifically, from Table 6 it can be seen that ethyl acetate to 2-propanol, ethyl acetate to heptane, and acetone to 2-propanol have $\Delta G_{mix}/RT$ values ranging from -0.626 to -0.31. Correspondingly, Figure 11 shows that particles formed from the mixing of these solvent/non-solvent pairs release the GLP-1 RA primarily by burst and diffusion, with the burst release ranging from 21% to 68% and the 24 hour release ranging from 62.19% to 97.81%.

Thus, from Figure 11 it appears that there is a correlation between the ΔG_{mix} of the solvent/non-solvent and the resulting particle encapsulation efficiency and mode of release. This correlation may potentially be explained by the supersaturation achieved based on the favorability of solvent/non-solvent mixing. Again, it is assumed that increasingly negative ΔG_{mix} between the solvent and non-solvent used to produce the particles indicates a more favorable and thus faster

rate of mixing. It was seen in the previous sections that increasingly negative ΔG_{mix} between the solvent and non-solvent used to produce drug and polymer particles resulted in smaller nanoparticle size. The reasoning for this was thought to be related to the degree of solute supersaturation induced by the mixing, with faster mixing inducing a higher degree of supersaturation and thus more nucleation and smaller growth of particle size. Here, we may again explain the GLP-1 RA burst release and mode of release as a function of supersaturation achieved by the ΔG_{mix} and the corresponding rate of solvent/non-solvent mixing. Increasingly negative ΔG_{mix} is thought to correspond to an increased rate of mixing between the solvent and nonsolvent in the PIN process. Accordingly, faster rates of mixing are expected to induce a higher state of polymer supersaturation. As the polymer becomes more thermodynamically unstable with increasing supersaturation, the micronized drug in the suspension may become a more favorable center for nucleation and result in better encapsulation.

On the other hand, solvent/non-solvent pairs with less negative ΔG_{mix} are thought to have a slower rate of mixing. Accordingly, slower rates of mixing are expected to induce lowers states of polymer supersaturation. It the previous sections it was shown that polymer and drug phase inversion from solvent/non-solvent pairs with less negative ΔG_{mix} resulted in larger particles sizes. Again, the underlying mechanism was attributed the degree of supersaturation achieved based on the rate of mixing. Less negative ΔG_{mix} results in slower mixing, which in turn results in lower degrees of solute supersaturation. With less supersaturation, the polymer is thought to form fewer nucleation centers and grow larger particles. Similarly, with less supersaturation the polymer may have a lower affinity for the suspended micronized drug as a nucleation center, resulting in less efficient encapsulation.

Encapsulation Efficiency and Release Profile as a function of X_{12}

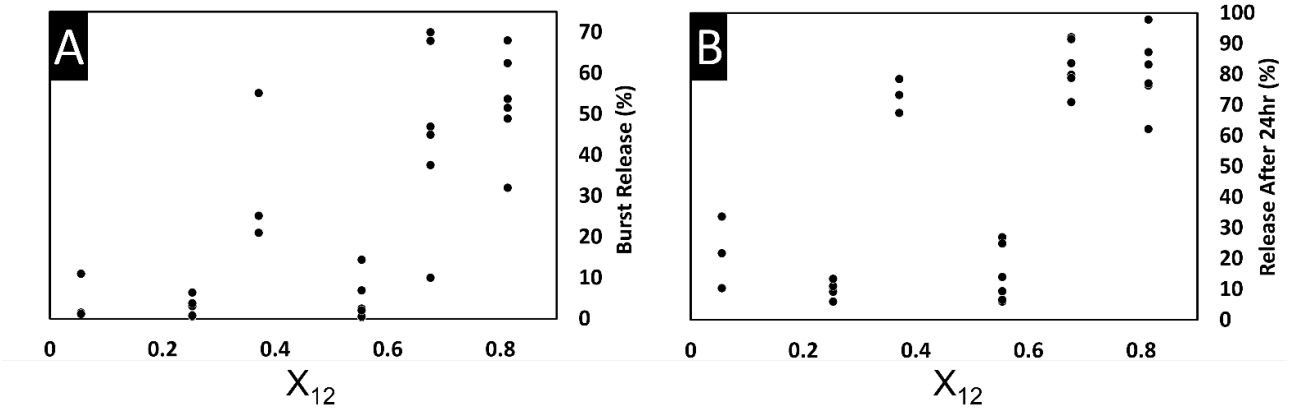

FIGURE 13. RELATIONSHIP BETWEEN THE PLGA AND SOLVENT X_{12} AND THE CORRESPONDING A) THE BURST RELEASE OF GLP-1 RA AT THE 0HR TIME POINT OR B) THE DIFFUSION RELEASE OF GLP-1 RA AFTER 24 HOURS

TABLE 9 INTERACTION PARAMETERS BETWEEN PLGA AND EACH SOLVENT USED IN THE ENCAPSULATION PROCESS

Polymer	Solvent	X_{12}
PLGA	Dichloromethane	0.25286
	Chloroform	0.553401
	Tetrahydrofuran	0.675793
	Ethyl Acetate	0.812947
	Acetone	0.370597
	Acetonitrile	0.055169

In addition to the ΔG_{mix} between solvent and non-solvent in the PIN process, here we also consider the PLGA interaction with the solvent and the corresponding impact on encapsulation and release of GLP-1 RA. Specifically, the Flory-Huggins interaction parameter (X_{12}) was used to analyze the affinity between the PLGA and each solvent used in the encapsulation process (Table 7). The interaction parameter X_{12} is a dimensionless parameter that depends on the nature of both polymer and solvent and defines the total of interactions between pairs of polymer segments, between pairs of solvent molecules, and between polymer segments and solvent molecules. It has been shown that X_{12} may be determined using the Hildebrand solubility parameter:

$$X_{12} = \frac{v_1}{RT}(\delta_1 - \delta_2)^2$$

Where v_1 is the molar volume of the solvent and δ_1 and δ_2 are the Hildebrand solubility parameters of the solvent and polymer respectively. The criterion of a good solvent is typically regarded as

the $\delta_1 \approx \delta_2$. Thus, for this analysis it is important to note that the general notation is such that a lower X_{12} value indicates more favorable interaction between polymer and solvent.

To this end, Figure 12 displays the relationship between GLP-1RA release from the PLGA nanoparticles and the PLGA interaction parameter, X_{12}, with the solvent used to create the particles. Specifically, Figure 12a shows the GLP-1RA burst release at the 0hr time point as a function of the X_{12} between the PLGA and solvent. Accordingly, Figure 12b shows the GLP-1RA release at the 24hr time point as a function of the X_{12} between the PLGA and solvent used to produce the particles. To aid in this analysis, Table 7 displays the X_{12} of each solvent with PLGA.

Generally, it can be seen in Figure 12 that particles produced from solvents with low interaction parameters with the PLGA tend towards a lower GLP-1 RA burst release (Figure 12a) and lower diffusion within the first 24 hours (Figure 12b). Specifically, from Table 7 it can be seen that dichloromethane, chloroform, and acetonitrile have comparatively low X_{12} values with PLGA, ranging from 0.055 to 0.55. Correspondingly, Figure 12 shows these formulations to have minimal burst release (ranging from 0.33% to 14.4%) and 24 hour diffusion (ranging from 5.95% to 33.64%). To this end, it can be seen in the release curves from Figure 9 and 10a that these formulations predominantly retain the GLP-1 RA through a lag period of approximately 200 hours and show the majority of release upon the initiation of polymer degradation.

On the other hand, ethyl acetate and tetrahydrofuran show comparatively higher X_{12} values with PLGA (Table 7) and particles formed from these solvent tended towards a larger GLP-1 RA burst release and 24 hour diffusion (Figure 12). Specifically, from Table 7 it can be seen that ethyl acetate has a X_{12} of 0.81 with PLGA, and tetrahydrofuran has a X_{12} of 0.68 with PLGA. Correspondingly, Figure 12 shows that particles formed from these solvents release the GLP-1 RA

primarily by burst and diffusion, with the burst release ranging from 10% to 70% and the 24 hour release ranging from 62.19% to 97.81%.

Thus from Figure 12, it appears that the interaction parameter between the PLGA and solvent may correspond to the ability of PLGA to encapsulate the micronized GLP-1 RA. This correlation may potentially be explained by the chain conformation of the solubilized PLGA in solvents of varying affinity. Solvents with lower PLGA X_{12} value are thought to have a higher affinity to the polymer and thus are expected to interact with a higher number of monomers within the polymer chain, overall resulting in a more extended chain conformation of the solubilized polymer. On the other hand, solvents with higher PLGA X_{12} values are thought to have a lower affinity to the polymer and thus are expected to interact less favorably with the monomers in the polymer chain, resulting in a more compact chain conformation of the solubilized polymer. To this end, the extended PLGA chain conformation facilitated by good solvents such as dichloromethane, chloroform, and acetonitrile may result in a higher state of super saturation and greater ability to encapsulate the micronized GLP-1 RA upon precipitation in the PIN process.

It should be noted that acetone appears to be an exception to this trend, showing a X_{12} value of 0.37 with PLGA. Despite having a comparatively low interaction parameter with PLGA (i.e. lower than that of chloroform), acetone was seen to release the GLP-1 RA primarily by burst release (ranging from 21% to 55%) and 24 hour diffusion (ranging from 67.4% to 78.4%) (Figure 12). To this end, this deviation may arise from the polar nature of acetone. Amongst the six polymer solvents tested in Table 7, acetone and acetonitrile are considered to be polar with dipole moments of 2.88 D and 3.92 D, respectively. Whereas, dichloromethane, chloroform, tetrahydrofuran, and ethyl acetate are considered to be non-polar or only 'borderline' polar with dipole moments ranging from 1.04 D to 1.78 D.[163] This is important as the encapsulated GLP-1 RA is most soluble

in highly polar solvents (i.e. water and methanol). While the suspended micronized GLP-1 RA is not soluble in acetone, it is expected to have a higher degree of solvation with a polar solvent compared to a non-polar solvent. This strong surface interaction of the micronized GLP-1 RA with acetone may in part inhibit its availability to act as a nucleation center upon polymer precipitation in the PIN process. However, it should also be noted that this phenomenon was not seen in the particles produced with acetonitrile (which is also considered highly polar). To this end, acetonitrile has lowest X_{12} value with PLGA of 0.055 and comparatively lower ΔG_{mix} with the non-solvent when compared to acetone (see Table 6). Thus, a combination of X_{12}, ΔG_{mix}, and polarity may be important when considering the ability of PLGA to encapsulate the micronized GLP-1 RA.

Effect of PLGA Monomer Ratio and Molecular Weight on Release

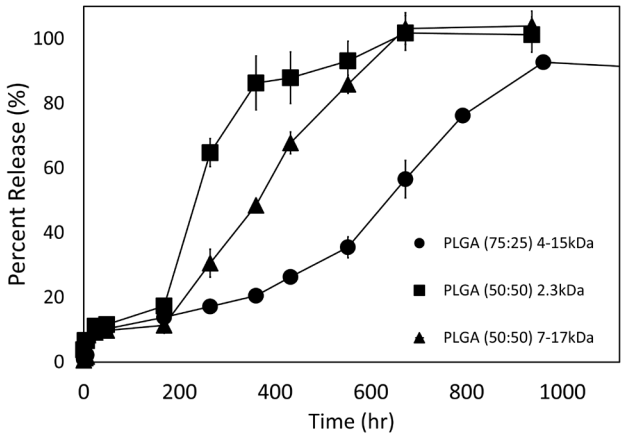

FIGURE 14. REPRESENTATIVE RELEASE CURVES PRODUCED WITH DICHLOROMETHANE AS A SOLVENT AND 2-PROPANOL AS A NON-SOLVENT, DEMONSTRATING THE VARIATION IN RELEASE BEHAVIOR BETWEEN DIFFERENT TYPES OF PLGAS

In this section, we explore the effect of varying PLGA monomer ratio and molecular weight on the release of GLP-1 RA from PLGA nanoparticles. Figure 13 depicts representative GLP-1 RA release curves from PLGA nanoparticles made under identical conditions. The only variable between each of the three release curves in Figure 13 was the type of PLGA used to encapsulate the peptide (i.e. PLGA (75:25) 4-15 kDa, PLGA (50:50) 2.3 kDa, or PLGA (50:50) 7-17 kDa). Figure 13 depicts all formulations produced with dichloromethane as a solvent and 2-propanol as a non-solvent, however similar trends were seen for formulations produced with dichloromethane/heptane, chloroform/2-propanol, chloroform/heptane, and acetonitrile/2-propanol (Figure 9 and 10a). Thus, Figure 13 serves to represent the overarching trend of varying PLGA type amongst these formulations.

It can be seen in Figure 13 that all three identical formulations with varying PLGA type had similar burst release, diffusion, and lag period. With burst release ranging from 0.57% to 3.80% and release after 24 hours ranging from 9.20% to 11.06%. In addition the lag period appeared to be approximately 200 hours for each formulation. Upon the onset of polymer degradation, each formulation began to release the GLP-1 RA and showed distinct release profile behavior based on the molecular weight and monomer ratio, with the PLGA (50:50) 2.3 kDa releasing the fastest and the PLGA (75:25) 4-15kDa releasing the slowest.

Generally speaking, PLGA degrades by hydrolysis of ester links resulting in bulk or heterogeneous erosion. Upon addition to an aqueous environment, PLGA will begin to hydrate as water penetrates the amorphous regions. Penetration of water molecules disrupts the secondary bonding within the PLGA network, resulting in a decrease in glass transition temperature. This ultimately leads to the initial degradation of the polymer, in which cleavage of covalent ester linkages occurs. Upon the onset of degradation, carboxylic end groups may auto catalyze the degradation process. Finally, the fragments of the degraded polymer chain begin to solubilize and diffuse into the aqueous environment.[164]

The degradation process of PLGA has been shown to be dependent on both molecular weight and monomer ratio.[164,165] Researchers have reported that increasing molecular weight from 10-20 to 100 kDa resulted in the degradation varying from several weeks to several months. [164] In addition, since lactic acid is more hydrophobic than glycolic acid, PLGA with higher lactic acid content is less hydrophilic, absorbs less water, and degrades more slowly.[164] Thus, in Figure 13 it appears that PLGA (50:50) 2.3 kDa degrades the fastest and releases the GLP-1 RA fastest due to the higher glycolic acid content and low molecular weight. Similarly, increasing the molecular weight but keeping the monomer ratio fixed (i.e. PLGA (50:50) 7-17 kDa) resulted in a decreased

degradation and release rate. Finally, increasing both the molecular weight and the lactic acid content (i.e. PLGA (75:25) 4-15 kDa) resulted in the slowest degradation and release rate.

CONCLUSION

The work presented here has demonstrated the ability to achieve the encapsulation and release of a GLP-1 RA peptide from PLGA nanoparticles using a process termed phase inversion nanoencapsulation. Specifically, we provide evidence towards the mechanism of particle formation by supersaturation, nucleation, and growth upon adding a solubilized polymer or drug solution to a miscible non-solvent. Here, this mechanism is correlated to the Gibbs energy of mixing (ΔG_{Mix}) between the solvent and non-solvent used in the phase inversion process, calculated using the activity coefficients obtained from the UNIFAC method. By choosing the appropriate solvent and non-solvent pairs for the phase inversion process, it is demonstrated that particle size, encapsulation efficiency, and release profile can be optimized and tailored for a desired function. It was shown that the size of GLP-1 RA and PLGA particles tends to decrease with increasingly negative ΔG_{Mix} of the solvent and non-solvent pairs used to produce them. For example, solvent and non-solvent pair with a $\Delta G_{Mix}/RT$ value of -1.293 (dichloromethane and heptane) yielded PLGA particles with a number average size of 260 nm while those with a less negative $\Delta G_{Mix}/RT$ value of -0.205 (acetone and heptane) yielded particles with a comparatively larger number average size of 638 nm. To this end, it was also shown that the ΔG_{Mix} of solvent and non-solvent pairs used in the phase inversion process correlates to the GLP-1 RA encapsulation efficiency and release behavior of the drug from PLGA particles. It was shown that GLP-1 RA encapsulated using solvent and non-solvent pairs with $\Delta G_{Mix}/RT$ values (between approximately -1.4 and -0.6) displayed low burst release (0-20% of the theoretical loading) and released the majority of drug after an approximate 8 day (200 hour) lag period. On the other hand,

GLP-1 RA encapsulation using solvent and non-solvent pairs with less negatives $\Delta G_{Mix}/RT$ values (between approximately -0.6 and -0.2) displayed large burst release (approximately 20-70% of the theoretical loading) with the majority of the drug being released by the 1 day (24 hour) time point (approximately 60-100% of the theoretical loading). Herein, we present this correlating between ΔG_{Mix} and particle size, encapsulation efficiency, and release profile through the mechanism of supersaturation, nucleation, and growth.

SUPPLEMENTAL MATERIALS

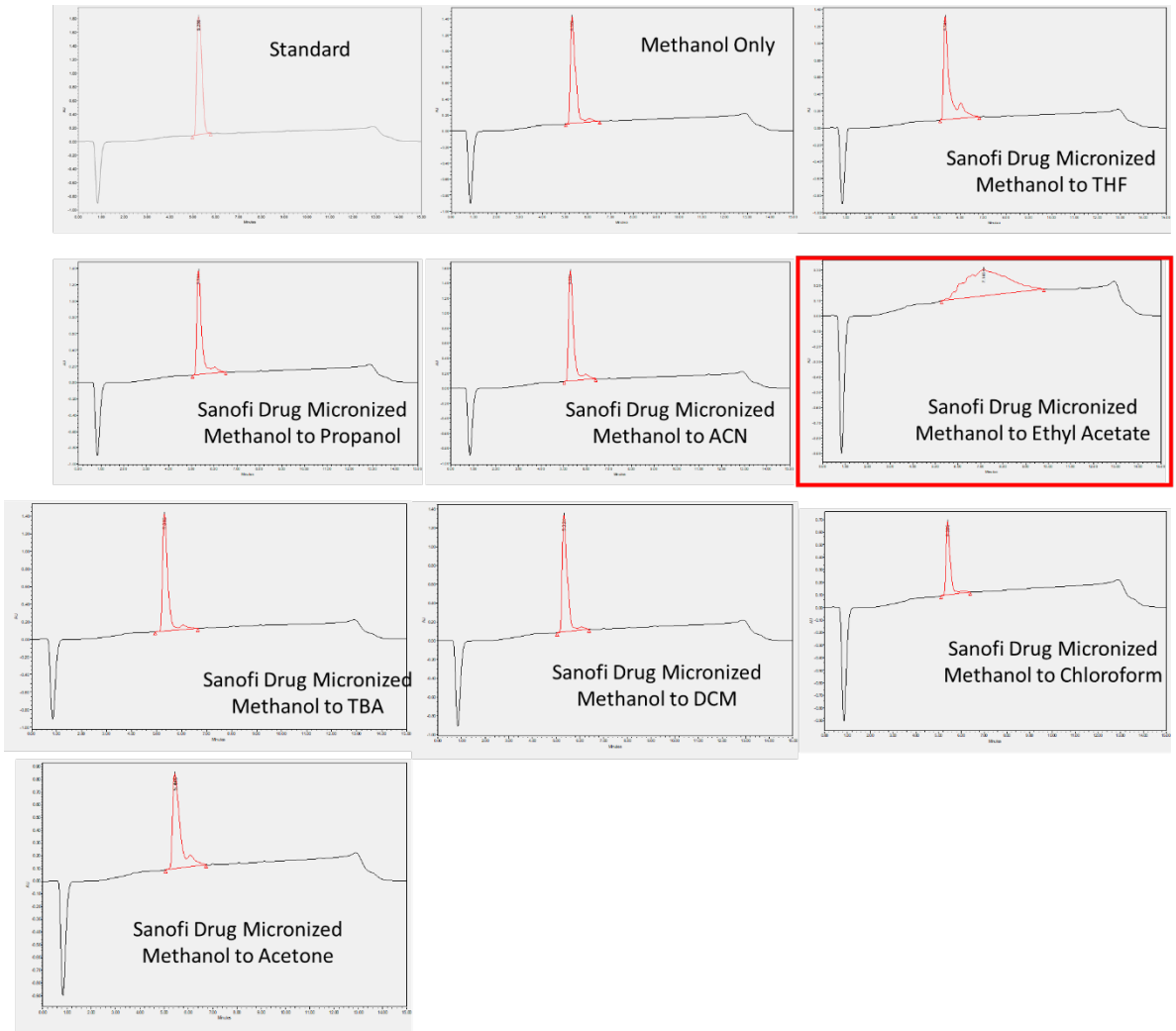

FIGURE 1S REPRESENTATIVE HPLC CHROMATOGRAMS OF GLP-1RA ELUTION AFTER MICRONIZATION WITH DIFFERENT SOLVENT AND NON-SOLVENT COMBINATIONS. THE SHAPE OF THE HPLC CURVE AND RETENTION TIME WAS USED TO GAIN INSIGHT INTO PEPTIDE STABILITY

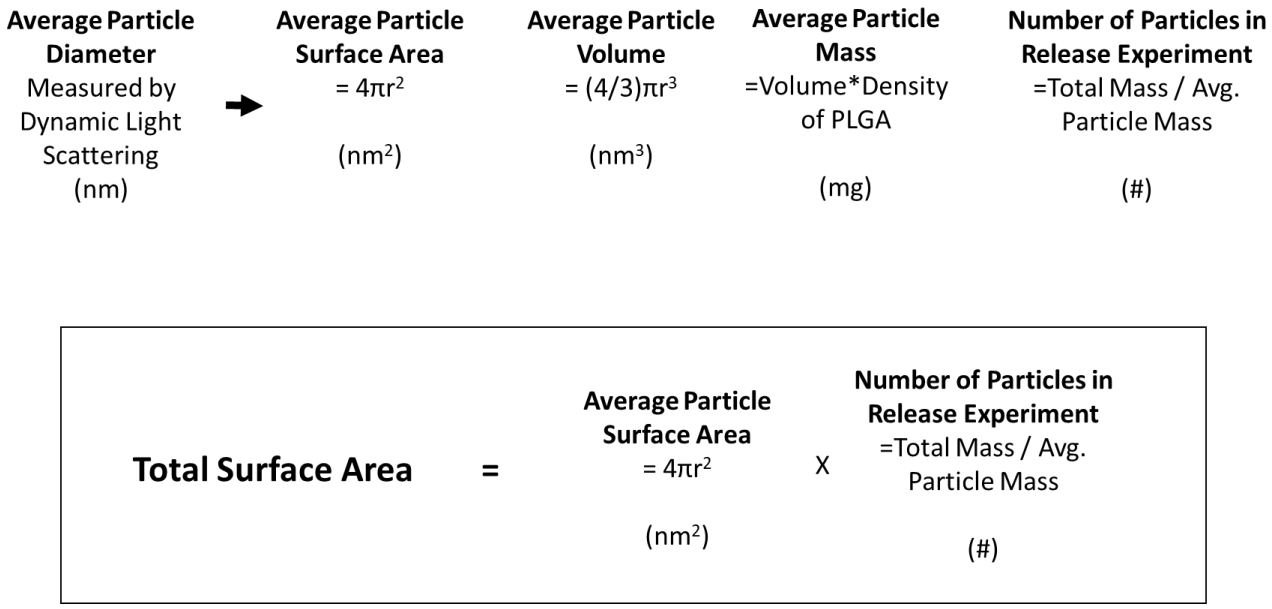

FIGURE 2S METHOD OF APPROXIMATING SURFACE AREA FROM PARTICLE DIAMETER

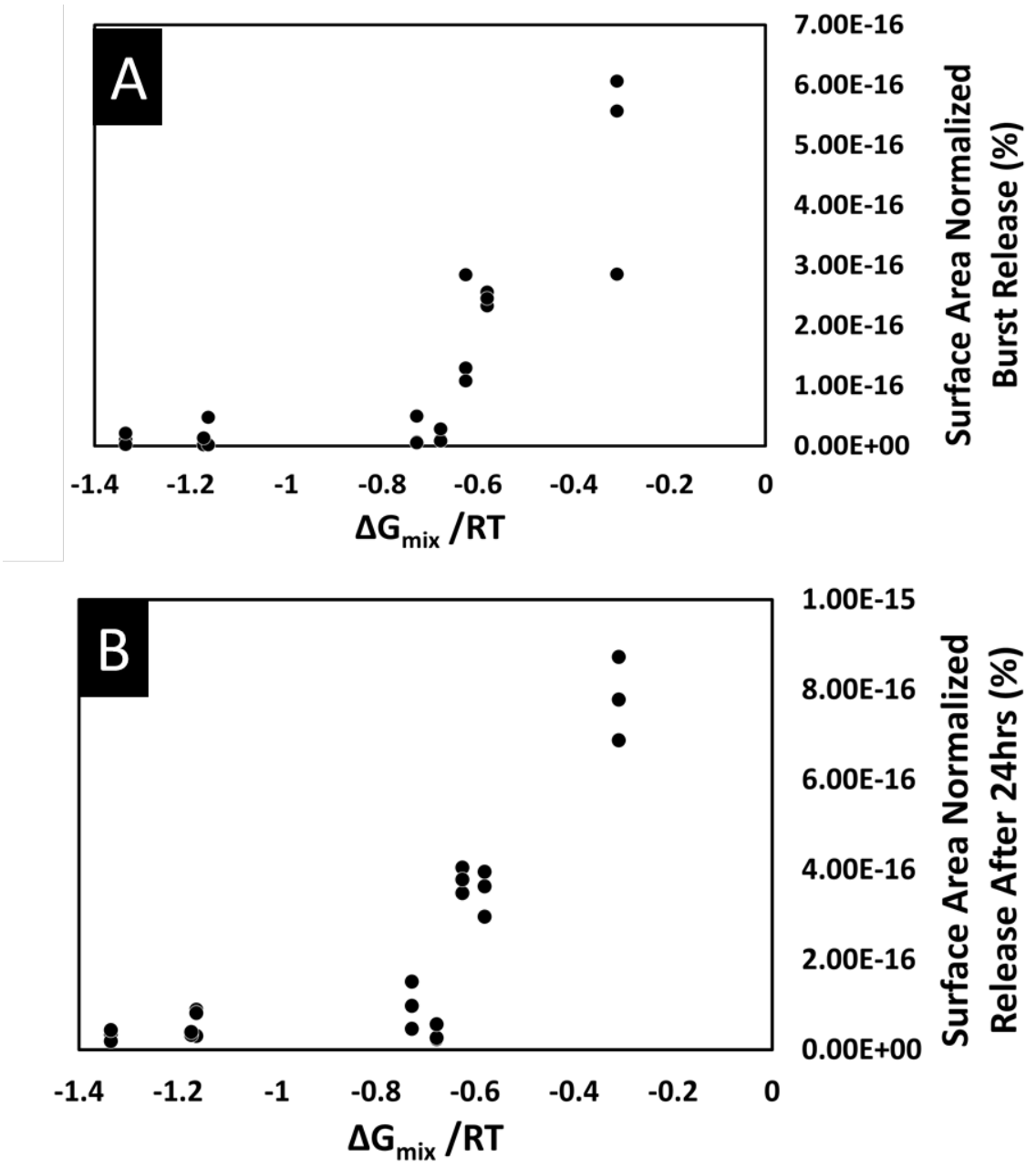

FIGURE 3S SURFACE AREA NORMALIZED RELATIONSHIP BETWEEN GIBBS ENERGY OF MIXING BETWEEN THE SOLVENT AND NON-SOLVENT USED IN THE PIN PROCESS AND A) THE BURST RELEASE OF GLP-1 RA AT THE 0HR TIME POINT OR B) THE DIFFUSION RELEASE OF GLP-1 RA AFTER 24 HOURS

CONCLUSIONS

The work presented in this dissertation has explored novel methods towards improving the use of polymeric biomaterials in drug delivery applications. Specifically, in **Project 1** we explored the ability to induce mesophase morphology into non-mesogenic biodegradable polymers, Poly-l-lactic acid (PLA) and Polycaprolactone (PCL), for the application of long-acting implants to deliver small molecule hydrophobic drugs. In **Project 2**, we explored the thermodynamics of nanoparticle formation by phase inversion and used this understanding towards the optimization of a nanoparticle formulation containing a GLP-1RA peptide for its long-acting treatment of type 2 diabetes. The conclusions and thoughts towards future directions will be discussed here.

PROJECT 1:

Long-Acting Polymeric Delivery Depots Containing Small Molecule Drugs

The specific aims for this project were to (1) Induce mesophase morphology in biocompatible polymers, PLA and PCL, and characterize their molecular arrangement using: XRD, DSC, and PLM and (2) Develop long-acting drug delivery depots containing hydrophobic small molecule drugs utilizing mesophase morphology.

Through specific aim 1, our lab has been amongst the first to demonstrate the ability to induce mesomorphic phases into PLA and PCL using hydraulic compression processing. In addition, while other reports have previously demonstrated PLA mesophase formation through other processing techniques, such as tensile stretching and extrusion, the work presented here has provided a novel characterization which suggests that two distinct types of mesophases may form in PLA, namely a nematic mesophase and a condis-crystal mesophase. To this end, it was also shown that PCL may form two distinct mesophases: a plastic crystal and condis-crystal mesophase.

This characterization of PCL is particularly significant as this work is possibly the first published evidence that indicates PCL can be formulated with induced mesophase morphology. These findings may point towards future directions, suggesting that it is also important to consider that other semi-crystalline or amorphous polymeric material might exhibit mesophase behavior under conditions of temperature and pressure processing. Polymeric mesophases in non-mesogenic polymers may be more ubiquitous than previously thought, particularly since high pressure manufacturing (such as hydraulic compression) is a common industrial practice. We have shown that these mesophases can cause multiple phase transitions, impact the rate and temperature at which crystallization occurs, and also impact the controlled release of a small molecule hydrophobic drug. Thus, even unintentionally, if the energy needed to induce a mesophase is exceed by some manufacturing processes, these phase changes can have a considerable impact on the properties of polymers in biomedical and other applications. The research demonstrated in this dissertation servers to provide new insight and methodology for a more detailed structural characterization of polymeric materials.

While properties of amorphous and crystalline morphologies are documented for many polymeric systems, the structural properties of more complex processing-induced mesophase morphologies have not been discussed at nearly the same level. A potential reason for this is that no single analytical method alone is sufficient in characterizing the formation of these structures. A key aspect of the work presented here was the use of a novel approach which combines traditional methods such as XRD, DSC, and PLM for the characterization these morphologies, particularly with an emphasis on hot-stage XRD and hot-stage PLM. Static XRD images were used to provide initial insight into the degree of positional, orientational, and conformation order of each processed polymer sample. However, many of the indicating factoring of these

morphologies can be misinterpreted from XRD artifacts that might result from sample topography, surface texture, or x-ray focusing. Thus, to build confidence in the analysis of these structures, supporting hot-stage XRD scans may be used to indicate the temperatures at which these morphologies are reversed in the sample. In addition, PLM may be used to corroborate the analysis through the visualization of birefringence which indicated structural long range orientation. In addition, through hot-stage PLM the temperature at which the birefringence become extinct is expected to align with the temperature at which anisotropy is reversed by hot-stage XRD. Thus it is established in this dissertation that a combination of these approaches, along with the more traditional analysis of thermal properties by DSC, may allow for a clear indication of mesophase formation and behavior.

Through specific aim 2, our lab has shown the ability to achieve a slow sustained release of a model small molecule hydrophobic drug, dexamethasone, for periods up to 6 months by using PCL matrix systems. As part of the Center for Biomedical Engineering and Department of Pathology at Brown, a major motivation for analyzing mesophase formation in PCL and PLA has been to understand the impact these morphologies may have on the diffusion and release of drugs from polymeric delivery vehicles. Thus the work presented here has explored the ability to induce mesophase morphologies into dexamethasone loaded PCL tablets via hydraulic compression processing. Specifically, it was seen here that many of the characteristics mesophase traits observed by XRD in specific aim 1, were also observed in the PCL dexamethasone delivery systems upon hydraulic compression. In-vitro release studies of these delivery systems which were processed under varying temperature and pressure conditions appeared to demonstrate varying diffusion flux of the drug from the PCL surface. Through the use of the Higuchi equation which models pseudo steady state diffusion from thin homogenously disperse polymer systems allowed

us to approximate the varying diffusion coefficient of dexamethasone through each PCL device. Upon comparing the diffusion coefficient and mesophase content of each device, it appeared that increasing mesophase content was correlated with a decrease in diffusion coefficient.

While it is generally regarded that diffusion-controlled release of small molecule drugs from a polymer is dependent on the structure of the polymer carrier, the work presented here provides a novel perspective on this understanding and is the first to suggest that processing induced mesophase formation may be used to tailor diffusion. It has been shown that control of the solute diffusion coefficient may be achieved by controlling the degree of crystallinity, crosslinking, or branching within the polymer carrier. The mechanism of this controlled diffusion coefficient is attributed to the hindrance or enhancement of diffusion based on the free volume within the morphological structure. Thus the work presented here may add to this mechanism, by providing the groundwork and preliminary evidence to suggest that the reduced free volume of mesophase formation upon hydraulic compression may hinder the rate of solute diffusion.

Pointing towards future direction, there are still many questions which remain towards understanding how mesophase morphology impacts small molecule diffusion and the development of a marketable implantable long term drug delivery device. Thus, the following areas are recommended to be explored. A detailed understanding of the porosity between hydraulically compressed devices may provide a deeper insight into the varying diffusion coefficient. This type of analysis may be achieved using SEM. In addition, broader questions remain regarding the use of varying polymers and small molecule drugs. The work presented here has demonstrated the release of a single drug, dexamethasone, from a single polymer, PCL. Varying polymer and drug systems should be explored for their behavior upon manufacturing with the methods described here. It is generally anticipated that small molecule drugs with varying degrees of hydrophobicity

will have varying degrees of phase separation throughout the polymer matrix. This dispersion and phase separation can have considerable impacts on the release behavior from a polymer matrix. For example, if a drug is completed phase separated from the polymer structure, this can result in large pores forming as the drug dissolves and releases. These pores can then create a network in which more deeply embedded drug can diffuse through. In this instance, drug diffusion would be mediated by the free volume of a network of pores rather than the structure of the polymer matrix. Drug distribution analysis may be achieved through PLM and TEM. Finally, it is also important to note that for a marketable implantable device to be achieved, there is a need for design and manufacturing techniques to be improved. The current study outlined here utilized tablets which were simply placed in the hydraulic press and compressed. These devices allowed for a proof of concept and systematic study of morphology and diffusion, however they may not be regarded as practical implantable devices.

PROJECT 2:

POLYMERIC NANOPARTICLES CONTAINING BIOLOGIC DRUGS

The specific aims for this project were to (1) Engineer drug and polymer particles using phase inversion nanoencapsulation and assess the impact of solvent and non-solvents pairs on the thermodynamics of particle formation and (2) Using a GLP-1 receptor agonist, for the treatment of diabetes, develop a polymer nanoparticle formulation and investigate the effect of solvent and non-solvents pairs on the drug encapsulation efficiency and release profiles.

Through specific aim 1, our lab has demonstrated the ability to produce nanoparticles of varying size based on solvent and non-solvent selection in the phase inversion process. Specifically, particle formation of both GLP-1 RA (drug) and PLGA (polymer) were seen to be

dependent on the solvent and non-solvent selection. Through utilization of the UNIFAC method for estimating activity coefficients, the Gibbs energy of mixing for each solvent and non-solvent pair was calculated. This energy of mixing appeared to correlate with the resulting particle size for both GLP-1RA and PLGA, with a more negative Gibbs energy tending towards smaller particles. This relationship between solvent and non-solvent mixing and particle size has several important implications for the formulation of PIN particles. First, it provides insight into the underlying thermodynamics and mechanism of particle formation by phase inversion. Inherently, upon addition to a non-solvent, polymer nanoparticles are a high energy state due to their maximized surface area. From a thermodynamic perspective, polymer precipitation into larger particles and aggregates is the more favored outcome. However, the work demonstrated here suggests that increasing the spontaneous rate of mixing between solvent and non-solvent in the PIN process can result in decreasing nanoparticle size. Ultimately, this points towards the validation of particle formation by the mechanism of supersaturation, nucleation, and growth. Where increasingly negative Gibbs energy of mixing between solvent and non-solvent is thought to increase the degree of supersaturation and nucleation in the PIN process.

In addition, this correlation between solvent and non-solvent mixing and particle size may serve as a means to improve the future optimization of PIN formulations. A key and unique aspect of the PIN process is the ability to encapsulate micronized drug into a polymer particle. Thus, typically the first step in optimizing these formulations is to develop a micronization process to achieve small nanoparticles of pure drug. For a PIN formulation to be successful, the size of the micronized drugs particles should be smaller than the resulting polymer particles. Our lab has observed that a single solvent and non-solvent pair (for example, water (solvent) and tert-butanol (non-solvent)) can result in drastically different micronization size depending on the drug

properties (i.e. molecular weight, hydrophobicity, excipients, lipidation, etc.). Herein, the results of this work which suggest that solvent and non-solvent selection may serve as a variable in controlling and optimizing the drug micronization size.

Through specific aim 2, our lab has demonstrated the ability to produce GLP-1RA loaded PLGA nanoparticles with varying release behavior based on the solvent and non-solvent selection in the PIN process. Specifically, it was seen that by choosing the appropriate solvent and non-solvent pairs for the phase inversion process, the particle size, encapsulation efficiency, and release profile can be optimized and tailored for a desired function. In the PIN process, the polymer is anticipated to precipitate around the micronized drug suspended in solution, acting as a nucleation point. Based on the work presented here it appears that more negative ΔG_{Mix} may increase the degree of polymer supersaturation which provides am increased affinity of the polymer to encapsulate the GLP-1 RA. Thus, solvent and non-solvent selection may serve as a variable in optimizing future PIN formulations. To this end, future directions are suggested to assess the mechanism of solvent and non-solvent selection on the formulation and release of other biologic drugs with varying properties, such as molecular weight and hydrophobicity.

REFERENCES

1. Brazel, C. & Rosen, S. *Fundamental Principles of Polymeric Materials*. (Wiley, 2012).

2. Nishida, H. & Tokiwa, Y. Effects of higher-order structure of Poly(3-hydrolxybutyrate) on biodegradation. ll Effects of crystal structure on microbial degradation. *J. Environ. Polym. Degrad.* **1**, 65–80 (1993).

3. Shalaev, E., Wu, K., Shamblin, S., Krzyzaniak, J. F. & Descamps, M. Crystalline mesophases: Structure, mobility, and pharmaceutical properties. *Adv. Drug Deliv. Rev.* **100**, 194–211 (2016).

4. Ulery, B. D., Nair, L. S. & Laurencin, C. T. Biomedical applications of biodegradable polymers. *J. Polym. Sci. Part B Polym. Phys.* **49**, 832–864 (2011).

5. Pawlak, A. Cavitation during tensile deformation of high-density polyethylene. *Polymer (Guildf).* **48**, 1397–1409 (2007).

6. Galeski, A. *Strength and toughness of crystalline polymer systems*. *Progress in Polymer Science (Oxford)* **28**, (2003).

7. Elias, H.-G. *Polymerization of Organized Systems*. (Gordon & Breach Science Publishers Ltd, 1977).

8. A. Cuculo, John & Chen, G. Extrusion, fiber formation, and characterization of thermotropic copolyesters. *J. Polym. Sci.* **26**, 179–200 (1988).

9. Li, D. & Xia, Y. Electrospinning of Nanofibers: Reinventing the Wheel? *Adv. Mater.* **16**, 1151–1170 (2004).

10. Snyder, J. Notch tip damage zone in biaxially oriented polypropylene at low temperature. *Appl. Polym. Sci.* **52**, 217 (1994).

11. Qiu, J., Murata, T., Wu, X., Kudo, M. & Sakai, E. Plastic deformation mechanism of crystalline polymer materials during the rolling process. *J. Mater. Sci.* **48**, 1920–1931 (2013).

12. Beslikas, T., Ioannis, G., Goulios, V. & Bikiaris, D. Crystallization Study and Comparative in vitro-in vivo hydrolysis of PLA reinforcement ligament. *Int. J. Mol. Sci.* **12**, (2011).

13. LAWRENCE, M. J. Biodegradable Polymers as Drug Delivery Systems. (Drugs in the Pharmaceutical Sciences Series/45): Edited by Mark Chasin and Robert Langer. *J. Pharm. Pharmacol.* **44**, 72–72 (1992).

14. Thornton, A. W., Nairn, K. M., Hill, A. J. & Hill, J. M. New relation between diffusion and free volume : I . Predicting gas diffusion. **338**, 29–37 (2009).

15. Crisóstomo, J. *et al.* Increasing levels of insulin secretion in bioartificial pancreas technology: co-encapsulation of beta cells and nanoparticles containing GLP-1 in alginate hydrogels. *Health Technol. (Berl).* **10**, 885–890 (2020).

16. Uhl, P. file:///C:/Users/cbaptist/Documents/Solubilit. P. 1039@c6nr00294. G.-1 P. double emulsion. pd. *et al.* Coating of PLA-nanoparticles with cyclic, arginine-rich cell penetrating peptides enables oral delivery of liraglutide. *Nanomedicine Nanotechnology, Biol. Med.* **24**, 102132 (2020).

17. Tomoda, K., Yabuki, N., Terada, H. & Makino, K. Surfactant free preparation of PLGA nanoparticles: The combination of antisolvent diffusion with preferential solvation. *Colloids Surfaces A Physicochem. Eng. Asp.* **457**, 88–93 (2014).

18. Zhang, L. *et al. Tf ligand-receptor-mediated exenatide-Zn2+ complex oral-delivery system for penetration enhancement of exenatide*. *Journal of Drug Targeting* **26**, (Taylor & Francis, 2018).

19. Zhang, L. *et al. The use of low molecular weight protamine to enhance oral absorption of exenatide*. *International Journal of Pharmaceutics* **547**, (2018).

20. Araújo, F. *et al.* In vivo dual-delivery of glucagon like peptide-1 (GLP-1) and dipeptidyl peptidase-4 (DPP4) inhibitor through composites prepared by microfluidics for diabetes therapy. *Nanoscale* **8**, 10706–10713 (2016).

21. Dong, N. *et al.* Development of composite PLGA microspheres containing exenatide-encapsulated lecithin nanoparticles for sustained drug release. *Asian J. Pharm. Sci.* **15**, 347–355 (2020).

22. Eissa, N. G., Elsabahy, M. & Allam, A. Engineering of smart nanoconstructs for delivery of glucagon-like peptide-1 analogs. *Int. J. Pharm.* **597**, 120317 (2021).

23. Ismail, R. *et al.* Encapsulation in polymeric nanoparticles enhances the enzymatic stability and the permeability of the glp-1 analog, liraglutide, across a culture model of intestinal permeability. *Pharmaceutics* **11**, 1–13 (2019).

24. Kankala, R. K. *et al.* Supercritical Fluid-Assisted Decoration of Nanoparticles on Porous Microcontainers for Codelivery of Therapeutics and Inhalation Therapy of Diabetes. *ACS Biomater. Sci. Eng.* **4**, 4225–4235 (2018).

25. Senduran, N. *et al.* Orally deliverable nanoformulation of liraglutide against type 2 diabetic rat model. *J. Drug Deliv. Sci. Technol.* **56**, 101513 (2020).

26. Shi, Y. *et al.* Fc-modified exenatide-loaded nanoparticles for oral delivery to improve

hypoglycemic effects in mice. *Sci. Rep.* **8**, 1–9 (2018).

27. Song, Y. *et al.* Synthesis of CSK-DEX-PLGA Nanoparticles for the Oral Delivery of Exenatide to Improve Its Mucus Penetration and Intestinal Absorption. *Mol. Pharm.* **16**, 518–532 (2019).

28. Yu, M. *et al.* Battle of GLP-1 delivery technologies. *Adv. Drug Deliv. Rev.* **130**, 113–130 (2018).

29. Li, T. *et al.* Characterization of attributes and in vitro performance of exenatide-loaded PLGA long-acting release microspheres. *Eur. J. Pharm. Biopharm.* **158**, 401–409 (2021).

30. Lewis, A. Formulation strategies for sustained release of proteins. *Ther. Deliv.* 457–479 (2010).

31. Wang, J., Wang, B. M. & Schwendeman, S. P. Characterization of the initial burst release of a model peptide from poly(D,L-lactide-co-glycolide) microspheres. *J. Control. Release* **82**, 289–307 (2002).

32. Tracy, M. A. *et al.* Factors affecting the degradation rate of poly(lactide-co-glycolide) microspheres in vivo and in vitro. *Biomaterials* **20**, 1057–1062 (1999).

33. Mathiowitz, E. *Encyclopedia of Controlled Drug Delivery*. (Wiley, 1999).

34. Alexis, F., Pridgen, E., Molnar, L. K. & Farokhzad, O. C. Factors affecting the clearance and biodistribution of polymeric nanoparticles. *Mol. Pharm.* **5**, 505–515 (2008).

35. Siepmann, J., Faisant, N., Akiki, J., Richard, J. & Benoit, J. P. Effect of the size of biodegradable microparticles on drug release : experiment and theory. **96**, 123–134 (2004).

36. Tsoi, K. M. *et al.* Mechanism of hard nanomaterial clearance by the liver. *Nat. Mater.* **15**,

1212–1221 (2016).

37. Wang, H. *et al.* Improved Oral Bioavailability and Liver Targeting of Sorafenib Solid Lipid Nanoparticles in Rats. *AAPS PharmSciTech* (2017). doi:10.1208/s12249-017-0901-3

38. Mathiowitz, E. Oral delivery of proteins by biodegradable nanoparticles. *Adv. Drug Deliv. Rev.* **65**, 811–821 (2013).

39. Klose, D., Siepmann, F., Elkharraz, K. & Siepmann, J. PLGA-based drug delivery systems : Importance of the type of drug and device geometry. **354**, 95–103 (2008).

40. Operti, M. C. *et al.* PLGA-based nanomedicines manufacturing: Technologies overview and challenges in industrial scale-up. *Int. J. Pharm.* **605**, 120807 (2021).

41. Richard, J. Challenges in the delivery of peptide drugs: an industry perspective. **6**, 149–163 (2015).

42. Pace, C. N. *et al.* Protein structure, stability and solubility in water and other solvents. *Philos. Trans. R. Soc. B Biol. Sci.* **359**, 1225–1235 (2004).

43. Cicerone, M. T., Pikal, M. J. & Qian, K. K. Stabilization of proteins in solid form. *Adv. Drug Deliv. Rev.* **93**, 14–24 (2015).

44. Aggarwal, V. & Richardson, J. Improving enzymes by using them in organic solvents. *Heteroat. Analog. Aldehydes Ketones* **409**, 1 (2004).

45. Jacob, J. S. & Mathiowitz, E. A Novel Mechanism for Spontaneous Encapsulation of Active Agents: Phase Inversion Nanoencapsulation. *Carr. Based Drug Deliv.* 214–223 (2004). doi:10.1021/bk-2004-0879.ch015

46. Martínez Rivas, C. J. *et al.* Nanoprecipitation process: From encapsulation to drug delivery.

Int. J. Pharm. **532**, 66–81 (2017).

47. Shibaev, V. & Lam, L. *Liquid Crystalline and Mesomorphic Polymers*. (1994).

48. Wunderlich, B. A classification of molecules, phases, and transitions as recognized by thermal analysis. *Thermochim. Acta* **340**, 37–52 (1999).

49. Hanna, S., Windle, A. & Donald, A. *Liquid Crystalline Polymers*. (Cambridge University Press, 2006).

50. Peters, S. T. *Handbook of Composites*. (Springer-Verlag, 1998).

51. Gordon, M. *Liquid Crystal Polymers II/III*. (Springer, 1984).

52. Hirte, R. No Title. *Acta Polym.* **36**, 242–242 (1985).

53. Gennes, P. G. de. *Physics of Liquid Crystals*. (Oxford Press, 1974).

54. Baker, C., Azagury, A. & Mathiowitz, E. Effect of pressure on poly-L-Lactic Acid morphology. *Polymer (Guildf).* **99**, 250–262 (2016).

55. PerkinElmer. Differential Scanning Calorimetry: A Beginner's Guide. 1–9 (2014).

56. Cassel, B. & Packer, R. Modulated Temperature DSC: A Step Up in Performanc. *PerkinElmer*

57. Post, B. X-ray diffraction methods in polymer science, Leroy E. Alexander, wiley-interscience, new york, 1970. xv + 582 pp. *J. Polym. Sci. Part B Polym. Lett.* **9**, 635–636 (1971).

58. Weber, M. F. Giant Birefringent Optics in Multilayer Polymer Mirrors. *Science (80-.).* **287**, 2451–2456 (2000).

59. Lorenz, M., Evers, A. & Wagner, M. Recent progress and future options in the development

of GLP-1 receptor agonists for the treatment of diabesity. *Bioorganic Med. Chem. Lett.* **23**, 4011–4018 (2013).

60. Inzucchi, S. E. *et al.* Management of Hyperglycemia in Type 2 Diabetes: A Patient-Centered Approach. *Diabetes Care* **35**, 1364–1379 (2012).

61. Collins L, C. R. Glucagon-like Peptide-1 Receptor Agonists. *StatPearls Publishing* (2021). Available at: https://www.ncbi.nlm.nih.gov/books/NBK551568/.

62. Anderson, J. M. & Shive, M. S. Biodegradation and biocompatibility of PLA and PLGA microspheres. **28**, 5–24 (1997).

63. Hoffman, A. S. The origins and evolution of " controlled " drug delivery systems. *J. Control. Release* **132**, 153–163 (2008).

64. Wischke, C. & Schwendeman, S. P. Principles of encapsulating hydrophobic drugs in PLA / PLGA microparticles. **364**, 298–327 (2008).

65. Carino, G. P., Jacob, J. S. & Mathiowitz, E. Nanosphere based oral insulin delivery. *J. Control. Release* **65**, 261–269 (2000).

66. Azagury, A. *et al.* Single Step Double-walled Nanoencapsulation (SSDN). *J. Control. Release* **280**, 11–19 (2018).

67. Sovan Lal Pal, Utpal Jana, P. K. Manna, G. P. Mohanta, R. M. Nanoparticle: An overview of preparation and characterization. *J. Appl. Pharm. Sci.* **6**, 228–234 (2011).

68. Stetefeld, J., McKenna, S. A. & Patel, T. R. Dynamic light scattering: a practical guide and applications in biomedical sciences. *Biophys. Rev.* **8**, 409–427 (2016).

69. So, P. & Broutman, L. J. Residual stresses in polymers and their effect on mechanical

behavior. *Polym. Eng. Sci.* **16**, 785–791 (1976).

70. ZOETELIEF, W. F., DOUVEN, L. F. A. & INGEN HOUSZ, A. J. Residual Thermal Stresses in Injection Molded Products. *Polym. Eng. Sci.* **36**, 1866–1896 (1996).

71. Schreiber, T., Schultz, H. & Schmidt, O. Stress-induced birefringence in large-mode-area micro-structured optical fibers. *Opt. Express* **13**, (2005).

72. Hammack, T. J. & Andrews, R. D. Temperature Dependence of Orientation Birefringence of Polymers in the Glassy and Rubbery States. II. *J. Appl. Phys.* **36**, 3574–3581 (1965).

73. Gent, A. . Stress-induced birefringence of swollen polymer networks. *Macromolecules* **2**, 262–265 (1969).

74. La Mantia, F. P., Ceraulo, M., Mistretta, M. C. & Morreale, M. Effect of cold drawing on mechanical properties of biodegradable fibers. *J. Appl. Biomater. Funct. Mater.* 0–0 (2016). doi:10.5301/jabfm.5000328

75. Stoclet, G., Seguela, R., Lefebvre, J. M., Elkoun, S. & Vanmansart, C. Strain-induced molecular ordering in polylactide upon uniaxial stretching. *Macromolecules* **43**, 1488–1498 (2010).

76. Lan, Q., Li, Y. & Chi, H. Highly Enhanced Mesophase Formation in Glassy Poly(l -lactide) at Low Temperatures by Low-Pressure CO2That Provides Moderately Increased Molecular Mobility. *Macromolecules* **49**, 2262–2271 (2016).

77. Liang, Y. Y., Tang, H., Zhong, G. J. & Li, Z. M. Formation of poly(L-lactide) mesophase and its chain mobility dependent kinetics. *Chinese J. Polym. Sci. (English Ed.* **32**, 1176–1187 (2014).

78. Stoclet, G., Seguela, R., Lefebvre, J. M. & Rochas, C. New insights on the strain-induced

mesophase of poly(d, l-lactide): In situ WAXS and DSC study of the thermo-mechanical stability. *Macromolecules* **43**, 7228–7237 (2010).

79. Lv, R. *et al.* Mesophase formation and its thermal transition in the stretched glassy polylactide revealed by infrared spectroscopy. *Polymer (Guildf).* **52**, 4979–4984 (2011).

80. Zhou, C., Li, H., Zhang, W., Li, J. & Huang, S. Direct investigations on strain-induced cold crystallization behavior and structure evolutions in amorphous poly (lactic acid) with SAXS and WAXS measurements. *Polymer (Guildf).* **90**, 111–121 (2016).

81. Androsch, R., Laura, M., Lorenzo, D., Schick, C. & Wunderlich, B. Mesophases in polyethylene , polypropylene , and poly (1-butene). *Polymer (Guildf).* **51**, 4639–4662 (2010).

82. Garlotta, D. A Literature Review of Poly (Lactic Acid). **9**, (2002).

83. Woodruff, M. A. & Hutmacher, D. W. The return of a forgotten polymer—Polycaprolactone in the 21st century. *Prog. Polym. Sci.* **35**, 1217–1256 (2010).

84. Langer, R. & Chasin, M. *Biodegradable polymers as drug delivery systemsitle*. (1990).

85. Dash, T. K. & Konkimalla, V. B. Poly-ε-caprolactone based formulations for drug delivery and tissue engineering: A review. *J. Control. Release* **158**, 15–33 (2012).

86. Jame, M. *Polymer Data Handbook*. (2009).

87. Labet, M. & Thielemans, W. Synthesis of polycaprolactone: a review. *Chem. Soc. Rev.* **38**, 3484 (2009).

88. Chandra, R. Biodegradable polymers. *Prog. Polym. Sci.* **23**, 1273–1335 (1998).

89. Middleton, J. C. & Tipton, J. Synthetic biodegradable polymers as orthopedic devices.

Biomaterials **21**, (2000).

90. Woodward, S. C., Brewer, P. S., Moatamed, F., Schindler, A. & Pitt, C. G. The intracellular degradation of poly(?-caprolactone). *J. Biomed. Mater. Res.* **19**, 437–444 (1985).

91. McEachin, Z. & Lozano, K. Production and characterization of polycaprolactone nanofibers via forcespinning™ technology. *J. Appl. Polym. Sci.* **126**, 473–479 (2012).

92. Hermanová, S. *et al.* The Effect of Processing of Polycaprolactone Films on Degradation Process Initiated by Aspergillus Oryzae Lipase. *Int. J. Polym. Anal. Charact.* **17**, 465–475 (2012).

93. Agarwal, S. & Speyerer, C. Degradable blends of semi-crystalline and amorphous branched poly(caprolactone): Effect of microstructure on blend properties. *Polymer (Guildf).* **51**, 1024–1032 (2010).

94. Wang, Y., Rodriguez-Perez, M. A., Reis, R. L. & Mano, J. F. Thermal and Thermomechanical Behaviour of Polycaprolactone and Starch/Polycaprolactone Blends for Biomedical Applications. *Macromol. Mater. Eng.* **290**, 792–801 (2005).

95. McKeen, L. Renewable Resource and Biodegradable Polymers. in *The Effect of Sterilization on Plastics and Elastomers* 305–317 (Elsevier, 2012). doi:10.1016/B978-1-4557-2598-4.00012-5

96. Hu, H. & Dorset, D. L. Crystal structure of poly(iε-caprolactone). *Macromolecules* **23**, 4604–4607 (1990).

97. Allegra, G. *Interphases and Mesophases in Polymer Crystallization II*. **181**, (Springer Berlin Heidelberg, 2005).

98. De Rosa, C. *et al.* Crystalline Ethylene−Norbornene Copolymers: Plastic Crystals from

Macromolecules. *Macromolecules* **36**, 3789–3792 (2003).

99. Keith, H. D. & Passaglia, E. Dislocations in Polymer Crystals. *J. Res. Natl. Bur. Stand. (1934).* **68A**, 513–518 (1964).

100. Tani, Y. C. H. A., Okita, Y., Adokoro, H. T. & Amashita, Y. Structural Studies of Polyesters . III . Crystal Structure of Poly-e-caprolactone. **1**, 555–562 (1970).

101. Bassett, D. C., Block, S. & Piermarini, G. J. A high-pressure phase of polyethylene and chain-extended growth. *J. Appl. Phys.* **45**, 4146–4150 (1974).

102. Wunderlich, B. & Arakawa, T. Polyethylene crystallized from the melt under elevated pressure. *J. Polym. Sci. Part A Gen. Pap.* **2**, 3697–3706 (1964).

103. Cheng, J. *et al.* Identification and quantitative analysis of the intermediate phase in a linear high-density polyethylene. *J. Polym. Sci. Part B Polym. Phys.* **32**, 2683–2693 (1994).

104. Chatani, Y., Okita, Y., Tadokoro, H. & Yamashita, Y. Structural Studies of Polyesters. III. Crystal Structure of Poly-ε-caprolactone. *Polym. J.* **1**, 555–562 (1970).

105. Yamamoto, T., Miyaji, H. & Asai, K. Structure and Properties of High Pressure Phase of Polyethylene. *Jpn. J. Appl. Phys.* **16**, 1891–1898 (1977).

106. Wunderlich, B., Möller, M., Grebowicz, J. & Baur, H. *Conformational Motion and Disorder in Low and High Molecular Mass Crystals*. **87**, (Springer Berlin Heidelberg, 1988).

107. Zhuravlev, E., Schmelzer, J. W. P., Wunderlich, B. & Schick, C. Kinetics of nucleation and crystallization in poly(ε-caprolactone) (PCL). *Polymer (Guildf).* **52**, 1983–1997 (2011).

108. Liu, X., Zhao, Y., Fan, X. & Chen, E. Crystal orientation and melting behavior of poly(ε-

Caprolactone) under one-dimensionally “hard” confined microenvironment. *Chinese J. Polym. Sci.* **31**, 946–958 (2013).

109. Wang, Y. *et al.* Unusual structural evolution of poly(lactic acid) upon annealing in the presence of an initially oriented mesophase. *Soft Matter* **10**, 1512–1518 (2014).

110. Wang, Y. *et al.* Spectroscopic analysis of post drawing relaxation in poly(lactic acid) with oriented mesophase. *Polym. Test.* **43**, 103–107 (2015).

111. Puchalski, M., Kwolek, S., Szparaga, G., Chrzanowski, M. & Krucińska, I. Investigation of the Influence of PLA Molecular Structure on the Crystalline Forms (α’ and α) and Mechanical Properties of Wet Spinning Fibres. *Polymers (Basel).* **9**, 18 (2017).

112. Grassia, L., Pastore Carbone, M. G., Mensitieri, G. & D’Amore, A. Modeling of density evolution of PLA under ultra-high pressure/temperature histories. *Polymer (Guildf).* **52**, 4011–4020 (2011).

113. Baptista, C. *et al.* The effect of temperature and pressure on polycaprolactone morphology. *Polymer (Guildf).* **191**, 122227 (2020).

114. Wasanasuk, K. *et al.* Crystal Structure Analysis of Poly(l -lactic Acid) α Form On the basis of the 2-Dimensional Wide-Angle Synchrotron X-ray and Neutron Diffraction Measurements. *Macromolecules* **44**, 6441–6452 (2011).

115. John, S. Structural Studies of Liquid Crystals by X-ray Diffraction. in *Handbook of Liquid Crystals* 635–655 (1998). doi:10.1002/9783527671403

116. Mulligan, J. & Cakmak, M. Nonlinear Mechanooptical Behavior of Uniaxially Stretched Poly (lactic acid): Dynamic Phase Behavior. 2333–2344 (2005). doi:10.1021/ma048794f

117. Monnier, X. *et al.* Molecular dynamics in electrospun amorphous plasticized polylactide

fibers. *Polymer (Guildf).* **73**, 68–78 (2015).

118. Na, B. *et al.* Unusual Cold Crystallization Behavior in Physically Aged Poly(l -lactide). *J. Phys. Chem. B* **115**, 10844–10848 (2011).

119. Park, J. B. & Uhlmann, D. R. Recovery of deformed polymers. III. Thermal properties. *J. Appl. Phys.* **44**, 201–206 (1973).

120. Hasan, O. . & Boyce, M. . Energy storage during inelastic deformation of glassy polymers. *Polymer (Guildf).* **34**, 5085–5092 (1993).

121. Pawlak, A. & Gałeski, A. Cavitation during tensile drawing of semicrystalline polymers. *Polimery/Polymers* **56**, 627–636 (2011).

122. Galeski, A. Strength and toughness of crystalline polymer systems. *Prog. Polym. Sci.* **28**, 1643–1699 (2003).

123. Z.-Q.HuA.-M.WangH.-F.Zhang. *Modern Inorganic Synthetic Chemistry (Second Edition)*. (2017). doi:https://doi.org/10.1016/B978-0-444-63591-4.00022-7

124. Spathis, G. & Kontou, E. Nonlinear viscoelastic and viscoplastic response of glassy polymers. *Polym. Eng. Sci.* **41**, 1337–1344 (2001).

125. Hasan, O. A. & Boyce, M. C. A constitutive model for the nonlinear viscoelastic viscoplastic behavior of glassy polymers. *Polym. Eng. Sci.* **35**, 331–344 (1995).

126. Di Vona, M. L. Annealing of Polymer Membranes. in *Encyclopedia of Membranes* 1–2 (Springer Berlin Heidelberg, 2014). doi:10.1007/978-3-642-40872-4_627-1

127. Parker, M. J. & Warton, B. A. E. S. Test Methods for Physical Properties.

128. Chung, Y. G., Lacks, D. J. & Chung, Y. G. *Sheared polymer glass and the question of*

mechanical rejuvenation Sheared polymer glass and the question of mechanical rejuvenation. **124907**, (2012).

129. Kulinski, Z. & Piorkowska, E. Crystallization, structure and properties of plasticized poly(l-lactide). *Polymer (Guildf).* **46**, 10290–10300 (2005).

130. Solarski, S., Ferreira, M. & Devaux, E. Characterization of the thermal properties of PLA fibers by modulated differential scanning calorimetry. *Polymer (Guildf).* **46**, 11187–11192 (2005).

131. Pluta, M. & Galeski, A. Crystalline and supermolecular structure of polylactide in relation to the crystallization method. *J. Appl. Polym. Sci.* **86**, 1386–1395 (2002).

132. Kim, M. S., Kim, J. C. & Kim, Y. H. Effects of take-up speed on the structure and properties of melt-spun poly(L-lactic acid) fibers. *Polym. Adv. Technol.* **19**, 748–755 (2008).

133. Pan, P., Zhu, B. & Inoue, Y. Enthalpy Relaxation and Embrittlement of Poly(<scp>l</scp> -lactide) during Physical Aging. *Macromolecules* **40**, 9664–9671 (2007).

134. Lee, S. C., Han, J. Il, Jeong, Y. G. & Kwon, M. Strain-Induced Enthalpy Relaxation in Poly(lactic acid). *Macromolecules* **43**, 25–28 (2010).

135. Na, B. *et al.* Spectroscopic Evidence of Melting of Ordered Structures in the Aged Glassy Poly(l -lactide). *Macromolecules* **43**, 1702–1705 (2010).

136. Kovarova, M. *et al.* Ultra-long-acting removable drug delivery system for HIV treatment and prevention. *Nat. Commun.* **9**, 4156 (2018).

137. Abdelkader, H. *et al.* Polymeric long-acting drug delivery systems (LADDS) for treatment of chronic diseases: Inserts, patches, wafers, and implants. *Adv. Drug Deliv. Rev.* **177**, 113957 (2021).

138. Siepmann, J. & Peppas, N. A. Higuchi equation: Derivation, applications, use and misuse. *Int. J. Pharm.* **418**, 6–12 (2011).

139. PEPPAS, N. A. & LUSTIG, S. R. The Role of Cross-links, Entanglements, and Relaxations of the Macromolecular Carrier in the Diffusional Release of Biologically Active Materials. *Ann. N. Y. Acad. Sci.* **446**, 26–40 (1985).

140. Baptista, C., Azagury, A., Baker, C. M. & Mathiowitz, E. The characterization and quantification of the induced mesophases of poly-l-lactic acid. *Polymer (Guildf).* **226**, 123822 (2021).

141. Higuchi, T. Rate of Release of Medicaments from Ointment Bases Containing Drugs in Suspension. *J. Pharm. Sci.* **50**, 874–875 (1961).

142. W.H.O. Diabetes (Fact sheet no. 312). *World Health Organization* Available at: https://www.who.int/en/news-room/fact-sheets/detail/diabetes. (Accessed: 15th October 2021)

143. I.D.F. IDF Diabetes Atlast Update, 5th ed. *International Diabetes Federation* (2012). Available at: http://www.idf.org/diabetesatlas. (Accessed: 15th October 2021)

144. Evers, A. *et al.* Dual Glucagon-like Peptide 1 (GLP-1)/Glucagon Receptor Agonists Specifically Optimized for Multidose Formulations. *J. Med. Chem.* **61**, 5580–5593 (2018).

145. Prausnitz, J., Lichtenthaler, R. & Gomes de Azevedo, E. *Molecular Thermodynamics of Fluid-Phase Equilibria*. (Prentice Hall PTR, 1999).

146. Fredenslund, A., Gmehling, J. & Rasmussen, P. *Vapor-liquid Equilibria Using Unifac*. (Elsevier, 1977). doi:10.1016/B978-0-444-41621-6.X5001-7

147. Lira, C. & Elliott, R. *Introductory Chemical Engineering Thermodynamics*. (Pearson,

2012).

148. Lira, C. & Elliott, R. Activity Coefficient Excel File. *Michigan State University* (2021). Available at: https://www.egr.msu.edu/~lira/computer/EXCEL/ACTCOEFF.XLS. (Accessed: 5th October 2021)

149. Daniel, J. & Renardy, Y. *Fundamentals of Two-Fluid Dynamics*. (Springer, 1993).

150. Donnelly, D. The structure and function of the glucagon-like peptide-1 receptor and its ligands. *Br. J. Pharmacol.* **166**, 27–41 (2012).

151. Nelson, D. & Cox, M. *Lehninger Principles of Biochemistry*. (Macmillian Learning, 2021).

152. Lapanje, S. *Physicochemical Aspects of Protein Denaturation*. (Wiley, 1978).

153. Fitzpatrick, P. A., Steinmetz, A. C., Ringe, D. & Klibanov, A. M. Enzyme crystal structure in a neat organic solvent. *Proc. Natl. Acad. Sci.* **90**, 8653–8657 (1993).

154. Yennawar, N. H., Yennawar, H. P. & Farber, G. K. X-ray Crystal Structure of .gamma.-Chymotrypsin in Hexane. *Biochemistry* **33**, 7326–7336 (1994).

155. Schmitke, J. L., Stern, L. J. & Klibanov, A. M. The crystal structure of subtilisin Carlsberg in anhydrous dioxane and its comparison with those in water and acetonitrile. *Proc. Natl. Acad. Sci.* **94**, 4250–4255 (1997).

156. Zhu, G. *et al.* X-ray studies on two forms of bovine β-trypsin crystals in neat cyclohexane. *Biochim. Biophys. Acta - Protein Struct. Mol. Enzymol.* **1429**, 142–150 (1998).

157. Gao, X.-G. *et al.* Crystal structure of triosephosphate isomerase from Trypanosoma cruzi in hexane. *Proc. Natl. Acad. Sci.* **96**, 10062–10067 (1999).

158. Klibanov, A. Enzymatic catalysis in anhydrous organic solvents. *Trends Biochem. Sci.* **14**,

141–144 (1989).

159. Adlercreutz, P. Modes of using enzymes in organic media. in *Enzymatic Reactions in Organic Media* 9–42 (Springer Netherlands, 1996). doi:10.1007/978-94-011-0611-5_2

160. Miller, L. M., Bourassa, M. W. & Smith, R. J. FTIR spectroscopic imaging of protein aggregation in living cells. *Biochim. Biophys. Acta - Biomembr.* **1828**, 2339–2346 (2013).

161. Jackson, M. & Mantsch, H. H. The Use and Misuse of FTIR Spectroscopy in the Determination of Protein Structure. *Crit. Rev. Biochem. Mol. Biol.* **30**, 95–120 (1995).

162. Bruce, D. G., Chisholm, D. J., Storlien, L. H., Kraegen, E. W. & Smythe, G. A. The effects of sympathetic nervous system activation and psychological stress on glucose metabolism and blood pressure in subjects with Type 2 (non-insulin-dependent) diabetes mellitus. *Diabetologia* **35**, 835–843 (1992).

163. Minkin, V. I., Osipov, O. A. & Zhdanov, Y. A. *Dipole Moments in Organic Chemistry*. (Springer US, 1970). doi:10.1007/978-1-4684-1770-8

164. Gentile, P., Chiono, V., Carmagnola, I. & Hatton, P. An Overview of Poly(lactic-co-glycolic) Acid (PLGA)-Based Biomaterials for Bone Tissue Engineering. *Int. J. Mol. Sci.* **15**, 3640–3659 (2014).

165. Houchin, M. L. & Topp, E. M. Physical properties of PLGA films during polymer degradation. *J. Appl. Polym. Sci.* **114**, 2848–2854 (2009).